UNIVERSIDAD COMPLUTENSE DE MADRID

FACULTAD DE CIENCIAS QUÍMICAS

Departamento de Química Orgánica I

TESIS DOCTORAL

Molecular engineering of hole and electron transporting materials for perovskite solar cells

Ingeniería molecular de materiales transportadores de huecos o electrones para células solares de perovskita

MEMORIA PARA OPTAR AL GRADO DE DOCTOR

PRESENTADA POR

Inés García Benito

Directores

Nazario Martín León
Agustín Molina Ontoria
Juan Luis Delgado de la Cruz

Madrid, 2017

UNIVERSIDAD COMPLUTENSE DE MADRID

FACULTAD DE CIENCIAS QUÍMICAS

Departamento de Química Orgánica I

MOLECULAR ENGINEERING OF HOLE AND ELECTRON TRANSPORTING MATERIALS FOR PEROVSKITE SOLAR CELLS

TESIS DOCTORAL

Inés García Benito

Madrid, 2017

UNIVERSIDAD COMPLUTENSE DE MADRID

FACULTAD DE CIENCIAS QUÍMICAS

Departamento de Química Orgánica I

Molecular engineering of hole and electron transporting materials for perovskite solar cells

Ingeniería molecular de materiales transportadores de huecos o electrones para células solares de perovskita

TESIS DOCTORAL

Inés García Benito

Directores

Nazario Martín León
Agustín Molina Ontoria
Juan Luis Delgado de la Cruz

Madrid, 2017

D. Nazario Martín León, Catedrático de Universidad del Departamento de Química Orgánica I de la Universidad Complutense de Madrid, **D. Agustín Molina Ontoria**, investigador de IMDEA nanociencia y **D. Juan Luis Delgado de la Cruz**, investigador de Ikerbasque (Instituto PolyMat), Universidad del País Vasco,

CERTIFICAN

Que la presente Memoria titulada "Molecular engineering of hole and electron transporting materials for perovskite solar cells" se ha realizado bajo su dirección en IMDEA nanociencia y en el Departamento de Química Orgánica I de la Universidad Complutense de Madrid, por la licenciada en Ingeniería Química Dña. Inés García Benito y autorizan su presentación para ser calificada como tesis doctoral.

Y para que conste, firmo el presente certificado en Madrid a 30 de marzo de 2017.

Fdo. Dr. Agustín Molina Ontoria

Fdo. Dr. Juan Luis Delgado de la Cruz

Fdo. Prof. Nazario Martín León

The results presented in this thesis have been published and listed below:

1. L. Cabau, I. García-Benito, A. Molina-Ontoria, N. F. Montcada, N. Martín, A. Vidal-Ferran, E. Palomares, "Diarylamino-substituted tetraarylethene (TAE) as an efficient and robust hole transport material for 11 % methyl ammonium lead iodide perovskite solar cells", *Chem. Commun.*, **2015**, *51*, 13980-13982.
2. A. Molina-Ontoria, I. Zimmermann, I. García-Benito, P. Gratia, C. Roldán-Carmona, S. Aghazada, M. Graetzel, M. K. Nazeeruddin, N. Martín, "Benzotrithiophene-based hole-transporting materials for 18.2 % perovskite solar cells", *Angew. Chem. Int. Ed.*, **2016**, *55*, 6270-6274.
3. M. Valles-Pelarda, B. C. Hames, I. García-Benito, O. Almora, A. Molina-Ontoria, R. S. Sánchez, G. Garcia-Belmonte, N. Martín, I. Mora-Sero, "Analysis of the hysteresis behavior of perovskite solar cells with interfacial fullerene self-assembled monolayers", *J. Phys. Chem. Lett.*, **2016**, *7*, 4622-4628.
4. I. García-Benito, I. Zimmermann, J. Urieta, J. Arago, A. Molina-Ontoria, E. Ortí, N. Martín, M. K. Nazeeruddin, "Isomerism effect on the photovoltaic properties of benzotrithiophene-based hole-transporting materials", *J. Mater. Chem. A*, **2017**, 5, 8317-8324.
5. European patent. A. Molina-Ontoria, I. Zimmermann, I. García-Benito, P. Gratia, C. Roldán-Carmona, M. Graetzel, M. K. Nazeeruddin, N. Martín, Application number PCT/IB2016/057475. *In progress.*

A mis padres y mi hermano

Acknowledgments

El presente trabajo ha sido realizado en el Instituto Madrileño de Estudios Avanzados (IMDEA) bajo la dirección del Prof. Nazario Martín León, del Dr. Agustín Molina Ontoria y del Dr. Juan Luis Delgado de la Cruz.

Para comenzar, quisiera expresar todo mi agradecimiento a mis directores de tesis. Nazario, gracias por la confianza que depositaste en mí y por darme la oportunidad de pertenecer a tu grupo de investigación. No creo que vuelva a tener la suerte de tener un jefe tan admirable como eres tú. Gracias por enseñarme tanto y por haber dedicado todo tu tiempo a sacar adelante este trabajo de investigación.

Agustín, gracias por tu paciencia y por tantas lecciones en el laboratorio. Tu atención y motivación durante mi estancia en Suiza fueron realmente de agradecer. Gracias por todo tu apoyo desde el primer día hasta el último y ayudarme a conseguir que el trabajo de estos años se haya convertido en esta tesis que tenemos entre las manos. Aquí tienes por fin la tesis de Chines. No has sido sólo mi director "Dóctor Agus", me has enseñado mucho más. Estoy segura de que tendrás mucha suerte en tu futuro como investigador. Te deseo todo lo mejor.

Juan Luis, gracias por ayudarme a dar los primeros pasos en un laboratorio de química orgánica y enseñarme a afrontar las dificultades que supuso el principio de este periodo. Te deseo mucha suerte con tu grupo de investigación.

También quiero dar las gracias de forma especial a la que fue mi segunda familia durante estos años, los chicos del laboratorio 127. Rafa, cuántas horas compartidas en el laboratorio, cuantas historias difíciles de olvidar. Gracias químico, por todas tus lecciones, consejos y sobre todo por sacarme siempre carcajadas, da igual cuál fuera el momento. Te deseo lo mejor en el futuro. Estoy segura que llegarás lejos con el esfuerzo y la constancia que te caracterizan. Javi, que bonitos trabajos compartidos. Gracias por estar siempre que se te ha necesitado, por ser tan atento y por todo lo que hemos compartido. Te deseo todo lo mejor y no dudo que tu tesis va a ser realmente excelente. Aprende todo lo que puedas de tus dos grandes directores. Por último, el otro gran pilar del laboratorio, Jose, el "gallego-canario". Muchas gracias por estar siempre dispuesto a resolver mis dudas y por tus clases de química, llegarías a ser un buen profesor.

En la realización de este trabajo han participado otros grupos de investigación, a los que agradezco enormemente su contribución:

Al grupo de investigación del Prof. Iván Mora de la Universidad Jaime I, Castellón (España) por la interesante colaboración y al Prof. Enrique Ortí de la Universidad de Valencia (España) por los cálculos teóricos que se recogen en la memoria. Al grupo del Prof. Henk Bolink del ICMol, Universidad de Valencia (España), por los resultados obtenidos al incorporar nuestros derivadores de fullerenos en dispositivos fovoltaicos.

To the research group of Prof. M. K. Nazeeruddin at EPFL, Sion (Switzerland). Thank you, Prof. M. K. Nazeeruddin for giving me the opportunity of working in your laboratory for three months. Some lines have to go to Dr. Iwan Zimmermann for his immeasurable patience, help and made me know almost all I know about perovskite solar cells. Thanks Paul and Sadig for your help and contribution to the projects. Muchas gracias también a Cristina y Olga por los buenos momentos durante la estancia.

A continuación, me gustaría agradecer a todos los miembros del grupo de investigación en la Complutense. Mª Ángeles, Carmen, Salvo, Marta, Luis, David, Beti, Ángel y Andreas gracias por vuestra atención y por estar siempre dispuestos a ayudar. A todos los que componen el "laboratorio de la Complutense" que siempre han estado ahí para hacerme sentir como en casa y para atenderme en todo lo que he necesitado. Gracias Sara, Rosa, Valentina, Marina, Alicia, Andrés, Antonio, Alfonso, Mikiko, Sonia, Laura, Chus, Paul, Marta y algunos de los que ya se fueron: Silvia, María, "Muchachito", Andreita y Carmen. Y por supuesto, a Virginia y Ana, por hacer que todo esto funcione. Todos me habéis tratado muy bien y agradezco vuestra disposición siempre que os he necesitado.

También me gustaría dar las gracias a todos los compañeros de IMDEA nanociencia. No podría haber tenido mejores vecinos. Gracias Leo, Rebeca, María, Diego, Fran, Teresa, Sofía y en especial Alberto, Alex, Leire y Emerson, gracias por toda vuestra ayuda y atención, por estar siempre dispuestos a ayudar. Gracias Marije, Isabel y Juani, se agradece vuestra profesionalidad y trato excepcional.

Así mismo, quiero agradecer a Javi y Zulay del servicio de resonancia de IMDEA nanociencia, al Sidi de la Facultad de Ciencias Químicas de la

Universidad Autónoma de Madrid y al CAI de la Facultad de Ciencias Químicas de la Universidad Complutense de Madrid su gran ayuda y dedicación en la realización de los experimentos.

Gracias a mi familia, en especial a mi tío Raúl por su interés en este proyecto, a mis amigos de Alcorcón, por los momentos que hemos vivido en estos años y al baile y lo que lo rodea. A mi gran amiga Isa, gracias por tus consejos, tus ánimos y por siempre buscar lo mejor para mí. Gracias Lara por tantos inolvidables momentos durante el master y por ser un gran apoyo en los inicios de esta tesis. Te deseo muchísima suerte, sé que llegarás lejos. Estefanía, gracias por ser como eres y por los buenos ratos compartidos en el laboratorio. Por último, gracias a toda esa gente que de una forma u otra ha contribuido con su apoyo a que llegue hasta aquí.

Para terminar, dar las gracias a las personas para mí más importantes:

A mis padres, gracias por confiar siempre en mí. Gracias por todo lo que me habéis dado día a día y por vuestro esfuerzo en que nunca me haya faltado nada y que siempre haya podido hacer realidad mis ilusiones. Por esto y mucho más esta memoria va dedicada a vosotros. A mi hermano, Diego. Gracias por todo tu cariño, por todo lo que como hermano pequeño me has dado y por sacarme tantas sonrisas. Te deseo todo lo mejor y que lo vayamos disfrutando juntos. A mi abuela Valentina, por toda su preocupación y cariño. Ojalá puedas ver desde donde estés esta tesis. Estoy segura que te hará mucha ilusión y que te sentirás orgullosa.

A Ito, no imagino cómo habría sido la recta final de esta tesis sin ti. Muchas gracias por tu cariño, tu ayuda y tu apoyo incondicional. Siempre has tenido una sonrisa cuando lo he necesitado y me has hecho sentir la persona más querida del mundo.

Y sobre todo gracias a ti, a aquél que abre esta tesis para aprender, para utilizar la ciencia y esfuerzo que se concentran en ella para un interesante fin.

Arigato gozai mashita

Muchas gracias

Inés García Benito

TABLE OF CONTENTS

References, abbreviations and acronyms

Bibliographic citations have been placed as footnotes in the pages where they were first cited in the section and at the end of this manuscript.

In addition to the standard abbreviations and acronyms in organic chemistry, defined in the *Journal of Organic Chemistry* author guidelines, the following terms have been used in this manuscript:

1D	One dimensional
2D	Two dimensional
3D	Three dimensional
a.u.	Arbitrary units
ACQ	Aggregation caused quenching
AIE	Aggregation induced emission
AM	Air mass
BF	Bisfluorenylidene
BHJ	Bulk-heterojunction
BTF	Benzotrifuran
BTP	Benzotripyrrole
BTT	Benzotrithiophene
ca.	Around, about, approximately (from latin *circa*)
$CDCl_3$	Deuterated chloroform
ClTBDPS	*Tert*-butyl(chloro)diphenylsilane
CV	Cyclic voltammetry
D-A-D	Donor - acceptor - donor
DCM	Dichloromethane
DCTB	*Trans*-2-[3-(4-*tert*-butylphenyl)-2-methyl-2-propenylidene] malononitrile
DFT	Density functional theory
DIPA	Diisopropylamine
DMF	*N, N*-Dimethylformamide
DMSO	Dimethyl sulfoxide
DPA	Diphenylamine
DPM-6	1',1'-Bis(4-hexyloxyphenyl)-1,2-methano[60]fullerene
DSC	Differential scanning calorimetry
DSSCs	Dye-sensitized solar cells
$E^{0\text{-}0}$	Optical band gap
$E_{1/2}$	Half-wave potential
E_{HOMO}	HOMO energy
E_{LUMO}	LUMO energy
E_{ox}	Oxidation potential
Eq	Equation

E_{red}	Reduction potential
ESI	Electrospray ionization
ETM	Electron-transporting material
eV	Electron-volt
FA	Formamidinium ($HC(NH_2)_2^+$)
Fc	Ferrocene
FF	Fill factor
FK102	Tris(2-(1*H*-pyrazol-1-yl)pyridine)cobalt(III) tri[bis(trifluoromethane)sulfonimide]
FK209	Tris(2-(1*H*-pyrazol-1-yl)-4-*tert*-butylpyridine)cobalt(III) tri[bis(trifluoromethane)sulfonimide]
FTIR	Fourier transform infrared spectroscopy
FTO	Fluorine-doped tin oxide
HOMO	Highest occupied molecular orbital
HTM	Hole-transporting material
Hz	Hertz
IR	Infrared
ITO	Indium-tin oxide
J	Current density
J_{sc}	Short-circuit current
J-V	Current density-voltage
Li-TFSI	Lithium bis(trifluoromethanesulfonyl)imide
LUMO	Lowest unocuppated molecular orbital
m-	*meta*-
MA	Methylammonium ($CH_3NH_3^+$)
MALDI	Matrix-assisted laser desorption/ionization
MHz	MegaHertz
Min	Minutes
MJ	Multijunction
ε	Molar absorption coefficient
Na^tBuO	Sodium tert-butoxide
NBS	*N*-Bromosuccinimide
NHE	Standard hydrogen electrode
NMP	*N*-Methylpyrrolidine
NMR	Nuclear magnetic resonance spectroscopy
o-	*ortho*-
o-DCB	1,2-Dichlorobenzene
OFET	Organic field-effect transistor
OLED	Organic light-emitting diode
OPV	Organic photovoltaic
p-	*para*-
$PC_{61}BM$	PhenylC_{61}-butyric acid methyl ester
PCE	Power conversion efficiency

PL	Photoluminescence
PolyTPD	Poly(*N,N′*-bis(4-butylphenyl)-*N,N′*-bis(phenyl)benzidine)
ppm	Parts-per million
PSCs	Perovskites solar cells
PV	Photovoltaic
r.p.m.	Revolutions per minute
r.t.	Room temperature
s	Seconds
SAM	Self-assembly monolayer
SEM	Scanning Electron Microscopy
spiro-OMeTAD	N^2,N^2,$N^{2'}$,$N^{2'}$,N^7,N^7,$N^{7'}$,$N^{7'}$-octakis(4-methoxyphenyl)-9,9′-spirobi[9*H*-fluorene]-2,2′,7,7′-tetramine
ss-DSSC	Solid state-dye-sensitized solar cell
T	Temperature
TAE	Tetraarylethene
$TBAPF_6$	Tetrabutylammonium hexafluorophosphate
TBDPS	*Tert*-butyldimethylsilyl chloride
t-BP	4-*Tert*-butylpiridine
TbT	Thieno[3,2-*b*]thiophene
T_c	Crystallization temperature
TCE-d_2	Deuterated 1,1,2,2-tetrachloroethane
T_{dec}	Decomposition temperature
T_g	Glass transition temperature
TGA	Thermogravimetric analysis
THF	Tetrahydrofuran
THF-d_8	Deuterated tetrahydrofuran
TIPS	6,13-Bis(triisopropylsilylethynyl)
T_m	Melting temperature
TMS	Trimethylsilyl
TMSA	Trimethylsilylacetylene
TPA	Triphenylamine
TPE	Tetraphenylethene
UV-vis	Ultraviolet-visible spectroscopy
V	Voltage
V	Volt
V_{oc}	Open circuit voltage
XRD	X-ray diffraction
λ	Wavelength
χ_w	Fraction weight

Summary

"Molecular engineering of hole and electron transporting materials for perovskite solar cells"

Introduction

The development of clean alternatives to current power generation technologies based on the consumption of fossil fuels, is crucially important to prevent the global environment and assuring sustained economic growth. One of the most reasonable alternatives in the search for clean and renewable energy sources is taking advantage of solar energy. As an emerging photovoltaic technology with significant potential for commercialization, perovskite-based solar cells (PSCs) have been tremendously developed in the recent years, reaching promising efficiencies for future low-cost solar cells.

Objectives

Chapter 1: Design, synthesis and characterization of new hole-transporting materials for improving the performance of the perovskite-based solar cells.

Chapter 2: Testing a series of fullerene derivatives with different chemical functionalization and LUMO energy levels as electron-transporting materials in inverted perovskite solar cells.

Results and discussion

Chapter 1. *Hole-transporting materials (HTMs) for perovskite solar cells*

i) HTMs based on tetraarylethene (TAE) and bifluorenylidene (BF)

It has been designed and synthesized novel molecules based on TAE and BF as central cores endowed with different electron donating units (figure S1). These *"*extremely*"* low-cost and the straightforward preparation of TAE- and BF-derivatives were spectroscopically, optically and electrochemically characterized, revealing their promising characteristics to be incorporated as HTMs in PSCs.

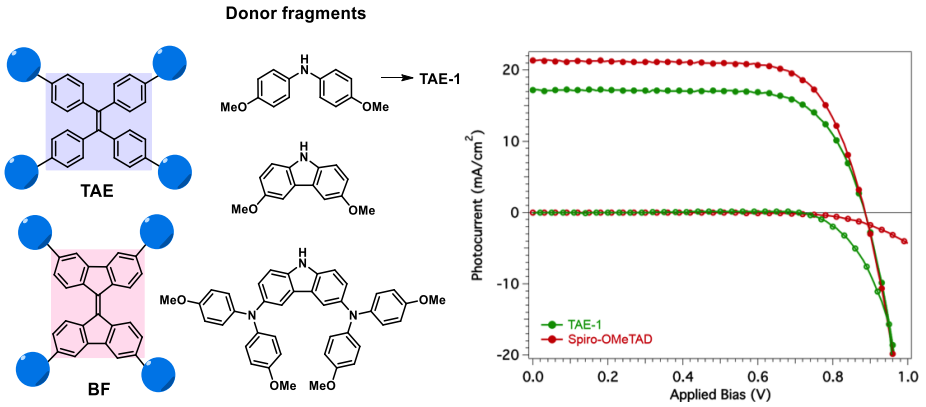

Figure S1. Simplified TAE- and BF-based HTMs structures (left); J-V curves of undoped **TAE-1** and spiro-OMeTAD in $MAPbI_3$-based solar cells (right).

Particularly, **TAE-1** was studied as a novel promising HTM in dopant-free $MAPbI_3$-based solar cells, reaching excellent results.

ii) HTMs based on benzotrithiophene (BTT)

In this section, the design of novel HTMs based on sulfur-rich central core is presented. In the first part, a systematic study on the impact of the electron donor units was carried out (figure S2a) by comparing the optical, electrochemical and photophysical properties. Secondly, two isomers which share *p*-methoxytriphenylamines as electron donor groups were compared depending on the arrangements of the sulfur atoms in the core (figure S2b).

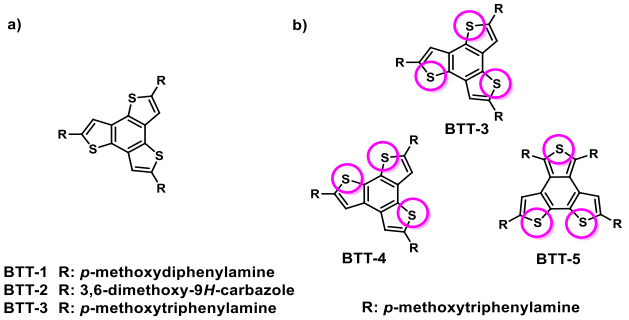

Figure S2. a) Study of the effect of different electron donor groups; **b**) study of the influence of the isomerism of BTT core.

Three new star-shaped small molecule hole-conducting materials **BTT-1**, **BTT-2** and **BTT-3** have been efficiently obtained by crosslinking BTT core with different diphenylamine based ligands following a facile straightforward synthetic route. Energy conversion efficiencies in the range of 16 % to 18 % comparable to the reference spiro-OMeTAD, were obtained employing them as HTMs in two different perovskite-based devices, namely $MAPbI_3$ and $(FAPbI_3)_{0.85}(MAPbBr_3)_{0.15}$ (figure S3).

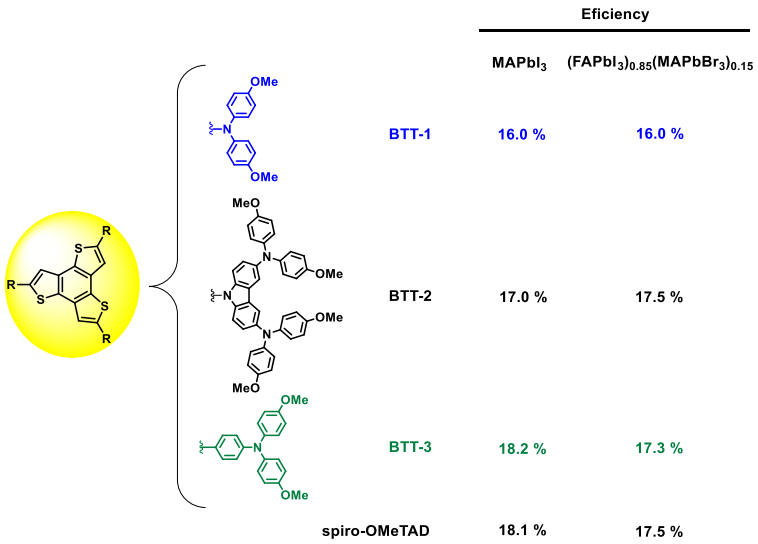

Figure S3. Chemical structures of **BTT-1**, **BTT-2** and **BTT-3** and their power conversion efficiency (PCE) values in $MAPbI_3$ and $(FAPbI_3)_{0.85}(MAPbBr_3)_{0.15}$-based solar cells.

Encouraged by the extraordinary result displayed by **BTT-3**, two new HTMs, based on isomeric forms of BTT, were prepared. The impact of the isomerism, which stems from the different arrangement of the sulfur atoms, on the optical, electrochemical properties and the photovoltaic performance was systematically investigated. Impressive light-to-energy conversion values of 19.0 % and 18.2 % were measured employing **BTT-4** and **BTT-5**, respectively as HTMs in $(FAPbI_3)_{0.85}(MAPbBr_3)_{0.15}$-based solar cells (figure S4). Additionally, conductivity measurements further confirmed that the *cis* positon of the sulfur atoms leads to better charge transport properties.

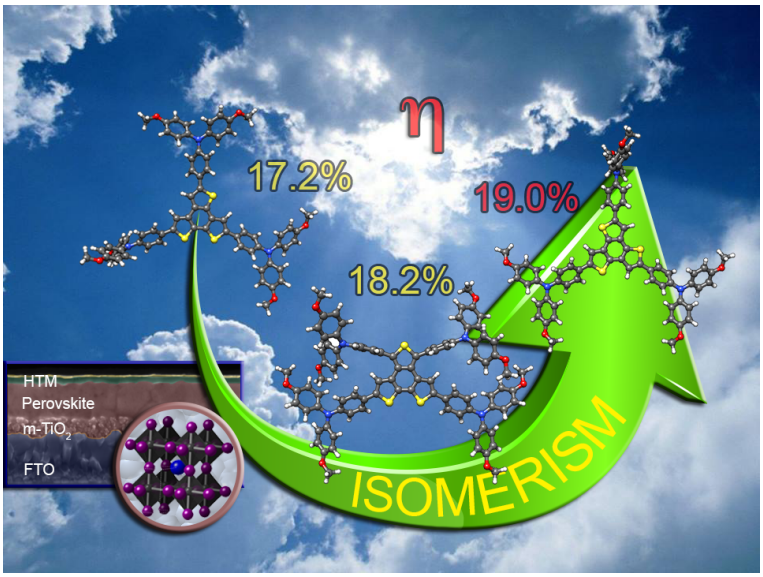

Figure S4. Isomerism effect of the HTM (**BTT-3**, **BTT-4** and **BTT-5**) in PSCs (cover back of *J. Mater. Chem. A*, **2017**, 5, 8317-8324).

iii) HTMs based on sulfur-free core

Furthermore, considering the strong beneficial impact that the presence of sulfur atoms has on the device performance, innovation in this field requires exploring other related heteroatoms, namely oxygen and nitrogen (figure S5) in new aromatic/heteroaromatic hybrids, thus broadening the scope of the application. With an eye toward carrying out a complete and systematic study of the molecular structure of the HTMs, herein it is explored the impact on the photovoltaic performance of two isostructural new three-armed sulfur-free HTMs analogously to the most efficient sulfur-containing isomer. The new derivatives show C_{3h} symmetry with three pyrrole or three furan rings fused to a benzene central ring, so-called **BTP** and **BTF**, respectively. In addition to the detailed optical, electrochemical and thermal properties of the new HTMs, mesoscopic PSCs were prepared showing remarkable efficiencies in combination with compositionally engineered perovskite $(FAPbI_3)_{0.85}(MAPbBr_3)_{0.15}$, comparable to those obtained by the state-of-the-art spiro-OMeTAD and higher than the isostructural **BTT-3**.

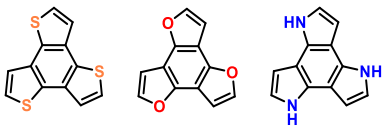

Figure S5. Incorporation of different heteroatoms in the central core of HTMs.

iv) HTMs based on thieno[3,2-*b*]thiophene (TbT)

Finally, thienothiophenes have been employed as central core in three novel HTMs, endowed with either *p*-methoxydiphenylamines or *p*-methoxytriphenylamines incorporating different spacer groups. The three TbT-derivatives (figure S6) prepared through a facile synthetic route showed a notable different behavior in PSCs, reaching efficiencies from 11.1 % to a promising 18.4 % with negligible hysteresis employing **TbT-3**.

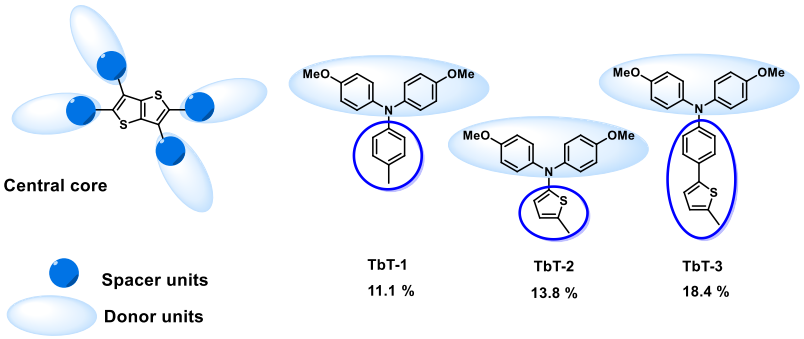

Figure S6. Chemical structure of **TbT-1**, **TbT-2** and **TbT-3** and their corresponding PCE in $(FAPbI_3)_{0.85}(MAPbBr_3)_{0.15}$-based solar cells.

Chapter 2. *Electron-transporting materials (ETMs) for perovskite solar cells*

i) Benzoic acid-containing C_{60}-monoadducts and bisadducts

It is important to note that although the main goals in this thesis are focused on the preparation of innovative HTMs, the study of related [60]fullerenes as ETMs was also considered in parallel with the ultimate goal of developing new and more efficient fullerenes by cutting down costs. It is well-stablished that the carboxylic acid is an effective anchoring group to the TiO_2. Therefore, a series of C_{60}-monoadducts and bisadducts bearing benzoic acid, were synthesized in order to be used as electron-transporting layer in PSCs. Particularly, three different fullerene derivatives (figure S7) were incorporated as self-assembled monolayers (SAMs) at interface in PSCs observing a decrease on hysteresis for

all the cases. This effect was produced by a decrease of the capacitive hysteresis. In addition, appropriated C_{60}-functionalization, such as introducing-CN groups, increases photocurrent and reduce hysteresis.

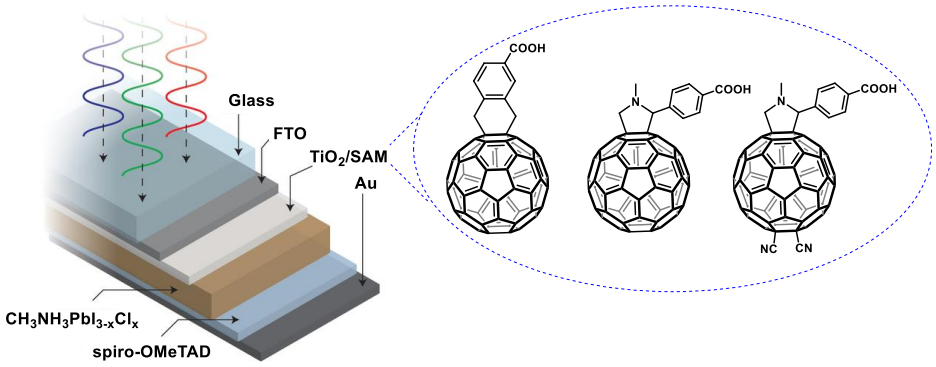

Figure S7. Study of interfacial fullerene self-assembled monolayers in PSCs.

ii) Synthesis of ThCBM

Taking into account that the long pair of the sulfur atom of the thiophene ring can interact through electronic attraction with the positive charge of the metal of the perovskite, 2-thienylC_{61}-butyric acid methyl ester (ThCBM) and with hexyl chain were employed as ETMs in PSCs (figure S8a). These derivatives were incorporated in planar inverted PSCs exhibiting PCEs similar to those obtained for $PC_{61}BM$. The perovskite layer was prepared from two different methods, solution-process and slow evaporation. In addition, DPM-6-$PC_{61}BM$ bisadduct was easily synthesized to study the influence of rising the LUMO energy level (figure S8b). The employment of these C_{60}-derivatives in $MAPbI_3$-based solar cells are currently under study.

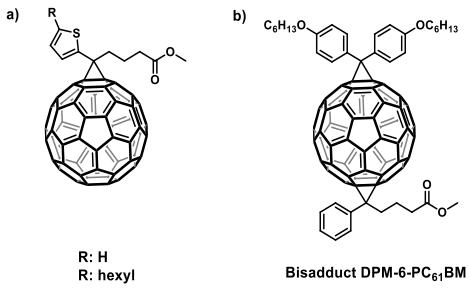

Figure S8. a) Chemical structure of ThCBM. **b**) Chemical structure of bisadduct DPM-6-$PC_{61}BM$.

Conclusions

Chapter 1: The design of novel low-cost and easy attainable hole-transporting materials has permitted to study the influence, stemming from different electron donor groups, isomerism or the incorporation of heteroatoms in the central core, of "a la carte" HTMs on the molecular properties and the perovskite-based devices performances. Furthermore, the laboratory synthesis costs of the HTMs were estimated, resulting in the range of 50-80 US$ g^{-1}, which is very competitive in comparison to other commercially available HTMs. These price values along with the high PCEs obtained, validate the potential of our readily available materials for competing favorably with spiro-OMeTAD in the perovskite-based photovoltaic market. In this regard, an applied patent is currently under consideration which could, eventually, result in a commercialization of some of these aforementioned HTMs.

Chapter 2: The design of new fullerene derivatives plays a very important role in the overall solar cell performance. The collection of fullerene derivatives presented in this thesis, has permitted a deep study in different PSCs architectures. The appropriate functionalization of C_{60}-derivatives has led to successful improvements in inverted solar cells, not only as ETMs but also incorporated as SAMs at interlayer in PSCs. C_{60}-SAM has been demonstrated to enhance the direct coupling with the perovskite layer, thus improving the solar cell parameters.

Resumen

"Ingeniería molecular de materiales transportadores de huecos o electrones para células solares de perovskita"

Introducción

El desarrollo de alternativas limpias para reemplazar las tecnologías de generación de energía actuales basadas en combustibles fósiles, es de crucial importancia para la sostenibilidad del medio ambiente y el desarrollo de un crecimiento económico sostenido. Una de las alternativas más razonables en la búsqueda de fuentes de energía limpias y renovables es el aprovechamiento de la energía solar. Dentro de las tecnologías fotovoltaicas emergentes con potenciales oportunidades de comercialización, las células solares basadas en perovskita (de sus siglas en inglés, PSCs) han sido ampliamente desarrolladas en los últimos años, alcanzando eficiencias prometedoras como futuros dispositivos solares de bajo coste.

Objetivos

Capítulo 1: Diseño, síntesis y caracterización de nuevos materiales transportadores de huecos (de sus siglas en inglés, HTMs) con el fin de mejorar el rendimiento de PSCs.

Capítulo 2: Estudio de la aplicación de una serie de derivados de fullereno con diferente funcionalización química y energía del LUMO como materiales transportadores de electrones (de sus siglas en inglés, ETMs) en PSCs invertidas.

Resultados y discusión

Capítulo 1. *Materiales transportadores de huecos (HTMs) para PSCs*

i) HTMs basados en tetraarileteno (TAE) y bifluorenilideno (BF)

Nuevas moléculas basadas en TAE y BF como unidad central han sido diseñadas y sintetizadas uniendo covalentemente diferentes fragmentos dadores de electrones (figura R1). Estos derivados de TAE y BF extremadamente baratos y de fácil preparación, han sido caracterizados espectroscópicamente, estudiándose sus propiedades ópticas y electroquímicas. Estas nuevas moléculas, mostraron características prometedoras al ser incorporadas como HTMs en PSCs.

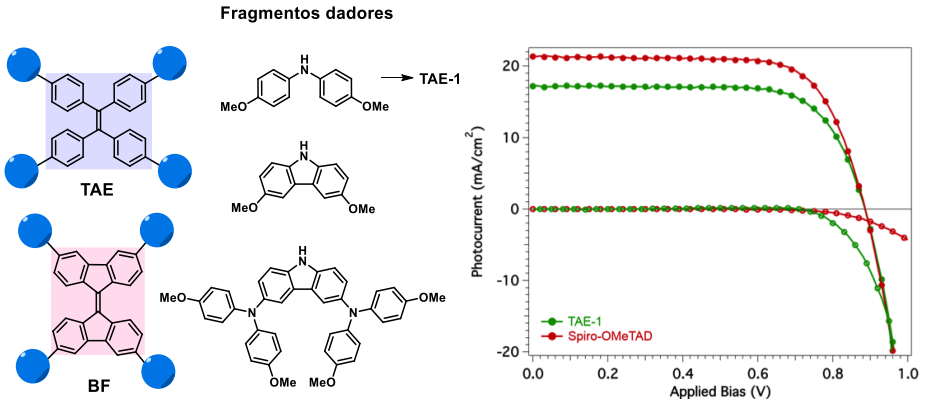

Figura R1. Estructura simplificada de los HTMs basados en TAE y BF (izq.); curvas J-V de **TAE-1** sin dopar y spiro-OMeTAD en PSCs basadas en $MAPbI_3$ (dcha.).

ii) HTMs basados en benzotritiofeno (BTT)

En esta sección se presenta el diseño de nuevos HTMs basados en una unidad central rica en átomos de azufre. En esta primera parte, se llevó a cabo un estudio sistemático de la influencia de la unidad dadora en las propiedades ópticas, electroquímicas y fotovoltaicas (figura R2a). A continuación, se sintetizó y comparó el comportamiento de dos nuevos isómeros de BTT que comparten la unidad dadora de electrones y que difieren en la posición del átomo de azufre en el fragmento central (figura R2b).

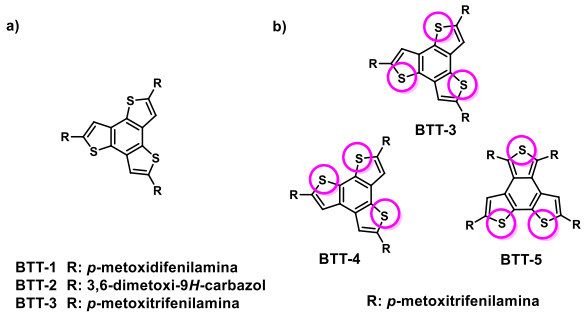

Figura R2. a) Estudio de la influencia de los fragmentos dadores y **b**) de la isomería en el fragmento central de BTT.

Se han sintetizado tres nuevos HTMs con forma de estrella, **BTT-1**, **BTT-2** y **BTT-3**, los cuales fueron obtenidos de manera satisfactoria a través de la unión del fragmento central BTT con diferentes unidades basadas en difenilamina

siguiendo una ruta sintética sencilla y eficaz. Los nuevos derivados han sido utilizados como transportadores de huecos en combinación con dos perovskitas diferentes, $MAPbI_3$ y $(FAPbI_3)_{0.85}(MAPbBr_3)_{0.15}$, alcanzando valores de eficiencia entre el 16 % y el 18 % (figura R3).

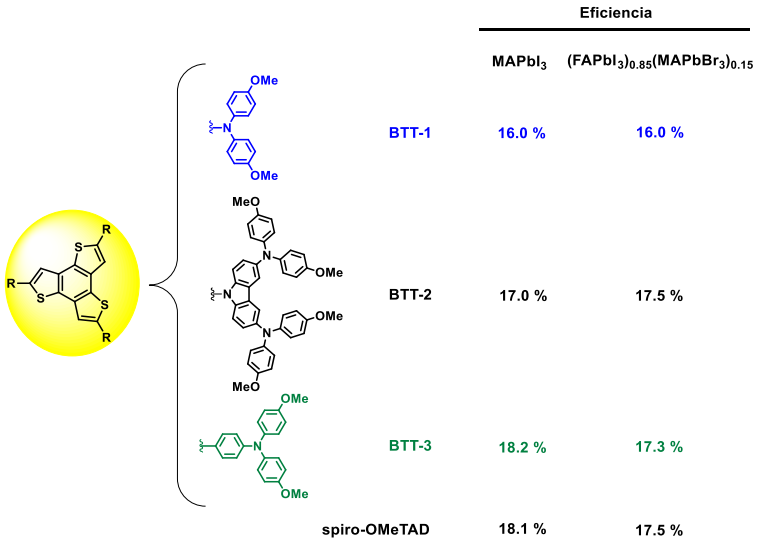

Figura R3. Estructura química de **BTT-1**, **BTT-2** y **BTT-3** y sus correspondientes valores de eficiencia en PSCs basados en $MAPbI_3$ y $(FAPbI_3)_{0.85}(MAPbBr_3)_{0.15}$.

Tras los excelentes resultados obtenidos para la molécula **BTT-3**, se sintetizaron dos nuevos HTMs basados en isómeros de BTT. El efecto de la isomería, derivada de la posición de los átomos de azufre en el fragmento central (figura R2b), ha sido sistemáticamente estudiado en las propiedades ópticas y electroquímicas de las moléculas objetivo, así como en su comportamiento fotovoltaico. Valores extraordinarios de eficiencia del 19.0 % y 18.2 % han sido alcanzados empleando **BTT-4** y **BTT-5**, respectivamente, como HTMs en células solares basadas en $(FAPbI_3)_{0.85}(MAPbBr_3)_{0.15}$ (figura R4). De forma complementaria, se realizaron medidas de conductividad las cuales permitieron confirmar que la conformación *cis* de los átomos de azufre favorece las propiedades de transporte de carga.

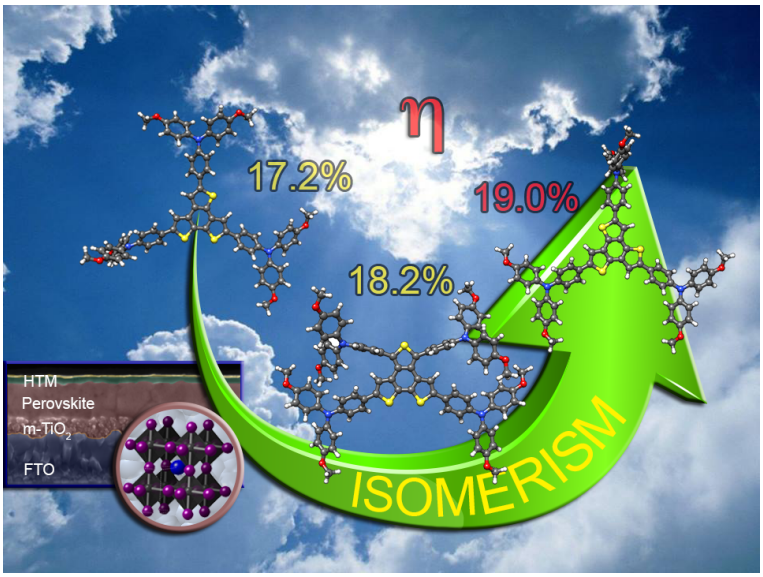

Figura R4. Efecto de la isomería en la estructura del HTM sobre la eficiencia en PSCs (portada trasera en *J. Mater. Chem.* A, **2017**, 5, 8317-8324).

iii) HTMs basados en un fragmento central libre de azufre

Considerando la notable mejora que ofrece la presencia, en la estructura del HTM, de átomos de azufre en la eficiencia del dispositivo fotovoltaico, se extendió el estudio a la incorporación de otros heteroátomos en el fragmento central, como oxígeno o nitrógeno, ampliando así el alcance de la aplicación (figure R5). Con este objetivo, se sintetizaron dos nuevas isoestructuras de simetría C_{3h}, con pirroles o anillos de furano fusionados a un anillo central de benzeno, **BTP** y **BTF**, respectivamente. De forma complementaria a la caracterización óptica, electroquímica y térmica de estos HTMs libres de azufre, se estudió su aplicación en dispositivos fotovoltaicos mesoporosos basados en $(FAPbI_3)_{0.85}(MAPbBr_3)_{0.15}$.

Los extraordinarios valores de eficiencia alcanzados, son comparables a los obtenidos con el HTM más utilizado actualmente, spiro-OMeTAD e incluso ligeramente superiores a los valores conseguidos con **BTT-3**.

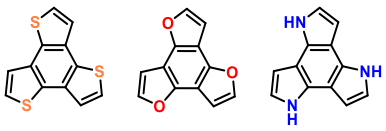

Figura R5. Incorporación de diferentes heteroátomos en el fragmento central de los HTMs.

iv) HTMs basados en tieno[3,2-*b*]tiofeno (TbT)

Finalmente, se empleó tienotiofeno como fragmento central en tres nuevos HTMs, unido covalentemente a unidades de *p*-metoxidifenilamina a través de diferentes grupos espaciadores. Los tres derivados de TbT (figura R6) fueron preparados mediante una sencilla ruta sintética mostrando interesantes diferencias en su comportamiento en dispositivos fotovoltaicos basados en perovskita. Se obtuvieron valores de eficiencia desde 11.1 % para el derivado **TbT-1** hasta 18.4 % empleando **TbT-3** con apenas histéresis.

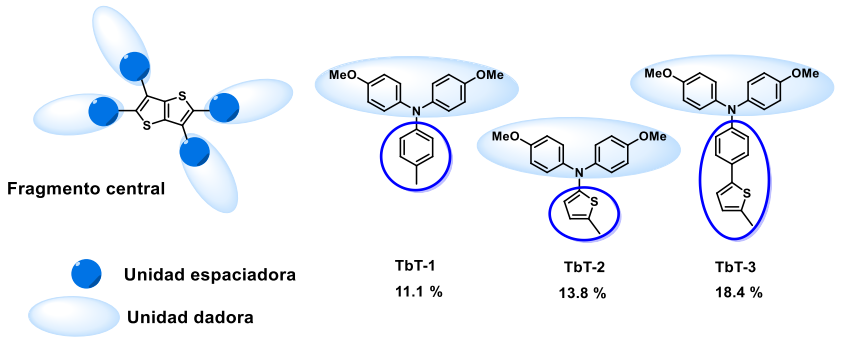

Figura R6. Estructura química de **TbT-1**, **TbT-2** y **TbT-3** y su correspondiente eficiencia en PSCs basadas en $(FAPbI_3)_{0.85}(MAPbBr_3)_{0.15}$.

Capítulo 2. *Materiales transportadores de electrones (ETMs) para PSCs*

i) Monoaductos y bisaductos de C_{60} funcionalizados con ácido benzoico

Es importante resaltar que, aunque los objetivos principales de esta tesis están focalizados en la preparación de nuevos HTMs, se ha desarrollado paralelamente el estudio de derivados de [60]fullereno como ETM con el fin último de desarrollar nuevos y eficientes materiales transportadores de electrones para dispositivos basados en perovskita. Es conocido en la literatura que los ácidos carboxílicos son un grupo de anclaje efectivo al TiO_2. Por ello, una serie de monoaductos y bisaductos de [60]fullereno, adecuadamente funcionalizados con

ácido carboxílico, fueron sintetizados con el fin de ser empleados como ETMs en PSCs. Concretamente, tres derivados de fullerenos, fueron incorporados como interface en PSCs en forma de monocapa autoensamblada (de sus siglas en inglés, SAM) (figure R7). En todos los casos, se observó una disminución en la histéresis, motivada por el descenso en la capacitancia. Adicionalmente, se observó que la apropiada funcionalización del [60]fullereno, mediante la incorporación adicional de grupos -CN, produce un aumento de la fotocorriente y una disminución en la histéresis.

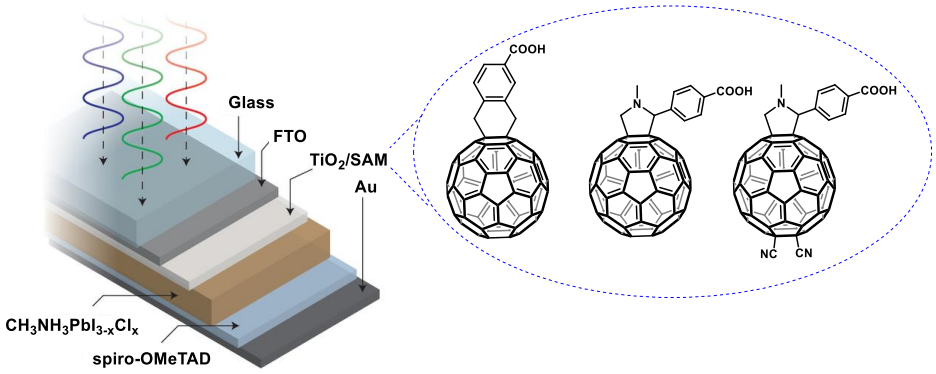

Figura R7. Estudio de la incorporación de [60]fullereno-SEM en PSCs.

ii) Diseño y síntesis de ThCBM

Considerando el efecto de las interacciones existentes entre el par electrónico libre del átomo de azufre del anillo de tiofeno y la carga positiva del metal presente en la perovskita, se decidió sintetizar dos análogos de $PC_{61}BM$, 2-tienilC_{61}-butirato de metilo (ThCBM) e incorporando una cadena de seis átomos de carbono (figura R8a), para su uso como ETMs en células solares de configuración invertida. Estos derivados mostraron un comportamiento en dispositivos invertidos basados en perovskita similares al ampliamente utilizado $PC_{61}BM$. La deposición de la capa de perovskita se llevó a cabo mediante dos métodos diferentes, procesado en disolución y mediante evaporación. Para finalizar, se presenta la síntesis del bisaducto de [60]fullereno que combina los fragmentos característicos del DPM-6 y $PC_{61}BM$ (figura R8b). El estudio de su aplicación en dispositivos fotovoltaicos basados en $MAPbI_3$ se encuentra actualmente en proceso de optimización.

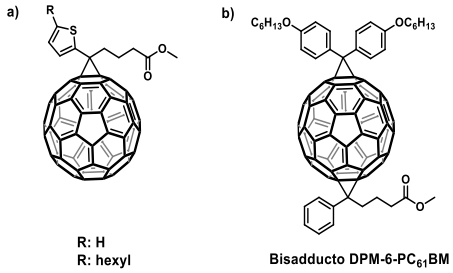

Figura R8. a) Estructura de ThCBM. **b**) Estructura del bisaducto DPM-6-PC_{61}BM.

Conclusiones

Capítulo 1. El diseño de nuevos HTMs de bajo coste y fácil preparación ha permitido el estudio de la influencia de diferentes unidades dadoras de electrones, isomerización e incorporación de heteroátomos en el fragmento central para diseñar "a la carta" HTMs con propiedades moleculares favorables para su utilización en dispositivos fotovoltaicos basados en perovskita. De forma adicional, se ha realizado una estimación de su coste de preparación a escala de laboratorio, en torno a 50-80 US$ g^{-1}, muy competitivo en comparación con otros HTMs ya comercialmente disponibles. Estos costes de preparación, junto con los altos valores de eficiencia alcanzados en dispositivos fotovoltaicos, validan el potencial de los nuevos HTMs presentados en esta tesis, compitiendo favorablemente con spiro-OMeTAD, en el mercado de las células solares basadas en pervoskita. Actualmente existe una solicitud de patente europea pendiente de resolución final.

Capítulo 2: El diseño de nuevos derivados de [60]fullereno tiene un papel importante en el funcionamiento de dispositivos fotovoltaicos. La preparación de los compuestos basados en [60]fullereno presentados en esta tesis, ha permitido el estudio en diferentes configuraciones de PSCs. Una apropiada funcionalización conlleva una notable mejora en dispositivos fotovoltaicos de configuración invertida, no solo como ETMs sino también incorporándose como interfase SAM. C_{60}-SAM ha demostrado mejorar el acoplamiento directo con la capa de perovskita, mejorando así los parámetros fotovoltaicos.

Introduction

INTRODUCTION

Dealing with change

Each generation has to face new challenges in the same way it should take advantages of new chances. However, opportunities discovered and exploited by a generation can provoke challenges to the subsequent ones.

Energy is one of the main driving forces for human society development. A great progress has been made due to massive exploitation of carbon-based fossil fuels as the energy resource.

The International Energy Outlook 2016 (IEO2016)[1] projects significant growth in worldwide energy demand from 2012 to 2040. Total world consumption of marketed energy expands from 549 quadrillion British thermal units (Btu) ($1.6 \cdot 10^{14}$ TWh) in 2012 to 629 quadrillion Btu ($1.8 \cdot 10^{14}$ TWh) in 2020 and to 815 quadrillion Btu ($2.4 \cdot 10^{14}$ TWh) in 2040, a total increase of 48 %.

The increasing consumption of fossil fuels has many harmful drawbacks, such as huge amounts of pollutants that threatens human health and carbon dioxide and greenhouse gases associated with global warming and degradation of the planet.[2]

Not only the environmental concerns related with the consumption of fossil fuels but the rising global energy demand, have raised increasing public awareness. Therefore, our society must urgently explore renewable alternatives and carbon-neutral energy sources to replace fossil fuels.[1]

Can scientists find an energy source capable of replacing fossil fuels? Can chemistry help in solving the energy problem? The answer is that chemists can help improving energy technologies through the synthesis of new and more efficient materials and, hopefully, finding scientific breakthroughs capable of solving energy sources' problematic roots.[2]

1. *http://www.iea.org.*
2. N. Armaroli, V. Balzani, "The future of energy supply: Challenges and opportunities", *Angew. Chem. Int. Ed.*, **2007**, *46*, 52-66.

Growth and potential of renewable energies

There is a fundamental attractiveness about harnessing renewables sources in an era where humans are more conscious of the environmental effects of burning fossil fuels. Currently, attention focuses on both the adequacy of long-term energy supplies as well as in their environmental implications. In the last few years, there has been a trend towards a sustainable development of various renewable energy sources. Figure 1 illustrates the average annual growth rates of renewable energy capacity and biofuels production from 2010 to 2015.[3]

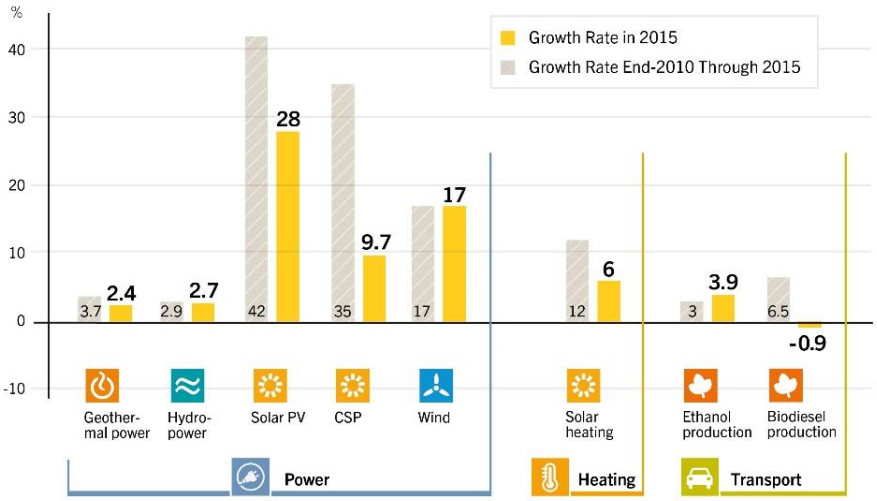

Figure 1. Average annual growth rates from 2010 to 2015.
Illustration from *REN21 Renewables 2016 Global Status Report.*

A variety of renewable-energy promotion policies have been adopted in thoughtful countries[2] such as China, USA, Norway and Sweden. In spite of the fast growth that have led, the contribution of renewable energy to the overall energy supply is still very low. Therefore, there is a need to accelerate the development of renewable energies, which depends mainly on scientific research and governments.

3. *http://www.ren21.net*

Solar photovoltaic

Taking into account the non-renewable nature of carbon-based fossil fuels and in order to satisfy the energy needs of our society, the most reasonable alternative is the search for clean and renewable energy sources.[4] Among them, solar energy is unarguably the largest exploitable source that potentially could be scaled up to guarantee our future energy supply.[2]

Our planet has an inexhaustible energy flow coming from the Sun and deposited on the surface of the Earth calculated as 120000 TW of electromagnetic radiation (5 % ultraviolet; 43 % visible and 52 % infrared).[5]

The spectral irradiance from the Sun is shown in figure 2 as a function of wavelength.

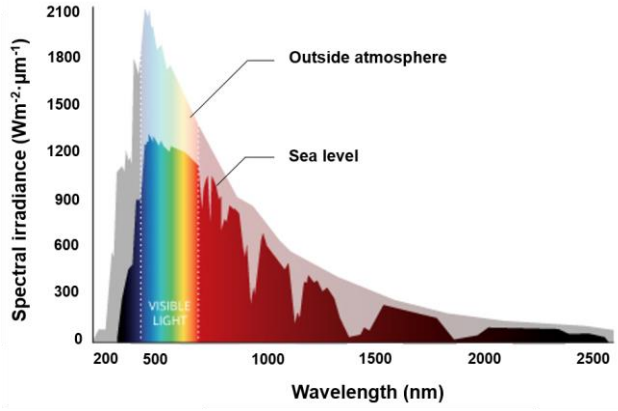

Figure 2. Solar radiation.

More solar energy strikes the Earth in one hour than all of the energy currently consumed globally by mankind in an entire year; in other words, harvesting less than 0.02 % of this energy would satisfy our present needs. For example, covering 0.16 % of the land of the Earth with 10 % efficient solar conversion systems would provide 20 TW of power, nearly twice the world's consumption rate of fossil energy.[6]

4. E. Espíldora, J. L. Delgado, N. Martín, "Donor-acceptor hybrids for organic electronics", *Isr. J. Chem.*, **2014**, *54*, 429-439.
5. J. L. Delgado, P. A. Bouit, S. Filippone, M. A. Herranz, N. Martin, "Organic photovoltaics: A chemical approach", *Chem. Commun.*, **2010**, *46*, 4853-4865.
6. R. F. Service, "Is it time to shoot for the sun?", *Science*, **2005**, *309*, 548-551.

"Within 6 hours the world's deserts receive more energy from the Sun than humankind consumes within a year" was one of the headlines of The DESERTEC Foundation,[7] a global civil society initiative aiming to shape a sustainable future established in 2009. This means that sufficient clean power can be generated from the world deserts to supply mankind with enough electricity on a sustainable basis.

Figure 3 clearly shows the large amount of solar irradiation received every year worldwide.[8]

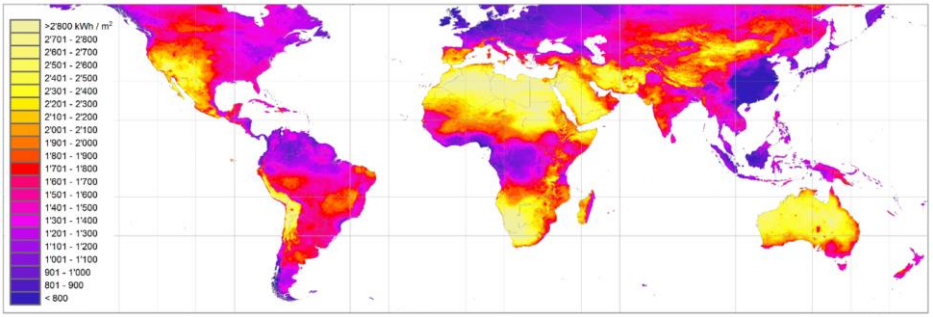

Figure 3. Yearly sum of direct normal irradiation (uncertainty 8 %).
Illustration from Meteonorm.

Sun represents an abundant, clean and economical energy source. However, its enormous potential cannot be employed as such. Since solar energy is diffuse and intermittent, it must be captured and converted into useful forms of energy which should involve concentration and storage.

Currently, none of the many routes used to convert solar energy into electricity, heat and fuel is competitive with fossil fuels at today's world market price yet. However, the cost comparison would give quite different results considering the "consequent" costs from fossil fuels. Thus, decisive research projects are being developed to make the use of solar power competitive in world market.

Photovoltaic devices

Photovoltaic (PV) cells are devices capable of directly converting solar energy into electrical power. Their development, improvement and optimization are currently a hot topic in science.

7. *http://www.desertec.org*
8. *http://www.meteonorm.com*

The current PV market is still dominated by the crystalline silicon-based solar cells: since the first 6 % efficiency silicon-based device prepared by Chapin[9] in 1954 to the more than 26 % conversion efficiency [10] in 2017.

Silicon has excellent charge transport properties and is an abundant element on Earth. However, its high-purity and the skilled manufacturing techniques that are required, prevent it from supplying energy necessities by itself.[11] Currently, different technologies complete the PV market together with silicon-based solar cells, such as semiconductor (e.g., GaAs) based cells, thin-film (e.g., CdTe) solar cells and organic photovoltaics (OPV). Companies such as Solaronix and Dyesol[12] already market dye-sensitized solar cells (DSSCs) as well as Heliatek,[13] bulk-heterojunction organic solar cells (BHJ).

Seeking to further reduce the costs of current PV technologies, researchers have developed a wide number of different semiconducting materials (inorganic, organic, molecular, polymeric, hybrids, quantum dots, etc.) as possible candidates to be used for transforming sunlight into chemical energy. Among them, photo- and electro-active organic compounds are promising materials due to key advantages, such as the possibility of processing them directly from solution, thus affording lighter, cheaper and flexible all-organic PV devices.[14] Therefore, the novel low-cost approaches are progressing to compete/coexist with the silicon-based devices.

9. D. M. Chapin, C. S. Fuller, G. L. Pearson, "A new silicon p-n junction photocell for converting solar radiation into electrical power", *J. Appl. Physics.*, **1954**, *25*, 676-677.
10. M. A. Green, K. Emery, Y. Hishikawa, W. Warta, E. D. Dunlop, D. H. Levi, A. W. Y. Ho-Baillie, "Solar cell efficiency tables (version 49)", *Prog. Photovolt.: Res. Appl.*, **2017**, *25*, 3-13.
11. J. Ahmad, K. Bazaka, L. J. Anderson, R. D. White, M. V. Jacob, "Materials and methods for encapsulation of OPV: A review", *Renew. Sustainable Energy Rev.*, **2013**, *27*, 104-117.
12. *https://www.solaronix.com; http://www.dyesol.com*.
13. *www.heliatek.com*.
14. N. Martín, "Carbon nanoforms for photovoltaics: Myth or reality?", *Adv. Energy Mater.*, **2016**, 1601102-1601110.

Background

BACKGROUND

1. The photovoltaic technology landscape

Photovoltaic is an established, though under-utilized, technology for generating electricity from Sun,[15] which coexists with other energy renewable sources offering a practical and suitable solution to the challenge of satisfying the increasing global energy demand.

A wide variety of PV cells based on different materials have been studied as devices capable of convert solar energy into chemical energy and then into electricity, representing a promising alternative to fossil fuels. The first example dates back to 1986, when Tang presented a two-layers organic PV cell, fabricated from copper phthalocyanine and a perylene tetracarboxylic derivative. A power conversion efficiency of about 1 % was achieved under simulated AM2 illumination.[16] However, the possibility to use devices based on molecular materials for building robust large-scale solar electricity production seemed inconceivable. Nevertheless, this widespread idea changed in 1991 with the seminal report by O'Regan and Graetzel,[17] which encouraged researchers to take on the challenge.[18]

Figure 4 illustrates the evolution, provided by National Renewable Energy Laboratory (NREL), of the best-research cell efficiencies in the last decades showing the certificated best efficiencies for a variety of PV technologies.

15. K. A. Mazzio, C. K. Luscombe, "The future of organic photovoltaics", *Chem. Soc. Rev.*, **2015**, *44*, 78-90.
16. C. W. Tang, "Two-layer organic photovoltaic cell", *Appl. Phys. Lett.*, **1986**, *48*, 183-185.
17. B. O'Regan, M. Graetzel, "A low-cost, high-efficiency solar cell based on dye-sensitized colloidal TiO_2 films", *Nature*, **1991**, *353*, 737-740.
18. A. Hagfeldt, G. Boschloo, L. Sun, L. Kloo, H. Pettersson, "Dye-sensitized solar cells", *Chem. Rev.*, **2010**, *110*, 6595-6663.

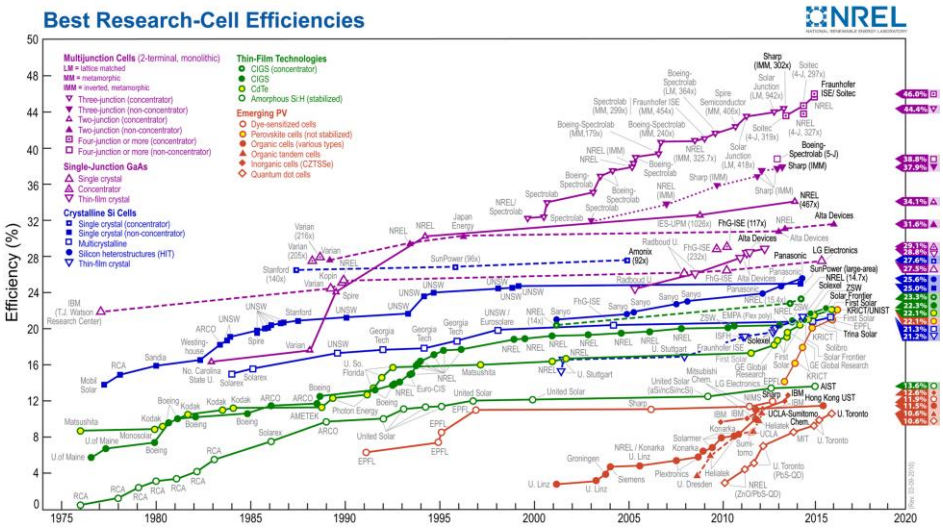

Figure 4. Certified best power conversion efficiencies over time for a variety of PV technologies, provided by NREL.

Currently, the champion efficiency is for inorganic multijunction cells which under solar concentration exceed 46 %. Single crystalline silicon and multicrystalline silicon solar cells exceeding 27 % and 23 % efficiency, respectively. Although these values are promising, efficiency of devices is not the only metric for determining the commercial viability of a particular PV technology. Mainly, inorganic PV technologies have production limitations due to their high cost.[15] The direct competition for materials with the microelectronics industry, the production requirements such as the amount of material, vacuum conditions, high installation costs, are key issues for the PV technology development.[19] The emerging solar cells, have led to a significant progress since their appearance with the first dye-sensitized solar cells in 1991. To date, a certificated efficiency of 12.6 % has been reached by organic solar cells, after a long period of intense research. Therefore, organic PV technologies based on π-conjugated small molecules and polymers have seen increasing attention in recent years as an alternative to inorganic PV.[15] Perovskite solar cells deserve a different consideration. From its first report in 2009 this PV technology has led to an impressive progress reaching nowadays efficiencies around 22 %.

19. J. Jean, P. R. Brown, R. L. Jaffe, T. Buonassisi, V. Bulovic, "Pathways for solar photovoltaics", *Energy Environ. Sci.*, **2015**, *8*, 1200-1219.

Key technological approaches to boost cell efficiency include identifying more conductive electrode materials to reduce resistive losses, employing advanced cell architectures, improving surface passivation to reduce recombination loss and engineering optical and electronic materials to improve current collection.[19]

2. Photovoltaic device structures

Photovoltaic devices can be classified in two categories:

i) Wafer-based, fabricated on semiconducting wafers, whose modules are typically covered with glass for mechanical stability and protection.

ii) Thin-film cells, which consist of semiconducting films deposited onto a glass, plastic or metal substrate. Some of them are commercial, while others are still considered emerging technologies.

Figure 5 illustrates the current classification of PV technologies.[19]

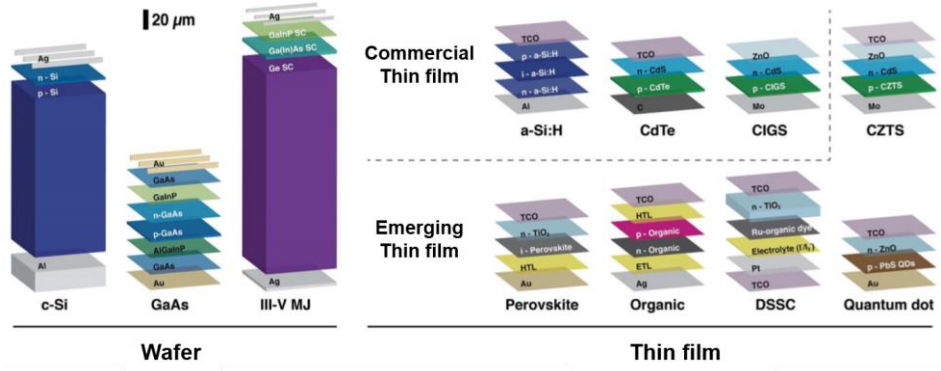

Figure 5. Typical solar PV device structures divided into wafer-based and thin-film technologies.

Currently, three primary wafer-based technologies can be distinguished:

- **Crystalline silicon (c-Si) solar cells** are the most mature PV technology which constitute about the 90 % of current global production capacity. Silicon solar cells are classified as single-crystalline (sc-Si) or multi-crystalline (mc-Si) being their record cell efficiencies of 26.3 ± 0.5 % and 21.3 ± 0.4 % respectively. However, these values are lower in large-area module, 24.4 ± 0.5 % and 19.9 ± 0.4 % respectively.[10]

- **Gallium arsenide (GaAs) solar cells** are almost perfectly suited for solar energy conversion. They exhibit strong absorption, a direct bandgap and very low non-radiative energy loss. GaAs-based devices have achieved the highest power conversion efficiencies of any material system, namely 28.8 ± 0.9 % for laboratory cells and 24.1 ± 1.0 % for modules.[10]

- **III-V multijunction (MJ) solar cells** are made of semiconducting compounds of group III (Al, Ga, In) and group V (N, P, As, Sb). Record cell efficiencies without concentration are 38.9 ± 2.5 %, 35.9 ± 1.8 % and 31.2 ± 1.2 % for 4J, 3J and 2J cells, respectively.[10]

On the other hand, thin film-based technologies can be classified in commercial and emerging thin-film:

i) Commercial thin-film technologies

- **Cadmium telluride (CdTe)** is the leading thin-film PV technology. CdTe is a favourable semiconductor for solar energy harvesting, with strong absorption across the solar spectrum and a direct bandgap of 1.45 eV. Record efficiencies of 21.0 ± 0.4 % for cells and 18.6 ± 0.6 % for module[10] are among the highest for thin-film solar cells.

- **Copper indium gallium diselenide ($CuIn_xGa_{1-x}Se_2$, or CIGS) solar cells** which record efficiencies stand at 21.0 ± 0.6 % for cells and 17.5 ± 0.5 % for modules.[10]

ii) Emerging thin-film PV

Several new thin-film PV cells, fabricated through solution-processable techniques, have emerged as a result of intense efforts in materials discovery and device engineering. Some emerging thin-film PV technologies as low cost alternatives to replace/complement silicon-based solar cells, include the following:

- **Organic photovoltaic solar cells.** Photovoltaics based on organic semiconductors have emerged as promising low-cost alternatives for electricity generation from sunlight. Next section is dedicated to organic PV devices, including dye-sensitized, bulk-heterojunction and perovskite solar cells.

3. Organic photovoltaic solar cells

Organic photovoltaic (OPV) technology offers a wide variety of promising properties such as favourable electronic properties and low production and installation costs. The potential simplicity of OPV processing is far beyond other current technologies. The component versatility with high absorption coefficients, the possibility of processing in solution and the generally lightweight of devices allow the fabrication on flexible substrates and the assemblage in large-area thin films. This technology started to develop 25 years ago, following an intense learning curve. Some up-scale examples can be already found like one of the walls at EPFL in Lausanne (Switzerland) and the world's largest solar facade installed in a Danish school (Denmark) (figure 6).

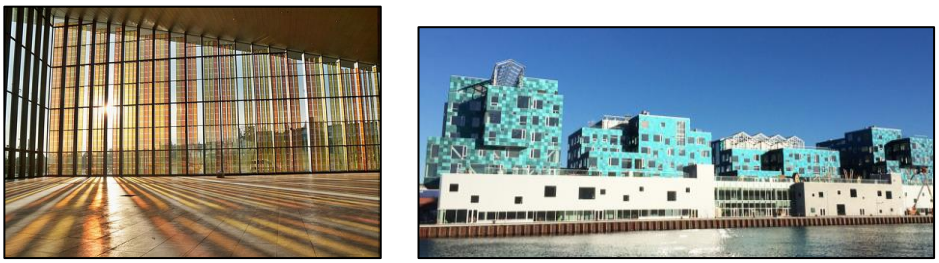

Figure 6. Examples of up-scale installed solar cells.

OPV solar cells are constituted by semiconducting organic materials formed by contacting electron donor and acceptor compounds. The transformation of solar energy into electricity is possible through optical and electronic processes which basically involve: i) optical absorption and formation of the exciton; ii) exciton migration to the donor-electron interface; iii) dissociation into electron and hole; iv) charge diffusion and collection at the electrodes.[5]

Following, OPV solar cells have been organized in different groups as it follows, dedicating special attention to the perovskite-based solar cells.

- Dye-sensitized solar cells (DSSCs) are among the most mature of nanomaterial-based PV technologies.[20] Since the pioneering work reported by Grätzel in 1991,[17] they have been intensively investigated as promising low-cost alternative to commercial solar cells due to their efficiency, decorative colourful nature and easy fabrication. The highest efficiency of liquid-based DSSCs

20. M. Graetzel, "Dye-sensitized solar cells", *J. Photochem. Photobiol. C: Photochem. Rev.*, **2003**, *4*, 145-153.

reported so far has reached 13.1 %.[21] However, several practical issues related to the presence of a liquid electrolyte, dye desorption and corrosive action of the iodide/iodine redox electrolyte couple, have withheld the large-scale technological development of such devices.

Encapsulations of liquid electrolytes at elevated temperatures have become a vital restriction in terms of long-term stability of these devices.[22] In this context, the first efficient solid-state DSSCs (ss-DSSCs) in which liquid electrolytes were replaced by an organic hole-transporting material was presented by Bach, Graetzel, *et al*. in1998.[23]

- Bulk heterojunction solar cells (BHJ). Organic photovoltaic based on π-conjugated polymers and small molecules have seen increasing interest in recent years as another alternative to inorganic PV. An intense research and improvements have been developed. Recently, Wei and co-workers reported a 11.3 % as the record efficiency in an inverted organic solar cell based on fluorinated small molecules.[24]

- Perovskite solar cells evolved from solid-state dye-sensitized cells[25] and have quickly become one of the most promising emerging thin-film PV technologies, with a certified efficiency of 22.1 %[26] in less than 7 years of research.[27] The following section is dedicated to this technology.

---

21. S. Mathew, A. Yella, P. Gao, R. Humphry-Baker, B. F. E. Curchod, N. Ashari-Astani, I. Tavernelli, U. Rothlisberger, M. K. Nazeeruddin, M. Graetzel, "Dye-sensitized solar cells with 13 % efficiency achieved through the molecular engineering of porphyrin sensitizers", *Nat. Chem.*, **2014**, *6*, 242-247.
22. Z. Yu, N. Vlachopoulos, M. Gorlov, L. Kloo, "Liquid electrolytes for dye-sensitized solar cells", *Dalton Trans.*, **2011**, *40*, 10289-10303.
23. U. Bach, D. Lupo, P. Comte, J. E. Moser, F. Weissortel, J. Salbeck, H. Spreitzer, M. Graetzel, "Solid-state dye-sensitized mesoporous TiO_2 solar cells with high photon-to-electron conversion efficiencies", *Nature*, **1998**, *395*, 583-585.
24. Y. Z. D. Deng, J. Zhang, Z. Wang, L. Zhu, J. Fang, B. Xia, Z. Wang, K. Lu, W. Ma, Z. Wei, "Fluorination-enabled optimal morphology leads to over 11 % efficiency for inverted small-molecule organic solar cells", *Nat. Comm.*, **2016**, *7*, 13740-13749.
25. M. M. Lee, J. Teuscher, T. Miyasaka, T. N. Murakami, H. J. Snaith, "Efficient hybrid solar cells based on meso-superstructured organometal halide perovskites", *Science*, **2012**, *338*, 643-647.
26. *N.R.E.L. (National Renewable Energy Laboratory)*, **2016**; *http://www.nrel.gov.*
27. A. Polman, M. Knight, E. C. Garnett, B. Ehrler, W. C. Sinke, "Photovoltaic materials: Present efficiencies and future challenges", *Science*, **2016**, *352, 307-317.*

4. Perovskite solar cells

A novel low-cost approach is progressing to compete/coexist with silicon-based devices.[28] That is, the new family of perovskite solar cells (PSCs) which have recently taken the PV research world by storm. Hybrid organic-inorganic perovskites have recently and spectacularly emerged as the next generation of promising materials for low cost thin-film solar cells.[29] Only 7 years of substantial work has been necessary to reach a conversion efficiency of 22.1 % which was certified by NREL.[26]

4.1. Perovskites: structure and properties

The term perovskite refers to the crystal structure of calcium titanate ($CaTiO_3$), which was discovered by the German mineralogist Gustav Rose, named after a Russian mineralogist Lev Perovski.[30] Organic-inorganic hybrid perovskites crystal structure can be ideally represented by the simple building block ABX_3, where A represents a cation, B is a divalent metal cation (Pb^{2+}, Sn^{2+}) and X is a monovalent halide anion (typically I^-, often with a small fraction of Cl^- or Br^-). As shown in figure 7, B and X form an ideal cubic-symmetry structure (BX_6 octahedral arrangement) where the B-cations are located in the middle of the octahedral surrounded by X-anions located at the corners. A-cations fill the hole formed by the eight adjacent octahedral in the 3D framework and balances the charge of the whole network. The most commonly used perovskite in solar cells is organic-inorganic hybrid perovskite, where A is an organic cation such as methylammonium, MA ($CH_3NH_3^+$) or formamidinium, FA ($HC(NH_2)_2^+$), which is enclosed by twelve nearest X anions.

28. S. Ameen, M. A. Rub, S. A. Kosa, K. A. Alamry, M. S. Akhtar, H. S. Shin, H. K. Seo, A. M. Asiri, M. K. Nazeeruddin, "Perovskite solar cells: Influence of hole transporting materials on power conversion efficiency", *ChemSusChem*, **2016**, *9*, 10-27.
29. M. A. Green, A. Ho-Baillie, H. J. Snaith, "The emergence of perovskite solar cells", *Nat. Photonics*, **2014**, *8*, 506-514.
30. L. J. Schmidt, "Tracking down the truth of Perovski", *38th Rochester Mineralogical Symp. Program Notes* **2011**, 31-32.

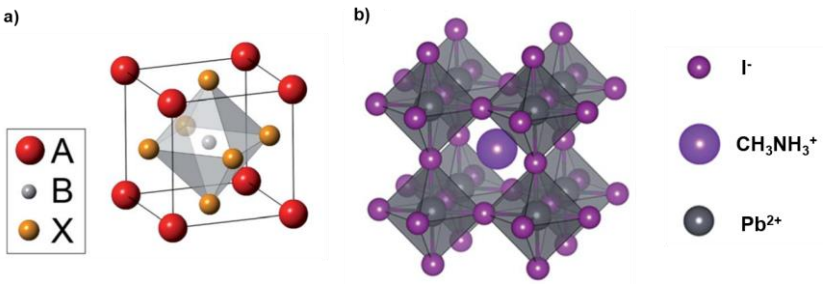

Figure 7. a) The ABX_3 perovskite crystal structure; **b**) Extended structure of cubic perovskite.

Ideally, perovskites have cubic geometry but in fact, they are pseudo-cubic or distorted cubic in nature.[31] Any sort of distortion will affect physical properties of perovskite materials, such as electronic, optical, magnetic and dielectric properties.[32] The size of cation (A, B) or anion (X) is an important parameter to modulate the optical and electronic properties of perovskite material.[19] In order to describe the limits on ionic sizes of each component, the tolerance factor for a particular perovskite was defined as:[33]

$$t = \frac{r_A + r_X}{\sqrt{2}\cdot(r_B + r_X)} \quad (1)$$

where r_A, r_B and r_X are the ionic radius of the A, B and X components of the perovskite lattice. A perfectly packed structure would correspond to t = 1 and it can be varied only in a restricted range. For most perovskites it has been stated to be between 0.8 and 0.9. With an eye in PV applications, some studies have reported the impact of changing the size of the ions in order to tune the bandgap of the perovskite absorber. Changing the B-X interionic distance was demonstrated to be important in the optical properties of the alloyed hybrid

31. D. B. Mitzi, "Organic-inorganic perovskites containing trivalent metal halide layers: The templating influence of the organic cation layer", *Inorg. Chem.*, **2000**, *39*, 6107-6113.
32. S. Kazim, M. K. Nazeeruddin, M. Graetzel, S. Ahmad, "Perovskite as light harvester: A game changer in photovoltaics", *Angew. Chem. Int. Ed.*, **2014**, *53*, 2812-2824.
33. C. C. Stoumpos, M. G. Kanatzidis, "The Renaissance of Halide Perovskites and Their Evolution as Emerging Semiconductors", *Acc. Chem. Res.*, **2015**, 48, 2791-2802.

perovskite by Seok in 2013.[34] The UV-vis absorption spectra for mesoporous-TiO_2 (m-TiO_2)/$MAPb(I_{1-x}Br_x)_3$ were measured changing the value of x: $0 \leq x \leq 1$, as shown in figure 8. The onset absorption band could be tuned from a 786 nm wavelength (1.58 eV) to 544 nm wavelength (2.28 eV), resulting in tunable colorful solar cells.[34]

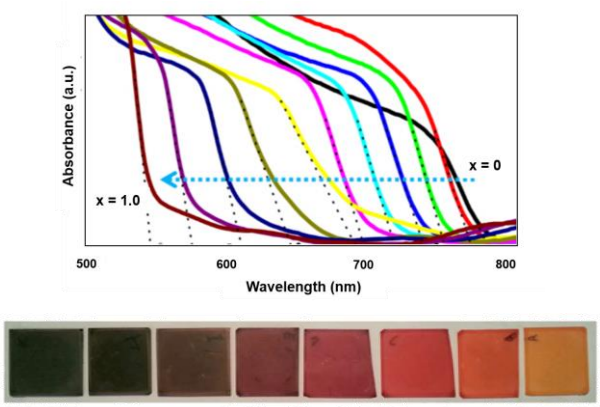

Figure 8. UV-vis absorption spectra of $MAPb(I_{1-x}Br_x)_3$-based cells and photographs of $MAPb(I_{1-x}Br_x)_3$ perovkiste.

Seok and co-workers demonstrated in that study that the lattice parameters and successive band gap energy of $MAPb(I_{1-x}Br_x)_3$ have linear relationships with Br content (x). The optical absorption caused by band gap engineering can be modified in a controlled manner to cover almost the entire visible spectrum. They demonstrated enhanced efficiency and stability through the chemical management of $MAPbX_3$. The cells fabricated from x = 0 to 0.2 in $MAPb(I_{1-x}Br_x)_3$ exhibit an average of more than 10 % with maximum 12.3 % in conversion efficiency and the relative stability under the same conditions was greatly improved at x = 0.2, while keeping the efficiency.[34] Motivated by this, a range of formamidinium lead bromide iodide mixed halide perovskites ($FAPbI_yBr_{3-y}$) were used to explore the range of bandgap tunability of this perovskite-system by Snaith and co-workers.[35] In addition, they reported how the bandgap could be

34. J. H. Noh, S. H. Im, J. H. Heo, T. N. Mandal, S. I. Seok, "Chemical management for colorful, efficient, and stable inorganic-organic hybrid nanostructured solar cells", *Nano Lett.*, **2013**, *13*, 1764-1769.
35. G. E. Eperon, S. D. Stranks, C. Menelaou, M. B. Johnston, L. M. Herz, H. J. Snaith, "Formamidinium lead trihalide: A broadly tunable perovskite for efficient planar heterojunction solar cells", *Energy Environ. Sci.*, **2014**, *7*, 982-988.

tuned by variation of the A cation size. A larger or smaller A cation can cause the whole lattice to expand or contract.

To investigate the effect of the A cation size upon the optical and electronic properties of the perovskite, perovskites based on methylammonium lead triiodide ($MAPbI_3$), replacing MA ($CH_3NH_3^+$) with cesium (Cs^+) and FA ($HC(NH_2)_2^+$) were prepared. The absorbance spectra for the $APbI_3$ perovskites, where A is either Cs, MA or FA are shown in figure 9. As it can be seen, $CsPbI_3$ absorbs up to a shorter wavelength, whereas $FAPbI_3$ absorbs to a longer wavelength than $MAPbI_3$.

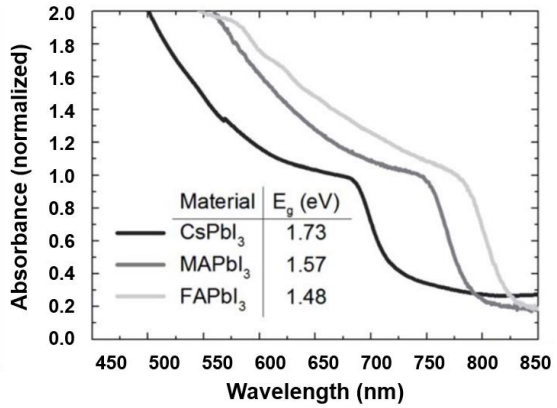

Figure 9. UV-vis spectra for the $APbI_3$ perovskites formed, where A is either cesium (Cs), methylammonium (MA) or formamidinium (FA).

Cesium has a smaller effective ionic radius compared to MA, whereas FA is slightly larger. As the A cation increases in ion radius, and hence the lattice would be expected to expand, the band gap decreases, causing a red-shift in the absorption onset. As an inset in figure 9, the estimations of the bandgap are shown. Just by replacing the MA with the slightly larger FA, it is possible to shift the bandgap closer to the optimum for a single junction solar cell. As such, this material is a likely candidate to be able to produce even more efficient solar cells than $MAPbI_3$.

In conclusion, changing the size of the A cation in $APbI_3$ perovskite, it is possible to tune the bandgap.[35] Replacing MA with FA in $MAPbI_3$ perovskite, narrows the bandgap, enabling broad bandgap tunability with the mixed halide $FAPbI_yBr_{3-y}$ perovskite system between 1.48 eV and 2.23 eV. Since $FAPbI_3$ displays a bandgap of 1.48 eV, it is closer to the 'ideal' single-junction solar cell

bandgap of between 1.1 eV and 1.4 eV. Apart from having the possibility of tuning the optical properties, such as its band gap, these promising materials possess other interesting intrinsic properties. Further studies demonstrated that perovskites exhibit ambipolar behaviour, indicating that the perovskite materials themselves can transport both electrons and holes between the cell terminals,[36] exhibiting long charge carrier diffusion lengths (~100 nm for $MAPbI_3$ and ~1000 nm for $MAPbI_{3-x}Cl_x$),[36,37] excellent carrier mobility (> 100 ns), very low exciton binding energy (25-50 meV), large optical absorption and simple fabrication processes.

4.2. Efficiency

The first attempt of using organo lead halide perovskite in PV applications was as a sensitizer in liquid-based DSSCs and dates back to the report of Miyasaka and co-workers in 2009.[38] Power conversion efficiencies (PCEs) of merely 3.8 % and 3.1 % were obtained employing $MAPbI_3$ and $MAPbBr_3$ as light absorbers, respectively. The PCE of the liquid-based $MAPbI_3$ solar cell was further improved by Park and co-workers through the modification of the TiO_2 surface and the processing method for the perovskite deposition, leading to a PCE of 6.5 % in 2011.[39] Unfortunately, these devices were found extremely unstable and degraded rapidly due to the dissolution of perovskite ions in liquid electrolytes.

A big breakthrough was made in 2012. Snaith *et al.*[25] and Graetzel *et al.*[40] independently developed solid-state PSCs using $MAPbI_{3-x}Cl_x$ and $MAPbI_3$ as

36. G. Xing, N. Mathews, S. Sun, S. S. Lim, Y. M. Lam, M. Graetzel, S. Mhaisalkar, T. C. Sum, "Long-range balanced electron- and hole-transport lengths in organic-inorganic $CH_3NH_3PbI_3$", *Science*, **2013**, *342*, 344-347.
37. S. D. Stranks, G. E. Eperon, G. Grancini, C. Menelaou, M. J. P. Alcocer, T. Leijtens, L. M. Herz, A. Petrozza, H. J. Snaith, "Electron-hole diffusion lengths exceeding 1 micrometer in an organometal trihalide perovskite absorber", *Science*, **2013**, *342*, 341-344.
38. A. Kojima, K. Teshima, Y. Shirai, T. Miyasaka, "Organometal halide perovskites as visible-light sensitizers for photovoltaic cells", *J. Am. Chem. Soc.*, **2009**, *131*, 6050-6051.
39. J. H. Im, C. R. Lee, J. W. Lee, S. W. Park, N. G. Park, "6.5 % Efficient perovskite quantum-dot-sensitized solar cell", *Nanoscale*, **2011**, *3*, 4088-4093.
40. H. S. Kim, C. R. Lee, J. H. Im, K. B. Lee, T. Moehl, A. Marchioro, S. J. Moon, R. Humphry-Baker, J. H. Yum, J. E. Moser, M. Graetzel, N. G. Park, "Lead iodide perovskite sensitized all-solid-state submicron thin film mesoscopic solar cell with efficiency exceeding 9 %", *Sci. Rep.*, **2012**, *2*, 591.

light absorbers deposited onto a mesoporous TiO_2 layer. Using spiro-OMeTAD as the HTM, PCEs of 7.6 % and 9.7 % were achieved respectively.

Great developments have been carried out in the design of new perovskite-based device architectures,[41,42] applications of various n-type nanostructures,[43,44] chemical managements of perovskite compositions[35,45] and different deposition techniques for high-quality perovskite films.[46,47] This has made possible a quick step forward of the overall conversion efficiencies of hybrid organic-inorganic perovskite solar cells to a certified 22.1 %.[26]

4.3. Perovskites device architectures

In the early stages, the function and working principle of the perovskite was analogous to that of the dye in DSSCs. However, its ambipolar behaviour led to the development of new configurations and materials. In this sense, perovskite could be used cumulatively as light absorber, electron conductor and hole conductor.[25] Nowadays, the typical device architectures of PSCs are analogous to and inspired by those used for ss-DSSCs.[48] PSCs technology has demonstrated

41. J. Y. Jeng, K. C. Chen, T. Y. Chiang, P. Y. Lin, T. D. Tsai, Y. C. Chang, T. F. Guo, P. Chen, T. C. Wen, Y. J. Hsu, "Nickel oxide electrode interlayer in $CH_3NH_3PbI_3$ perovskite/PCBM planar-heterojunction hybrid solar cells", *Adv. Mater.*, **2014**, *26*, 4107-4113.
42. F. Zhang, X. Yang, H. Wang, M. Cheng, J. Zhao, L. Sun, "Structure engineering of hole–conductor free perovskite-based solar cells with low-temperature-processed commercial carbon paste as cathode", *ACS Appl. Mater. Interfaces*, **2014**, *6*, 16140-16146.
43. A. Yella, L. P. Heiniger, P. Gao, M. K. Nazeeruddin, M. Graetzel, "Nanocrystalline rutile electron extraction layer enables low-temperature solution processed perovskite photovoltaics with 13.7 % efficiency", *Nano Lett.*, **2014**, *14*, 2591-2596.
44. D. Y. Son, J. H. Im, H. S. Kim, N. G. Park, "11 % efficient perovskite solar cell based on ZnO nanorods: An effective charge collection system", *J. Phys. Chem. C*, **2014**, *118*, 16567-16573.
45. F. Hao, C. C. Stoumpos, R. P. H. Chang, M. G. Kanatzidis, "Anomalous band gap behavior in mixed sn and pb perovskites enables broadening of absorption spectrum in solar cells", *J. Am. Chem. Soc.*, **2014**, *136*, 8094-8099.
46. M. Liu, M. B. Johnston, H. J. Snaith, "Efficient planar heterojunction perovskite solar cells by vapour deposition", *Nature*, **2013**, *501*, 395-398.
47. N. J. Jeon, J. H. Noh, Y. C. Kim, W. S. Yang, S. Ryu, S. I. Seok, "Solvent engineering for high-performance inorganic–organic hybrid perovskite solar cells", *Nat. Mater.*, **2014**, *13*, 897-903.
48. T. Swetha, S. P. Singh, "Perovskite solar cells based on small molecule hole transporting materials", *J. Mater. Chem. A*, **2015**, *3*, 18329-18344.

considerable prospects in achieving efficiencies comparable to or even better than those of thin film solar cells. The remarkable performances thus far seem not to be limited to any specific device architecture.[49] Figure 10 illustrates the main architectures of perovskite devices: mesoscopic nanostructure, planar structure and inverted structure, which show excellent device performances. [50]

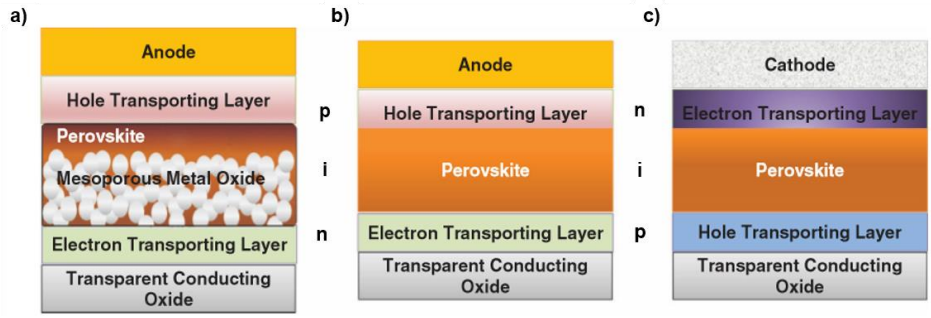

Figure 10. Schematic diagram of **a**) regular mesoporous structure, **b**) regular planar structure, **c**) inverted planar structure, perovskite solar cells.

The variation in device architectures occurs in the nature of the positive (p) and negative (n) selective contact materials, with the optional insertion of a thin interlayer of mesoporous scaffold to either aid film formation or charge extraction. The perovskite is an intrinsic semiconductor and light enters through the n-type or the p-type layer. The ambipolar charge transport property of perovskite makes the designs of PSCs quite versatile, leading to the division of planar structure into two categories depending on the selective contact, that is regular (n-i-p) and inverted (p-i-n) architectures. The regular n-i-p structures have been extensively studied and could be traced back to DSSCs. They consist in a transparent conductive oxide substrate, such as fluorine-doped tin oxide (FTO) on a glass - compact TiO_2 (c-TiO_2) blocking layer as electron-selective contact (n) - perovskite (i) (on a mesoporous TiO_2 scaffold (m-TiO_2) in the case of the regular mesoporous cells) - positive-selective contact (p) and, finally, a metal electrode such as Au or Ag. In planar structures, the perovskite layer is sandwiched between the c-TiO_2 blocking layer and the HTM. This makes the

49. T. Salim, S. Sun, Y. Abe, A. Krishna, A. C. Grimsdale, Y. M. Lam, "Perovskite-based solar cells: Impact of morphology and device architecture on device performance", *J. Mater. Chem. A*, **2015**, *3*, 8943-8969.
50. T. Liu, K. Chen, Q. Hu, R. Zhu, Q. Gong, "Inverted perovskite solar cells: Progresses and perspectives", *Adv. Energy Mater.*, **2016**, *6*, 1600457-1600474.

fabrication process much simpler when compared to the mesoscopic configurations. On the other hand, the inverted configuration consists in p-i-n structure and it is derivate from OSCs. Several charge transport layers used in OSCs have successfully been transferred into PSCs.[51]

Regardless of device architecture, device performance is highly dependent on the film morphology. The deposition method, material composition, additives and film treatment are some of the factors that can influence on the film morphology. The key for obtaining good quality film morphology and hence performance is essentially lowering the energy barrier for nucleation and promote uniform growth of the perovskite crystals.

4.4. Device operating principles

The main charge-transfer processes involved in PSCs (desirable and undesirable) are depicted in figure 11 together with the energy levels of the different components of the device.

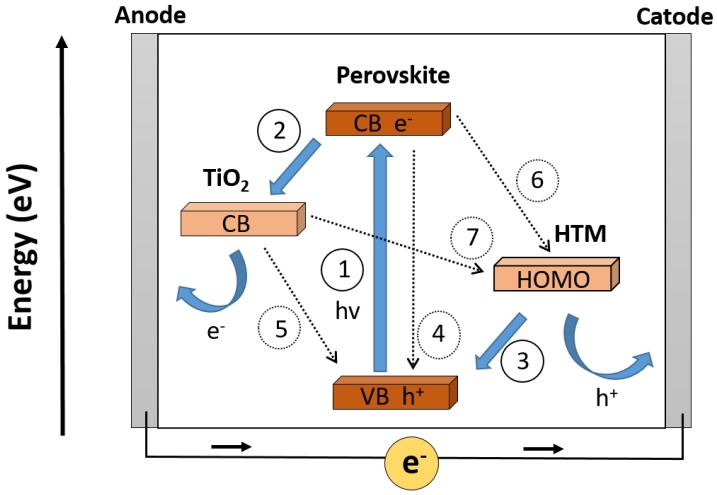

Figure 11. Schematic representation of the energy levels and electron transfer process in PSCs.

51. L. Meng, J. You, T. F. Guo, Y. Yang, "Recent advances in the inverted planar structure of perovskite solar cells", *Acc. Chem. Res.*, **2016**, *49*, 155-165.

The working principle of PSCs involves:[52] 1) photo-excitation of the perovskite light absorber: creation of electron-hole pairs. 2) Transfer the excited electrons into the conduction band of the semi-conductor TiO_2 while 3) holes on the perovskite are transferred to hole conductor. These photo-generated charge carriers are subsequently collected as photocurrent at the front and back contacts of the solar cell. The undesirable processes include 4) recombination of photogenerated charge carrier species, either radiative or non-radiative as a result of exciton annihilation, as well as 5) back electron transfer at the interface of TiO_2 with perovskite, 6) back hole transfer at the interface of the HTM with perovskite and 7) charge recombination at the TiO_2/HTM interface, this may occur only in the case of incomplete coverage of perovskite. It is clear that for high PCE, the charge recombination processes (4-7) should occur at a higher time scale than charge generation, separation and extraction processes (1-3).

4.5. J-V Hysteresis

One of the main limitations to the advancement of PSCs is the presence of the anomalous hysteresis in the J-V curves of the device performance. Hysteresis is observed by varying the direction and the rate of voltage sweep (see an example in figure 12).

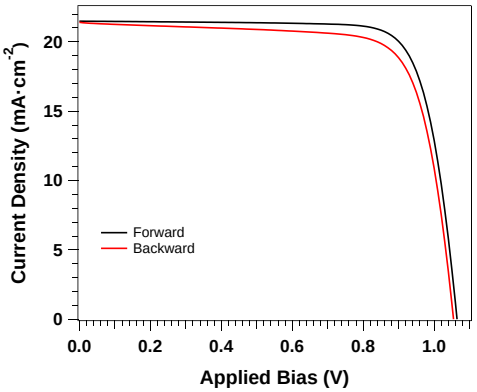

Figure 12. Example of hysteresis in a perovskite-based device.

52. A. Marchioro, J. Teuscher, D. Friedrich, M. Kunst, R. Van De Krol, T. Moehl, M. Graetzel, J. E. Moser, "Unravelling the mechanism of photoinduced charge transfer processes in lead iodide perovskite solar cells", *Nat. Photon.*, **2014**, *8*, 250-255.

The presence of J-V hysteresis may lead to questionable and erroneous device efficiency.[53] That is because higher efficiency may be obtained holding a perovskite device at a forward bias voltage before measurement, than that found when the device has been reverse biased or when the device is held at the maximum power point or at short circuit.[54] In addition, measuring the device at a rate faster than its response time may also result in varying efficiency measurements.[55]

Although the origins of hysteresis remain controversial, three possible reasons have been proposed to account for it which are, ion migration,[56] unbalanced charge collection rates,[57] and ferroelectricity.[58] Recent investigations have shown that the first two are more likely to cause the J-V hysteresis.[59, 60]

53. Z. Song, S. C. Watthage, A. B. Phillips, M. J. Heben, "Pathways toward high-performance perovskite solar cells: Review of recent advances in organo-metal halide perovskites for photovoltaic applications", *J. Photon. Energy*, **2016**, *6*, 22001-22001.
54. W. Tress, N. Marinova, T. Moehl, S. M. Zakeeruddin, M. K. Nazeeruddin, M. Graetzel, "Understanding the rate-dependent J-V hysteresis, slow time component, and aging in $CH_3NH_3PbI_3$ perovskite solar cells: The role of a compensated electric field", *Energy Environ. Sci.*, **2015**, *8*, 995-1004.
55. E. L. Unger, E. T. Hoke, C. D. Bailie, W. H. Nguyen, A. R. Bowring, T. Heumuller, M. G. Christoforo, M. D. Mcgehee, "Hysteresis and transient behavior in current-voltage measurements of hybrid-perovskite absorber solar cells", *Energy Environ. Sci.*, **2014**, *7*, 3690-3698.
56. C. Eames, J. M. Frost, P. R. F. Barnes, B. C. O'Regan, A. Walsh, M. S. Islam, "Ionic transport in hybrid lead iodide perovskite solar cells", *Nat. Commun.*, **2015**, *6*, 7497-7505.
57. V. W. Bergmann, S. a. L. Weber, F. Javier Ramos, M. K. Nazeeruddin, M. Graetzel, D. Li, A. L. Domanski, I. Lieberwirth, S. Ahmad, R. Berger, "Real-space observation of unbalanced charge distribution inside a perovskite-sensitized solar cell", *Nat. Commun.*, **2014**, *5*, 5001-5010.
58. J. M. Frost, K. T. Butler, A. Walsh, "Molecular ferroelectric contributions to anomalous hysteresis in hybrid perovskite solar cells", *APL Materials*, **2014**, *2*, 81506-81516.
59. T. Leijtens, G. E. Eperon, N. K. Noel, S. N. Habisreutinger, A. Petrozza, H. J. Snaith, "Stability of metal halide perovskite solar cells", *Adv. Energy Mater.*, **2015**, *5*, 1500963-1500986.
60. S. Van Reenen, M. Kemerink, H. J. Snaith, "Modeling anomalous hysteresis in perovskite solar cells", *J. Phys. Chem. Lett.*, **2015**, *6*, 3808-3814.

4.6. Stability of perovskite solar cells

One of the most important criteria for a potentially commercial PV technology is the capacity of maintaining a stable power output under a standard working condition. PSCs stability data during one to four months have been reported.[59,61] However, long-term stability that could be comparable to the 30-year standard of commercial PV panels has yet to be demonstrated. Perovskite devices without encapsulation have shown hundreds of hours stability when stored in the dark and measured infrequently, however, they rapidly degraded after sustained exposure to sunlight.[62] In addition to light exposure, elevated temperature and humidity may accelerate the degradation due to the moisture-induced decomposition of perovskite crystals. These are the greatest barriers to address for their commercial implementation.[27]

4.7. Toxicity of perovskite solar cells

Because most PSCs are lead-based, there are even greater environmental concerns with the possibility of large-scale PSCs development than for CdTe and GaAs as an example, because the much higher water solubility and lower vaporization temperature. However, intense research in lead-free perovskite, encapsulation and recycling is underway to become this PV technology viable for large-scale application.[27]

In addition, life-cycle analysis and environmental impact assessment of PSCs have revealed that the lead bears very little proportion on the overall environmental impact during manufacturing process.[63] Compared with other lead emission sources (such as mining, fossil fuels, manufacturing of batteries, plumbing, soldering, electronics and so on).[64]

61. A. Mei, X. Li, L. Liu, Z. Ku, T. Liu, Y. Rong, M. Xu, M. Hu, J. Chen, Y. Yang, M. Graetzel, H. Han, "A hole-conductor–free, fully printable mesoscopic perovskite solar cell with high stability", *Science*, **2014**, *345*, 295-298.
62. S. D. Stranks, H. J. Snaith, "Metal-halide perovskites for photovoltaic and light-emitting devices", *Nat. Nanotechnol.*, **2015**, *10*, 391-402.
63. J. Gong, S. B. Darling, F. You, "Perovskite photovoltaics: Life-cycle assessment of energy and environmental impacts", *Energy Environ. Sci.*, **2015**, *8*, 1953-1968.
64. B. Hailegnaw, S. Kirmayer, E. Edri, G. Hodes, D. Cahen, "Rain on methylammonium lead iodide based perovskites: Possible environmental effects of perovskite solar cells", *J. Phys. Chem. Lett.*, **2015**, *6*, 1543-1547.

Objectives

OBJECTIVES

Significant research efforts have been dedicated to improve the performance of solar cells based on perovskites, including chemical optimization of the perovskite composition, different deposition methods and device architectures. In addition, the design and improvement of hole- and electron-transporting layers, seem to be crucial to successfully reach high performances of perovskite-based devices. Therefore, the main objective of this thesis is the development of new hole- and electron-transporting materials with undeniable high impact in the efficiency for low cost of perovskite solar cells.

Chapter 1. Hole-transporting materials for perovskite solar cells

Although there is not a clear relationship between chemical structure of a HTM and PV performance in the literature, it is well-known that spiro-OMeTAD works in a very efficient manner. Due to its complex and costly preparation, the main objective in chapter 1 is to design and develop new molecularly engineered small-organic molecules to achieve low-cost and effective HTMs for perovskite solar cells. It is divided in four different sections.

The first part of this chapter is focused on the design and synthesis of easily attainable hole-transporting molecules. To reach this goal, TAE- and BF-derivatives have been synthesized following a straightforward methodology, in just two synthetic steps. In particular, the new central cores are decorated with different electron donor groups. Furthermore, this study is intended to shed light about the rigidity of the 3D molecular arrangement and its impact as dopant-free HTMs in $MAPbI_3$-based solar cells.

The next section is divided in two different consecutive projects. These projects are presented in chronological order and the results obtained in each case are employed for the design and development of the next one, thus optimizing the structures for better performance HTMs.

Firstly, the preparation and characterization of competitive HTMs based on a planar sulfur rich central core (benzotrithiophene, BTT) with different electron donor units is presented. It has been devoted a special attention to the synthetic cost and the thermal, optical and electrochemical properties of the molecules. The aim of these HTMs is to evaluate the device performance, with two different perovskites, $MAPbI_3$ and $(FAPbI_3)_{0.85}(MAPbBr_3)_{0.15}$, stemming from these planar structures which are endowed with different electron donor groups.

In a second stage and inspired by the results obtained with the previous BTT-derivatives, it was decided to synthesize two novel three- and four-armed molecules based on isomeric structures of BTT. The goal of this idea is to study the isomerism effect on the thermal, electrochemical, optical and photovoltaic properties of benzotrithiophene-based HTMs. For this purpose, the new molecules will be incorporated as HTMs for the compositionally engineered perovskite $(FAPbI_3)_{0.85}(MAPbBr_3)_{0.15}$ solar cells.

One of the central challenges in the design of HTMs is to achieve both good thermal stability and decent conductivity. Indeed, this scenario was easily accomplished with sulfur-rich derivatives and spiro-like compounds. In this sense, this study was extended to tailor the molecular properties by introducing fused-heterocycles (nitrogen and oxygen), which until now have not been extensively studied. The new HTMs will be employed as sulfur-free HTMs in PSCs.

Finally, novel HTMs based on thieno[3,2-*b*]thiophene as central fragment have been designed and synthesized, studying the influence of the different spacers between the central core and the *p*-methoxydiphenylamine units in the performance and hysteresis of PSCs.

Chapter 2. Electron-transporting materials for perovskite solar cells

The main objective of the second chapter is to develop more effective fullerene derivatives with different chemical functionalization and LUMO energy levels by cutting down costs in order to be used as ETMs in PSCs.

Firstly, a series of [60]fullerenes monoadducts and bisadducts bearing a benzoic acid moiety have been prepared by a simple and straightforward route of synthesis. Particularly, three fullerene derivatives have been incorporated as self-assembled monolayers (SAMs) at the interface in PSCs.

On the other hand, analogous of the most used ETM, $PC_{61}BM$, are synthesized in order to be explored as ETMs in inverted perovskite-based devices.

Chapter 1

Hole-transporting materials for perovskite solar cells

• Background

Chapter 1. Hole-transporting materials
for perovskite solar cells

1. BACKGROUND

Within the last recent years, a new class of PV devices made an impressive arrival in the PV field: the organic-inorganic halide perovskite-based solar cells. The overall PCE of PSCs have quickly jumped to certified 22.1 %.[26] Significant research efforts have been dedicated to improve the PCE, which include chemical optimization of the perovskite compositions,[35,65] deposition techniques,[47,66] device architectures[67,68] and application of different hole[69] and electron-transporting materials.[50,51] Particularly, the synthesis and employment of new materials as hole-transporting layer in perovskite devices, have been widely studied with the main objective of increasing the efficiency and improving the stability of the cell.

1.1. Role of hole-transporting material in PSCs

An ideal HTM has to fulfill some requirements such as sufficient hole mobility, minimal absorption in the visible and near IR-region of the solar spectrum as well as excellent thermal and photochemical stability, etc.[28,70] (figure 13).

65. J. W. Lee, D. J. Seol, A. N. Cho, N. G. Park, "High-efficiency perovskite solar cells based on the black polymorph of $CH(NH_2)_2PbI_3$", *Adv. Mater.*, **2014**, *26*, 4991-4998.
66. J. H. Im, I. H. Jang, N. Pellet, M. Graetzel, N. G. Park, "Growth of $CH_3NH_3PbI_3$ cuboids with controlled size for high-efficiency perovskite solar cells", *Nat. Nanotechnol.*, **2014**, *9*, 927-932.
67. D. Bi, S. J. Moon, L. Haggman, G. Boschloo, L. Yang, E. M. J. Johansson, M. K. Nazeeruddin, M. Graetzel, A. Hagfeldt, "Using a two-step deposition technique to prepare perovskite ($CH_3NH_3PbI_3$) for thin film solar cells based on ZrO_2 and TiO_2 mesostructures", *RSC Adv.*, **2013**, *3*, 18762-18766.
68. G. E. Eperon, V. M. Burlakov, P. Docampo, A. Goriely, H. J. Snaith, "Morphological control for high performance, solution-processed planar heterojunction perovskite solar cells", *Adv. Funct. Mater.*, **2014**, *24*, 151-157.
69. L. Calió, S. Kazim, M. Graetzel, S. Ahmad, "Hole-transport materials for perovskite solar cells", *Angew. Chem. Int. Ed.*, **2016**, *55*, 14522-14545.
70. Z. Yu, L. Sun, "Recent progress on hole-transporting materials for emerging organometal halide perovskite solar cells", *Adv. Energy Mater.*, **2015**, *5*, 1500213-1500230.

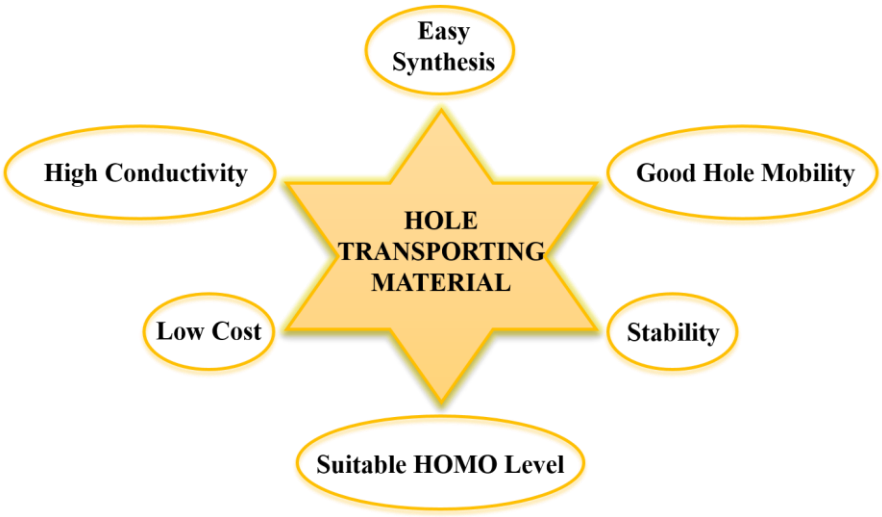

Figure 13. Ideal features of a hole-transporting material.

In this section, the different features that HTMs must exhibit for an efficient PSC are presented. The most important role of an effective HTM is to facilitate hole transfer process from the perovskite layer, by presenting suitable energy levels adapted to the valence band of the perovskite. Therefore, the HOMO (Highest Occupied Molecular Orbital) of positive charge extraction layer has to be compatible to the valence band energy of the perovskite. The presence of a thick layer of HTM is required to avoid short circuits; however, it is observed that a HTM can also lead to high series resistance. Thus, it is essential to find an optimum HTM thickness that provides desirable conductivity and charge mobility to reduce series resistance and yet, at the same time, achieving an effective hole extraction.[28] HTMs can be divided in different categories: small organic molecules, oligomers, polymers, organometallic complexes and inorganic HTMs. The latter will be explained in detail in the following sections.

1.2. State-of-the-art HTMs

- Spiro-OMeTAD

The first solid-state HTM used in perovskite-sensitized TiO_2 electrodes was the well-known spiro-OMeTAD. This organic molecule was previously used in the ss-DSSC architecture (figure 14) due to its ability to infiltrate at high concentrations in the nanoscale porosity of monocrystalline TiO_2 electrodes over

several micrometers thick. The first attempt of solid-state PSCs was made by the substitution of the liquid electrolyte with this molecule as a HTM.[23]

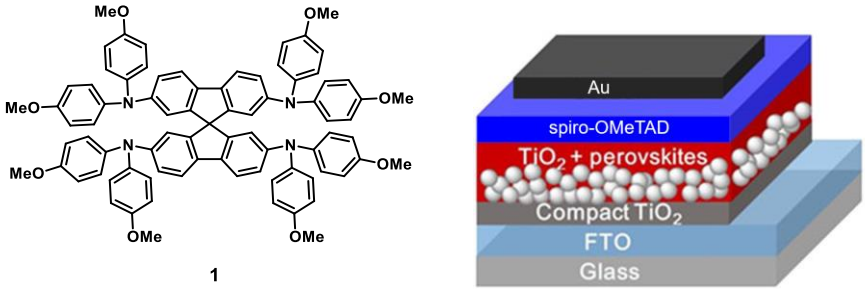

Figure 14. Molecular structure of spiro-OMeTAD (left) and perovskite-based solar cell architecture (right).

The chemical structure of spiro-OMeTAD (**1**, figure 14) is based on a bifluorene central core endowed with four units of diphenylamine. Currently, this twisted spirobifluorene-based molecule is the most featured small organic molecule, exhibiting an impressive PV performance when used as the HTM for PSCs. Relevantly, the preparation of the spirobifluorene central core present in this material requires a complicated five-step synthetic protocol as well as subsequently difficult purification steps. Therefore, low temperature (-78 ºC), sensitive (*n*-butyllithium or Grignard) and aggressive (Br_2) reagents have to be employed.[71] In addition, high-purity sublimation-grade spiro-OMeTAD is required to obtain high-performance devices.[72]

Initially, the performance of ss-DSSCs employing spiro-OMeTAD, increased by the addition of 4-*tert*-butylpiridine (*t*-BP) and lithium-bis(trifluoromethane sulfonyl)imide (Li-TFSI) in the HTM solution, leading to a PCE of 2.6 %.[73] This value was further improved by Graetzel's group by adding a Co^{III} complex (FK102), that enhanced the hole mobility of the spiro-OMeTAD, reaching

71. T. P. I. Saragi, T. Spehr, A. Siebert, T. Fuhrmann-Lieker, J. Salbeck, "Spiro compounds for organic optoelectronics", *Chem. Rev.*, **2007**, *107*, 1011-1065.
72. T. Malinauskas, M. Saliba, T. Matsui, M. Daskeviciene, S. Urnikaite, P. Gratia, R. Send, H. Wonneberger, I. Bruder, M. Graetzel, V. Getautis, M. K. Nazeeruddin, "Branched methoxydiphenylamine-substituted fluorene derivatives as hole transporting materials for high-performance perovskite solar cells", *Energy Environ. Sci.*, **2016**, *9*, 1681-1686.
73. J. Krüger, R. Plass, L. Cevey, M. Piccirelli, M. Graetzel, U. Bach, "High efficiency solid-state photovoltaic device due to inhibition of interface charge recombination", *Appl. Phys. Lett.*, **2001**, *79*, 2085-2087.

7.2 % at 1 sun illumination.[74] The first two additives are still used in order to increase the mobility and the open circuit voltage (V_{oc}) in the device, whereas many different Co^{III} complexes were investigated, in order to further enhance the hole mobility of spiro-OMeTAD. Both Graetzel and Snaith's groups were the first to report in 2012 its association with hybrid perovskite absorbers exhibiting PCEs of ≈ 10 % (V_{oc} = 0.89 mV and J_{sc} = 17.6 $mA \cdot cm^{-2}$) in mesoscopic cell structures.[25,40] Through judicious morphology control of the perovskite absorber by sequential deposition methods and the addition of dopants in HTM solution, the PCEs were remarkably improved to over 15 %.[66,75] After several optimization processes of the active layer properties and processing steps, high performance in planar PSCs have also been obtained using spiro-OMeTAD as HTMs, with high PCEs ranging between 15-19 %.[46,76] Recently, Bi *et al.* employed mixed perovskite formed by optimization of the ratio of lead iodide (PbI_2)/formamidinium iodide (FAI). The small excess of PbI_2 suppresses nonradiative charge carrier recombination, enhancing the electrical properties of the absorber. In the mesoscopic configuration, using mixed perovskite and doped spiro-OMeTAD as a HTM, PCE of 20.8 % was achieved.[77] Even higher PCE (21.1 %) was reached employing a mixture of a triple Cs/MA/FA cation with spiro-OMeTAD as the HTM by Graetzel and co-workers.[78]

74. J. Burschka, A. Dualeh, F. Kessler, E. Baranoff, N. L. Cevey-Ha, C. Yi, M. K. Nazeeruddin, M. Graetzel, "Tris(2-(1*H*-pyrazol-1-yl)pyridine)cobalt(III) as p-type dopant for organic semiconductors and its application in highly efficient solid-state dye-sensitized solar cells", *J. Am. Chem. Soc.*, **2011**, *133*, 18042-18045.
75. J. Burschka, N. Pellet, S. J. Moon, R. Humphry-Baker, P. Gao, M. K. Nazeeruddin, M. Graetzel, "Sequential deposition as a route to high-performance perovskite-sensitized solar cells", *Nature*, **2013**, *499*, 316-319.
76. F. Huang, Y. Dkhissi, W. Huang, M. Xiao, I. Benesperi, S. Rubanov, Y. Zhu, X. Lin, L. Jiang, Y. Zhou, A. Gray-Weale, J. Etheridge, C. R. Mcneill, R. A. Caruso, U. Bach, L. Spiccia, Y. B. Cheng, "Gas-assisted preparation of lead iodide perovskite films consisting of a monolayer of single crystalline grains for high efficiency planar solar cells", *Nano Energy*, **2014**, *10*, 10-18.
77. D. Bi, W. Tress, M. I. Dar, P. Gao, J. Luo, C. Renevier, K. Schenk, A. Abate, F. Giordano, J. P. Correa Baena, J. D. Decoppet, S. M. Zakeeruddin, M. K. Nazeeruddin, M. Graetzel, A. Hagfeldt, "Efficient luminescent solar cells based on tailored mixed-cation perovskites", *Sci. Adv.*, **2016**, *2*, 1-7.
78. M. Saliba, T. Matsui, J. Y. Seo, K. Domanski, J. P. Correa-Baena, M. K. Nazeeruddin, S. M. Zakeeruddin, W. Tress, A. Abate, A. Hagfeldt, M. Graetzel, "Cesium-containing triple cation perovskite solar cells: Improved stability, reproducibility and high efficiency", *Energy Environ. Sci.*, **2016**, *9*, 1989-1997.

Spiro-OMeTAD possesses large solubility, easy processability, reasonably large hole mobility and its deposition does not require any post-annealing step. In addition, its suitable affinity with the perovskite layer, associated with a favorable energetic configuration, reduces charge recombination, leading to a reduction of the potential losses.[79] Spiro-OMeTAD has become the reference for all HTMs. The remarkable improvements in the perovskite devices are commonly compared employing spiro-OMeTAD.

Although, spiro-OMeTAD seems an excellent small molecule HTM, it presents some disadvantages. Its main drawbacks are the requirement for doping strategies in order to improve its intrinsic charge mobility. The additives temporally enhance the performance a few days (2-3) after the production of the solar cell[79] but it is one of the reasons for instability in the device. In addition, its high cost (commercial price 170-475 $/g) accompanied by complex multi-step synthesis and purification processes curtail it commercial profitability.[72,80]

For these reasons, intense research efforts are on-going to find relevant low-cost and efficient HTM alternatives to replace spiro-OMeTAD in order to achieve high performance and stable perovskite-based devices.

1.3. New HTMs

In the quest for promising HTMs, a large number of organic molecules have been synthesized and tested for PSCs. In this section, novel HTMs will be divided in different subsections for a better understanding.

1.3.1. Small-organic molecules as HTMs

A large number of excellent reviews have been published summarizing all HTMs used in PSCs.[28,69,79] Different classifications have been done based on their optoelectronic properties, devices' performance, etc. In this section, the most relevant HTMs reported in the literature and their principal PV properties have been gathered from a chemical point of view. They usually present most of the previously mentioned characteristics for being an effective HTM (figure 13).

79. A. Gheno, S. Vedraine, B. Ratier, J. Bouclé, "π-conjugated materials as the hole-transporting layer in perovskite solar cells", *Metals*, **2016**, *6*, 21.
80. K. Zhang, L. Wang, Y. Liang, S. Yang, J. Liang, F. Cheng, J. Chen, "A thermally and electrochemically stable organic hole-transporting material with an adamantane central core and triarylamine moieties", *Synth. Met.*, **2012**, *162*, 490-496.

In addition, following the spiro-OMeTAD structure as a general model, most of the small molecules explored as hole-transporting candidates exhibit a star-shaped configuration.

The most common structure is formed by a central core endowed with electron donor units in the periphery, which allows tuning the HOMO energy level of the final molecule. Different central cores have been used in the search for new HTMs for PV devices, namely 9,9'-spirobifluorene, spiro-liked derivatives, thiophene derivatives, triphenylamine, bridged-triphenylamines, pyrene, 3,4-ethylene dioxythiophene, linear π-conjugated, sililothiophene or triazines. However, the electron donor units employed are less extensive. Generally, the central core has been endowed with diphenylamines, triphenylamines and/or carbazole derivatives. Taking into account the chemical nature of the central structure of the most remarkable HTMs reported so far, these have been classified as spiro-based, aromatic and nonaromatic systems. For better understanding, the main PV properties of small molecules based HTMs are summarized in a table at the end of each category.

1.3.2. Spiro-like HTMs

Taking into account the impressive PV performance that spiro-OMeTAD exhibits, slightly modifications of its structure are one of the main approaches that have been tackled for improving the PCEs. Some representative examples of these modifications are shown in figure 15.

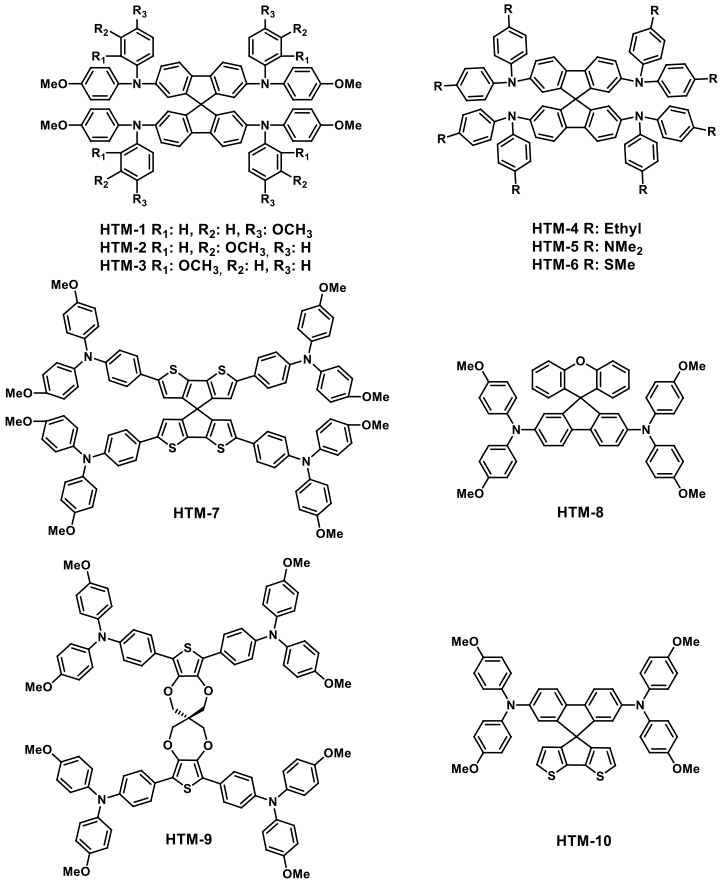

Figure 15. Structure of spiro-like HTMs.

From a structural point of view, the presence of methoxy groups (-OMe) in the HTM's structure not only plays an important role in anchoring the material onto the perovskite layer but also they are responsible for adjusting the HOMO level of the material. As a result of the inductive effect, the methoxy group presents electron-withdrawing properties, however, as Hammett demonstrated,[81] depending on the substitution position it can show electron-withdrawing or electron-donating properties in the *meta*- and *para*-positions, respectively, whereas the *ortho*-position has a more important steric effect.[69] Seok and co-workers beautifully exemplified this effect by synthesizing spiro-OMeTAD with *para*-methoxy (pp-OMe, HTM-**1**), *ortho*-(po-OMe, HTM-**2**) and *meta*-(pm-

81. L. P. Hammett, "The effect of structure upon the reactions of organic compounds. Benzene derivatives", *J. Am. Chem. Soc.*, **1937**, *59*, 96-103.

OMe, **3**) positions. The different arrangement of the methoxy groups not only leads to a different HOMO energy but also affects the energy of the LUMO (Lowest Unoccupied Molecular Orbital). These isomers were applied as HTMs in $MAPbI_3$ perovskite-based solar cells reaching a PCE of 16.7 %. The superior performance of HTM-**2** is mainly attributed to the increased fill factor (FF) due to the lower LUMO energy that, effectively, blocks the electron transport from the perovskite to the Au contact, resulting in low series resistance and high shunt resistance.[82]

Another approach for tailoring the HOMO energy of the spiro-OMeTAD structure was reported by Huang and co-workers. By replacing the *para*-methoxy substituent with ethyl groups (HTM-**4**), *N*,*N*-dimethylamino (HTM-**5**) and methylsulfanyl (HTM-**6**), the optoelectronic properties, PCE and charge-transport behaviour in PSCs are affected. Compared with spiro-OMeTAD, HTM-**4** and HTM-**6** show closer HOMO energy levels, which are well matched with that of $MAPbI_3$. Moreover, HTM-**4** and HTM-**6** also exhibited greater hydrophobicity, which contributes to the larger grain size and better quality perovskite polycrystalline films. PCEs of 15.8 %, 11.9 % and 15.9 % were obtained with HTM-**4**, HTM-**5** and HTM-**6**, respectively. HTM-**4** and HTM-**6** presented significantly higher values than that of spiro-OMeTAD (11.6 %).

A novel spirothiophene core-based HTM (HTM-**7**) was designed and employed in efficient PSCs by Zakeeruddin, Graetzel and co-workers. The new triphenylamine-substituted spiro-cyclopentadithiophene exhibited red-shifted absorption compared to spiro-OMeTAD in both solution and thin films. Its employment in PSCs gave impressive PCEs of up to 13.4 % without any doping which is very close to *p*-doped spiro-OMeTAD devices. This was one of the highest values reported for chemically undoped PSCs fabricated using a sequential deposition method.[83]

Hagfeldt and co-workers reported an efficent PSC employing a newly designed and easily attainable spiro-type HTM-**8**. Based on the high quality perovskite layer, devices with the new HTM were optimized changing the dopants. An

82. N. J. Jeon, H. G. Lee, Y. C. Kim, J. Seo, J. H. Noh, J. Lee, S. I. Seok, "O-methoxy substituents in spiro-ometad for efficient inorganic–organic hybrid perovskite solar cells", *J. Am. Chem. Soc.*, **2014**, *136*, 7837-7840.
83. M. Franckevicius, A. Mishra, F. Kreuzer, J. Luo, S. M. Zakeeruddin, M. Graetzel, "A dopant-free spirobi[cyclopenta[2,1-*b*:3,4-*b'*[dithiophene] based hole-transport material for efficient perovskite solar cells", *Mater. Horiz.*, **2015**, *2*, 613-618.

impressive champion PCE of 19.8 % was achieved which is comparable to the efficiency of the device using spiro-OMeTAD under the same conditions (20.8 %). Moreover, the highly optimized devices employing HTM-**8** exhibited minimized hysteresis, excellent reproducibiliy and promising stability under dark and dry conditions.[84]

In the quest of spiro-like HTMs, a simple novel molecule (HTM-**9**) was employed in PSC by Nazeeruddin and co-workers. XRD analysis confirmed the presence of a tetrahedral sp^3-hybridized carbon in between the two propylenedioxythiophenes that adopted spiro-structure. The presence of Co^{III} dopant in the HTM solution increased charge carrier density and a PCE of 13.4 % was reached. In contrast, the dopant-free devices achieved very similar PCE of 12.7 %, which was commensurate with the performance of spiro-OMeTAD in the presence of dopants.[85]

Notably, Nazeruddin and co-workers synthesized a molecularly engineered HTM (HTM-**10**) with a simple dissymmetric fluorene-dithiophene core substituted by *N*,*N*-di-*p*-methoxyphenylamine donor groups. Simulations carried out on the spiro-OMeTAD interface with $MAPbI_3$ revealed that the HTM-**10**/perovskite interaction occurred mainly between the HTM methoxy groups and the perovskite methylammonium sites, whereas the interaction with the surface iodine atoms was repulsive. Docking of HTM-**10** on the perovskite surface revealed an additional interaction between the HTM's core and the perovskite surface, mediated by the thiophene-iodine interaction, suggesting a stronger adhesion and enhanced interfacial coupling between HTM-**10** and perovskite. The HTM-**10**-based devices outperformed spiro-OMeTAD in all performance tests, yielding excellent PCEs up to 20.2 %, which was one of the highest reported values for small molecule HTMs.[86]

84. D. Bi, B. Xu, P. Gao, L. Sun, M. Graetzel, A. Hagfeldt, "Facile synthesized organic hole transporting material for perovskite solar cell with efficiency of 19.8 %", *Nano Energy*, **2016**, *23*, 138-144.
85. P. Ganesan, K. Fu, P. Gao, I. Raabe, K. Schenk, R. Scopelliti, J. Luo, L. H. Wong, M. Graetzel, M. K. Nazeeruddin, "A simple spiro-type hole transporting material for efficient perovskite solar cells", *Energy Environ. Sci.*, **2015**, *8*, 1986-1991.
86. M. Saliba, S. Orlandi, T. Matsui, S. Aghazada, M. Cavazzini, J.-P. Correa-Baena, P. Gao, R. Scopelliti, E. Mosconi, K.-H. Dahmen, F. De angelis, A. Abate, A. Hagfeldt, G. Pozzi, M. Graetzel, M. K. Nazeeruddin, "A molecularly engineered hole-transporting material for efficient perovskite solar cells", *Nat. Energy*, **2016**, *1*, 15017.

Table 1. Performance parameters of spiro-like HTMs.

HTM	J_{sc} (mA·cm^{-2})	V_{oc} (V)	FF (%)	PCE (%)
HTM-1	20.7	1.00	71.1	14.9
HTM-2	21.2	1.02	77.6	16.7
HTM-3	21.1	1.01	65.2	13.9
HTM-4	18.2	1.07	80.0	15.8
HTM-5	16.6	0.96	75.0	11.9
HTM-6	19.2	1.06	78.0	15.9
HTM-7	19.3	0.97	72.0	13.4
HTM-8	23.4	1.13	73.0	19.8
HTM-9	17.6	1.02	73.0	13.4
HTM-10	22.7	1.15	76.0	20.2

1.3.3. Aromatic core-based HTMs

- **Carbocyclic cores**

This is probably the HTM category that has been studied most in detail. They are usually composed of small fragments as central scaffold, such a benzene rings, biphenyls or by other more complicated structures, which are holding different electron donor groups. Excellent PCEs were obtained with these HTMs (figure 16, table 2) stemming from their excellent charge transport properties and good stability.

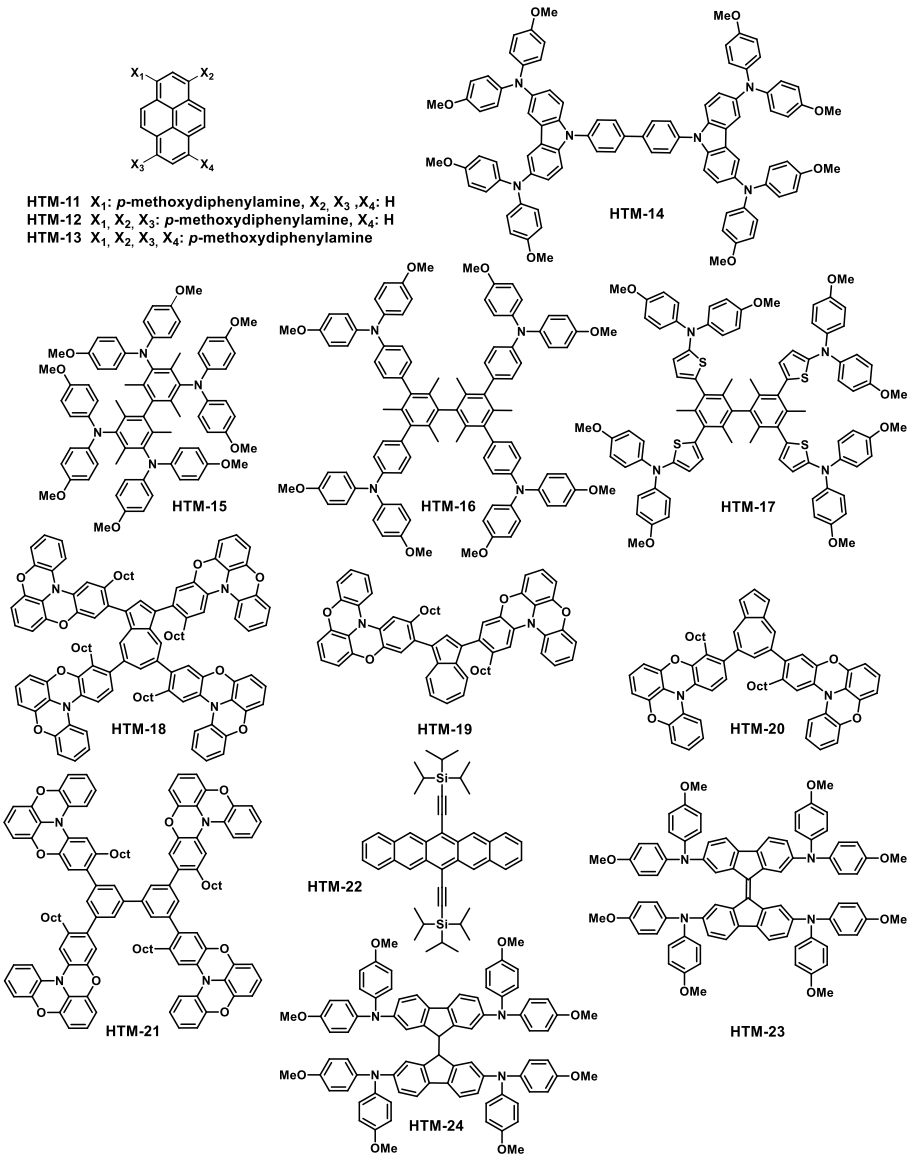

Figure 16. Structure of carbocyclic core-based HTMs.

Seok and co-workers replaced the spirobifluorene core with a pyrene as central scaffold for building HTMs decorated with *N*,*N*-di-*p*-methoxyphenylamine substituents. Three pyrene core arylamine derivatives were developed as HTMs in mesoscopic PSCs based on $MAPbI_3$ absorber. Compounds HTM-**12** and HTM-**13** exhibit comparable overall efficiencies (≈ 12.4 %) with respect to that of spiro-OMeTAD (12.7 %). However, a much lower performance is observed

for HTM-**11**, mainly due to an insufficient driving force for hole injections related to its deeper HOMO energy level (-5.41 eV) as compared to the valence band edge of $MAPbI_3$ perovskite (-5.43 eV).[87]

Su and co-workers demonstrated that the use of molecular engineering to develop novel and efficient HTMs with high hole mobility and high conductivity is a feasible strategy for ss-DSSCs and PSCs. Two new carbazole-based small molecules employed as organic HTMs exhibit different molecular weight, oxidation potential, hole mobility and electrical conductivity. Theoretical studies show that HTM-**14** clearly exhibits low reorganization energy implying fast hole transport, which is in good agreement with the expected influence of a larger conjugation system. Focussing on perovskite-based devices those containing HTM-**14** exhibited a PCE of 9.8 %, comparable to 10.2 % obtained in devices based on spiro-OMeTAD.[88]

A series of new arylamine HTMs with a bimesitylene core were designed and synthesized through simple procedures by Sun, Chow and co-workers. The HOMO levels of the HTM-**15** and HTM-**16** are estimated to be lower than that of spiro-OMeTAD, which led to higher measured V_{oc} values. The PSCs fabricated using HTM-**15** showed a PCE up to 12.1 %, which is comparable to the device fabricated using spiro-OMeTAD (12.7 %). It was shown that the film of HTM-**15** is smoother than those of HTM-**16** and HTM-**17**, and is responsible for the best PCE among the three. In addition, a stability test revealed that HTM-**15**-based cell exhibited a longer life-time than spiro-OMeTAD cell, presumably owing to an improved film morphology.[89]

87. N. J. Jeon, J. Lee, J. H. Noh, M. K. Nazeeruddin, M. Graetzel, S. I. Seok, "Efficient inorganic-organic hybrid perovskite solar cells based on pyrene arylamine derivatives as hole-transporting materials", *J. Am. Chem. Soc.*, **2013**, *135*, 19087-19090.
88. B. Xu, E. Sheibani, P. Liu, J. Zhang, H. Tian, N. Vlachopoulos, G. Boschloo, L. Kloo, A. Hagfeldt, L. Sun, "Carbazole-based hole-transport materials for efficient solid-state dye-sensitized solar cells and perovskite solar cells", *Adv. Mater.*, **2014**, *26*, 6629-6634.
89. Y. D. Lin, B. Y. Ke, K. M. Lee, S. H. Chang, K. H. Wang, S. H. Huang, C. G. Wu, P. T. Chou, S. Jhulki, J. N. Moorthy, Y. J. Chang, K. L. Liau, H. C. Chung, C. Y. Liu, S. S. Sun, T. J. Chow, "Hole-transporting materials based on twisted bimesitylenes for stable perovskite solar cells with high efficiency", *ChemSusChem*, **2016**, *9*, 274-279.

A non-benzenoid aromatic hydrocarbon-based material, azulene, has also been employed in PSCs. A 2D expanded π-system in which a sheet-shaped packing was achieved by using four oxygen-bridged triphenylamines attached to an azulene core (HTM-**18**, HTM-**19**, HTM-**20** and HTM-**21**) has been reported. The tetra-substituted azulene, HTM-**18**, in which the conjugated π-system is two-dimensionally expanded over four quasiplanar skeletons and a central azulene core, gave the superior performance comparable to spiro-OMeTAD (PCE ≤ 16.5 %), when applied to perovskites using solvent dripping in a one-step method, and 15.7 % using sequential deposition of perovskites.[90]

The same year, Ahmad and co-workers developed solution processable, cost effective and easily synthesized 6,13-bis(triisopropylsilylethynyl) pentacene (TIPS-pentacene, HTM-**22**) for PSC. The two TIPS side groups at the C-6 and C-13 positions of the pentacene core stabilized the HOMO level, facilitated stability and solubility in organic solvents and resulted in a 2D lamellar structure with a brick wall style in the solid state. In addition, the co-facial π-π stacking of HTM-**22** allowed for improved charge-transport properties over unsubstituted pentacene.[91] The devices gave very competitive performance 11.8 % without the need of additional dopants (8.2 % doped with LiTFSI and *t*-BP), comparable to doped spiro-OMeTAD. These results show the potentiality of HTM-**22** in PSCs and represent a promising candidate to achieve efficient and cost effective thin film PV devices.[92]

Two new spiro-OMeTAD analogues were designed by replacing the spiro linkage between the two planar fluorene halves in spiro-OMeTAD by a covalent "C=C" linkage in HTM-**23** and a "C-C" linkage in HTM-**24**. A facile two-step synthesis process was developed to obtain them. A change in the 3D geometry of the HTMs was observed, such as the rigid central connection for spiro-OMeTAD and HTM-**23** compared to a rotatable linkage in HTM-**24**. A decrease of the degree of perpendicular arrangement for spiro-OMeTAD > HTM-**24** >

90. H. Nishimura, N. Ishida, A. Shimazaki, A. Wakamiya, A. Saeki, L. T. Scott, Y. Murata, "Hole-transporting materials with a two-dimensionally expanded π-system around an azulene core for efficient perovskite solar cells", *J. Am. Chem. Soc.*, **2015**, *137*, 15656-15659.
91. C. C. Mattheus, G. A. De Wijs, R. A. De Groot, T. T. M. Palstra, "Modeling the polymorphism of pentacene", *J. Am. Chem. Soc.*, **2003**, *125*, 6323-6330.
92. S. Kazim, F. J. Ramos, P. Gao, M. K. Nazeeruddin, M. Graetzel, S. Ahmad, "A dopant free linear acene derivative as a hole transport material for perovskite pigmented solar cells", *Energy Environ. Sci.*, **2015**, *8*, 1816-1823.

HTM-**23** occurs. HTM-**24** and especially HTM-**23**, with lower degree of perpendicular arrangement, show lower conductivities but more homogeneous thin film morphologies and effective hole extraction than those for spiro-OMeTAD. A promising PCE of 19.8 % was recorded for the HTM-**24** based PSCs, as compared to PCEs of 16.6 % and 18.9 % for the HTM-**23** and spiro-OMeTAD based devices, respectively.[93]

Table 2. Performance parameters of aromatic carbocyclic core-based HTMs.

HTM	J_{sc} (mA·cm^{-2})	V_{oc} (V)	FF (%)	PCE (%)
HTM-11	10.8	0.89	34.6	3.3
HTM-12	20.4	0.95	63.7	12.3
HTM-13	20.2	0.89	69.4	12.4
HTM-14	16.8	0.88	66.0	9.8
HTM-15	18.9	1.01	64.0	12.1
HTM-16	17.3	0.98	57.0	9.7
HTM-17	7.6	0.89	34.0	2.3
HTM-18	21.7	1.08	71.0	16.5
HTM-19	15.9	0.91	67.0	9.7
HTM-20	17.3	0.91	54.0	8.5
HTM-21	2.3	0.70	28.0	0.5
HTM-22	20.8	0.91	60.0	11.5
HTM-23	22.7	1.07	69.0	16.6
HTM-24	24.2	1.15	71.0	19.8

93. J. Zhang, Y. Hua, B. Xu, L. Yang, P. Liu, M. B. Johansson, N. Vlachopoulos, L. Kloo, G. Boschloo, E. M. J. Johansson, L. Sun, A. Hagfeldt, "The role of 3D molecular structural control in new hole transport materials outperforming spiro-OMeTAD in perovskite solar cells", *Adv. Energy Mater.*, **2016**, *6*, 1601062-1601071.

- **Heterocyclic cores**

In the state-of-the-art of organic structures for HTMs used in PSCs, many of them possess heteroatoms in their central core. Here, it has been classified in three different groups depending on the heteroatom: sulfur (figure 17), oxygen (figure 18) and nitrogen (figure 19), present in the ring.

a) Sulfur-containing heterocycles

A successfully novel HTM-**25** which displays a swivel 3,3-bithiophene as the central unit was synthesized and employed in PSCs by Mhaisalkar and co-workers. Swivel-cruciform thiophene-based moiety with four methoxy triphenylamine groups as donor units has been synthesized by Suzuki coupling reaction. HTM-**25** showed optimum HOMO level and exhibited good solubility for further synthetic functionalization, allowing the modification of the molecular properties by manipulating the pendant group. Devices based on HTM-**25** exhibited a maximum PCE of 11.4 % and a higher V_{oc} (1.08 V) and fill factor (78.0 %) than spiro-OMeTAD.[94]

A new simpler HTM, HTM-**26**, based on 3,4-ethylenedioxythiophene, confirms that it is possible to introduce suitable heterocyclic structures into the HTM design to achieve high performances. Device based on HTM-**26** was further improved through chemical doping with FK102 (15 %; PCE: 13.8 %), making HTM-**26** an excellent candidate to replace spiro-OMeTAD. Furthermore, HTM-**26** presents a simpler chemical structure and low production costs. Thus, it becomes easier and more accessible to increase the mobility and tune the band gap. They claim that, because of the ability of this material to be processed in cell and module manufacturing, it could be envisaged large-scale production methods, such as melting and printing techniques.[95]

94. T. Krishnamoorthy, F. Kunwu, P. P. Boix, H. Li, T. M. Koh, W. L. Leong, S. Powar, A. Grimsdale, M. Graetzel, N. Mathews, S. G. Mhaisalkar, "A swivel-cruciform thiophene based hole-transporting material for efficient perovskite solar cells", *J. Mater. Chem. A*, **2014**, *2*, 6305-6309.
95. H. Li, K. Fu, A. Hagfeldt, M. Graetzel, S. G. Mhaisalkar, A. C. Grimsdale, "A simple 3,4-ethylenedioxythiophene based hole-transporting material for perovskite solar cells", *Angew. Chem. Int. Ed.*, **2014**, *53*, 4085-4088.

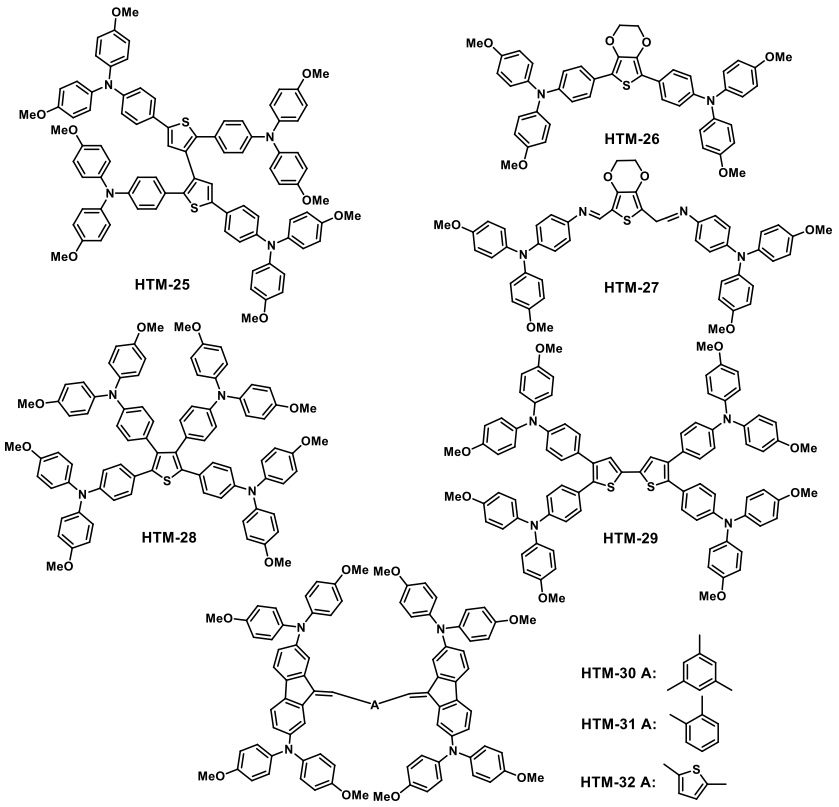

Figure 17. Structure of heterocyclic (sulfur) core-based HTMs.

Docampo and co-workers designed an analogous structure based on an azomethine bond that allows using a less complicated synthesis route based on Schiff-base condensation chemistry. This offers a cost-effective and more environmentally friendly route towards up-scalable HTMs. HTM-**27** exhibits a lower HOMO energy level (-5.28 eV compared to -5.09 eV for HTM-**26**) which results in a better alignment with the valence band of the perovskite. However, the PCE value by using planar $MAPbI_3$ perovskite-based devices with HTM-**27** is exceeding 11 %, which is relatively low compared to HTM-**26**.[96]

Two new phenylamine-type HTMs with tetrasubstituted thiophene and bithiophene units as the core were developed by Mhaisalkar, Grimsdale and co-workers. These new candidates, HTM-**28** and HTM-**29**, are equally simple, use

96. M. L. Petrus, T. Bein, T. J. Dingemans, P. Docampo, "A low cost azomethine-based hole transporting material for perovskite photovoltaics", *J. Mater. Chem. A*, **2015**, *3*, 12159-12162.

cheaper starting materials than those for HTM-**26** (thiophene instead of 3,4-ethylenedioxythiophene) and have stable intermediates. In addition, the glass transition (T_g) values for the new HTMs are much higher, which should enhance their thermal stability within the devices, and the HOMO levels are much deeper than that of HTM-**26**, which accounts for the higher V_{oc} value of the former. Maxima PCEs of 15.4 % and 15.2 % were achieved with HTM-**28** and HTM-**29**, respectively.[97]

Malinauskas *et al.* reported three new small-molecule hole conductors (HTM-**30**, HTM-**31** and HTM-**32**) that yield a very high efficiency (17.8 %, 19.5 % and 20.0 %, respectively) in PSCs, comparable to the best-performing spiro-OMeTAD. In addition, their syntheses and purification are significantly less costly and complicated. HTM-**30**, HTM-**31** and HTM-**32** can be produced in two steps synthesis from commercially available materials and the estimated chemical synthesis cost is 68.56 $/g cheaper for HTM-**32** as example, with respect to spiro-OMeTAD (estimated material cost for the synthesis of 1 g of product).[72]

Table 3. Performance parameters of heterocyclic (sulfur) core-based HTMs.

HTM	J_{sc} (mA·cm^{-2})	V_{oc} (V)	FF (%)	PCE (%)
HTM-25	13.0	1.08	78.0	11.4
HTM-26	20.5	1.04	65.0	13.8
HTM-27	18.9	0.95	61.0	11.0
HTM-28	19.8	1.08	72.0	15.4
HTM-29	20.0	1.07	70.0	15.2
HTM-30	21.7	1.14	71.0	17.8
HTM-31	23.3	1.12	75.0	19.5
HTM-32	22.5	1.14	77.0	20.0

97. H. Li, K. Fu, P. P. Boix, L. H. Wong, A. Hagfeldt, M. Graetzel, S. G. Mhaisalkar, A. C. Grimsdale, "Hole-transporting small molecules based on thiophene cores for high efficiency perovskite solar cells", *ChemSusChem*, **2014**, *7*, 3420-3425.

b) Oxygen-containing heterocycles

The novel HTM-**33** based on a furan core was designed and synthesized by Krishna *et al.* PCE up to 13 % was achieved employing HTM-**33** in PSCs, comparable to spiro-OMeTAD, while a simpler and more economical synthesis is required.[98] Two new small molecule HTMs based on methoxyaniline-substituted dibenzofuran derivatives (HTM-**34** and HTM-**35**) were designed by Zhang and wo-workers. Both novel HTMs exhibit stable thermodynamic and optical properties, high conductivity and moderate HOMO energy levels. The devices fabricated from HTM-**34** and HTM-**35** show PCEs of 14.2 % and 14.1 %, which are comparable to that (15.0 %) of the spiro-OMeTAD based cell,[99] (figure 18, table 4).

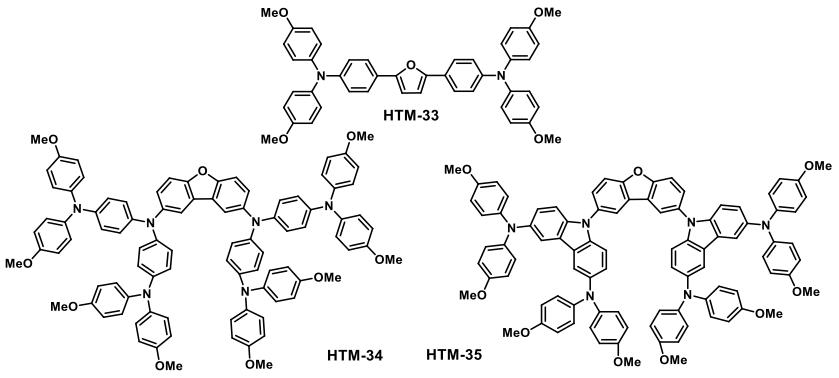

Figure 18. Structure of heterocyclic (oxygen) core-based HTMs.

Table 4. Performance parameters of heterocyclic (oxygen) core-based HTMs.

HTM	J_{sc} (mA·cm^{-2})	V_{oc} (V)	FF (%)	PCE (%)
HTM-33	19.6	1.10	60.8	13.0
HTM-34	21.6	1.01	65.0	14.2
HTM-35	21.2	1.03	64.0	14.1

98. A. Krishna, D. Sabba, J. Yin, A. Bruno, P. P. Boix, Y. Gao, H. A. Dewi, G. G. Gurzadyan, C. Soci, S. G. Mhaisalkar, A. C. Grimsdale, "Facile synthesis of a furan-arylamine hole-transporting material for high-efficiency, mesoscopic perovskite solar cells", *Chem. Eur. J.*, **2015**, *21*, 15113-15117.
99. Y. Shi, K. Hou, Y. Wang, K. Wang, H. Ren, M. Pang, F. Chen, S. Zhang, "Two methoxyaniline-substituted dibenzofuran derivatives as hole-transport materials for perovskite solar cells", *J. Mater. Chem. A*, **2016**, *4*, 5415-5422.

c) Nitrogen-containing heterocycles

Compared to the aforementioned oxygen-containing heterocycles, the number of nitrogen-containing heterocycles is significantly larger (figure 19).

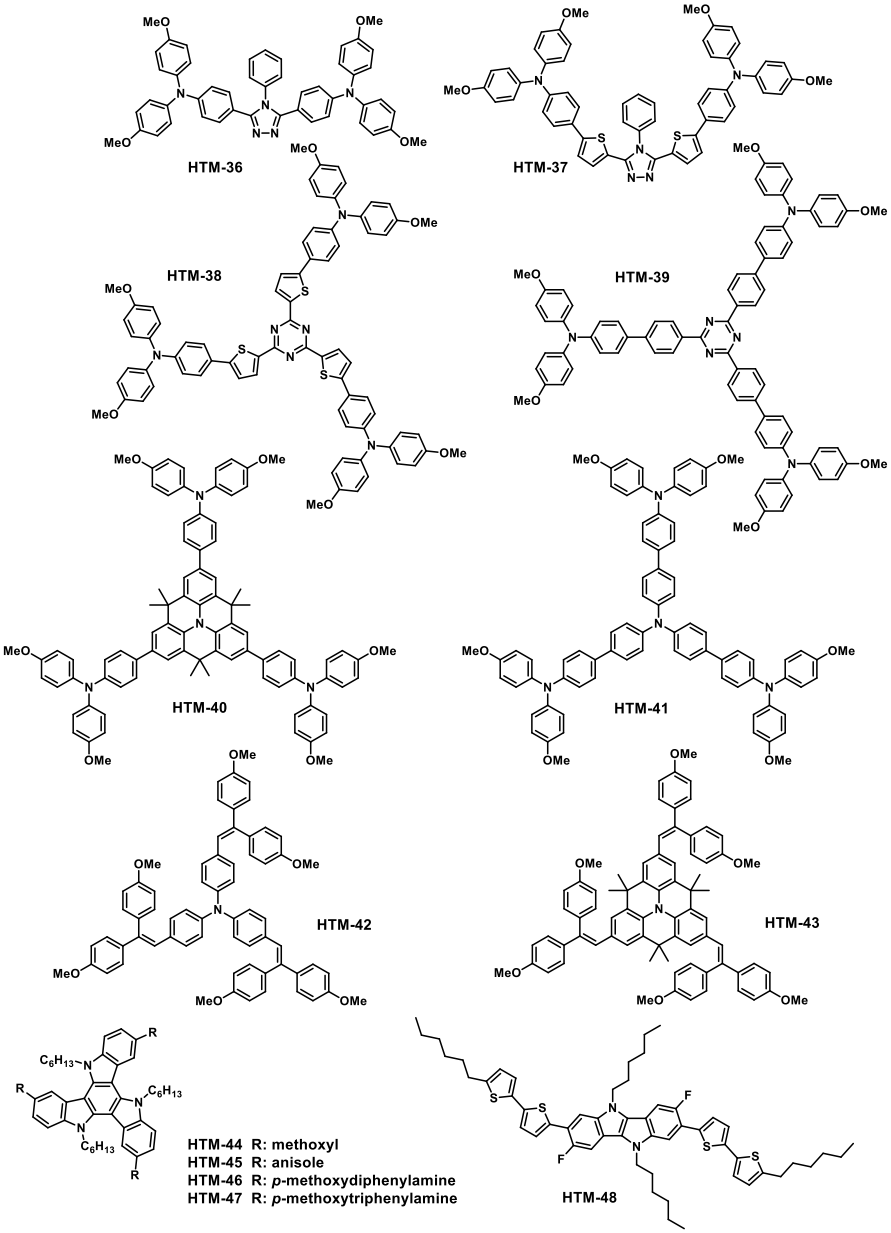

Figure 19. Structure of heterocyclic (nitrogen) core-based HTMs.

Two efficient HTMs with a triazole core and two electron-rich diphenylamine side arms were synthesized and employed in PSCs. HTM-**36** and HTM-**37** present D-A-D molecular structures, which improve their hole-transportation properties through efficient intramolecular charge transfer. The structural modification of HTMs by thiophene bridging might increase intermolecular π-π stacking in the solid state and provide the better spectral response in longer π-conjugation. Devices fabricated with these materials exhibited some hysteretic J-V behavior between opposite scan directions, as typical n-i-p perovskite-based solar cells do. However, the average PCE obtained in both directions showed notable values that are about 6 % reduced compared to the maximum PCE values which are 10.9 % and 14.4 % for HTM-**36** and HTM-**37**, respectively (14.7 % for spiro-OMeTAD under the same conditions).[100]

Ko and co-workers designed two HTMs, coded as HTM-**38** and HTM-**39** with D-π-A systems by incorporating an electron-deficient 1,3,5-triazine core and an electron-rich diphenylamino unit. The HOMO levels of HTM-**38** and HTM-**39** were measured as -5.04 and -5.11eV, respectively, which are well above the perovskite conduction band level ($MAPbI_3$, -5.43 eV). An impressive enhancement in PCE was achieved by increasing the conductivity through doping (*t*-BP, LiTFSI and FK102). The HTM-**39** based device exhibits a PCE of 10.9 %. Under similar conditions, HTM-**38** and spiro-OMeTAD-based cells show PCEs of 12.5 and 13.5 %, respectively. The high J_{sc} of the HTM-**38** based cell (20.7 $mA \cdot cm^{-2}$) relative to HTM-**39** based cell (19.1 $mA \cdot cm^{-2}$) is responsible for the broad and red-shifted absorption of the mp-TiO_2/$MAPbI_3$/HTM-**38** device.[101] HTMs display triazine-based structure replacing the spacer units to fluorenes have also been reported.[102]

Ko and co-workers designed additional new types of HTMs containing a planar amine or star-shaped triphenylamine derivatives coded HTM-**40** and HTM-**41**.

100. H. Choi, H. Jo, S. Paek, K. Koh, H. M. Ko, J. K. Lee, J. Ko, "Efficient hole-transporting materials with triazole core for high-efficiency perovskite solar cells", *Chem. Asian. J.*, **2016**, *11*, 548-554.
101. K. Do, H. Choi, K. Lim, H. Jo, J. W. Cho, M. K. Nazeeruddin, J. Ko, "Star-shaped hole transporting materials with a triazine unit for efficient perovskite solar cells", *Chem. Commun.*, **2014**, *50*, 10971-10974.
102. K. Lim, M. S. Kang, Y. Myung, J. H. Seo, P. Banerjee, T. J. Marks, J. Ko, "Star-shaped hole transport materials with indeno[1,2-*b*] thiophene or fluorene on a triazine core for efficient perovskite solar cells", *J. Mater. Chem. A*, **2016**, *4*, 1186-1190.

The solid-state perovskite-based device using HTM-**40** yielded a maximum conversion efficiency of 13.6 % with three additives and 12.7 % without. Under the same conditions, HTM-**41**- and spiro-OMeTAD-based cells gave PCEs of 12.3 % and 14.7 %, respectively. Moreover, the HTM-**40** based device stored for 500 h with any encapsulation under outdoor conditions retained its PV performances. After this study, it could be concluded that the development of highly efficient hybrid solar cells with robustness is possible through the structural modification of hole conductors by tuning the HOMO level and work on these is now in progress.[103]

Two additional star-shaped HTMs coded as HTM-**42** and HTM-**43** were also designed and used in PSCs. Their structures possess a triphenylamine or a fused triphenylamine core and diphenylethenyl side arms. The UV-vis spectra of HTM-**42** and HTM-**43** measured in chlorobenzene exhibit an intense peak at 396 nm. The absorption peak maximum of HTM-**43** (414 nm) is red-shifted by about 18 nm compared with HTM-**42**, which is attributed to the more planar configuration in HTM-**43** as compared with a larger twist angle (48.98º) between the core nitrogen and phenyl unit in HTM-**42**. The fluorescence spectrum of HTM-**43** exhibits a maximum emission at 488 nm with a small Stokes shift of 74 nm relative to 86 nm for HTM-**42**, demonstrating that a small structural change in the excited state occurs in HTM-**43** and HTM-**42** owing to their rigid configuration. The PV performance is quite sensitive to the structural modification of HTMs. The HOMO levels are measured a -5.29 eV for HTM-**42** and -5.15 eV for HTM-**43**, displaying suitable energy level with the $MAPbI_3$ (-5.43 eV). The perovskite-based cells using HTM-**43** gave an overall conversion efficiency of 11.9 %. Under similar conditions, HTM-**42**- and spiro-based cells presented 10.8 % and 12.8 %, respectively. Moreover, the HTM-**43** based cell stored for 250 h without any encapsulation showed a relative stability.[104]

103. H. Choi, S. Paek, N. Lim, Y. H. Lee, M. K. Nazeeruddin, J. Ko, "Efficient perovskite solar cells with 13.63 % efficiency based on planar triphenylamine hole conductors", *Chem. Eur. J.*, **2014**, *20*, 10894-10899.
104. H. Choi, S. Park, S. Paek, P. Ekanayake, M. K. Nazeeruddin, J. Ko, "Efficient star-shaped hole transporting materials with diphenylethenyl side arms for an efficient perovskite solar cell", *J. Mater. Chem. A,* **2014**, *2*, 19136-19140.

Novel triazatruxene-based 2D HTMs comprising electron-rich methoxy-engineered substituents were reported by Rakstys *et al.* HTM-**44** to HTM-**47** were synthesized from simple and inexpensive starting materials merely in four scalable synthetic steps. These novel HTMs offer potentially much lower production costs in comparison to the most widely used spiro-OMeTAD. They claim that an efficient hole injection from the valence band of perovskite into the HOMO of a HTM occurs as a result of the surface interaction between the molecularly engineered triazatruxene derivatives and the perovskite. PCEs of 8.9 %, 15.8 % and 11.5 % were reached with HTM-**44**, HTM-**46** and HTM-**47**, respectively. Remarkably, PCE of 17.7 % was realized using HTM-**45** with perovskite as absorber, which is similar to that of spiro-OMeTAD (17.1 %).[105]

Fluorinated indoloindole derivative (HTM-**48**) was presented by Seon, Seok, Park and co-workers as a high performance crystalline HTM for PSCs. By single crystal analysis, it was confirmed that planar π-conjugated backbone linked with a flexible alkyl chain that presents HTM-**48**, enabled a formation of molecular stacked arrangement by strong π-π interactions. Therefore, the film based on HTM-**48** presents higher hole mobility and the photoluminescence (PL) quenching occurred more effectively at the perovskite/HTM-**48** interface than that of spiro-OMeTAD. The device fabricated using HTM-**48** showed a better performance as compared to spiro-OMeTAD, exhibiting a best PCE of 19.1 %.[106]

105. K. Rakstys, A. Abate, M. I. Dar, P. Gao, V. Jankauskas, G. Jacopin, E. Kamarauskas, S. Kazim, S. Ahmad, M. Graetzel, M. K. Nazeeruddin, "Triazatruxene-based hole transporting materials for highly efficient perovskite solar cells", *J. Am. Chem. Soc.*, **2015**, *137*, 16172-16178.
106. I. Cho, N. J. Jeon, O. K. Kwon, D. W. Kim, E. H. Jung, J. H. Noh, J. Seo, S. I. Seok, S. Y. Park, "Indolo[3,2-*b*]indole-based crystalline hole-transporting material for highly efficient perovskite solar cells", *Chem. Sci.*, **2017**, *8*, 734-741.

Table 5. Performance devices of heterocyclic (nitrogen) core-based HTMs.

HTM	J_{sc} (mA·cm^{-2})	V_{oc} (V)	FF (%)	PCE (%)
HTM-36	20.3	0.97	55.0	10.9
HTM-37	21.8	1.00	66.0	14.4
HTM-38	20.7	0.92	66.0	12.5
HTM-39	19.1	0.93	61.0	10.9
HTM-40	21.0	0.97	67.0	13.6
HTM-41	20.9	0.95	62.0	12.3
HTM-42	17.3	0.99	62.7	10.8
HTM-43	18.4	0.92	69.8	11.9
HTM-44	16.0	0.97	58.0	8.9
HTM-45	20.7	1.15	75.0	17.7
HTM-46	20.4	1.13	68.0	15.8
HTM-47	18.4	0.95	66.0	11.5
HTM-48	23.6	1.05	77.2	19.1

1.3.4. Non-Aromatic core-based HTMs

Only a relatively scarce number of non-conjugated central cores have been reported in the literature, which are difficult to fit from a chemical point of view. Some representative examples of these systems have been gathered in this section (figure 20, table 6).

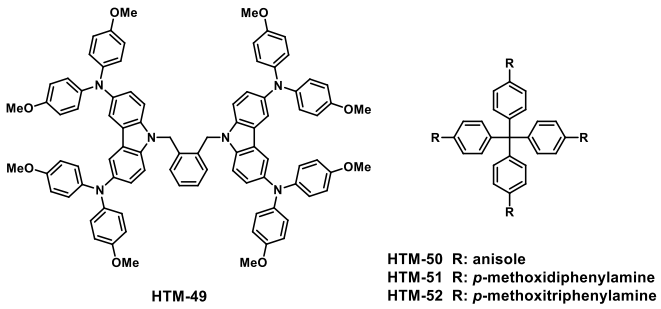

Figure 20. Structure of non-aromatic core-based HTMs.

Getautis, Nazeeruddin and co-workers presented an effective small-molecule hole conductor HTM-**49** for $MAPbI_3$-based solar cells. HTM-**49** is less expensive than the spiro-OMeTAD and it can be synthesized in two steps from commercially available materials, useful for large-scale production of PSCs. The good solubility and film-forming properties allow the formation of thicker films of high quality reaching very high J_{sc} (> 21 $mA \cdot cm^{-2}$) and an overall efficiency close to 17 %. In addition, HTM-**49** absorbs only in the UV region, while the oxidized form obtained by addition of 10 % FK209 shows a peak over 800 nm, that does not compete with the perovskite absorption. This evidence shows that, in addition to the enhancement in conductivity by the use of additives, doping increases carrier concentration and, thus, an enhancement in PCE.[107]

A series of novel tetraphenylmethane-based HTMs (HTM-**50**, HTM-**51** and HTM-**52**) were employed by Liu *et al.* in PSCs. Particularly, HTM-**50** shows good film-forming ability, suitable band alignments with $MAPbI_3$, high thermal stability and comparable hole mobility. Therefore, HTM-**52** shows a better performance when applied in PSCs.[108]

107. P. Gratia, A. Magomedov, T. Malinauskas, M. Daskeviciene, A. Abate, S. Ahmad, M. Graetzel, V. Getautis, M. K. Nazeeruddin, "A methoxydiphenylamine-substituted carbazole twin derivative: An efficient hole-transporting material for perovskite solar cells", *Angew. Chem. Int. Ed.,* **2015**, *54*, 11409-11413.
108. X. Liu, F. Kong, T. Cheng, W. Chen, Z. A. Tan, T. Yu, F. Guo, J. Chen, J. Yao, S. Dai, "Tetraphenylmethane-arylamine hole-transporting materials for perovskite solar cells", *ChemSusChem,* **2017**, 968-975.

Table 6. Performance parameters of non-aromatic core-based HTMs.

HTM	J_{sc} (mA·cm^{-2})	V_{oc} (V)	FF (%)	PCE (%)
HTM-49	21.4	1.09	73.4	16.9
HTM-50	12.8	0.87	42.0	4.6
HTM-51	15.8	0.92	64.0	9.3
HTM-52	19.2	1.07	73.0	15.1

1.3.5. π-Conjugated oligomeric and polymeric cores-based HTMs

1.3.5.1. HTMs based on organic oligomers

Novel low band gap A-D-A-type oligothiophenes (figure 21) comprising electron-rich thiophene-pyrrole-based *S,N*-heteropentacene central units and terminal dicyanovinylene acceptor groups, HTM-**53** and HTM-**54**, were developed by Mishra, Graetzel and co-workers. PCEs of 10.5 % and 9.5 % were obtained with undoped HTM-**53** and HTM-**54**, respectively in solution-processed heterojunction solar cells. In addition, a contribution of oligomer HTM-**53** to the light absorption in the low energy region of the solar spectrum was observed, forming a dual light absorbing system with the perovskite. The present findings demonstrate that the appropriate combination of conjugated building blocks can lead to light harvesting organic semiconductors that have suitable frontier orbital energy levels for using as HTMs in PSCs.[109]

109. P. Qin, H. Kast, M. K. Nazeeruddin, S. M. Zakeeruddin, A. Mishra, P. Bauerle, M. Graetzel, "Low band gap s,n-heteroacene-based oligothiophenes as hole-transporting and light absorbing materials for efficient perovskite-based solar cells", *Energy Environ. Sci.*, **2014**, *7*, 2981-2985.

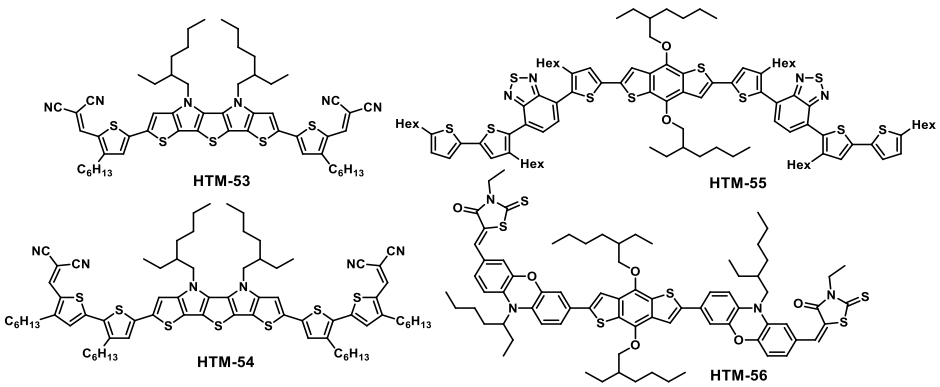

Figure 21. Structure of organic oligomeric HTMs.

The central benzodithiophene unit was functionalized by thiophene and benzo-[*c*][1,2,5]-thiadiazole derivatives to generate HTM-**55** with extended π-conjugation. A-D-A conjugated molecular material, HTM-**55**, exhibits high hole mobility and conductivity. In addition, it presents an appropriate energy level alignment with respect to both $MAPbI_3$ and $PC_{70}BM$, making it a good candidate for the application in PSCs as a dopant-free HTM and in organic solar cells as a donor material. When HTM-**55** is used as dopant-free HTM in PSCs, a good PCE close to 14 % was achieved with better stability than spiro-OMeTAD due to better protection of the perovskite material from humidity, being attributed to a higher hydrophobicity of HTM-**55**. On the other hand, a 6.1 % PCE was reached with HTM-**55** as a donor material together with $PC_{70}BM$ as acceptor material in organic solar cells.[110]

Recently, Sun and co-workers reported an A-D-A structured small molecule phenoxazine-based HTM-**56**, containing an electron-rich benzo[1,2*b*:4,5*b′*]-dithiophene unit as a central building block, flanked by phenoxazine units and end-capped with electron-withdrawing 3-ethylrhodanine. This novel and high-performing material is synthesized from relatively inexpensive and commercially available reactants and in five synthetic steps with a high overall yield of 52 %. The unique characteristics of HTM-**56**, such as suitable energy levels, strong optical absorption in the visible region and high hole mobility, make possible to use it as a HTM in $MAPbI_3$-based PSCs and as photoactive donor material in BHJ solar cells. Focusing on PSCs, a PCE of 13.2 % was

110. C. Chen, M. Cheng, P. Liu, J. Gao, L. Kloo, L. Sun, "Application of benzodithiophene based A-D-A structured materials in efficient perovskite solar cells and organic solar cells", *Nano Energy*, **2016**, *23*, 40-49.

achieved in devices fabricated with HTM-**56** with and without dopants, which is even a little bit higher than that of devices based on the well-known spiro-OMeTAD with dopants.[111]

Table 7. Performance parameters of organic oligomeric-based HTMs.

HTM	J_{sc} (mA·cm^{-2})	V_{oc} (V)	FF (%)	PCE (%)
HTM-53	16.4	0.99	65.0	10.5
HTM-54	15.2	0.90	68.0	9.5
HTM-55	18.4	1.00	75.7	13.9
HTM-56	19.1	1.02	67.8	13.2

1.3.5.2. HTMs based on organic polymers

π-Extended conjugated oligomers display beneficial properties for OPV applications. These A-D-A structures are characterized by an easily tunable HOMO energy, high carriers mobility due to the strong intermolecular interactions between their π-extended backbone and strong absorption in the visible. Although, these remarkable properties have been widely exploited for small-molecule BHJ solar cells, they have not been extensively explored for PSCs. In figure 22, there are some representative examples of A-D-A structures that have been used as HTMs for PSCs.

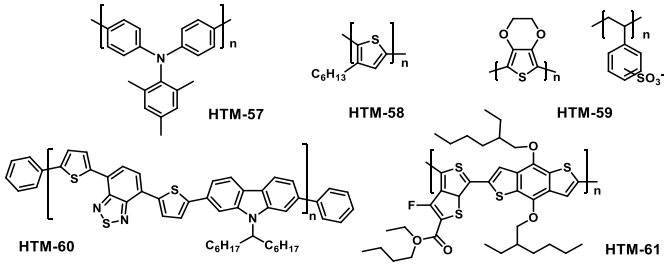

Figure 22. Structure of organic polymeric HTMs.

111. M. Cheng, B. Xu, C. Chen, X. Yang, F. Zhang, Q. Tan, Y. Hua, L. Kloo, L. Sun, "Phenoxazine-based small molecule material for efficient perovskite solar cells and bulk heterojunction organic solar cells", *Adv. Energy Mater.*, **2015**, *5*, 1401720-1401729.

In addition to the classical spiro-OMeTAD and the recent reports performances with other small molecules, polymers are also being explored as HTMs in PSCs. Poly(3,4-ethylenedioxythiophene) (PTAA, HTM-**57**) was the first polymer to be tested in PSCs[112] and holds the record for the highest PCE reported from any polymeric HTM reaching a valued of 20.1 %.[113] On the other hand, poly(3-hexylthiophene-2,5-diyl) (P3HT, HTM-**58**) and [poly(3,4-ethylenedioxy thiophene):polystyrene sulfonate] (PEDOT:PSS, HTM-**59**) were tested extensively, despite the initial results were not satisfactory. Shortly after, Tanaka, Nakamura and co-workers employed HTM-**60** in PSCs. An ionic dopant Li-TFSI contributed to the increase in PCE by increasing the conductivity of the HTM and a neutral additive D-TBP did so by enhancing the ordering of polymer's chains of HTM-**60** in the hole-transporting layer. A PCE of 12.4 % was reached with a high reproducibility.[114]

On the other hand, D-A based copolymers such as poly[*N*90-heptadecanyl-2,7carbazole-alt-3,6-bis(thiophen-5-yl)-2,5dioctyl-2,5-dihydropyrrolo[3,4] pyrrole-1,4-dione] (PCPDTBT, HTM-**60**) have also been used as HTMs in PSCs. In addition, poly[[2,6'-4,8-di(5-ethylhexylthienyl)benzo[1,2-*b*;3,3-*b*]di thiophene][3-fluoro-2[(2-ethylhexyl)carbonyl]thieno[3,4-*b*]thiophenediyl]] (PTB7-Th, HTM-**61**) was employed by Lee *et al.* with the use of an additional layer of MoO_3 and the device in a planar configuration gave a PCE value of 11.0 %.[115]

112. J. H. Heo, S. H. Im, J. H. Noh, T. N. Mandal, C. S. Lim, J. A. Chang, Y. H. Lee, H.-J. Kim, A. Sarkar, M. K. Nazeeruddin, M. Graetzel, S. I. Seok, "Efficient inorganic-organic hybrid heterojunction solar cells containing perovskite compound and polymeric hole conductors", *Nat. Photonics*, **2013**, *7*, 486-491.
113. W. S. Yang, J. H. Noh, N. J. Jeon, Y. C. Kim, S. Ryu, J. Seo, S. I. Seok, "High-performance photovoltaic perovskite layers fabricated through intramolecular exchange", *Science*, **2015**, *348*, 1234-1237.
114. Y. Guo, C. Liu, K. Inoue, K. Harano, H. Tanaka, E. Nakamura, "Enhancement in the efficiency of an organic-inorganic hybrid solar cell with a doped P3HT hole-transporting layer on a void-free perovskite active layer", *J. Mater. Chem. A*, **2014**, *2*, 13827-13830.
115. J. Kim, G. Kim, T. K. Kim, S. Kwon, H. Back, J. Lee, S. H. Lee, H. Kang, K. Lee, "Efficient planar-heterojunction perovskite solar cells achieved via interfacial modification of a sol-gel zno electron collection layer", *J. Mater. Chem. A*, **2014**, *2*, 17291-17296.

1.3.6. HTMs based on organometallic complexes

Organometallic complexes have also been explored as HTMs in PSCs. Ramos *et al.* employed green non-aggregated Zn^{II} octa(2,6-diphenylphenoxy) phthalocyanine (HTM-**62**, figure 23) doped with Li-TFSI and *t*-BP in mesoscopic PSCs and an encouraging PCE of 6.7 % was obtained.[116] Similarly, another metal phthalocyanine, titanyl phthalocyanine (TiOPc, HTM-**63**) was reported comparing the deposition by evaporation and by solvent annealing. A maximum PCE of 5 % was obtained employing HTM-**63** deposited by evaporation and without dopants.[117] Recently, tetramethyl-subtituted Cu^{II} phthalocyanine (CuMePc, HTM-**64**) was employed as the HTM in mesoscopic PSCs. They claimed that methyl substitution favours stronger π-π interactions and higher charge carrier mobility what have a small effect on overall solar cell efficiency. They reported a PCE only of 5 %.[118] Recently, a series of easily accessible zinc phthalocyanines as HTMs in mixed-ion PSCs were reported by Torres, Nazeeruddin and co-workers. The optimized devices exhibit PCE values of 17.5 %, 15.5 % and 13.3 % employing HTM-**65**, HTM-**66** and HTM-**67**, respectively.[119]

116. F. J. Ramos, M. Ince, M. Urbani, A. Abate, M. Graetzel, S. Ahmad, T. Torres, M. K. Nazeeruddin, "Non-aggregated Zn(II)octa(2,6-diphenylphenoxy) phthalocyanine as a hole transporting material for efficient perovskite solar cells", *Dalton Trans.*, **2015**, *44*, 10847-10851.
117. M. Sun, S. Wang, Y. Xiao, Z. Song, X. Li, "Titanylphthalocyanine as hole transporting material for perovskite solar cells", *J. Energy Chem.*, **2015**, *24*, 756-761.
118. G. Sfyri, C. V. Kumar, Y. L. Wang, Z. X. Xu, C. A. Krontiras, P. Lianos, "Tetra methyl substituted Cu(II) phthalocyanine as alternative hole transporting material for organometal halide perovskite solar cells", *Appl. Surf. Sci.*, **2016**, *360, Part B*, 767-771.
119. K. T. Cho, O. Trukhina, C. Roldán-Carmona, M. Ince, P. Gratia, G. Grancini, P. Gao, T. Marszalek, W. Pisula, P. Y. Reddy, T. Torres, M. K. Nazeeruddin, "Molecularly engineered phthalocyanines as hole-transporting materials in perovskite solar cells reaching power conversion efficiency of 17.5 %", *Adv. Energy Mater.*, **2016**, 1601733-1601740.

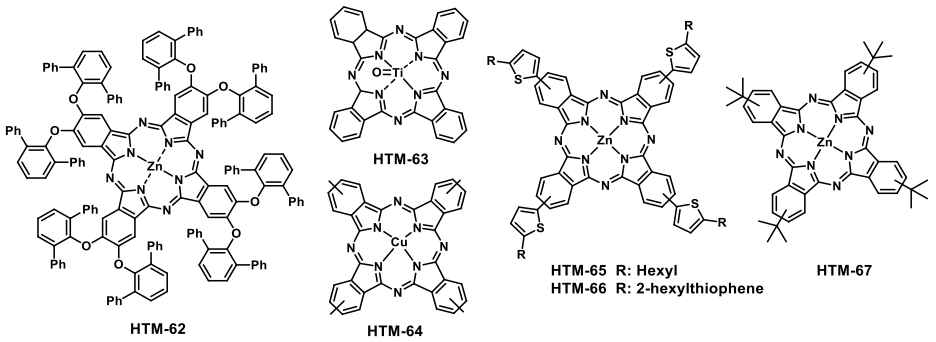

Figure 23. Structures of organometallic complexes HTMs.

Table 8. Performance parameters of organometallic complexes HTMs.

HTM	J_{sc} (mA·cm^{-2})	V_{oc} (V)	FF (%)	PCE (%)
HTM-62	16.4	0.80	50.3	6.7
HTM-63	12.6	0.73	53.0	5.1
HTM-64	16.9	0.70	50.0	5.2
HTM-65	20.3	1.05	80.3	17.1
HTM-66	20.2	1.10	69.4	15.5
HTM-67	20.2	1.03	66.3	13.3

1.3.7. Inorganic HTMs

As another alternative, inorganic p-type semiconductors have also been explored as HTMs in PSCs owing to their high hole mobility, intrinsically high stability, ease of synthesis and low cost fabrication. However, so far, only few studies in terms of using inorganic HTMs in PSCs have been reported due to the limited choices of suitable materials. In a quest to explore new inorganic HTMs, the first example was copper iodide (CuI) reported by Kamat and co-workers in 2014 in mesoscopic PSCs.[120] CuI-based devices exhibit a highest PCE value of 8.3 %. The maximum V_{oc} (≈ 0.62 V) is found to be lower as compared to devices using spiro-OMeTAD (0.78 V), attributed to faster charge recombination rates. In

120. J. A. Christians, R. C. M. Fung, P. V. Kamat, "An inorganic hole conductor for organo-lead halide perovskite solar cells. Improved hole conductivity with copper iodide", *J. Am. Chem. Soc.*, **2014**, *136*, 758-764.

addition, it was determined that CuI presents higher electrical conductivity than spiro-OMeTAD, which allowed significantly higher FF observed in CuI-based devices. Another copper-based inorganic p-type hole-conductor that has been actively studied in PSCs[121] is copper thiocyanate (CuSCN). Further efforts led to better results by optimization of the HTM thickness, the deposition process of the perovskite and so on. An impressive maximum PCE of 16.6 % was achieved using CuSCN in an optimized planar structure of PCS by Bian, Liu *et al.* They employed a one-step fast deposition crystallization method for the $MAPbI_3$ formation and electrodeposition to deposit the HTM.[122]

Nickel oxide (NiO) thin films were employed successfully as a HTM in DSSC and OPV devices.[123,124] Optimizing the thickness of the HTM and doping with oxygen, Chen *et al.* improved the performance leading to a maximum PCE of 11.6 %.[125] A ternary oxide $Li_xMg_yNi_{1-x-y}O$ was employed by Chen, Wu and co-workers. After a thickness optimization of the HTM an efficiency of 16.2 % in 1.02 cm^2 area device was obtained.[126]

121. S. Chavhan, O. Miguel, H. J. Grande, V. Gonzalez-Pedro, R. S. Sanchez, E. M. Barea, I. Mora-Sero, R. Tena-Zaera, "Organo-metal halide perovskite-based solar cells with CuSCN as the inorganic hole selective contact", *J. Mater. Chem. A*, **2014**, *2*, 12754-12760.
122. S. Ye, W. Sun, Y. Li, W. Yan, H. Peng, Z. Bian, Z. Liu, C. Huang, "CuSCN-based inverted planar perovskite solar cell with an average PCE of 15.6 %", *Nano Lett.*, **2015**, *15*, 3723-3728.
123. L. Li, E. A. Gibson, P. Qin, G. Boschloo, M. Gorlov, A. Hagfeldt, L. Sun, "Double-layered NiO photocathodes for p-type DSSCs with record IPCE", *Adv. Mater.*, **2010**, *22*, 1759-1762.
124. J. R. Manders, S. W. Tsang, M. J. Hartel, T. H. Lai, S. Chen, C. M. Amb, J. R. Reynolds, F. So, "Solution-processed nickel oxide hole transport layers in high efficiency polymer photovoltaic cells", *Adv. Funct. Mater.*, **2013**, *23*, 2993-3001.
125. K. C. Wang, P. S. Shen, M. H. Li, S. Chen, M. W. Lin, P. Chen, T. F. Guo, "Low-temperature sputtered nickel oxide compact thin film as effective electron blocking layer for mesoscopic $NiO/CH_3NH_3PbI_3$ perovskite heterojunction solar cells", *ACS Appl. Mater. Interfaces*, **2014**, *6*, 11851-11858.
126. W. Chen, Y. Wu, Y. Yue, J. Liu, W. Zhang, X. Yang, H. Chen, E. Bi, I. Ashraful, M. Graetzel, L. Han, "Efficient and stable large-area perovskite solar cells with inorganic charge extraction layers", *Science*, **2015**, *350*, 944-948.

• Results and discussion

Chapter 1. Hole-transporting materials for perovskite solar cells

2. RESULTS AND DISCUSSION

The tremendous interest of PSCs does not only lie in their high power conversion efficiencies (PCEs), but also in their stability for commercial applications. So far, a large number of organic and inorganic materials have been developed and incorporated as hole-transporting layer in PSCs.[28, 79, 127, 128]

The ideal hole-selective contact should have a good hole mobility and a HOMO energy level compatible with the valence band edge of the perovskite. In addition, minimal absorption in the visible and near-IR region of the solar spectrum as well as excellent thermal and photochemical stability are important requirements.[70] Organic materials have been selected as good candidates to be used in PV devices owing to their easy synthesis and manipulation, and the ability to tune their properties through chemical modifications.[129]

Although there is not a clear relationship between chemical structure and PV performance in the literature, it is well known that spiro-OMeTAD and spiro-like compounds work in a very efficient manner. On the other hand, a wide number of multi-armed organic molecules have been reported reaching promising efficiencies and, in a few cases, outperforming that of spiro-OMeTAD.

Two different elements could be usually distinguished in the design of these molecules: i) a central unit, mostly planar or slightly twisted, which is endowed with; ii) electron donor fragments. Both of them play an important role determining the final properties of the molecule. The central fragment acts as a scaffold and could eventually affect some properties such as hole mobility, thermal and optical properties. On the other hand, electron donor moieties allow to tune the HOMO energy level of the final molecule as well as the electrochemical properties.

127. I. S. Yang, M. R. Sohn, S. D. Sung, Y. J. Kim, Y. J. Yoo, J. Kim, W. I. Lee, "Formation of pristine CuSCN layer by spray deposition method for efficient perovskite solar cell with extended stability", *Nano Energy*, **2017**, *32*, 414-421.
128. J. Ge, C. R. Grice, Y. Yan, "Cu-based quaternary chalcogenide Cu_2BaSnS_4 thin films acting as hole transport layers in inverted perovskite $CH_3NH_3PbI_3$ solar cells", *J. Mater. Chem. A*, **2017**, *5*, 2920-2928.
129. S. F. Völker, S. Collavini, J. L. Delgado, "Organic charge carriers for perovskite solar cells", *ChemSusChem*, **2015**, *8*, 3012-3028.

2.1. Electron donor groups

In this work, different electron donor molecules have been employed, from simple triphenylamine (TPA) and diphenylamine (DPA) derivatives, to more complex ones, combining DPA with carbazoles.

TPA derivatives are well-known for their strong electron-donating character and hole-transport properties.[130] Thanks to their starburst structure, TPA can be chemically engineered to tune its electron donor ability by the introduction of electron-rich groups to an adjacent phenyl ring. With this in mind, four electron donor derivatives were synthesized, *p*-methoxydiphenylamine (**68**), *p*-methoxytriphenylamine (**69**), 3,6-dimethoxy-9*H*-carbazole (**70**) and *p*-methoxydiphenylamine-substituted carbazole (**71**) whose molecular structures are illustrated in figure 24.

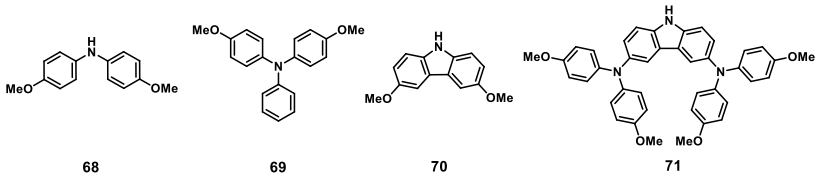

Figure 24. Electron donor derivatives for further HTMs.

Firstly, the synthesis of *p*-methoxydiphenylamine (**68**) was carried out according to scheme 1. A previously described procedure was followed, employing a Buchwald-Hartwig cross coupling amination between commercially available reagents, 1-iodo-4-methoxybenzene and 4-methoxyaniline.[131]

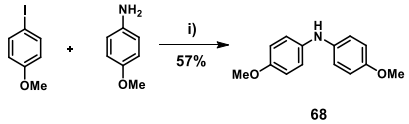

Scheme 1. *Reagents and conditions:* **i**) $Pd_2(dba)_3$, XPhos, Na^{t}BuO, toluene, 111 ºC.

130. J. Wang, K. Liu, L. Ma, X. Zhan, "Triarylamine: Versatile platform for organic, dye-sensitized, and perovskite solar cells", *Chem. Rev.*, **2016**, *116*, 14675-14725.
131. X. Zhu, Q. Zhang, W. Su, "Solvent-free *N*-arylation of amines with arylboronic acids under ball milling conditions", *RSC Adv.*, **2014**, *4*, 22775-22778.

On the other hand, TPA was chosen as slightly weaker electron donor moiety than DPA to systematically compare the influence on the PV performances. TPA derivative was firstly synthesized by Merz and Weith in 1873.[132] Thereafter, different procedures have been reported employing copper-mediated Ullmann reaction, modified Ullmann reaction and Buchwald-Hartwig reaction to obtain this widely used building block for functional materials.[130] In this particular case, the corresponding boronic-ester-derivative of TPA was necessary for synthetic reasons. Thus, TPA (**69**) was synthesized by a two-fold Buchwald-Hartwig reaction between aniline and 4-bromoanisole as starting materials. After iodination in the presence of I_2 and periodic acid in ethanol and subsequent Miyaura borylation reaction between compound **72** and bis(pinacolato)diboron afforded the molecularly engineered TPA, compound **73** (scheme 2).

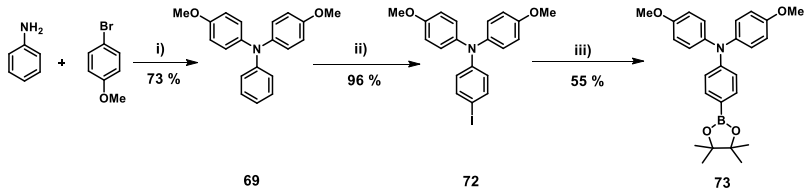

Scheme 2. *Reagents and conditions:* **i**) $Pd_2(dba)_3$, XPhos, Na^{t}BuO, toluene, 111 ºC; **ii**) I_2, periodic acid, ethanol, r.t.; **iii**) bis(pinacolato)diboron, KOAc, Pd[$(Cl_2(dppf)_2$]·DCM, DMF, 80 ºC.

In addition, carbazole derivatives (**70** and **71**) were also used as electron donor groups. Like TPA, carbazole exhibits strong electron-donating ability and excellent hole transporting properties which has been extensively studied for DSSC.[133] Thus, interesting photophysical and electrochemical properties arise from minor changes in the geometry of the donor structure. Among all the electron donating fragments described in the present work, carbazole (**70**) is the weakest, which closely matches the valence band edge of the perovskite. The selective carbazole bromination in 3 and 6 positions is illustrated in scheme 3. Di-brominated carbazole **74**, was easily synthesized in excellent yield using two equivalents of NBS in DMF starting from commercially available carbazole.

132. V. Merz, W. Weith, "Vermischte mittheilungen", *Berichte der deutschen chemischen Gesellschaft*, **1873**, *6*, 1511-1520.
133. C. Y. Chen, J. G. Chen, S. J. Wu, J. Y. Li, C. G. Wu, K. C. Ho, "Multifunctionalized ruthenium-based supersensitizers for highly efficient dye-sensitized solar cells", *Angew. Chem. Int. Ed.*, **2008**, *47*, 7342-7345.

Finally, the nucleophilic substitution of bromine by methoxide groups gave rise to carbazole derivative **70**.

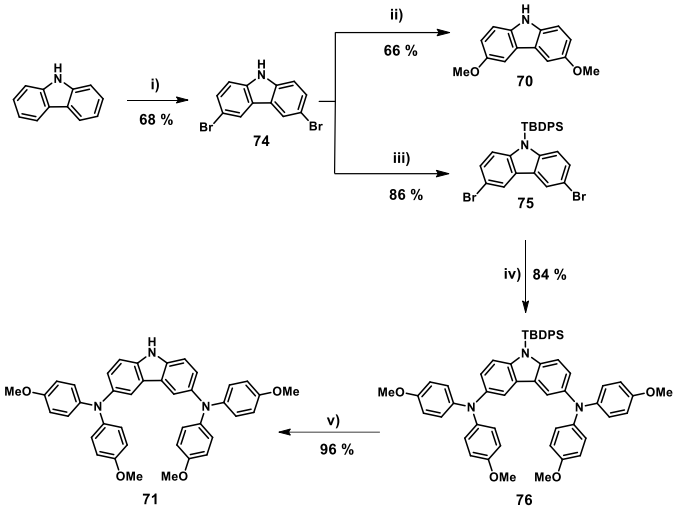

Scheme 3. *Reagents and conditions:* **i**) NBS, DMF, DCM, r.t.; **ii**) CuI, Na, methanol, 153 ºC; **iii**) NaH, ClTBDPS, DMF, r.t.; **iv**) **68**, $Pd_2(dba)_3$, XPhos, Na^{t}BuO, toluene, 111 ºC; **v**) TBAF, toluene, r.t.

With an eye towards the optimization of the electron donor abilities of the carbazole-based derivatives, *p*-methoxydiphenylamine (**68**) was introduced in order to obtain the fourth desired electron donor (**71**) (scheme 3).

The carbazole derivative **75** was synthesized by a facile synthetic route using the *tert*-butyl(chloro)diphenylsilane (ClTBDPS) group to protect the carbazole nitrogen atom. TBDPS group could be cleavaged within a few minutes using tetrabutylamine fluoride (TBAF) in sharp contrast with other protecting group, such as benzyl or tosyl. Finally, two-fold Buchwald-Hartwig cross-coupling reaction with *p*-methoxydiphenylamine (**68**) followed by the cleavage of the TBDPS group furnished the desire electron donor compound, **71**.

In the present thesis, different families of small-organic molecules are reported as potential candidates for perovskite solar cells. These families are classified depending on the central fragment, since all of them are endowed with the aforementioned efficient electron donor units.

2.2. Series of TAE-based and BF-based HTMs

The novel molecules presented in this section display a structure similar to the-state-of-the-art, spiro-OMeTAD, in which its central core renders a perpendicular arrangement of the two molecular halves linked by a central carbon atom (sp^3). The molecular interactions between the conjugated systems are efficiently suppressed in the rigid structure of the spiro configuration in spiro-OMeTAD.[134] However, there are no clear indications whether the spiro structure plays a key role in its superior performance over other alternatives. To shed light about this question, structural changes have been introduced, obtaining spiro-like analogues with an evolution from "open" to "close" form of the fluorene rings and from "single carbon atom" configuration to a "C=C" configuration between the two halves.

The first family possess a gradually rigid molecular arrangement based on tetraphenyethene (TAE) central core. Increasing the rigidity of the 3D molecular arrangement, two more molecules are studied where bisfluorenylidene (BF) will be described as central unit (figure 25). Therefore, the rotation or rigidity of the linkage between the fluorene planes could be studied as an important factor for the change of their molecular properties.

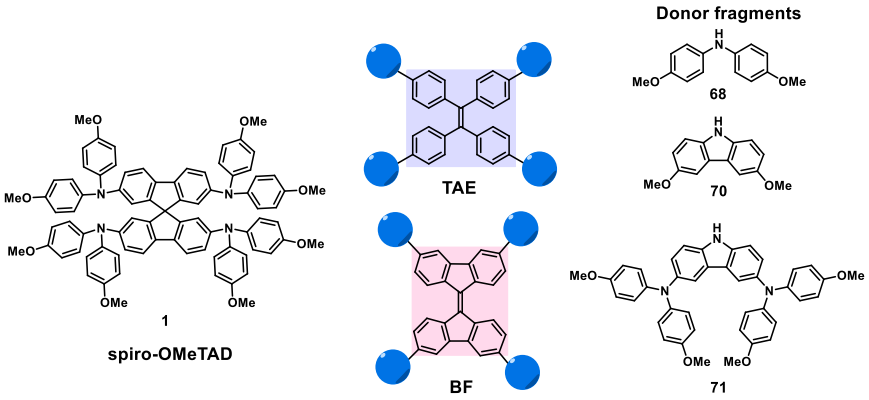

Figure 25. Simplified TAE- and BF-based HTMs structures.

134. C. W. Chu, J. Ouyang, J. H. Tseng, Y. Yang, "Organic donor–acceptor system exhibiting electrical bistability for use in memory devices", *Adv. Mater.*, **2005**, *17*, 1440-1443.

Following, a detailed synthetic procedure for the preparation of these novel molecules and their spectroscopic and photophysical properties are presented.

2.2.1. Central structure: tetraarylethene (TAE) and bifluorenylidene (BF)

TAE, also known as tetraphenylethene (TPE), presents a simple molecular structure based on four phenyl rings which are linked to a central ethene rod through single bonds (figure 26). Its four phenyl rings are twisted out of the central alkene plane by about 50º. This propeller-like conformation presents π-π stacking interactions. Therefore, multiple C-H···π intermolecular interactions take place between the hydrogen of the phenyl rings of one TAE and the π electrons of an adjacent molecule. These interactions lock the molecular conformation bestowing highly emissive properties in the aggregated state (figure 26). [135]

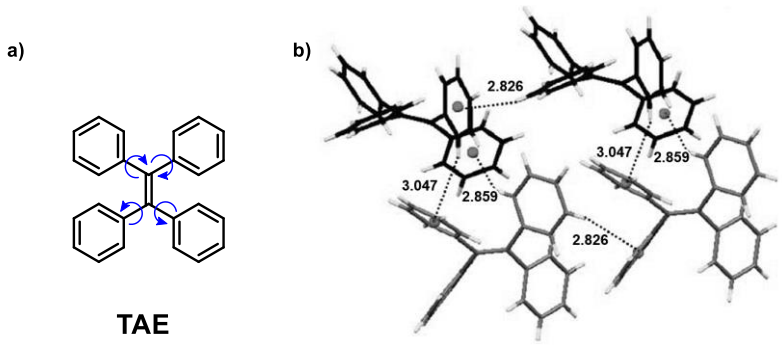

Figure 26. a) Molecular structure of tetraarylethene (TAE); **b**) C-H···π hydrogen bonds with indicated distance (Å) between adjacent TAE molecules in the crystal state.

TAE is very soluble in acetonitrile, THF and chloroform and slightly soluble in methanol, but completely insoluble in water. It is practically nonluminescent when is molecularly dissolved in any organic solvent, almost no PL signals are detected from its dilute solutions. However, when a nonsolvent, such as water, is added into its solution, intense emission is observed under identical conditions. As TAE is not soluble in water, it must aggregate in the THF/water mixtures with high water contents. Therefore, TAE exhibits the phenomenon of aggregation induced emission (AIE) as the emission of TAE is induced by

135. Z. Zhao, B. Z. Tang, "Aggregation-induced emission of tetraarylethene luminogens", *Curr. Org. Chem.*, **2010**, *14*, 2109-2132.

aggregate formation. This phenomenon was first found in propeller-like siloles by Tang and co-workers in 2001.[136] The emission of those derivatives is very weak in solution but become intense as aggregates are formed. The opposite phenomenon, aggregation-caused quenching (ACQ), happens when many luminophores exhibit strong PL in dilute solutions and their light emission is often weakened or even completely quenched in concentrated solutions or in the solid state,[137] because the luminophores aggregate during film formation. Under these circumstances, the aromatic rings of the neighboring fluorophores experience strong π-π stacking interactions. The excited states of the aggregates often decay via nonradiative relaxation pathways, which are a consequence of the ACQ phenomenon in the condensed phase.[138,139]

Some new design of luminescent materials utilizing TPE as a building block (figure 27) are an effective strategy to create efficient solid state emitters.[139]

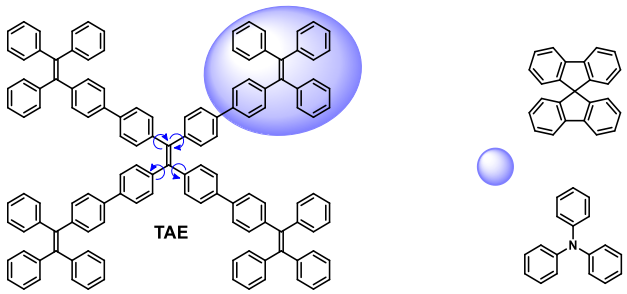

Figure 27. Some examples of TPE-cored luminogen structures.

136. J. Luo, Z. Xie, J. W. Y. Lam, L. Cheng, H. Chen, C. Qiu, H. S. Kwok, X. Zhan, Y. Liu, D. Zhu, B. Z. Tang, "Aggregation-induced emission of 1-methyl-1,2,3,4,5-pentaphenylsilole", *Chem. Commun.*, **2001**, 1740-1741.
137. K. K. T. Förster, *Int. J. Res. Phys. Chem. Chem. Phys.*, **1954**, *1*, 275.
138. K. Y. Pu, B. Liu, "Conjugated polyelectrolytes as light-up macromolecular probes for heparin sensing", *Adv. Funct. Mater.*, **2009**, *19*, 277-284.
139. Z. Zhao, J. W. Y. Lam, B. Z. Tang, "Tetraphenylethene: A versatile AIE building block for the construction of efficient luminescent materials for organic light-emitting diodes", *J. Mater. Chem. A*, **2012**, *22*, 23726-23740.

In addition, arising from these attractive properties, TPE has been extensively studied for the fabrication of non-planar OLEDs, memory chips, sensor,[140] and for biological and optoelectronics applications.[141]

On the other hand, 9,9'-bifluorenylidene (BF) molecule, whose structure is shown in the scheme 4, has also been used as a central unit for the final target HTMs. 99'-BF could be considered a tetrabenzofulvalene with an atom numbering that reflects fluorene linked by a double bond between the 9 and 9' carbon atoms. In the ground state, it is forced to be coplanar because of the presence of the double bond, but the repulsive interaction between the H1-H1' and H8-H8' atoms twists the structure of the dimer. The addition of one electron across the C9-C9' bond (scheme 4)[142] is highly favourable for two main reasons: steric ("twist") strain relief as Weitzen-Dagan and co-workers described in 1974[143] and gain in aromaticity to a 14-π-electron system as Rabinovitz and co-workers reported in 1986.[144] Thus, BF displays an electron-acceptor behaviour.

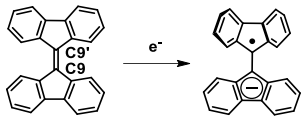

99'-BF

Scheme 4. Formation of 99'-BF 14-π-electron fluorenide anion after the addition of one electron across the C9-C9' double bond.

99'-BF was first synthesized in 1875 and it could be classified into homomerous bistricyclic enes. The smallest overcrowded bistricyclic aromatic ene is a unique case among the homomerous bistricyclic enes, because of its central five

140. Y. Sagara, T. Kato, "Mechanically induced luminescence changes in molecular assemblies", *Nat Chem*, **2009**, *1*, 605-610.
141. Z. Chi, X. Zhang, B. Xu, X. Zhou, C. Ma, Y. Zhang, S. Liu, J. Xu, "Recent advances in organic mechanofluorochromic materials", *Chem. Soc. Rev.*, **2012**, *41*, 3878-3896.
142. F. G. Brunetti, X. Gong, M. Tong, A. J. Heeger, F. Wudl, "Strain and Hückel aromaticity: Driving forces for a promising new generation of electron acceptors in organic electronics", *Angew. Chem. Int. Ed.*, **2010**, *49*, 532-536.
143. M. Rabinovitz, I. Agranat, A. Weitzen-Dagan, "Pathways for thermal z,e isomerization in tetrabenzopentafulvalenes: Transition-state stabilization combined with ground-state destabilization", *Tetrahedron Lett.*, **1974**, *15*, 1241-1244.
144. Y. Cohen, J. Klein, M. Rabinovitz, "Stable polycyclic anions: Dianions from overcrowded ethylenes", *J. Chem. Soc., Chem. Commun.*, **1986**, 1071-1073.

membered rings. This topology introduces planarity to the tricyclic moieties and is sterically less demanding at the same time, especially in twisted conformations. BFs are the only known homomerous bistricyclic aromatic enes with a twisted global minimum conformation. For its characteristics, it is a potential candidate for molecular switches,[145] preparation of low band-gap polymers, even as an acceptor for OPV applications[142] and for the preparation of buckyballs since it is a fragment of fullerene C_{60}.[146]

A total of five new HTMs are presented below, whose elaboration does not require an expensive synthetic procedure. These new HTMs offer a cost-effective and up-scalable synthetic route, leading to a significant reduction of materials cost compared to the state-of-the-art materials. These novel organic compounds based on TAE and BF central fragments constitute an easy to prepare methodology for HTMs which were prepared employing a straightforward two-step strategy. The central fragments were endowed with electron donor groups, such as *p*-methoxydiphenylamine (**68**) (**TAE-1** and **BF-3**), 3,6-dimethoxy-9*H*-carbazole (**70**) (**TAE-2** and **BF-4**) and *p*-methoxydiphenylamine-substituted carbazole (**71**) (**TAE-3**).

2.2.2. Design and synthesis of new TAE-based HTMs

This section will address the preparation and properties of three TAE-derivatives. As it was mentioned before, their structure is constituted by two elements, TAE as central core decorated with different electron donor groups as it is illustrated in figure 28.

145. B. L. Feringa, A. M. Schoevaars, W. F., Jager, B. De Lange, N. P. M. Huck, "Switching of chirality by light", *Enantiomer*, **1996**, *273*, 325-335.
146. P. U. Biedermann, J. J. Stezowski, I. Agranat, "Conformational space and dynamic stereochemistry of overcrowded homomerous bistricyclic aromatic enes -a theoretical study", *Eur. J. Org. Chem.*, **2001**, *2001*, 15-34.

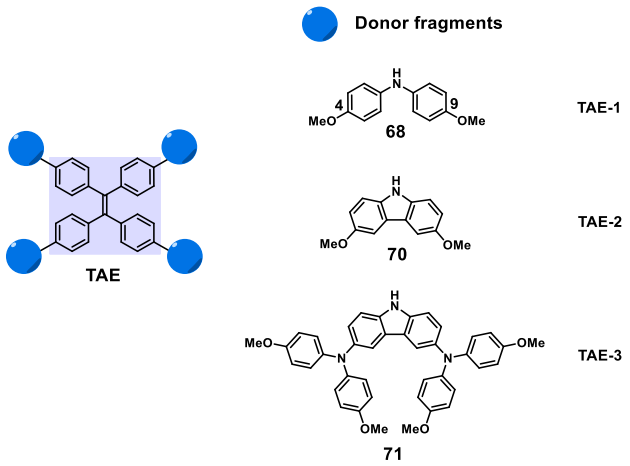

Figure 28. Simplified molecular structure of TAEs-based HTMs.

Target compound **TAE-1** was achieved as depicted in scheme 5, following a straightforward two-step procedure. Starting from commercially available 4,4-diaminobenzophenone, two-fold copper-catalysed Ullmann reaction in the presence of 4-iodoanisole leads to the intermediate compound **77**. Finally, a McMurry reductive coupling of ketone (**77**) using a low-valent titanium reagent successfully furnished the desired **TAE-1** molecule in 72 % yield.

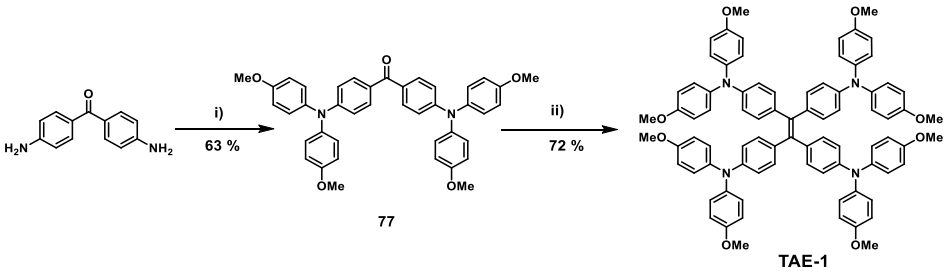

Scheme 5. *Reagents and conditions:* **i**) 1-iodo-4-methoxybenzene, Cu, 18-crown-6, K_2CO_3, nitrobenzene, 188 ºC; **ii**) Zn, $TiCl_3$, THF/DCM, 40 ºC.

As a curiosity and owing to the remarkable properties exhibited by central fragment of **TAE-1**, fluorescence measurements were performed. To this end, the fluorescence of **TAE-1** in THF and in the presence of increasing amounts of water were monitored (figure 29).

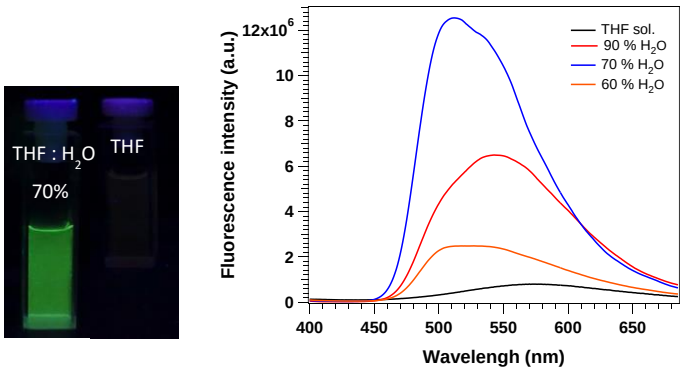

Figure 29. Evidence of AEI phenomenon exhibited by **TAE-1** molecule.

In diluted THF solution, the rotation of the pheripheral phenyl against the olefin double bond of the TPE central core quenched the fluorescence of **TAE-1**. However, a dramatic enhancement of the fluorescence was observed upon increasing the water contents (χ_w = 30 - 90 %). The fluorescence intensity of **TAE-1** was boosted by twelve-fold when the water fraction was increased from 30 to 70 % with a maximum λ_{em} centered at 510 nm. These experimental finding indicated that **TAE-1** is AIE-active.

TAE-1 was first synthesized in our research group with the aim to be used as an effective HTM component in PSCs. Its application in dopant-free perovskite solar cell was reported in 2015 in collaboration with Prof. Emilio Palomares's group and it will be described in section 3. Since then, several research groups have employed **TAE-1** or modified **TAE-1** for dopant-PSCs.[147]

One strategy to design new functional materials, in order to compare their behaviour as HTMs in PSCs, is the modification of the donor group. Thus, the first idea was to change the *p*-methoxydiphenylamine donor units for carbazole derivatives, keeping the same central-acceptor structure of the molecule. The well-known donor carbazole was modified introducing methoxy- or methoxydiphenylamine- groups at 3 and 6 positions to tune their HOMO energy level.

147. H. Choi, K. Do, S. Park, J. S. Yu, J. Ko, "Efficient hole transporting materials with two or four *N*,*N*-di(4-methoxyphenyl)aminophenyl arms on an ethene unit for perovskite solar cells", *Chem. Eur. J.*, **2015**, *21*, 15919-15923.

Firstly, for the preparation of **TAE-2**, the same synthetic approach as that for **TAE-1** was followed, as depicted in scheme 6. Unfortunately, the McMurry reductive coupling of ketone **78** did not work. For that reason, Lawesson's reagent was employed by treating ketone **78** at reflux. Sadly, the formation of the corresponding thione was obtained due to its stability when electron donors are substituted in *para*-position.

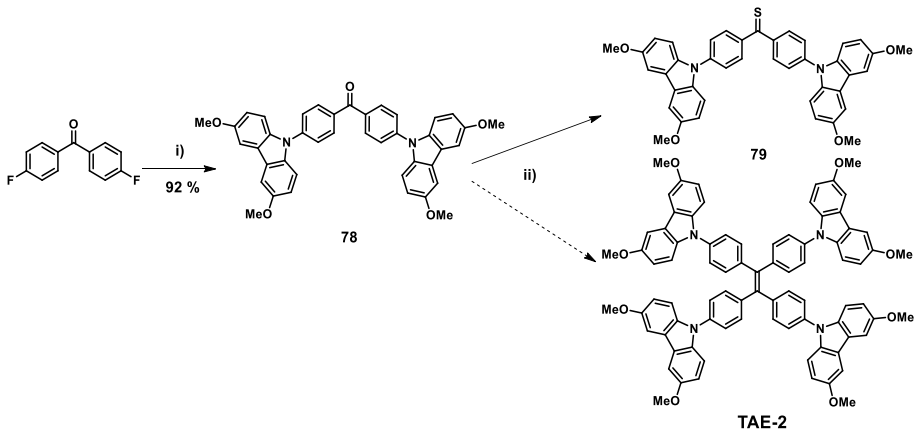

Scheme 6. *Reagents and conditions:* **i**) **70**, $CsCO_3$, DMSO, 75 ºC; **ii**) Zn, $TiCl_3$, DCM/THF, 40 ºC or Zn, $TiCl_4$, THF, 65 ºC or Lawesson's reagent, toluene, 111 ºC.

Thus, the two-step synthetic procedure followed to prepare the target molecules **TAE-2** and **TAE-3** starts with the synthesis of the central bromo-derivative **80**. As it is illustrated in scheme 7, starting from the commercially available 4,4'-dibromobenzophenone, it was possible to prepare TPE derivative bearing four bromine atoms (**80**) by McMurry coupling reaction in the presence of low-valent titanium reagent and Zn in DCM/THF. Previously synthesized electron donor groups (compounds **70** and **71**) were introduced to derivative **80** by a four-fold Buchwald-Hartwig cross-coupling reaction to afford the new **TAE-2** and **TAE-3** molecules in a 61 % and 88 % yield, respectively.

Compared with **TAE-1** and **TAE-2**, the presence of bulkier groups in **TAE-3** endows it with less significant AIE effect.

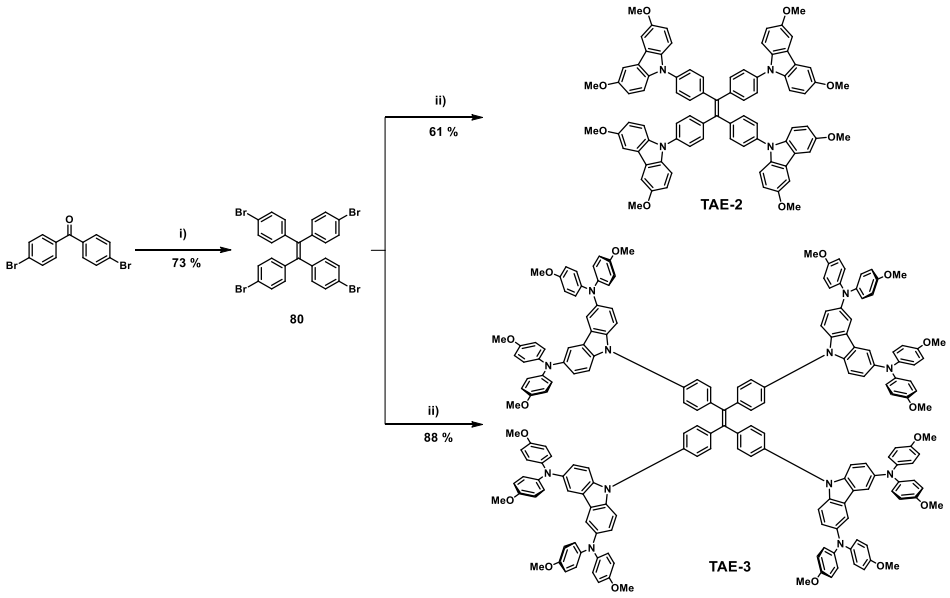

Scheme 7. *Reagents and conditions:* **i**) Zn, $TiCl_3$, DCM/THF, 65 ºC; **ii**) **70** or **71**, $Pd_2(dba)_3$, XPhos, Na^tBuO, toluene, 100 ºC.

Complete structural characterization of the tetraarylethene derivatives **TAE-1**, **TAE-2** and **TAE-3** and the corresponding intermediates was accomplished using standard spectroscopic techniques such as ^{1}H NMR, ^{13}C NMR, FTIR, and UV-vis. As representative spectroscopic features ^{1}H NMR spectrum of **TAE-1** in $CDCl_3$ is shown in figure 30. **TAE-1** exhibited the typical signals of an AA'BB' system, corresponding to the tetraphenylethene central unit. In addition, the same trend is observed for the protons corresponding to the *p*-methoxydiphenylamine. The methoxyl protons appeared as a singlet at 3.77 ppm, integrating for 24 protons.

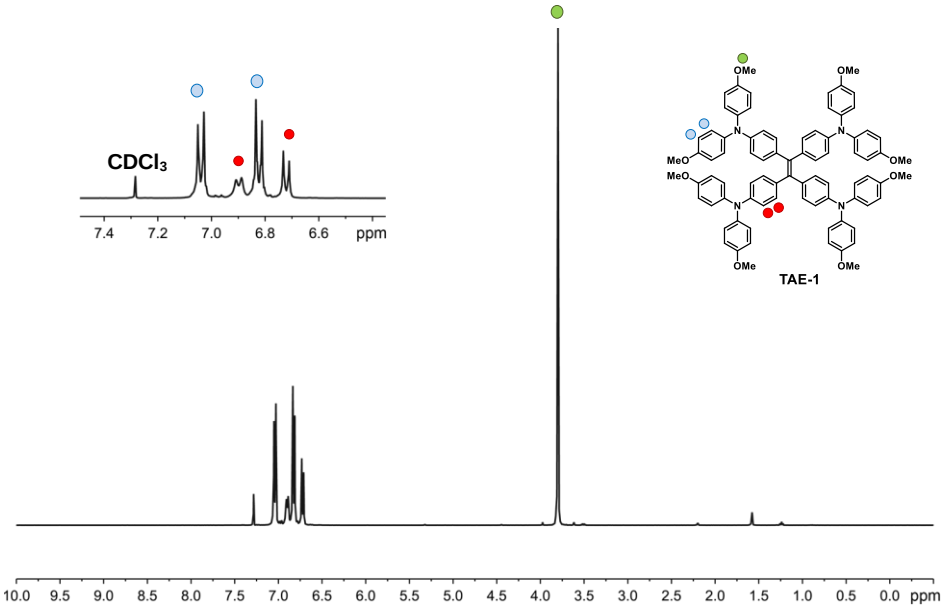

Figure 30. ^{1}H NMR (400 MHz, $CDCl_3$, 298 K) of **TAE-1**.

In the same manner, the ^{1}H NMR spectrum of **TAE-2** and **TAE-3** reveals the representative spectroscopic features corresponding to TAE core and the donor units as for **TAE-1**. Complementary, mass spectrometry HRMS [MALDI-TOF] confirmed the presence of **TAE-1** with a molecular ion peak $[M]^+$ at 1240.5334 m/z (calcd. 1240.5345 m/z), **TAE-2** at 1232.4703 m/z (calcd. 1232.4719 m/z) and **TAE-3** with a molecular ion peak $[M]^+$ at 2809.1430 m/z (calcd. 2809.1444 m/z).

2.2.3. Design and synthesis of new BF-based HTMs

In the previous section, TAE derivatives, endowed with electron donor groups, have been synthesized from inexpensive precursor materials, offering potentially much lower production cost in comparison to the most widely used spiro-OMeTAD. Nowadays, there is a lack of fundamental criteria for designing new alternatives to spiro-OMeTAD. Thus, finding a compromise between structure and the required properties is an important task to tackle in the coming years.

Considering the above points, there are several alternative chemical approaches for designing high-efficient HTMs. In the previous section, tuning the electron donor moieties was afforded. In this segment modifying the central core was envisaged as a useful strategy for designing new functional materials for PSCs.

The central unit chosen for this purpose is bifluorenylidene (BF), which presents similar molecular structure to TAE. However, the spatial configuration is different. BF possesses a notable rigid structure because of the presence of the central five-membered rings, between the two benzene rings, linked by a double bond. 9,9'-BF is a very versatile scaffold with 12 different sites for functionalization. In addition, 9,9'-BF exhibit an electron acceptor character. Accordingly, the 9,9'-BF derivatives, described in the present thesis, not only allow to study the influence in the performance of more rigid structures, but also to study systems with a D-A feature. BF as central unit was decorated with donor groups namely *p*-methoxydiphenylamine (**68**) and 3,6-dimethoxy-9*H*-carbazole (**70**) to afford **BF-1** and **BF-2**, respectively, which are schematically presented in figure 31.

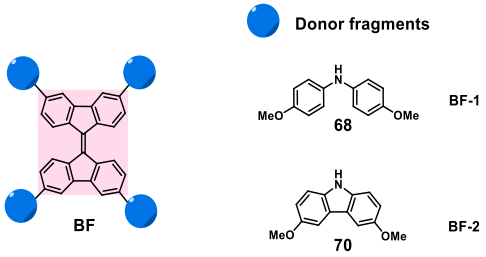

Figure 31. Simplified molecular structure of BF-based HTMs.

These new derivatives were prepared following a straightforward two-step synthetic procedure. The synthetic route illustrated in scheme 8 allows to obtain **BF-1** and **BF-2**. Firstly, compound **83** was obtained from a one-pot reaction by treating 3,6-dibromo-9*H*-fluoren-9-one, synthesized by reported procedures, in the presence of Lawesson's reagent in refluxing toluene. This reductive dimerization occurs via formation of the corresponding thione followed by a carbine dimerization.[148] Finally, *p*-methoxydiphenylamine (**68**) or 3,6-dimethoxy-9*H*-carbazole (**70**) were covalently linked to the central unit by a four-fold Buchwald-Hartwig cross-coupling reaction to obtain **BF-1** and **BF-2** respectively in good yields.

148. A. Levy, M. Goldschmidt, I. Agranat, "A simple facile synthesis of bifluorenylidenes", *Lett. Org. Chem.*, **2006**, *3*, 579-584.

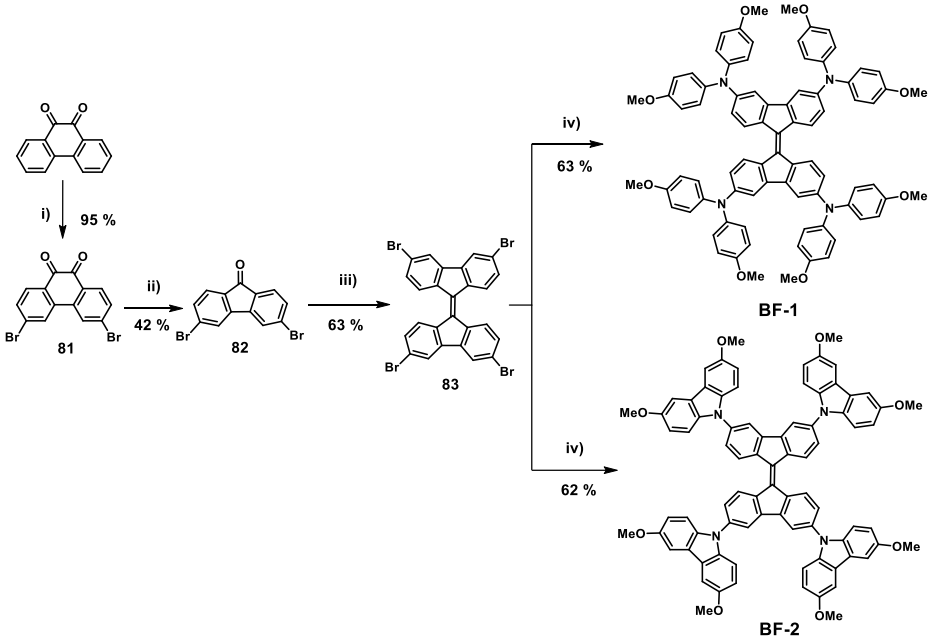

Scheme 8. *Reagents and conditions*: **i**) Br_2, $(PhCO_2)_2O$, nitrobenzene, 110 ºC; **ii**) *a.* KOH, water, 85 ºC, *b.* $KMnO_4$, 100 ºC, *c.* water, $NaHSO_3$, 100 ºC; **iii**) Lawesson's Reagent, toluene, 111 ºC; **iv**) **68** or **70**, $Pd_2(dba)_3$, XPhos, Na^{t}BuO, toluene, 111 ºC.

Complete structural characterization of the final compound **BF-1** and **BF-2** and the corresponding intermediates was accomplished using standard spectroscopic techniques such as ^{1}H NMR, ^{13}C NMR, FTIR and UV-vis. The ^{1}H NMR spectra of the final molecules reveal the characteristic signals of the BF core (two doublets and one double doublet corresponding to 4 protons each) and the representative signals of the donor units. In addition, mass spectrometry HRMS [MALDI-TOF] confirmed the presence of **BF-1** with a molecular ion peak $[M]^+$ at 1236.5029 m/z (calcd. 1236.5032 m/z) and **BF-2** at 1228.4446 m/z (calcd. 1228.4406 m/z).

Interestingly, **BF-1** and **BF-2** which possess BF as a central core, do not show the AIE phenomenon because the topology of BF introduces planarity to the tricyclic moieties being sterically less demanding at the same time, thus making the molecule nonemissive in the solid state.

2.2.4. Thermal, optical and electrochemical properties

a) Thermogravimetric analysis (TGA) and differential scanning calorimetry (DSC)

Relevant insights into the thermal properties of the new HTMs were provided by thermogravimetric analysis (TGA) and differential scanning calorimetry (DSC) (figure 32). Detailed thermal features are collected in table 9.

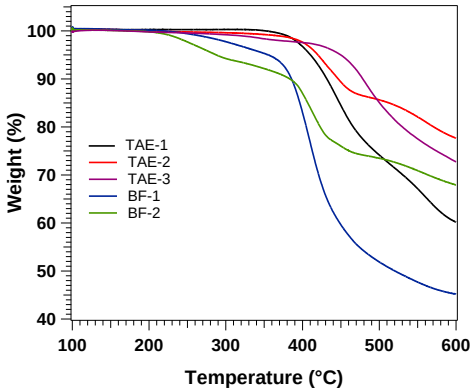

Figure 32. Thermogravimetric analysis of **TAE-1**, **TAE-2**, **TAE-3**, **BF-1** and **BF-2** at scan rate of 10 ºC /min and under N_2 atmosphere.

From the TGA curves it can be observed a different behaviour between TAE-based and BF-based molecules. **TAE-1**, **TAE-2** and **TAE-3** exhibit good thermal stability and start decomposing at temperatures (T_{dec}) above 350 ºC (5 % weight loss under N_2 atmosphere), being **TAE-3** the most stable. In contrast **BF-1** and **BF-2** showed a noticeable lower stability against temperature, starting to decompose at (T_{dec}) 250 ºC. This clearly indicates that the stability of the molecule changes with the difference in the central moiety of the HTMs.

The thermal transitions of the new HTMs were studied by DSC and compared with those for spiro-OMeTAD. The corresponding DSC curves of each molecule are illustrated in figure 33.

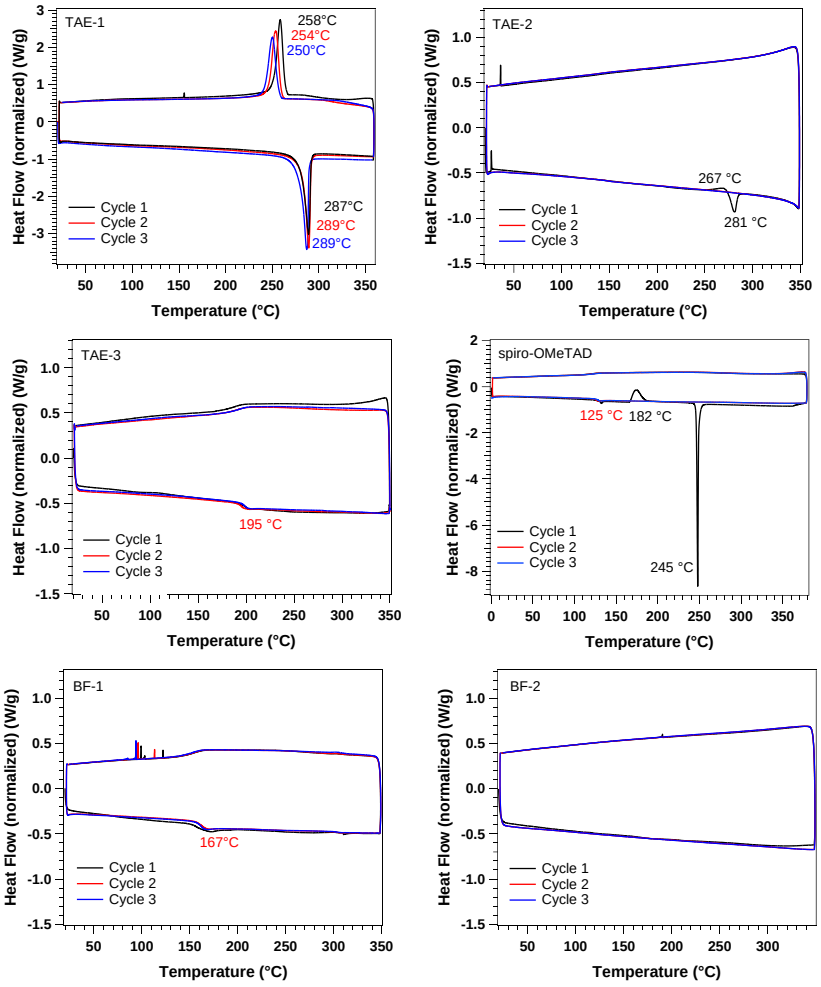

Figure 33. DSC experiment of **TAE-1**, **TAE-2**, **TAE-3**, spiro-OMeTAD, **BF-1** and **BF-2** (left to right, up to down) at scan rate of 20 ºC /min under N_2 atmosphere.

The DSC of **TAE-1** revealed sharp endothermic peaks corresponding to melting temperature (T_m) at 287 ºC and a crystallization peak at (T_c) 258 ºC. After consecutive heating/cooling cycles rather small changes in the T_m and T_c were observed, which further confirms the crystalline nature of this material. During the first heating scan, **TAE-2** presents a melting peak at 281 ºC whereas no crystallization was observed upon cooling nor in consecutive scans. **TAE-3** and **BF-1** show similar behaviour; after consecutive heating and cooling cycles only their glass transition (T_g), at 195 ºC and 165 ºC appears respectively, is observed,

which is indicative of their amorphous nature. On the contrary, **BF-2** does not show any thermal features. In comparison, the well-studied spiro-OMeTAD display both glass transition at 125 ºC and melting of the crystal at 245 ºC. Additionally, a crystallization process is detected at 182 ºC.

Table 9. Thermal properties of TAE- and BF-derivatives in comparison to spiro-OMeTAD.

HTM	T_{dec} (ºC)[a]	T_m (ºC)[b]	T_c (ºC)[c]	T_g (ºC)[d]
TAE-1	410	287	258	-
TAE-2	425	281	-	-
TAE-3	460	-	-	195
BF-1	360	-	-	167
BF-2	290	-	-	-
spiro-OMeTAD[e]	449	245	182	125

[a] Decomposition temperature determined from TGA (5 % weight loss). [b] Melting temperature and [c] crystal temperature determined from the first cycle. [d] Glass transition temperature determined from the second cycle. All experiments were performance under N_2 atmosphere. [e] Values reported[149]

From table 9 it can be confirmed that TAE-derivatives exhibit a T_{dec} in the same range of the most studied HTM in PV devices, spiro-OMeTAD. However, T_{dec} for BF-derivatives is noticeable lower.

On the other hand, **TAE-1** and **TAE-2** present higher T_m than spiro-OMeTAD (245 ºC). In addition, spiro-OMeTAD shows a T_g value lower (125 ºC) than those of **TAE-3** and **BF-1**. Taking into account the general device operating temperature (-40 to 60 ºC),[150] T_g is higher in all cases which is considered essential for the stability of hole-transporting layer and the final PV device.

149. T. Malinauskas, D. Tomkute-Luksiene, R. Sens, M. Daskeviciene, R. Send, H. Wonneberger, V. Jankauskas, I. Bruder, V. Getautis, "Enhancing thermal stability and lifetime of solid-state dye-sensitized solar cells via molecular engineering of the hole-transporting material spiro-OMeTAD", *ACS Appl. Mater. Interfaces*, **2015**, *7*, 11107-11116.
150. M. C. Alonso García, J. L. Balenzategui, "Estimation of photovoltaic module yearly temperature and performance based on nominal operation cell temperature calculations", *Renew. Energ.*, **2004**, *29*, 1997-2010.

b) Optical characterization

The optical properties of the new HTMs were inspected by means of UV-vis absorption and fluorescence. Figure 34 shows both spectra for each **TAE** and **BF** derivatives. The recorded absorption and emission wavelengths are collected in table 10.

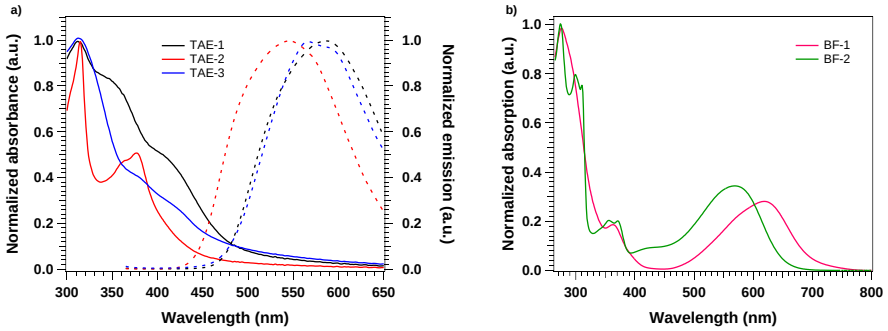

Figure 34. a) Normalized absorption spectra in THF (solid line) and emission spectra in THF:90 % water (dashed line) of **TAE-1** to **TAE-3**; **b**) absorption spectra in DCM of **BF-1** and **BF-2**. All samples were measured at r.t.

The absorption spectra in solution of the new TAE-derivatives confirm that none of them show significant absorption in the visible range (400-700 nm) which could be favourable for their application in perovskite-based devices. The UV-vis absorption spectra in solution of THF have been normalized with the relative maximum ($\lambda_{max,abs}$) centered at 314, 317 and 315 nm for **TAE-1**, **TAE-2** and **TAE-3**, respectively. **TAE-1** exhibits small shoulders at 360 and 420 nm. These peaks probably arise from the π-π^* electron transition of the large molecular conjugated system. On the other hand, **TAE-2** exhibits two more peaks of absorption at 365 and 380 nm, while **TAE-3** shows the maximum previously mentioned as well as two weak shoulders at around 380 nm and 430 nm. Owing to the characteristic behaviour of the TAE derivatives, 90 % of water was added in order to monitor their fluorescence. **TAE-1**, **TAE-2** and **TAE-3** exhibit a maximum centred at 543, 565 and 589 nm in THF-water (10:90 v/v), respectively. The fluorescence of **TAE-2** is blue-shifted in comparison with **TAE-1** and **TAE-3** that could be attributed to the different electron donor moieties used in each derivative. Furthermore, the emission spectra of **TAE-1**, **TAE-2** and **TAE-3** showed a large Stokes' shift that is typical for these kind of systems.

In sharp contrast, **BF-1** and **BF-2** in DCM exhibit a broad optical absorption in the visible region centered at 620 nm and 568 nm, respectively, which is attributed to an enhanced conjugation through bifluorenylidene double bond with better π-electron delocalization. Their optical band gaps ($E^{0\text{-}0}$) were determined from the onset of absorption to be 1.74 eV for **BF-1** and 1.85 eV for **BF-2**.

In the case of TAE-derivatives, the energy value of the optical gap ($E^{0\text{-}0}$) was estimated at the intersection of normalized absorption and emission spectra ($\lambda^{0\text{-}0}$), which is defined as the lowest energy transition. It has an approximate value of 2.58 eV ($\lambda^{0\text{-}0}$ = 481 nm), 2.80 eV ($\lambda^{0\text{-}0}$ = 443 nm) and 2.58 eV ($\lambda^{0\text{-}0}$ = 480 nm), for **TAE-1**, **TAE-2** and **TAE-3**, respectively. The values have been calculated following the equation 2:

$$E^{0\text{-}0}\ (eV) = h \cdot v = h \cdot \frac{C}{\lambda^{0\text{-}0}} = \frac{1240\ (nm \cdot eV)}{\lambda^{0\text{-}0}\ (nm)} \qquad (2)$$

Table 10. Optical parameters of TAE- and BF-derivatives in comparison to spiro-OMeTAD.

HTM	$\lambda_{max,\ abs}$ (nm)[a]	$\lambda_{max,\ em}$ (nm)[a]	$E^{0\text{-}0}$ (eV)
TAE-1	314	543	2.58[b]
TAE-2	317	565	2.80[b]
TAE-3	315	589	2.58[b]
BF-1	620	-	1.74[c]
BF-2	568	-	1.72[c]
spiro-OMeTAD	386	419	3.05

[a] λ_{max} of absorption and emission were measured in solution. [b] $E^{0\text{-}0}$ was determined at the intersection of normalized absorption and emission spectra and by using eq. 2. [c] Calculated from the absorption onset.

c) Cyclic voltammetry (CV) experiments and energy levels

To determine the HOMO and LUMO of the new HTMs, it is of paramount importance to ensure: i) efficient hole transport from the HTM to the perovskite and; ii) efficient electron transfer from the HTM to the TiO_2 through the perovskite layer and to block the electron from the perovskite. To this end, the

redox properties were determined by cyclic voltammetry as shown in figure 35. Table 11 summarizes the redox potentials of **TAE-1**, **TAE-2**, **TAE-3**, **BF-1** and **BF-2** and also the HOMO energies estimated from the first half-wave oxidation potential (first $E^{ox}_{1/2}$). The measurements were conducted in 0.1 M solution of (*n*-Bu)$_4$NPF$_6$ (TBAPF$_6$) in dry DCM under N_2 atmosphere. Glassy carbon was used as working electrode, platinum wire as reference electrode and platinum as counter electrode. In this particular case, ferrocene was added as internal standard and the potentials were determined with reference to the normal hydrogen electrode (NHE). Therefore, it is observed an oxidation wave at 0.7 V *vs.* NHE in all voltammograms which corresponds to Fc/Fc^+.

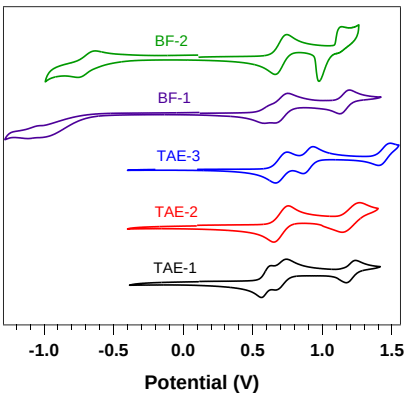

Figure 35. Cyclic voltammograms for TPA- and BF-derivatives (with Fc as internal reference) measured at r.t.

The electrochemical behaviour of both series are noticeably different. The TAE-derivatives are only active in the anodic scan revealing two reversible oxidation waves for **TAE-1** ($E^{ox}_{1/2}$: 0.59 V and 1.21 V) and **TAE-3** ($E^{ox}_{1/2}$: 0.89 V and 1.45 V) and one reversible oxidation wave for **TAE-2** ($E^{ox}_{1/2}$: 1.21 V) which correspond to the electron donor units and, the oxidation wave at higher potential, to the central core. The values for the first $E^{ox}_{1/2}$ differ depending on the electron donor strength. **TAE-1** exhibits the lowest oxidation potential at 0.59 V *vs.* NHE, followed by **TAE-3** (0.89 V) and **TAE-2** (1.21 V) which is the weakest electron donor. No reduction waves were observed in any case.

In contrast, BF-derivatives are active in both directions of the scan. On the oxidative scan, two oxidation processes were observed for **BF-1** ($E^{ox}_{1/2}$: 0.59 V and 1.6 V), which are tentatively assigned to a three-electron reversible oxidation

and one-electron oxidation of the *p*-diphenylamine. On the catodic scan, one irreversible reduction is detected at -1.07 V arising from the BF central core. The same observation was made for **BF-2**, with one irreversible oxidation wave at 1.08 V assigned to the carbazole fragment and one irreversible reduction at -0.64 V corresponding to the BF central core.

For small molecules, a direct relationship has been observed between $E^{ox}_{1/2}$ and the HOMO energy. Therefore, the HOMO energy level was estimated from the $E^{ox}_{1/2}$ values previously indicated.

Assuming that the formal potential of ferrocene is 0.7 *vs.* NHE the molecular orbital energies could be calculated directly from electrochemical results calibrated with ferrocene with a value of -4.4 eV as shown below.

$$E_{HOMO}\ (eV) = -\ (E^{ox}{}_{1/2\ vs.Fc+/Fc} + 4.4) \qquad (3)$$

where $E^{ox}_{1/2}$ is the first half-wave oxidation potential *vs.* NHE. The HOMO energy levels estimated from the oxidation potential of the cyclic voltammetry are -4.99 eV, -5.61 eV and -5.29 eV for **TAE-1**, **TAE-2** and **TAE-3** and -5.00 eV and -5.48 eV for **BF-1** and **BF-2**, respectively.

Finally, LUMO energy level were calculated according to the equation 4 for TAE-derivatives.

$$E_{LUMO}\ (eV) = E_{HOMO} + E^{0\text{-}0} \qquad (4)$$

where $E^{0\text{-}0}$ is the optical band gap which was determined at the intersection of normalized absorption and emission spectra (figure 34 and table 10).

However, the LUMO energy value for BF-derivatives were determined according to the equation 5.

$$E_{LUMO}\ (eV) = E^{red}_{1/2} + 4.4 \qquad (5)$$

Table 11. Oxidation potentials and HOMO-LUMO energy levels calculated for TAE- and BF-derivatives in comparison to spiro-OMeTAD.

HTM	$E^{ox}_{1/2}$ (V)[a]	HOMO (eV)[b]	LUMO (eV)
TAE-1	0.59	-4.99	-2.41[c]
TAE-2	1.21	-5.61	-2.81[c]
TAE-3	0.89	-5.29	-2.71[c]
BF-1	0.60	-5.00	-3.33[d]
BF-2	1.08	-5.48	-3.76 [d]
spiro-OMeTAD[e]	0.72	-5.16	-2.11

[a] First half-wave oxidation potential from CV measurements vs. NHE. [b] E_{HOMO} was estimated by using eq. 3. [c] E_{LUMO} was estimated by using eq. 4. [d] E_{LUMO} was estimated by using eq. 5. [e] For comparison purposes, CV experiment of the spiro-OMeTAD was measured under the same conditions.

TAE-1 and **BF-1** possess higher HOMO energy levels than that of spiro-OMeTAD. On the other hand, **TAE-2**, **TAE-3** and **BF-2** display a significantly lower HOMO. In all cases, matching to the valence band edge of the perovskite which not only block the electrons from the perovskite but also ensure cascade of electron transfer at the interface when HTMs are extracted. Therefore, fulfilling the necessary requirements of a good HTM.

2.3. Series of BTT-based HTMs

2.3.1. Central structure: Benzotrithiophene (BTT)

Thiophenes are one of the most important types of heterocyclic molecules, not only as structural units of compounds with interesting biological activities but also in the field of material chemistry.[151]

The electron-donating character of thiophene- and fused thiophene-based π-conjugated organic materials qualifies them as promising organic semiconductors. Considerable interest has been focused on their donor capacity in order to construct D-A copolymers, which has proven to be an effective strategy to adjust the properties of conjugated polymers for applications in OPV,[152] organic field-effect transistors (OFET)[153] and organic light-emitting diodes (OLEDs),[154] among others.

Benzotrithiophene molecules (BTTs) are often reported as examples of thiophene based π-conjugated organic materials. BTT structure consists in three thiophene rings fused to a central benzene ring. The planar and rigid π-framework can promote strong intermolecular interactions which makes them potential candidates for developing organic semiconducting materials.

This interesting heteroaromatic compound presents seven possible isomers regarding the position of the sulfur atoms (figure 36). The different arrangement of this heteroatom endows BTT-molecules with different structural, electrochemical and photophysical properties.

151. A. Mishra, P. Bäuerle, "Small molecule organic semiconductors on the move: Promises for future solar energy technology", *Angew. Chem. In. Ed.*, **2012**, *51*, 2020-2067.
152. H. Bronstein, Z. Chen, R. S. Ashraf, W. Zhang, J. Du, J. R. Durrant, P. Shakya Tuladhar, K. Song, S. E. Watkins, Y. Geerts, M. M. Wienk, R. a. J. Janssen, T. Anthopoulos, H. Sirringhaus, M. Heeney, I. Mcculloch, "Thieno[3,2-*b*]thiophene-diketopyrrolopyrrole-containing polymers for high-performance organic field-effect transistors and organic photovoltaic devices", *J. Am. Chem. Soc.*, **2011**, *133*, 3272-3275.
153. P. Liu, Y. Wu, H. Pan, Y. Li, S. Gardner, B. S. Ong, S. Zhu, "Novel high-performance liquid-crystalline organic semiconductors for thin-film transistors", *Chem. Mater.*, **2009**, *21*, 2727-2732.
154. J. H. Seo, E. B. Namdas, A. Gutacker, A. J. Heeger, G. C. Bazan, "Solution-processed organic light-emitting transistors incorporating conjugated polyelectrolytes", *Adv. Funct. Mater.*, **2011**, *21*, 3667-3672.

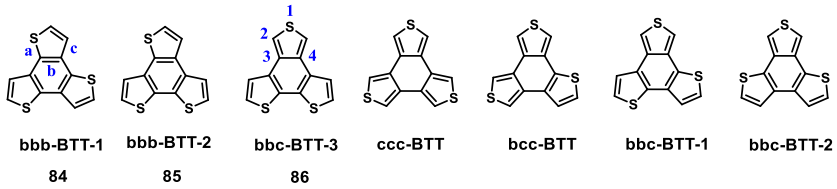

Figure 36. Molecular structures of BTT isomers cores.

According to IUPAC nomenclature for fused rings, the side of the heterocyclic ring is labelled by the letters a, b, c, etc., starting from the atom numbered 1. Therefore, side 'a' being between atoms 1 and 2, side 'b' between atoms 2 and 3, and so on. The appropriate name for each BTT-isomer is shown in figure 36. In the literature, oxidative photocyclization and intermolecular cyclic condensation are reported as synthetic routes for the preparation of bbb-BTT-1 (three *b*-fused thiophene rings),[155,156] bbb-BTT-2 (three *b*-fused thiophene rings)[157] and ccc-BTT (three *c*-fused thiophene rings).[158,159] However, there is hardly any report on other BTT isomers containing one or two *c*-fused thiophene rings (i.e., bcc-BTT, bbc-BTT-1, bbc-BTT-2 and bbc-BTT-3), probably owing to the tougher synthesis compared with the isomers containing three *b*- or *c*-fused thiophene rings previously mentioned.[160] Toward the purpose of this work, bbb-BTT-1, bbb-BTT-2 and bbc-BTT-3 were selected as the central scaffold for the new collection of HTMs for PSCs.

155. Y. Nicolas, P. Blanchard, E. Levillain, M. Allain, N. Mercier, J. Roncali, "Planarized star-shaped oligothiophenes with enhanced π-electron delocalization", *Org. Lett.*, **2004**, *6*, 273-276.
156. T. Taerum, O. Lukoyanova, R. G. Wylie, D. F. Perepichka, "Synthesis, polymerization, and unusual properties of new star-shaped thiophene oligomers", *Org. Lett.*, **2009**, *11*, 3230-3233.
157. T. Kashiki, S. Shinamura, M. Kohara, E. Miyazaki, K. Takimiya, M. Ikeda, H. Kuwabara, "One-pot synthesis of benzo[*b*]thiophenes and benzo[*b*]selenophenes from *o*-halo-substituted ethynylbenzenes: Convenient approach to mono-, bis-, and tris-chalcogenophene-annulated benzenes", *Org. Lett.*, **2009**, *11*, 2473-2475.
158. R. De Bettignies, Y. Nicolas, P. Blanchard, E. Levillain, J. M. Nunzi, J. Roncali, "Planarized star-shaped oligothiophenes as a new class of organic semiconductors for heterojunction solar cells", *Adv. Mater.*, **2003**, *15*, 1939-1943.
159. R. Proetzsch, D. Bieniek, F. Korte, "Hochdruckreaktionen IV: Verhalten von thiolactonen unter hohen drucken", *Tetrahedron Lett.*, **1972**, *13*, 543-544.
160. X. Guo, S. Wang, V. Enkelmann, M. Baumgarten, K. Müllen, "Making benzotrithiophene a stronger electron donor", *Org. Lett.*, **2011**, *13*, 6062-6065.

The first synthesis of compound **84** dates back to the early work of Proetzsch *et al.*, in 1972[159] and Jayasuriya *et. al.*, in 1989.[161] However, the tediousness of the synthesis hindered its wide use. Thanks to the more recently established straightforward procedure for the synthesis of molecule **84** reported by Kuwabara and co-workers,[157] it is now available in multigram scale in the laboratory. Benzo[1,2-*b*:3,4-*b′*:5,6-*b″*]trithiophene (**84**) is a potential π-core for a new class of organic semiconductors for the following reasons: i) its planar and rigid π-framework can promote strong intermolecular interaction that would be suitable for developing organic semiconducting materials; ii) a rare structure having three identical thiophene moieties with C_{3h} symmetry that enables 2D molecular extension and even more dendritic 3D extension with star-shaped structures, provided that multiple BTT oligomerization is possible. In the state-of-the-art, bbb-BTT (**84**) has been considerably studied, being used as a core for the construction of star-shaped oligomers, polymers and dendrimers.[155, 156, 162] Moreover, small molecules based on compound **84**, have been studied as components in efficient OPV devices.[163]

In this thesis, bbb-BTT (**84**) is employed as central moiety for new series of star-shaped molecules. Its preparation was carried out by stepwise synthesis following the Kuwabara protocol,[157] as it is summarized in scheme 9.

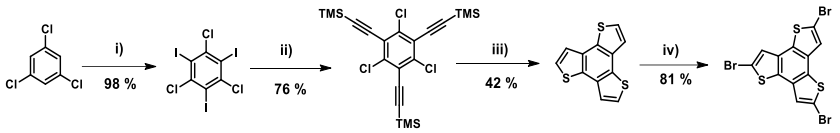

Scheme 9. *Reagents and conditions*: **i**) I_2, H_5IO_6, sulfuric acid, r.t.; **ii**) TMSA, $Pd(PPh_3)_4$, CuI, DIPA, THF, 66 ºC; **iii**) $Na_2S{\cdot}9H_2O$, NMP, 188 ºC; **iv**) NBS, 2:1 chloroform/acetic acid, 60 ºC.

161. N. Jayasuriya, J. Kagan, J. E. Owens, E. P. Kornak, D. M. Perrine, "Photocyclization of terthiophenes", *J. Org. Chem.*, **1989**, *54*, 4203-4205.
162. T. Kashiki, M. Kohara, I. Osaka, E. Miyazaki, K. Takimiya, "Synthesis and characterization of benzo[1,2-*b*:3,4-*b′*:5,6-*b″*]trithiophene (BTT) oligomers", *J. Org. Chem.*, **2011**, *76*, 4061-4070.
163. L. Meng, F. Wu, H. Liu, B. Zhao, J. Zhang, J. Zhong, Y. Pei, H. Chen, S. Tan, "Novel solution-processible small molecules based on benzo[1,2-*b*:3,4-*b′*:5,6-*b″*]trithiophene for effective organic photovoltaics with high open-circuit voltage", *RSC Adv.*, **2015**, *5*, 14540-14546.

Commercially available 1,3,5-trichlorobenzene was subjected to a three-fold iodination reaction to obtain derivative **87**, in excellent yield. Three-fold Sonogashira reaction of the latter with ethynyltrimethylsilane using $Pd(PPh_3)_4$/CuI as catalytic system, led to compound **88** in 76 % yield. Three *b*-fused thiophene rings, **84**, was obtained by a facile thiophene annulation reaction promoted at reflux of NMP in the presence of $Na_2S{\cdot}9H_2O$, an efficient source of sulfur atoms for aromatic nucleophilic substitution (S_NAr) reaction.[164] Finally, bromination at the α position of derivative **84** affords the desired tribromo derivative (**89**).

On the other hand, bbb-BTT (**85**) will be used as central moiety as well. Benzo[1,2-*b*:3,4-*b'*:6,5-*b''*]trithiophene (**85**) was firstly synthesized in 1989[161] and its derivatives have been reported in a wide number of applications in the literature. This asymmetric three *b*-fused thiophene rings, has been studied in OFET,[165,166] as planar electron-rich building block in organic semiconductors[167] and also for PV applications.[168,169]

A straightforward two-step synthetic route was carried out in order to obtain compound **85** in good overall yield, including an intermolecular cyclic

164. M. Nakano, K. Takimiya, "Sodium sulfide-promoted thiophene-annulations: Powerful tools for elaborating organic semiconducting materials", *Chem. Mater.*, **2017**, *29*, 256-264.
165. C. B. Nielsen, E.-H. Sohn, D. J. Cho, B. C. Schroeder, J. Smith, M. Lee, T. D. Anthopoulos, K. Song, I. Mcculloch, "Improved field-effect transistor performance of a benzotrithiophene polymer through ketal cleavage in the solid state", *ACS Appl. Mater. Interfaces*, **2013**, *5*, 1806-1810.
166. G. Zhang, M. Zhu, J. Guo, J. Ma, X. Wang, H. Lu, L. Qiu, "Benzodithiophene and benzotrithiophene-based conjugated polymers for organic thin-film transistors application: Impact of conjugated- and acyl-side chain", *Org. Electron.*, **2014**, *15*, 2608-2615.
167. C. B. Nielsen, J. M. Fraser, B. C. Schroeder, J. Du, A. J. P. White, W. Zhang, I. Mcculloch, "Benzotrithiophene - a planar, electron-rich building block for organic semiconductors", *Org. Lett.*, **2011**, *13*, 2414-2417.
168. M. L. Keshtov, Y. Geng, S. A. Kuklin, A. R. Khokhlov, E. N. Koukaras, G. D. Sharma, "Synthesis, optical and electrochemical properties new donor–acceptor (D-A) copolymers based on benzo[1,2-*b*:3,4-*b'*:6,5-*b''*] trithiophene donor and different acceptor units: Application as donor for photovoltaic devices", *Org. Electron.*, **2015**, *17*, 167-177.
169. C. B. Nielsen, R. S. Ashraf, S. Rossbauer, T. Anthopoulos, I. Mcculloch, "Post-polymerization ketalization for improved organic photovoltaic materials", *Macromolecules*, **2013**, *46*, 7727-7732.

condensation and the subsequent bromination reaction. The first step of the synthesis (scheme 10) involves two-fold Stille Pd-catalyzed reaction between commercially available 2,3-dibromothiophene and 2-(tributylstannyl)thiophene, followed by an oxidative photocyclization after irradiation in the range of 320-400 nm. Finally, regioselective bromination at the α-position of BTT **85** employing NBS gave rise to the desired tribromo derivative, **91**.

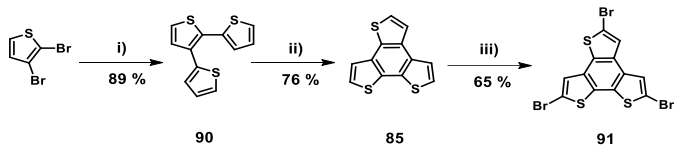

Scheme 10. *Reagents and conditions:* **i**) 2-(tributylstannyl)thiophene, $Pd(PPh_3)_2Cl_2$, DMF, 130 ºC; **ii**) I_2, toluene, *hv*; **iii**) NBS, 2:1 CH_3Cl/AcOH, 70 ºC.

Finally, with an eye toward carrying out a complete and systematic strategy, bbc-BTT (**86**) as central moiety of the novel candidates as HTMs is also used. Benzo[1,2-*b*:6,5-*b'*:3,4-*c''*]trithiophene (**86**) is a fully planar and extended aromatic system which should facilitate the formation of highly ordered 1D structures via a self-organization process,[170] which is particularly important for OFET application among others. Additionally, this BTT-isomer possesses a higher HOMO level than all other isomers according to DFT calculations,[160] which provides a theoretical support as an electron-richer unit. In addition, compound **86** exhibits C_{2v} symmetry and it has four active positions, which allows further functionalization to extend the molecular system.

As previously mentioned bbb-BTT (**85**) derivatives are accessible by oxidative photocyclization or intermolecular cyclic condensation. However, this method could not be applied to bbc-BTT (**86**) as described by Perrine and co-workers in 1989.[161] Therefore, the approach that is presented below is up to now the only feasible way to synthesize it.[160] Tetrabrominated-compound **93** was obtained in three synthetic steps in a moderate yield as it is shown in scheme 11. 3,3´-Dibromo-2,2´-bithiophene was subjected to a two-fold Sonogashira reaction with ethynyltrimethylsilane (TMSA) and Pd/Cu as catalytic system. The third thiophene ring was formed by treating the intermediate **92** with the Wilkinson

170. X. Guo, S. R. Puniredd, M. Baumgarten, W. Pisula, K. Müllen, "Benzotrithiophene-based donor–acceptor copolymers with distinct supramolecular organizations", *J. Am. Chem. Soc.*, **2012**, *134*, 8404-8407.

catalyst $Rh(PPh_3)_3Cl$ in refluxing benzene, followed by the addition of sulfur powder. Trimethylsilyl (TMS) groups of the thus-obtained intermediate **86** were partially removed during the purification through silica-gel column chromatography. Finally, subsequent treatment of the one *c*-fused thiophene ring, **86**, with NBS in a mixture of acetic acid and chloroform provided the tetrabrominated derivative, **93**.

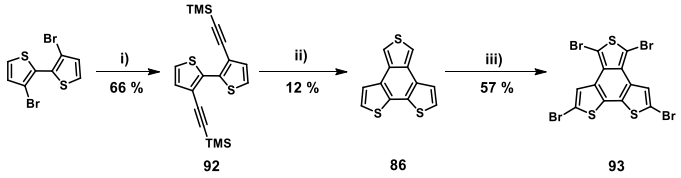

Scheme 11. *Reagents and conditions*: **i**) TMSA, $Pd(PPh_3)_2Cl_2$, CuI, DIPA, 80 ºC; **ii**) S_8, $Rh(PPh_3)_3Cl$, benzene, 80 ºC, N_2; **iii**) NBS, 2:1 $CHCl_3$/AcOH, 70 ºC.

The formation of the bromo-derivatives **89**, **91** and **93** was confirmed mainly by mass spectrometry due to their low solubility, which made difficult their identification by other spectroscopy techniques. Mass spectrometry further confirm the presence of each of them showing the typical isotopic distribution. Although the brominated intermediates **89**, **91** and **93** are essentially insoluble, further reaction with electron donor units successfully furnished the target molecules.

2.3.2. Design and synthesis of new BTT-based HTMs

The aforementioned planar and sulfur-rich polycyclic aromatic hydrocarbons (**84**, **85** and **86**) were covalently linked to different electron donor units through a facile synthetic route by crosslinking triphenylamine-based electron donor groups (compounds **68**, **69** and **71**) with the respective brominated compounds (**89**, **91** and **93**) (figure 37, scheme 12 and 13).

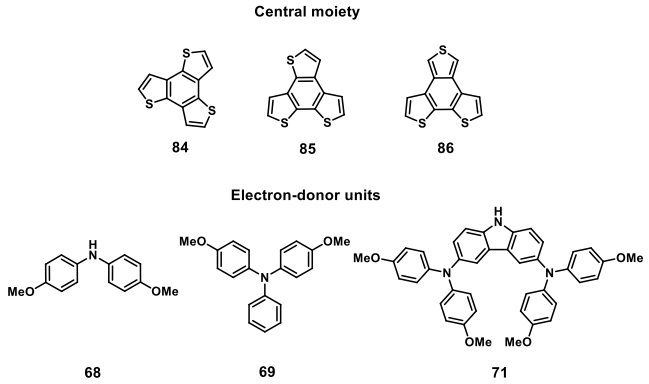

Figure 37. Molecular structure of the central moieties and electron donor units.

Firstly, the final molecules **BTT-1**, **BTT-2** and **BTT-3** are presented. They constitute a new ease to prepare family of HTMs based on compound **84** endowed with *p*-methoxydiphenylamine (**68**), *p*-methoxydiphenylamine-substituted carbazole (**71**) and *p*-methoxytriphenylamine (**69**) as electron donor units. The synthetic route for preparing the new sulfur-rich HTMs was conducted by stepwise synthesis as it follows in scheme 12.

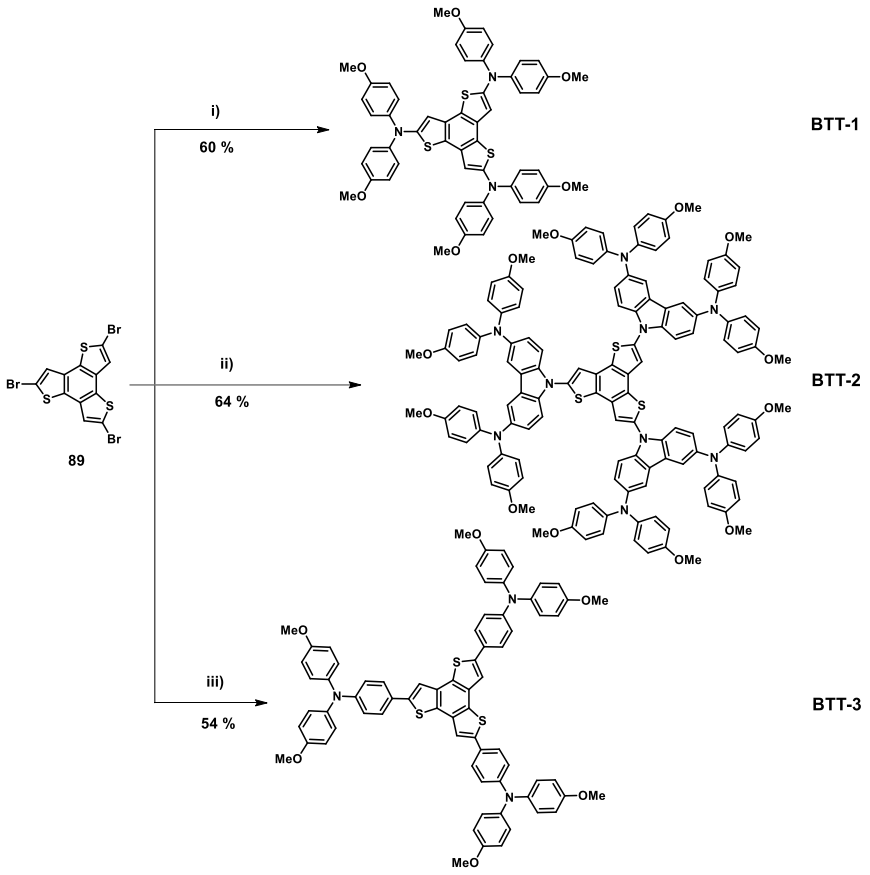

Scheme 12. *Reagents and conditions*: **i)** **68**, **ii)** **71**, $Pd_2(dba)_3$, XPhos, Na^tBuO, toluene, 100 ºC; **iii)** **73**, $Pd(PPh_3)_4$, K_3PO_4, DMF, 80 ºC.

The tribromo derivative **89**, synthesized according to scheme 9, was subjected to a three-fold Buchwald-Hartwig reaction with *p*-methoxydiphenylamine (**68**) and *p*-methoxydiphenylamine-substituted carbazole (**71**) to afford the desired compounds **BTT-1** and **BTT-2**, respectively. On the other hand, three-fold Suzuki cross-coupling reaction between derivative **89** and *p*-methoxytriphenylamine (**69**) leads to the formation of **BTT-3** (scheme 12).

The crystal structure of three-arms star-shaped **BTT-3** was unambiguously confirmed by XRD. The structural drawings can be found in figure 38 (solvent molecules have been omitted for clarity) and the crystallographic parameters are listed in table 12.

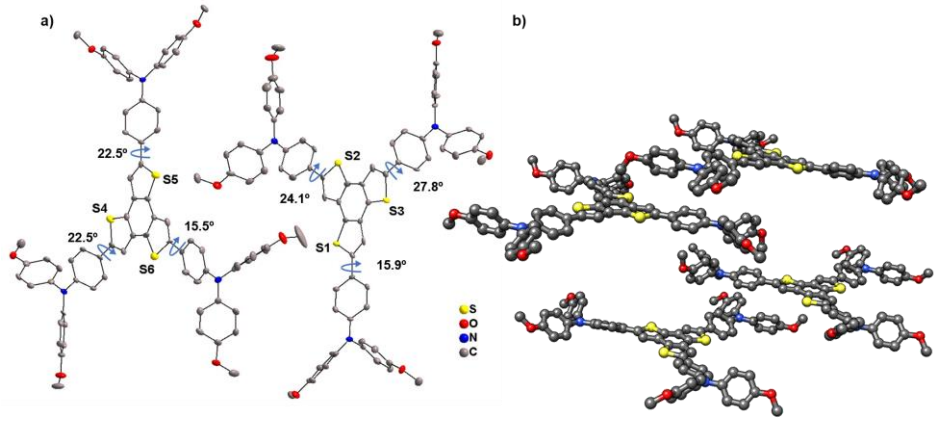

Figure 38. a) Asymmetric unit of **BTT-3** including relevant torsion angles. **b**) Packing of two **BTT-3** molecules.

Table 12. Summary of crystallographic parameters for **BTT-3** asymmetric unit.

Crystallographic parameters of BTT-3			
Formula	$C_{179}H_{154}N_6O_{12}S_6$	**Min/max *h k l***	$-13 \le h \le 13$ $-21 \le k \le 21$ $-22 \le l \le 22$
Crystal system	Triclinic	**Reflections, measured**	60935
Space group	*P*-1	**Reflections, independent**	12477
Temperature (K)	120 (2)	**Absorption coefficient (mm^{-1})**	0.162
Lattice constants (Å/º)	a=14.3218 (9) b=22.8206 (14) c=24.0118 (14)	α=106.3934 (16) β=93.7133 (17) γ=140.1851 (16)	**Absorption correction** Multi-Scan
Volume ($Å^3$)	7223.1 (13)	**Crystal habit**	Block
Z	2	**Refined parameters**	1989
$D_{calculated}$ (g/cm^3)	1.27	**R1 [I > 2 σ (I)]**	0.0603
Radiation	Mo-Kα (λ=0.71069 Å)	**wR2**	0.1594
θ Range (º)	2.28-19.51	**Density (e^-/ $Å^3$)**	1.005 and -0.627

Single crystals were obtained by cooling down a supersaturated solution of **BTT-3** in toluene from 100 ºC to r.t. The data collection was performed at 120 K. **BTT-3** crystallizes in the triclinic space group *P*-1 with two formula units in the asymmetric unit. The HTM molecule is packed with the central cores parallel to each other and disordered toluene molecule fill up the empty space in between. The intermolecular distance is around 13.5 Å.

BTT-1, **BTT-2** and **BTT-3** were prepared by employing different electron donor groups. Subsequently, different arrangements of sulfur atoms in the central moiety will be addressed as chemical approach for designing new HTMs.

The new candidates, namely **BTT-4** and **BTT-5**, possess *p*-methoxy triphenylamine (**69**) as electron donor moiety linked to the central cores (**85** and **86**) which differ in the arrangement of the sulfur atoms. The synthetic route for preparing these two new candidates as HTMs was conducted in one-pot syntheses as it is illustrated in scheme 13. Three- and four-fold Suzuki coupling reaction with *p*-methoxytriphenylamine (**69**) successfully furnished the targets **BTT-4** and **BTT-5** in 72 % and 61 % yield, respectively.

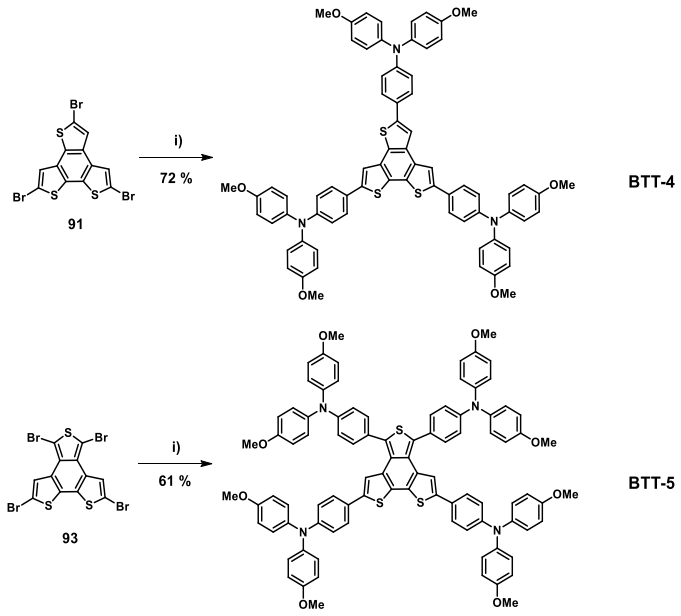

Scheme 13. *Reagents and conditions*: **i) 73**, $Pd(PPh_3)_4$, K_3PO_4, DMF, 100 ºC.

The formation of the aforementioned HTMs was confirmed by ^{1}H and ^{13}C NMR, FTIR, and HRMS [MALDI-TOF] techniques. Mass spectrometry HRMS [MALDI-TOF] confirmed the presence of **BTT-1**, **BTT-2**, **BTT-3**, with a molecular ion peak $[M]^{+}$ at 927.2446 m/z (calcd. 927.2465 m/z), 2103.7085 m/z (calcd. 2103.7039 m/z), 1155.3374 m/z (calcd. 1155.3404 m/z), respectively and **BTT-4** and **BTT-5** with a molecular ion peak $[M]^{+}$ at 1155.3362 m/z (calcd. 1155.3404 m/z) and 1458.4706 m/z (calcd. 1458.4663 m/z), respectively.

In the case of the three-armed **BTT-1**, **BTT-2**, **BTT-3** and the four-armed **BTT-5**, the ^{1}H NMR spectra reveal the symmetry of the molecular structure, which exhibits only one singlet ($\delta \approx 6.53$, 7.99, 7.82 and 7.38, respectively) for the β protons of thiophene rings. In contrast, **BTT-4** is less symmetric and shows three different singlets for the β protons at $\delta \approx 8.04$, 8.03 and 7.78. It is also observed the characteristic signals of the donor units in each case and the protons corresponding to the terminal methoxyl groups. As a representative example, ^{1}H NMR spectrum of **BTT-5** is shown in figure 39.

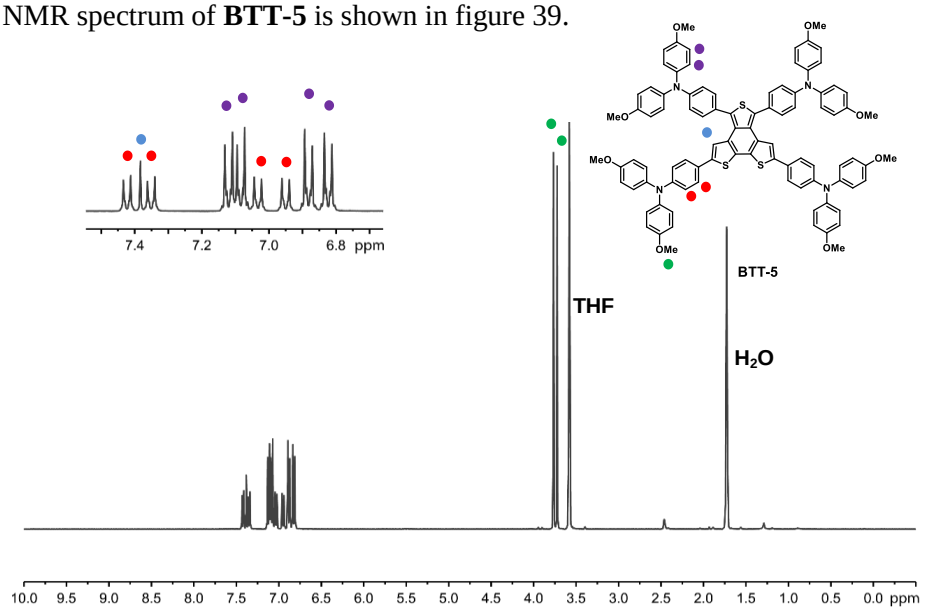

Figure 39. ^{1}H NMR spectrum (400 MHz, THF-d_8, 298K) of **BTT-5**.

2.3.3. Thermal, optical and electrochemical properties

a) Thermogravimetric analysis (TGA) and differential scanning calorimetry (DSC)

To unveil the thermal properties of the novel family of BTT-derivatives, TGA and DSC measurements were performed. Detailed thermal features are collected in table 13.

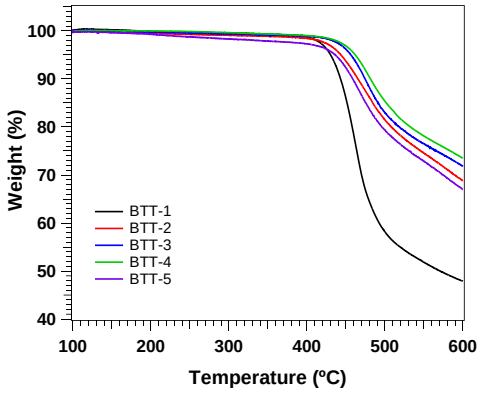

Figure 40. Thermogravimetric analysis of **BTT-1**, **BTT-2**, **BTT-3**, **BTT-4** and **BTT-5** at scan rate of 10 ºC/min under N_2 atmosphere.

The new molecules show good thermal stability, starting to slowly decompose at temperatures higher than 400 ºC (figure 40). Surprisingly, **BTT-1** presents a noticeable loss of weight exceeding 430 ºC. The decomposition temperature (5 % weight loss under N_2 atmosphere) are: **BTT-1**: 436 ºC, **BTT-2**: 449 ºC, **BTT-3**: 456 ºC, **BTT-4**: 460 ºC and **BTT-5**: 430 ºC.

Figure 41 illustrates the differential scanning calorimetry curves, which shed light on the thermal behaviour of each molecule.

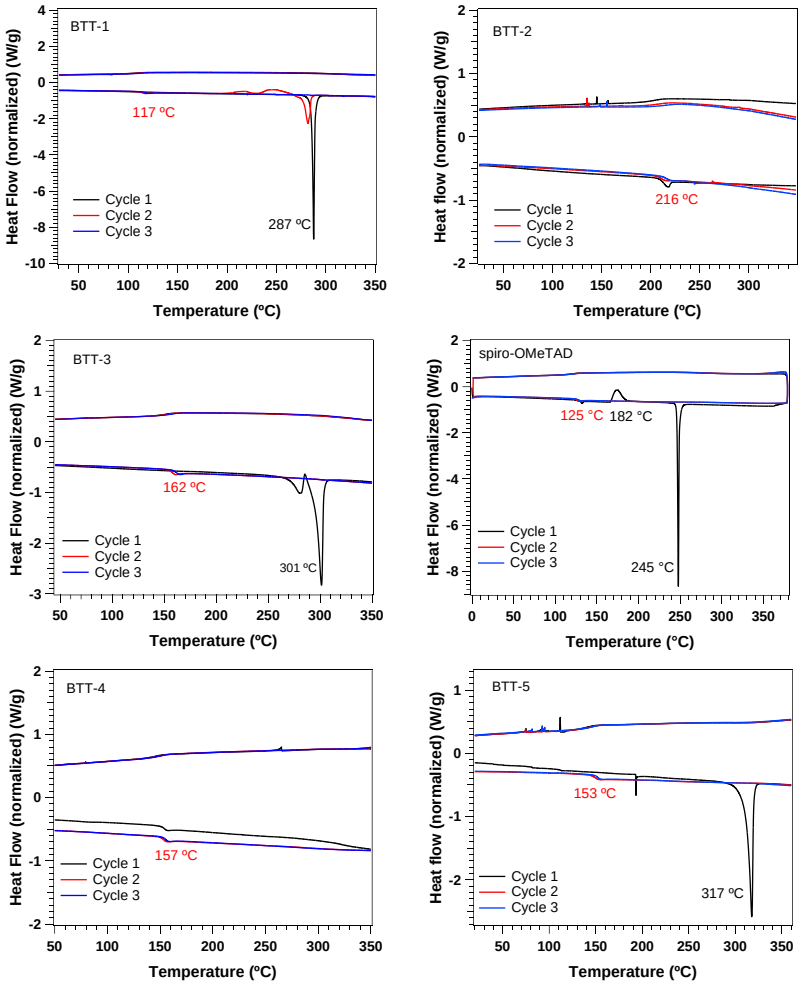

Figure 41. DSC experiments of BTT-derivatives and spiro-OMeTAD at scan rate of 20 ºC/min under nitrogen atmosphere.

BTT-1, **BTT-3** and **BTT-5** exhibit essentially the same thermal behaviour in DSC. During the first heating scan their melting point were detected as a sharp endothermic peak at 287 ºC, 301 ºC and 317 ºC, respectively, which are not observed after consecutive heating/cooling cycles. However, a small amount of **BTT-1** melts during the second heating cycle. On the successive heating cycles, a T_g of 117 ºC, 162 ºC and 153 ºC, respectively appeared, which indicate their crystalline and amorphous nature. Likewise, spiro-OMeTAD exhibits a comparable behaviour, with a melting temperature detected at 245 ºC during the

first scan. After consecutives steps, only glass transition was observed at 125 ºC. On the contrary, **BTT-2** and **BTT-4** are essentially amorphous showing a glass transition temperature of 216 ºC and 157 ºC, respectively, which implies a reduced tendency to crystallize.

Table 13. Thermal properties of BTT-derivatives in comparison to spiro-OMeTAD.

HTM	T_{dec} (ºC)[a]	T_m (ºC)[b]	T_c (ºC)[c]	T_g (ºC)[d]
BTT-1	436	287	-	117
BTT-2	449	-	-	216
BTT-3	456	301	-	162
BTT-4	460	-	-	157
BTT-5	430	317	-	153
spiro-OMeTAD[e]	449	245	182	125

[a] Decomposition temperature determined from TGA (5 % weight loss). [b] Melting temperature and [c] crystal temperature determined from the first cycle. [d] Glass transition temperature determined from the second cycle. All experiments were performance under N_2 atmosphere. [e] Values reported.[149]

All compounds exhibit a similar thermal behaviour. Decomposition temperatures are in the same range, being **BTT-2**, **BTT-3** and **BTT-4** equally stable to spiro-OMeTAD. Additionally, all HTMs exhibit higher T_g than spiro-OMeTAD, except **BTT-1**.

b) Optical characterization

UV-vis absorption and fluorescence experiments were carried out in order to know the optical properties of the new compounds. Figure 42 shows the normalized absorption and emission curves of **BTT-1** to **BTT-3** (42a) and **BTT-3** to **BTT-5** (42b). The recorded absorption and emission wavelengths are collected in table 14.

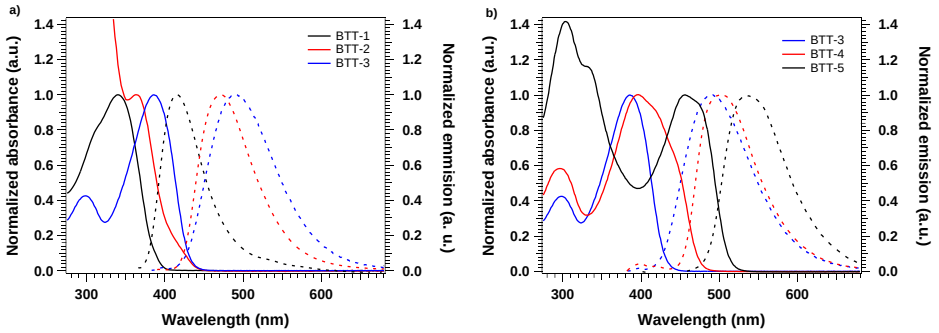

Figure 42. Normalized absorption (solid line) and emission (dashed line) spectra of **a**) **BTT-1** to **BTT-3** and **b**) **BTT-3** to **BTT-5** in DCM at r.t.

In solution, the absorption for **BTT-1**, **BTT-2** and **BTT-3** is very limited in the visible range, the absorption maxima ($\lambda_{max,abs}$) were centered at 340 nm ($\varepsilon = 10 \cdot 10^4$ $M^{-1} \cdot cm^{-1}$), 363 nm ($\varepsilon = 18 \cdot 10^4$ $M^{-1} \cdot cm^{-1}$) and 387 nm ($\varepsilon = 14 \cdot 10^4$ $M^{-1} \cdot cm^{-1}$), respectively (figure 42a). Relevantly, by changing the arrangement of the sulfur atoms in the case of **BTT-4** and **BTT-5**, resulted in a wider absorbance in the visible range, with maxima centered at 397 nm ($\varepsilon = 11 \cdot 10^4$ $M^{-1} \cdot cm^{-1}$) and 459 nm ($\varepsilon = 9 \cdot 10^4$ $M^{-1} \cdot cm^{-1}$), respectively (figure 42b).

The absorption band is progressively red-shifted from **BTT-1** to **BTT-3**. On the other hand, the absorption of **BTT-5** is significantly red-shifted in comparison to the other two three-armed compounds (**BTT-3** and **BTT-4**) due to the enhanced π-electron delocalization. An intense absorption band below 350 nm is also registered for **BTT-5**. The broad absorption presented by **BTT-4** implies the contribution of weaker absorption peaks derived from the direct conjugation between the two *cis* thiophene rings, in contrast to the *meta* arrangement with the central benzene ring in **BTT-3**. The emission spectra possess a maximum centered at 413 nm, 470 nm, 489 nm, 502 nm and 536 nm for **BTT-1** to **BTT-5**, respectively.

The optical band gap corresponding to E^{0-0} value, was estimated at the intersection of normalized absorption and emission spectra for each molecule. In this way, the more red-shifted is the absorption spectrum, the lower the value of the optical bang gap of the molecule.

Table 14. Optical parameters of BTT-derivatives in comparison to spiro-OMeTAD.

HTM	$\lambda_{max,\ abs}$ (nm)[a]	$\lambda_{max,\ em}$ (nm)[a]	E^{0-0} (eV) [b]
BTT-1	340	413	3.22
BTT-2	363	470	2.92
BTT-3	387	489	2.89
BTT-4	397	502	2.67
BTT-5	459	536	2.48
spiro-OMeTAD	386	419	3.05

[a] λ_{max} of absorption and emission were measured in DCM solution. [b] E^{0-0} was determined at the intersection of normalized absorption and emission spectra and by using eq. 2.

c) Cyclic voltammetry (CV) experiments and energy levels

To determine the HOMO and LUMO levels of the new HTMs, which is important to estimate the future behaviour in the PV device, the electrochemical properties of the BTT-derivatives were studied by cyclic voltammetry. The redox potentials are summarized in table 15 along with the HOMO values estimated from the first half-wave oxidation potential ($E^{ox}_{1/2}$) and the LUMO energies. Redox properties were determined by cyclic voltammograms (figure 43) in 0.1 M solution of (n-Bu)$_4$NPF$_6$ (TBAPF$_6$) in dry DCM solutions under N_2 atmosphere. The measurements were conducted at a scan rate of 100 mV/s using glassy carbon as working electrode and platinum wire as reference and counter electrode. Fc/Fc$^+$ was used as internal standard although its oxidation wave has been omitted for clarity.

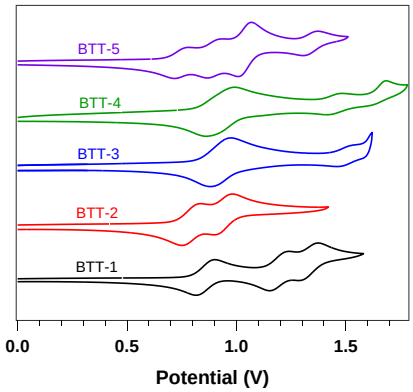

Figure 43. Cyclic voltammograms of **BTT-1** to **BTT-5** in DCM at r.t.

As shown in figure 43, the electrochemical properties of the new derivatives are not only affected by the different electron donor, but also by the chemical structure of the isomeric BTT core. The cyclic voltammogram of **BTT-1** shows three oxidation waves with $E^{ox}_{1/2}$ value of 0.80 V, 1.27 and 1.30 V vs. NHE. These oxidation waves are assigned to the consecutive electron extraction, mainly, from the diphenylamines. **BTT-2** exhibits only two oxidation waves (0.74 V and 0.89 V) attributed to the oxidation process of the diphenylamines and the carbazole units. On the other hand, **BTT-3** shows two oxidation waves ($E^{ox}_{1/2}$: 0.93 V and 1.50 V vs. NHE). The first oxidation wave is assigned to a simultaneous three-oxidation process where the three electrons are extracted from the triphenylamine units and the second one to the central core. **BTT-4** is slightly better donor than **BTT-3** and exhibits three reversible oxidation waves. The first $E^{ox}_{1/2}$ at 0.89 V, corresponds to two overlapping oxidation processes, which imply the consecutive extraction of two-electron of the *p*-methoxy triphenylamine units, and one-electron extraction the second $E^{ox}_{1/2}$ at 1.45 V. In addition, the $E^{ox}_{1/2}$ at 1.45 V is assigned to the central core. Finally, the cyclic voltammogram of **BTT-5**, reveals four oxidation waves with $E^{ox}_{1/2}$ values of 0.74 V, 0.89 V, 1.03 V and 1.33 V corresponding to one-, one-, two- and one-electron processes, respectively. The first oxidation wave is assigned to an electron extraction mostly involving the BTT core and two of the triphenylamine-based arms, according to the computed HOMO (see section 2.3.4). The second and third oxidation waves involved the extraction of three additional electrons, mainly from the triphenylamine groups.

Therefore, the electron donor ability recorded from the first oxidation potential is **BTT-5** > **BTT-2** > **BTT-1** > **BTT-4** > **BTT-3**. The HOMO energies experimentally estimated from $E^{ox}_{1/2}$ are found to be -5.20 eV, -5.16 eV, -5.37 eV, -5.33 eV and -5.18 eV for **BTT-1**, **BTT-2**, **BTT-3**, **BTT-4** and **BTT-5**, respectively. The energy inferred for the HOMO level of **BTT-1**, **BTT-2** and **BTT-5** are indeed similar to that obtained for the reference spiro-OMeTAD (-5.16 eV). Therefore, the novel sulfur-rich HTMs of this section feature an excellent alignment with the valence edge of the perovskite (ca. -5.4 eV).

Table 15. Oxidation potentials and HOMO-LUMO energy levels calculated for BTT-derivatives in comparison to spiro-OMeTAD.

HTM	$E^{ox}_{1/2}$ (V)[a]	HOMO (eV) [b]	LUMO (eV) [c]
BTT-1	0.80	-5.20	-1.98
BTT-2	0.74	-5.16	-2.28
BTT-3	0.93	-5.37	-2.48
BTT-4	0.89	-5.33	-2.66
BTT-5	0.74	-5.18	-2.70
spiro-OMeTAD[d]	0.72	-5.16	-2.11

[a] First half-wave oxidation potential from CV measurements vs. NHE. [b] E_{HOMO} estimated by using eq. 3. [c] E_{LUMO} estimated by using eq. 4. [d] For comparison purposes, the CV of the spiro-OMeTAD was measured under the same conditions.

The different arrangements of sulfur atoms could endow the final molecules not only with different chemical structure, electrochemical and photophysical properties but also with different behaviour in PV performances. Considering these points, there are several alternative chemical approaches for designing high-efficient HTMs. In the previous section, **BTT-1** to **BTT-3** were prepared employing different electron donor groups, and **BTT-4** and **BTT-5** different arrangement of the sulfur atoms. As an alternative strategy for designing new functional materials for PSCs, new heteroatoms will be included in the central moiety in next section.

2.3.4. Structural and electronic properties

To gain more insight into the effects that the isomerism of the BTT core has on the structural and electronic properties of the BTT derivatives, DFT calculations were performed at the B3LYP/6-31G** level in the presence of solvent (DCM) for the **BTT-3**, **BTT-4** and **BTT-5** compounds, in collaboration with Prof. Enrique Ortí (University of Valencia). The central moieties **84**, **85** and **86**, the pendant *p*-methoxytriphenylamine (OMeTPA) group (**71**), as well as the reference spiro-OMeTAD compound, were calculated for comparison purposes (figure 44).

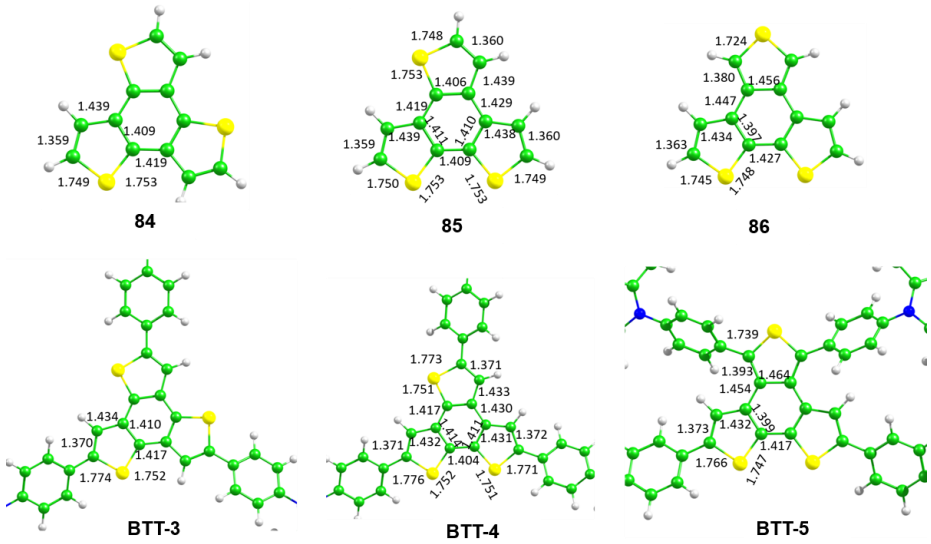

Figure 44. Optimized bond lengths (in Å) calculated at the B3LYP/6-31G** level, in DCM solution, for the isomeric BTT-cores (**84**, **85** and **86)** and the HTMs (**BTT-3**, **BTT-4** and **BTT-5**). For the latter, the terminal OMeTPA pendant groups have been partially omitted and only the bond lengths for the cores are shown. Symmetry constraints were used for **84** (C_{3h}), **BTT-3** (C_3), **85** (C_s), **86** (C_{2v}) and **BTT-5** (C_2).

The C_{3h}-symmetric core **84** shows similar carbon-carbon (C-C) distances of 1.408 and 1.418 Å for the central benzene indicating the aromatic character of this ring. In contrast, the central benzene ring of the C_{2v}-symmetric core **86** presents quite different bond lengths (from 1.397 to 1.454 Å) showing that the aromatic character is lost. Compound **86** actually exhibits a single/double CC bond pattern characteristic of a *cis*-bithiophene where an extra thiophene ring is linked to the central *β* positions. The formation of a bithiophene-type structure

favors an efficient π-conjugation path. The core **85** can be considered as an intermediate case where the aromatic character of the central benzene ring is still maintained although it presents larger differences between the C=C bond lengths compared to compound **84**. The structural features discussed for the BTT cores are preserved in the extended **BTT-3**, **BTT-4** and **BTT-5** derivatives, the main difference being the lengthening of the peripheral CC and carbon-sulfur bonds to which the OMeTPA groups are attached. Despite the bulky OMeTPA groups, **BTT-3** and **BTT-4** exhibit quite planar structures that, in principle, can favor stacking aggregation in the solid state. In contrast, **BTT-5** presents a more crowded structure due to the presence of four OMeTPA arms.

Figure 45 displays the frontier molecular orbitals calculated for the OMeTPA pendant groups, the BTT cores, the BTT-based HTMs and spiro-OMeTAD.

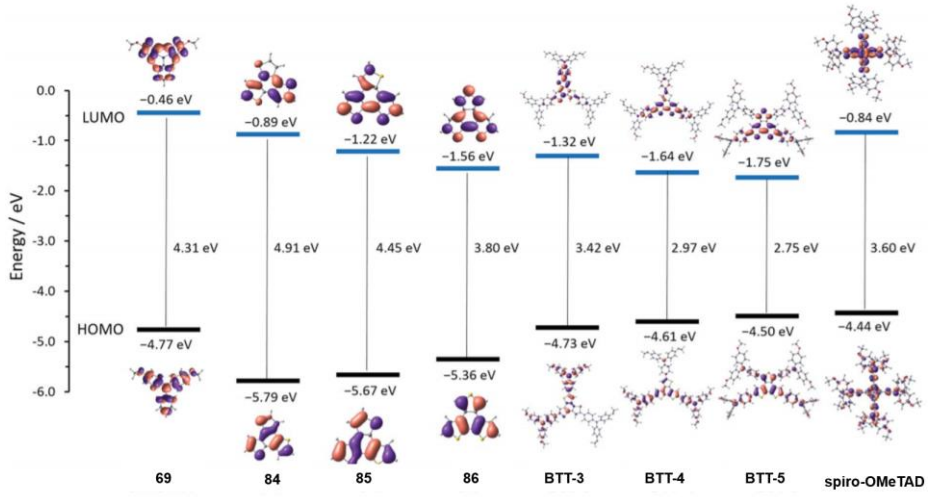

Figure 45. Energy diagram showing the frontier molecular orbitals computed for OMeTPA, BTT cores (**84**, **85** and **86**), **BTT-3**, **BTT-4**, **BTT-5** and spiro-OMeTAD at the B3LYP/6-31G** level in DCM.

The structural changes are in line with the electronic properties computed for the BTT derivatives. For instance, the HOMO/LUMO of the BTT cores is significantly destabilized/stabilized in passing from compound **84** (-5.79/ -0.89 eV) to compound **85** (-5.67/-1.22 eV) and to compound **86** (-5.36/ -1.56 eV). This destabilization/stabilization is due to the more effective conjugation of the core, especially for the BTT-derivative **86**, and gives rise to a decrease of the HOMO-LUMO gap along the series. The topology of the HOMO

for molecule **86** indeed resembles that computed for the HOMO of 2,2'-bithiophene, following the single/double CC bond conjugated pathway with no contribution from the sulfur atoms.[171,172] The HOMO of the three-armed and four-armed BTT derivatives is destabilized when compared with the respective cores owing to the antibonding interaction with the OMeTPA units (figure 45). **BTT-3** exhibits doubly-degenerate HOMO and LUMO levels which mainly spread over the OMeTPA groups. In contrast, the HOMO and LUMO of **BTT-4**, and especially of **BTT-5**, show a larger contribution of the BTT cores. The energy of the HOMOs, similarly to that found for the BTT cores, undergoes a destabilization when passing from **BTT-3** (-4.73 eV) to **BTT-4** (-4.61 eV) and to **BTT-5** (-4.50 eV) approaching the HOMO level calculated for the archetypical spiro-OMeTAD (-4.44 eV). It is important to note that a significant charge transfer takes place from the peripheral OMeTPA groups to the central BTT unit. The BTT core has a total net charge of -0.39 e for **BTT-3** and **BTT-4** that increases to -0.45 e for **BTT-5** due to its four-armed structure. The electronic structure of the BTT-based HTMs is, therefore, predicted to be significantly polarized.

2.4. Heterocyclic core-based HTMs

In the previous section, the effect of different electron donor units in the electrochemical and photophysical properties of the HTMs candidates has been studied. In addition, different arrangements of the sulfur atoms in the central moiety was further investigated. Owing to the promising advantages of the new candidates in comparison to the most widely used spiro-OMeTAD and with an eye toward carrying out a complete and systematic study of the properties and PV behaviour of new HTMs, a modification in the central core of the molecules is addressed in this segment. New heteroatoms were introduced to replace sulfur atoms in the central moiety, which was envisaged as a useful strategy for designing new functional materials for PSCs.

171. A. Prlj, B. F. E. Curchod, C. Corminboeuf, "Excited state dynamics of thiophene and bithiophene: New insights into theoretically challenging systems", *Phys. Chem. Chem. Phys.*, **2015**, *17*, 14719-14730.
172. J. Arago, P. M. Viruela, J. Gierschner, E. Orti, B. Milian-Medina, "Oligothienoacenes versus oligothiophenes: Impact of ring fusion on the optical properties", *Phys. Chem. Chem. Phys.*, **2011**, *13*, 1457-1465.

2.4.1. Central structure: O- or N-containing cores

Benzotri-fused heterocycles offer a wide variety of opportunities for structural design and properties tunability. The new presented central units allow to study the effects of different heteroatoms (oxygen or nitrogen) in the optical, electrochemical and PV behaviour of the final HTMs candidates in comparison to the analogues BTT-derivative **84**. The new employed central moieties, compounds **94** and **95** (figure 46), possess three pyrrole and furane rings, respectively, fused to a benzene central ring, showing C_{3h}-symmetry.

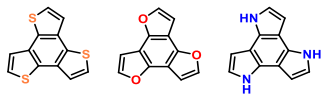

Figure 46. Fused-heterocycles structures as new central cores for HTMs.

Compound **94** and **95** are already known in the literature. Considering that these materials based on furans and pyrroles may have enhanced octupolar properties compared to the corresponding all-carbon congeners (triphenylene, truxene, and hexabenzocoronene), they have been studied in order to achieve a better control of the 2D and 3D molecular organization and to determine their solid-state photophysical properties.[173] Particularly, difuran-derivatives have been used in OLED devices,[174,175] OFETs[176] and as HTMs in PV devices[177] taking advantage of its high hole mobility.

173. H. Tsuji, G. Cantagrel, Y. Ueda, T. Chen, L. J. Wan, E. Nakamura, "Synthesis of benzotrifuran and benzotripyrrole derivatives and molecular orientations on the surface and in the solid state", *Chem. Asian. J.*, **2013**, *8*, *2377-2382.*
174. H. Tsuji, C. Mitsui, Y. Sato, E. Nakamura, "Bis(carbazolyl)benzodifuran: A high-mobility ambipolar material for homojunction organic light-emitting diode devices", *Adv. Mater.*, **2009**, *21*, 3776-3779.
175. H. Tsuji, Y. Yokoi, C. Mitsui, L. Ilies, Y. Sato, E. Nakamura, "Tetraaryl-substituted benzo[1,2-*b*:4,5-*b′*]dipyrroles: Synthesis, properties, and applications to hole-injection materials in OLED devices", *Chem. Asian. J.* **2009**, *4*, 655-657
176. C. Mitsui, J. Soeda, K. Miwa, H. Tsuji, J. Takeya, E. Nakamura, "Naphtho[2,1-*b*:6,5-*b′*]difuran: A versatile motif available for solution-processed single-crystal organic field-effect transistors with high hole mobility", *J. Am. Chem. Soc.*, **2012**, *134*, 5448-5451.
177. H. Tsuji, C. Mitsui, L. Ilies, Y. Sato, E. Nakamura, "Synthesis and properties of 2,3,6,7-tetraarylbenzo[1,2-*b*:4,5-*b′*]difurans as hole-transporting material", *J. Am. Chem. Soc.*, **2007**, *129*, 11902-11903.

Herein the impact on the properties of two isostructural new three-armed sulfur-free HTMs are explored. Instead of presenting sulfur atoms in the central core, oxygen and nitrogen occupy its position in the new molecules **BTF** and **BTP**, respectively. A comparative study of their properties has been carried out in this work.

2.4.2. Design and synthesis of new O- or N-containing HTMs

The new sulfur-free HTMs display a simple structure, analogue to the previously studied benzotrithiophene-based HTM (**BTT-3**), with three-armed substituted by *p*-methoxytriphenylamine (**69**) as electron donor fragment.

Benzotrifuran-derivative (**BTF**) exhibits a nearly planar structure similar to that showed by **BTT-3**. The larger electronegativity of the oxygen atom may result in different electronic properties but maintaining the possibility of intermolecular interactions. On the other hand, benzotripyrrol-derivative (**BTP**), displays a non-planar structure due to the presence of the *N*-phenyl substitution, which may affect the charge extraction and transport.

The synthetic pathway toward the preparation of the new HTMs is illustrated in scheme 14 and 15.

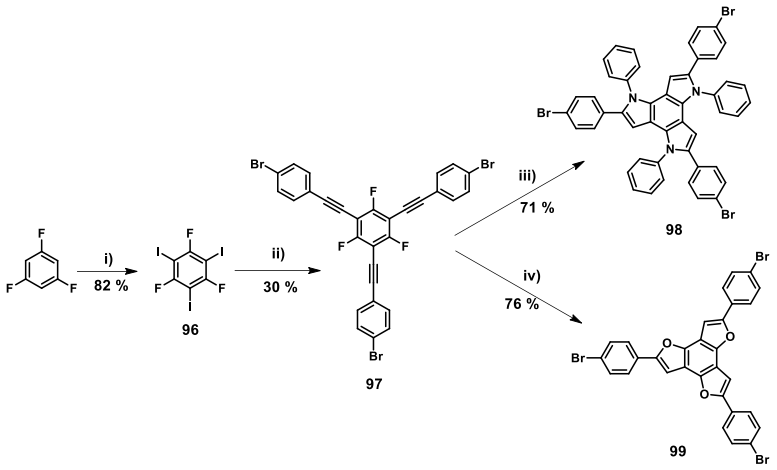

Scheme 14. *Reagents and conditions*: **i**) H_5IO_6, KI, H_2SO_4, 70 ºC; **ii**) 1-bromo-4-ethylnylbenzene, $Pd(PPh_3)_2Cl_2$, CuI, DIPA, 80 ºC; **iii**) NaH, aniline, 100 ºC; **iv**) $CsOH{\cdot}H_2O$, DMA, 166 ºC.

Commercially available 1,3,5-trifluorobenzene was subjected to a three-fold iodination reaction to obtain derivative **96** in a good yield. Subsequently, compound **96** was subjected to a three-fold Sonogahira Pd/Cu catalysed cross-coupling reaction with 1-bromo-4-ethylnylbenzene. The central cores of the target compounds were prepared following a triple cyclization reaction according to the expeditious synthetic route previously reported by Nakamura and co-workers.[173] Finally, *p*-methoxydiphenylamine (**68**) was covalently linked to compounds **98** and **99** by a three-fold Buchwald-Hartwig amination reaction successfully furnishing the desired **BTP** and **BTF** as stable solids in 66 % and 68 % yield, respectively (scheme 15).

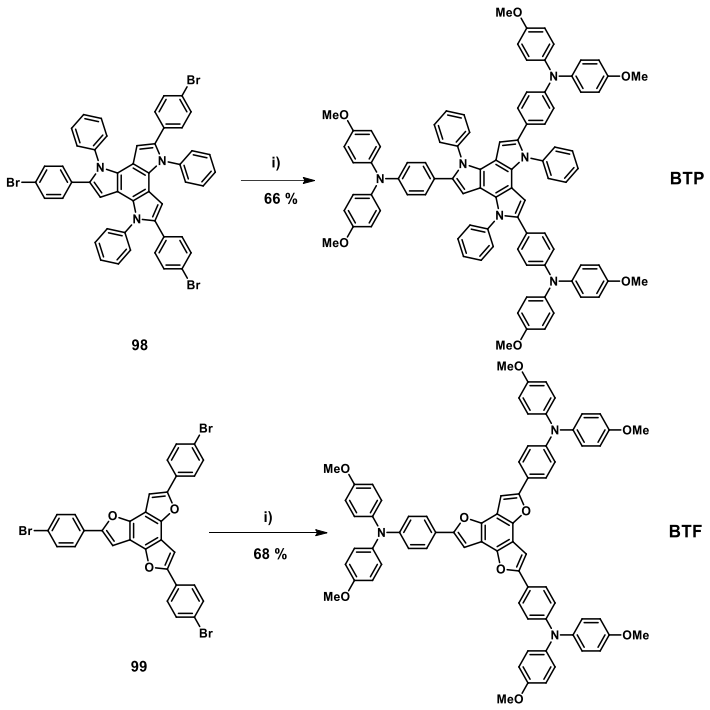

Scheme 15. *Reagents and conditions:* **i) 68**, $Pd_2(dba)_3$, XPhos, Na^tBuO, toluene, 100 ºC.

Complete structural characterization of the two new three-armed sulfur-free HTMs was undertaken using analytical and spectroscopic techniques such as ^1H NMR, ^{13}C NMR and FTIR which confirmed the presence of **BTP** and **BTF**. Mass spectrometry HRMS [MALDI-TOF] evidenced the presence of **BTF** with

a molecular ion peak $[M]^+$ at 1107.4071 m/z (calcd. 1107.4089 m/z) and **BTP** with a molecular ion peak $[M]^+$ at 1332.5471 m/z (calcd. 1332.5508 m/z).

The ^{1}H NMR spectra reveal in both cases the C_{3h}-symmetry of the molecular structures, which exhibit only one singlet ($\delta \approx 5.74$ and 7.37 for **BTP** and **BTF**, respectively) for the β protons of thiophene rings as well as it can be observed in the ^{1}H NMR spectrum of the analogous **BTT-3**. In the same way as in previous cases, it can also be observed the characteristic signals of the donor units in each case and the protons corresponding to the terminal methoxyl groups. In addition, a multiplet signal corresponding to 15 protons confirms the presence of the benzene rings in the core in the case of **BTP**. As an example, figure 47 illustrates the ^{1}H NMR spectra of **BTF**.

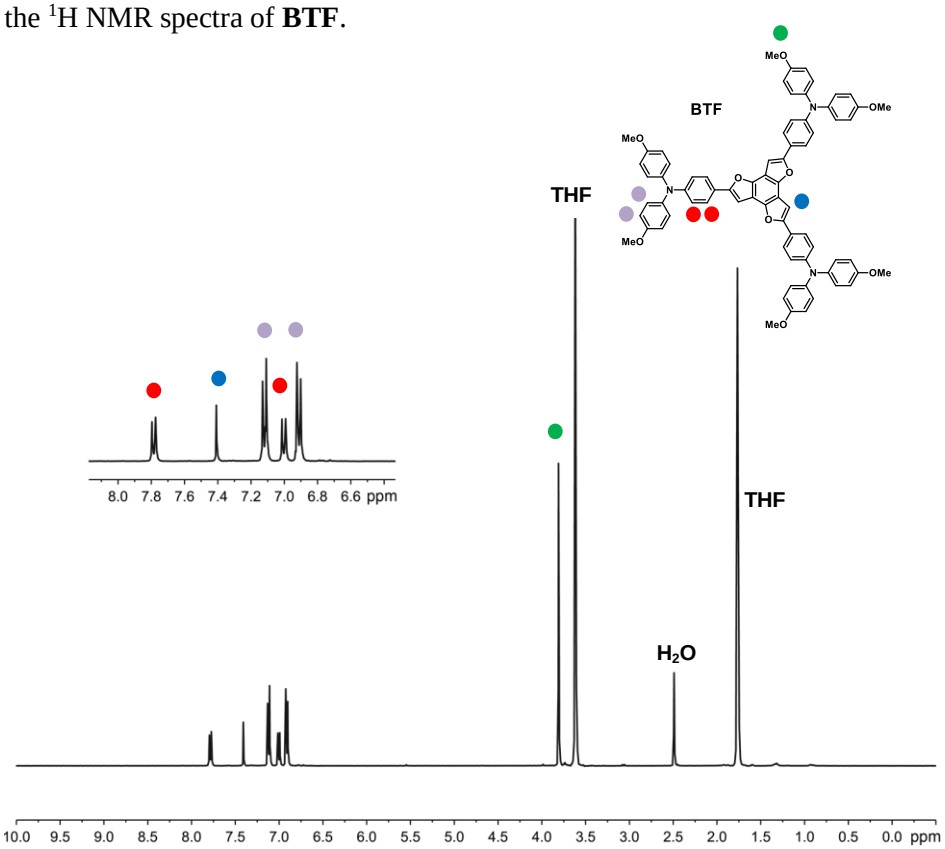

Figure 47. ^{1}H NMR spectrum (400 MHz, THF-d_8, 298 K) of **BTF**.

The crystal structure of **BTF** was unambiguously confirmed by XRD of a single crystal. The structural drawings can be found in figure 48 and the crystallographic parameters are listed in table 16. Single crystals were obtained by slowly cooling a supersaturated solution of **BTF** in toluene. Suitable crystals were manually transferred into immersion oil and fixed on a Kapton tip. The data collection was performed at 120 K. All atoms except hydrogens were refined anisotropically. Hydrogen atoms and toluene solvent molecules are omitted for clarity.

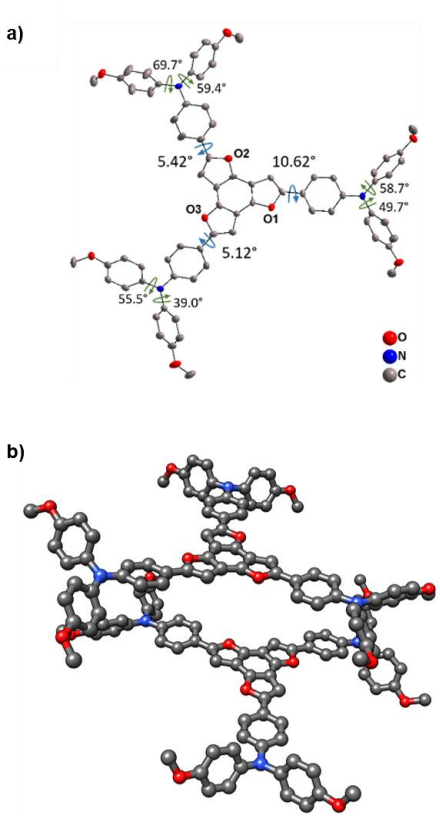

Figure 48. a) Asymmetric unit of **BTF** including relevant torsion angles. **b**) Packing of two **BTF** molecules. The central cores are arranged perfectly planar to each other separated by approx. 7.5 Å.

Table 16. Summary of crystallographic parameters for **BTF** asymmetric unit.

Crystallographic parameters of BTF				
Formula	$C_{86}H_{73}N_3O_9$	**Min/max *h k l***		-16 ≤ *h* ≤ 16 -20 ≤ *k* ≤ 20 -20 ≤ *l* ≤ 20
Crystal system	Triclinic	**Reflections, measured**		98902
Space group	*P*-1	**Reflections, independent**		12222
Temperature (K)	120 (2)	**Absorption coefficient (mm^{-1})**		0.082
Lattice constants (Å/º)	a=13.7025 (7) b=16.8675 (9) c=16.9950 (9)	α=97.515 (2) β=112.1350 (10) γ=105.3780 (10)	**Absorption correction**	Multi-Scan
Volume ($Å^3$)	3389.2 (3)	**Crystal habit**		Block
Z	2	**Refined parameters**		930
$D_{calculated}$ (g/cm^3)	1.23	**R1 [I > 2 σ (I)]**		0.0657
Radiation	Mo-Kα (λ=0.71069 Å)	**wR2**		0.1495
θ Range (º)	2.25-25.38	**Density (e^-/ $Å^3$)**		0.403 and -0.294

2.4.3. Thermal, optical and electrochemical properties

In this section, the properties of previous **BTT-3** have also been included for comparison purposes due to its analogous structure. In this way, it is possible to carry out a comparative study of the influence of the heteroatom on the properties of the final isostructural new three-arms HTMs.

a) Thermogravimetric analysis (TGA) and differential scanning calorimetry (DSC)

Relevant insights into the thermal properties of the new **BTP** and **BTF** were provided by TGA and DCS experiments. The TGA curves are shown in the comparative figure 49 and the detailed thermal features are listed in table 17.

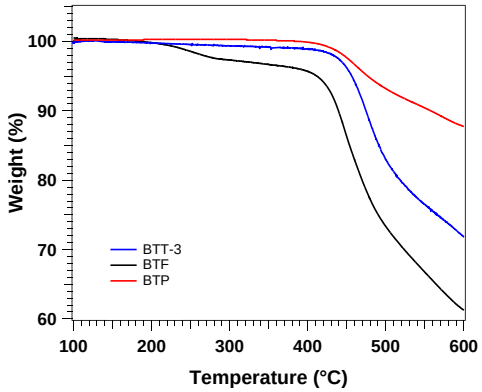

Figure 49. Thermal analysis of **BTP**, **BTF** and **BTT-3** at scan rate of 10 ºC/min under N_2 atmosphere.

A remarkable change in the thermal behaviour occurs as a result of the core modification. **BTP** is clearly the most thermally stable, even more than **BTT-3**, both stable at temperatures above 450 ºC. In contrast, **BTF** exhibits lower thermal stability than the reference isostructural **BTT-3**. **BTF** losses 3.3 % of its weight at 325 ºC, although its decomposition temperature (5 % weight loss) is 410 ºC, which is sufficient for its application in PV devices. This 3.3 % weight loss is attributed to traces of solvent trapped after the purification of this material.

The morphological investigation of both sets of samples was carried out using DSC analysis. Figure 50 shows the DSC of **BTP** and **BTF** after three consecutive heating/cooling cycles under N_2 atmosphere.

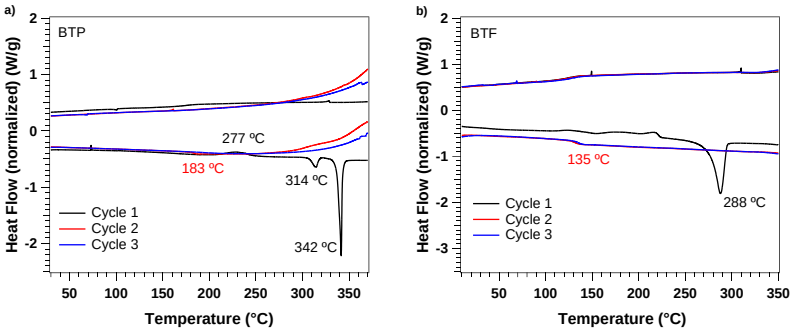

Figure 50. DSC experiment of **a**) **BTP** and **b**) **BTF** at scan rate of 20 ºC/min under N_2 atmosphere.

DSC of **BTP** (figure 50a) indicates a mixture of amorphous and crystalline material. A first crystallization is detected at 227 ºC, which could be attributed to the formation of nucleation points during sample preparation, followed by a melting temperature of those crystallites at 314 ºC. Furthermore, another melting temperature of the remaining amorphous material is detected at 342 ºC. No crystallization process was observed upon cooling and second heating steps, only glass transition at 183 ºC. On the other hand, **BTF** (figure 50b) exhibits an endothermic peak corresponding to a melting process at temperature of 288 ºC during the first cycle. After consecutive cycles only glass transition of 132 ºC and 135 ºC were detected.

The influence of the molecular structure on the morphological properties could be identified by DSC. **BTT-3** and **BTP** exhibit very similar DSC behaviour and **BTF** leads to reduction of glass transition and the melting process compared to isostructural **BTT-3** and **BTP**. This is attributed to the non-planar structure of **BTP** due to the *N*-phenyl substitution. In contrast to **BTP**, **BTF** exhibits a T_{dec} higher than that for the most studied HTM in PV devices, spiro-OMeTAD. On the other hand, the new HTMs show T_m higher than that for spiro-OMeTAD (245 ºC).

Table 17. Thermal properties of **BTP** and **BTF** in comparison to **BTT-3** and spiro-OMeTAD.

HTM	T_{dec} (ºC)[a]	T_m (ºC)[b]	T_c (ºC)[c]	T_g (ºC)[d]
BTP	410	314 / 342	227	183
BTF	478	288	-	135
BTT-3	456	301	-	162
spiro-OMeTAD[e]	449	245	-	125

[a] Decomposition temperature determined from TGA (5 % weight loss). [b] Melting temperature and [c] crystal temperature determined from the first cycle. [d] Glass transition temperature determined from the second cycle. All experiments were performance under N_2 atmosphere. [e] Values reported.[149]

b) Optical characterization

The photophysical properties of the new HTMs were inspected by means of UV-vis absorption and emission as it is outlined in figure 51. The absorption and emission curves of **BTT-3** has been included for comparison purposes. The

fundamental parameters that can be drawn from these experiments are summarized in table 18.

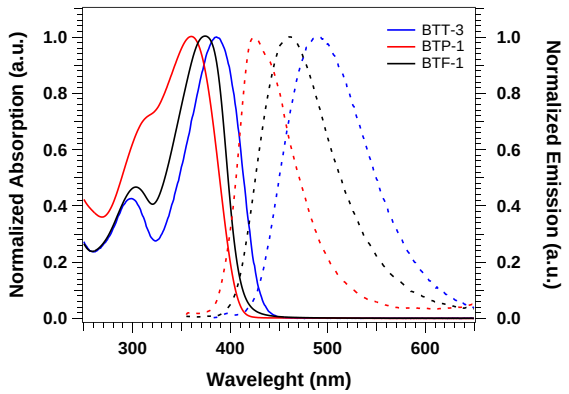

Figure 51. Normalized absorption (solid line) and emission (dashed line) spectra of **BTF** and **BTP** in comparison to **BTT-3** in DCM at r.t.

In solution, the absorption maxima ($\lambda_{max,abs}$) for **BTP**, **BTF** and **BTT-3** were bathochromically shifted from N → O → S, centered at 361 nm ($\varepsilon = 5 \cdot 10^4$ $M^{-1} \cdot cm^{-1}$), 376 nm ($\varepsilon = 8 \cdot 10^4$ $M^{-1} \cdot cm^{-1}$) and 387 nm ($\varepsilon = 14 \cdot 10^4$ $M^{-1} \cdot cm^{-1}$), respectively. The emission spectra show a maximum centered at 425 nm for **BTP**, 461 nm for **BTF** and 489 nm for **BTT-3**. The new HTMs display no significant absorption in the visible range, thus showing relative large lowest energy transition ($E^{0\text{-}0}$) of 3.11 eV (398 nm), 3.02 eV (410 nm) and 2.89 eV (429 nm) for **BTF**, **BTP** and **BTT-3**, respectively.

Table 18. Optical parameters of **BTP**, **BTF**, **BTT-3** and spiro-OMeTAD.

HTM	$\lambda_{max,\ abs}$ (nm)[a]	$\lambda_{max,\ em}$ (nm)[a]	$E^{0\text{-}0}$ (eV) [b]
BTP	361	425	3.11
BTF	376	461	3.02
BTT-3	387	489	2.89
spiro-OMeTAD	386	419	3.05

[a] λ_{max} of absorption and emission measured in DCM. [b] $E^{0\text{-}0}$ was determined at the intersection of normalized absorption and emission spectra and by using eq. 2.

c) Cyclic voltammetry (CV) experiments and energy levels

The electrochemical properties of **BTP** and **BTF** were studied by cyclic voltammetry (figure 52) in (*n*-Bu)$_4$NPF$_6$ (TBAPF$_6$)/dry DCM solutions at a scan rate of 100 mV/s under N_2 atmosphere. Glassy carbon was used as working electrode and platinum wire as counter and reference electrode. Fc/Fc$^+$ was employed as internal reference and its electrochemical signal has not been included in the voltammograms for clarity. The redox potentials are gathered in table 19.

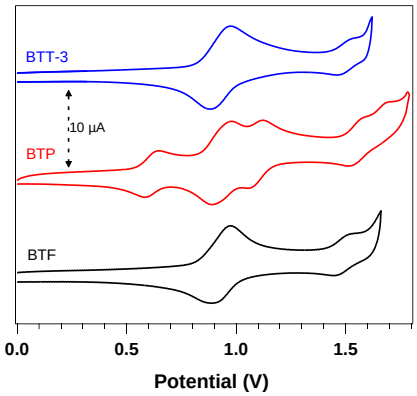

Figure 52. Cyclic voltammograms of **BTP**, **BTF** and **BTT-3** measured at r.t.

The cyclic voltammetry of **BTF** shows two oxidation waves ($E^{ox}_{1/2}$: 0.94 V and 1.48 V). The first $E^{ox}_{1/2}$, 0.94 V *vs.* NHE, is similar to that observed for **BTT-3** ($E^{ox}_{1/2}$: 0.93 V). Thus, the experimental HOMO energy estimated according to the equation 3, is also similar: -5.38 eV for **BTF** and -5.37 eV for **BTT-3**. On the other hand, **BTP** shows four-step reversible oxidation waves with $E^{ox}_{1/2}$values of 0.61 V, 0.93 V, 1.09 V and 1.55 V. The first oxidation potential are shifted around 0.33 V with respect to the first $E^{ox}_{1/2}$ of the **BTF**, which could be attributed to the electron donation from the pyrrole moieties to the central π-system.[173] The HOMO energy for **BTP** lies at -5.05 eV, which indicates a stronger electron donor character. Therefore, the novel **BTF** and **BTP** feature a suited band alignment with the valence band edge of the perovskite (ca. -5.65 eV), which ensures an efficient hole extraction from the perovskites to the HTM.

Table 19. Oxidation potentials and HOMO-LUMO energy levels calculated for **BTP** and **BTF** in comparison to **BTT-3** and spiro-OMeTAD.

HTM	$E^{ox}_{1/2}$ (V)[a]	HOMO (eV)[b]	LUMO (ºC)[c]
BTP	0.61	-5.05	-1.92
BTF	0.94	-5.38	-2.31
BTT-3	0.93	-5.37	-2.48
spiro-OMeTAD[e]	0.72	-5.16	-2.11

[a] First half-wave oxidation potential from CV measurements vs. NHE. [b] E_{HOMO} was estimated by using eq. 3. [c] E_{LUMO} was estimated by using eq. 4. [d] For comparison purposes, the CV of the spiro-OMeTAD was measured under the same conditions.

2.5. Series of thieno[3,2-*b*]thiophene-based derivatives, TbTs

2.5.1. Central structure: Thieno[3,2-*b*]thiophene (TbT)

Thienothiophenes are the simplest fused thiophenes which consist on two fused thiophene rings. Four isomers can be formed, thieno[3,2-*b*]thiophene (**100**), thieno [3,4-*b*]thiophene (**101**), thieno[2,3-*b*]thiophene (**102**) and thieno[3,4-*c*]thiophene (**103**) as it is illustrated in figure 53. Three of them (**100** to **102**) are useful building blocks for the preparation of organic semiconductors of different conjugation length.[153,178]

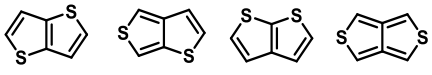

Figure 53. The possible four thienothiophene isomers.

Among these electron-rich thiophene-containing donors, thieno[3,2-*b*]thiophene (TbT, **100**) will be studied as a central core for further series of HTMs. This thienothiophene (**100**) has already been explored in the literature. As an example, TbT was part of the structure of the novel thieno[3,2-*b*]thiophene-diketopyrrolopyrrole based monomer, whose synthesis and polymerization was reported in 2011 by McCulloch and co-workers (scheme 16). In that study, the copolymerization with thiophene afforded a polymer with a maximum hole mobility of 1.95 $cm^2 \cdot V^{-1} \cdot s^{-1}$. BHJ solar cells comprising this polymer and $PC_{71}BM$ gave a PCE of 5.4 %.[152]

178. Y. Liu, C. A. Di, C. Du, Y. Liu, K. Lu, W. Qiu, G. Yu, "Synthesis, structures, and properties of fused thiophenes for organic field-effect transistors", *Chem. Eur. J.*, **2010**, *16*, 2231-2239.

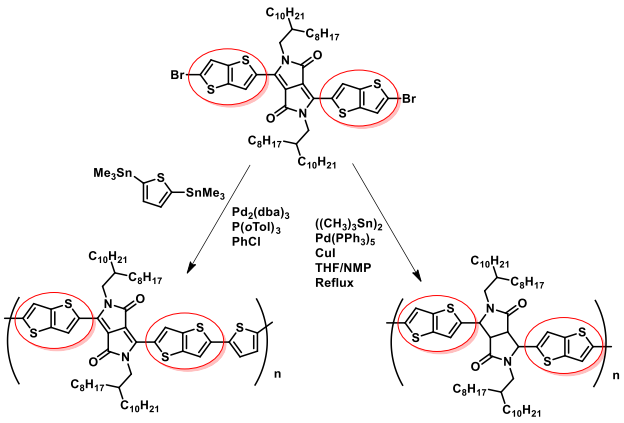

Scheme 16. Example of TbT molecule being part of diketopyrrolopyrrole polymer.

However, the study of this molecule as a central core for HTMs is not very broad in the literature. Because of that, in this thesis, a new series of three molecules based on the TbT core were synthesized and studied as new HTMs in PSCs.

2.5.2. Design and synthesis of new TbT-based HTMs

This section will address the preparation and properties of three new TbT-derivatives. Their structure is constituted by a thieno[3,2-*b*]thiophene (TbT) as central moiety endowed with different electron donor groups as it is illustrated in figure 54. Therefore, it is possible to study the influence of the bridging units (phenyl or thiophene groups) on the molecular properties.

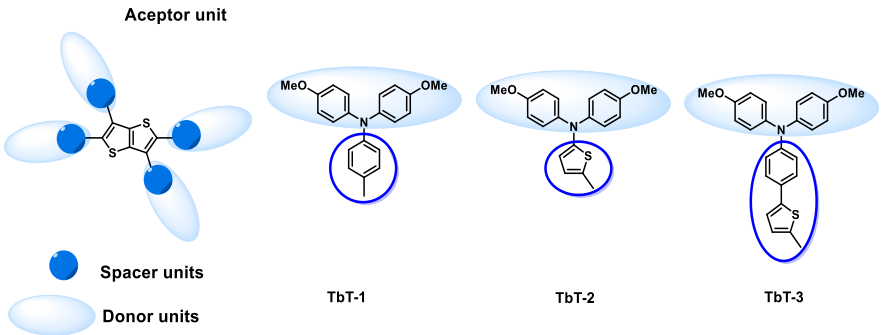

Figure 54. Simplified molecular structure of TbT-based HTMs.

These novel organic compounds constitute a new family of ease to prepare HTMs based on TbT endowed with *p*-methoxydiphenylamine (**68**) or *p*-methoxytriphenylamine (**69**) and the corresponding bridging unit. The synthetic

route for preparing the new HTMs was conducted by stepwise synthesis as it is shown in scheme 17. Target compound **TbT-1** was achieved following a straightforward two-step procedure. Starting from commercially available thieno[3,2-*b*] thiophene, four-fold bromination reaction in the presence of a mixture of water and acetic acid leads to the intermediate compound **104**. The tetrabromo derivative **104**, was subjected to a four-fold Buchwald-Hartwig reaction with *p*-methoxytriphenylamine (**71**) to afford the desired compound **TbT-1**.

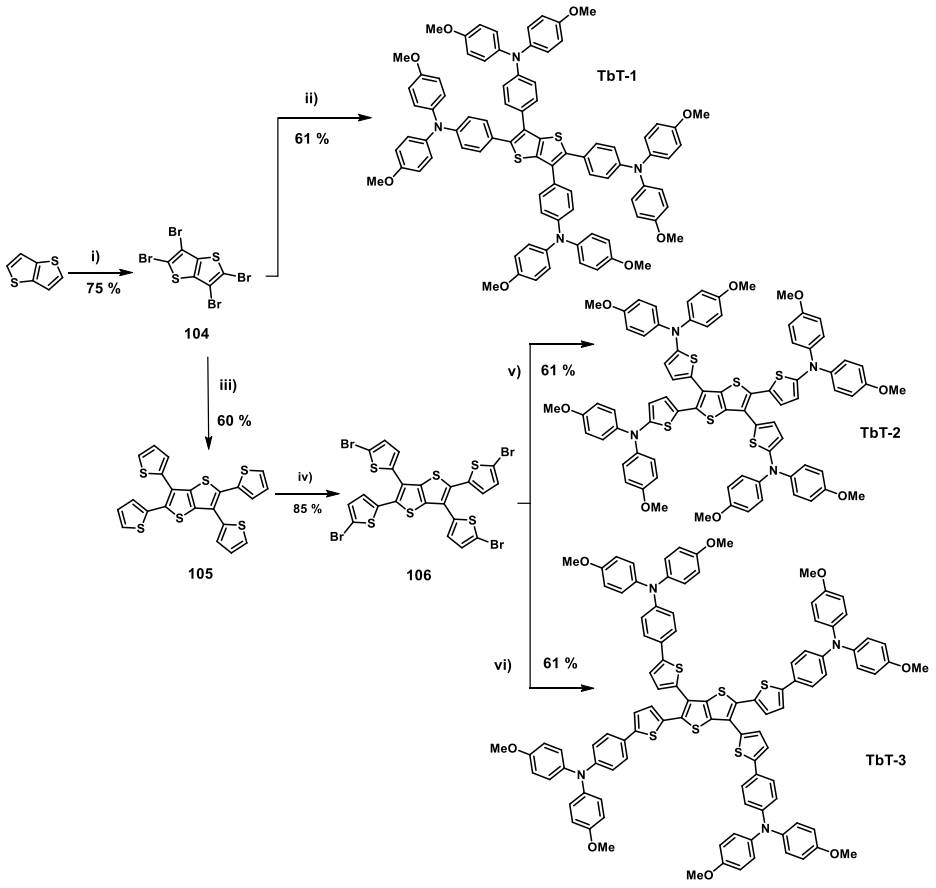

Scheme 17. *Reagents and conditions:* **i**) Br_2, 3:1 H_2O / acetic acid, 65 ºC; **ii**) **73**, $Pd(PPh_3)_4$, K_3PO_4, DMF, 100 ºC; **iii**) thiophen-2-ylboronic acid, $Pd(PPh_3)_4$, THF, 65 ºC; 0.1 M aq. K_2CO_3; **iv**) NBS, THF, r.t.; **v**) **68**, $Pd_2(dba)_3$, XPhos, Na^{t}BuO, toluene, 110 ºC; **vi**) **73**, $Pd(PPh_3)_4$, K_3PO_4, DMF, 100 ºC.

Additionally, the synthetic route illustrated in the scheme 17 allows to obtain **TbT-2** and **TbT-3** following a straightforward four-step procedure. Firstly, compound **105** was obtained from a one-step Pd-catalized reaction treating the previously synthesized compound **104** in the presence of thiophen-2-ylboronic acid in THF. Subsequent treatment of compound **105** with NBS in THF provided the tetrabrominated derivative **106**. Finally, compound **106** was subjected to a four-fold Buchwald-Hartwig reaction with *p*-methoxydiphenylamine (**68**) to afford the desired compounds **TbT-2**. On the other hand, four-fold Suzuki cross-coupling reaction between derivative **106** and *p*-methoxytriphenylamine (**71**) leads to the formation of **TbT-3**.

The formation of the aforementioned HTMs was confirmed by ^{1}H and ^{13}C NMR, FTIR and HRMS [MALDI-TOF] techniques. Mass spectrometry HRMS [MALDI-TOF] confirmed the presence of **TbT-1** with a molecular ion peak $[M]^{+}$ at 1352.4766 m/z (calcd. 1352.4786 m/z), **TbT-2** with a molecular ion peak $[M]^{+}$ at 1376.3043 m/z (calcd. 1376.3020 m/z) and **TbT-3** with a molecular ion peak $[M]^{+}$ at 1680.4310 m/z (calcd. 1680.4295 m/z). The ^{1}H NMR spectra of these compounds, do not present any signal related to the TbT central core. Therefore, all characteristic signals are assigned to the bridging and electron donor units of the structure. Figure 55 illustrates the ^{1}H NMR spectrum of **TbT-3**, where the assignments of the signal are shown.

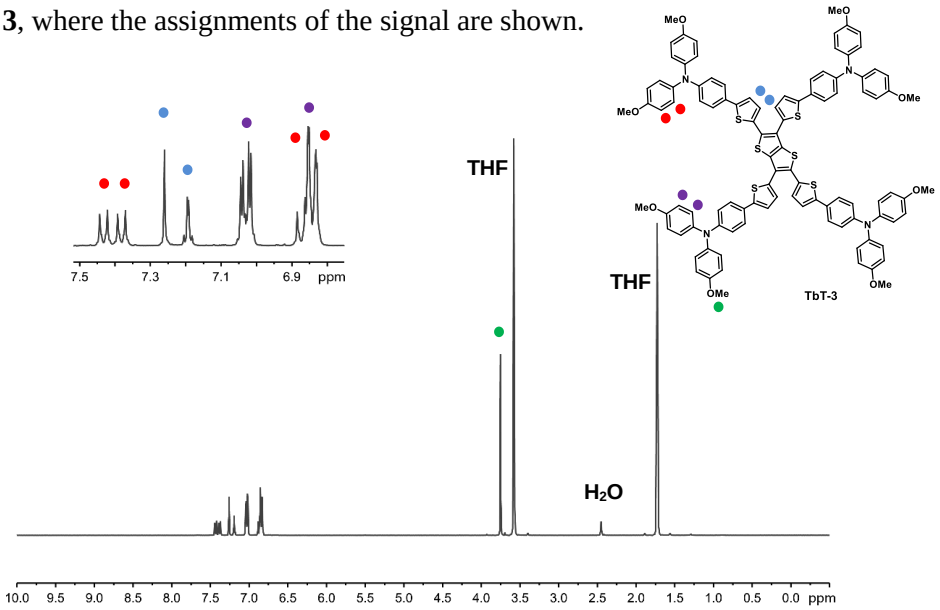

Figure 55. ^{1}H NMR spectrum (400 MHz, THF-d_8, 298K) of **TbT-3**.

2.5.3. Thermal, optical and electrochemical properties

a) Thermogravimetric analysis (TGA) and differential scanning calorimetry (DSC)

TGA and DSC measurements were performed with the purpose of knowing the thermal properties of the novel family of TbT-derivatives. To better understanding, detailed thermal features are collected in table 20.

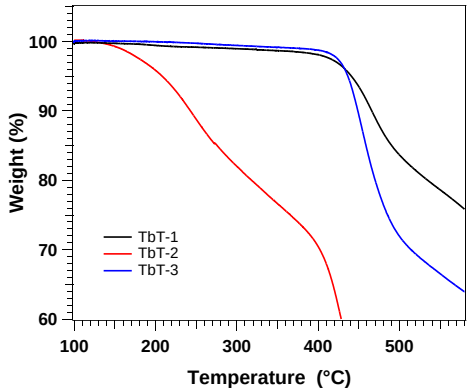

Figure 56. Thermogravimetric analysis of **TbT-1**, **TbT-2** and **TbT-3** at scan rate of 10 ^{o}C /min under N_2 atmosphere.

From the TGA curves (figure 56) it can be observed a notably different thermal behaviour between TbT-based molecules. **TbT-1** and **TbT-3** exhibit good thermal stability and start decomposing at temperatures (T_{dec}) above 440 ^{o}C (5 % weight loss under N_2 atmosphere). In contrast **TbT-2** showed a noticeable loss of weight, starting to decompose at (T_{dec}) 210 ^{o}C. This clearly indicates that the stability of the molecule changes significantly depending on the bridging unit.

The thermal transitions of the new HTMs were studied by DSC and compared with those for spiro-OMeTAD. The corresponding DSC curves of each molecule are illustrated in figure 57.

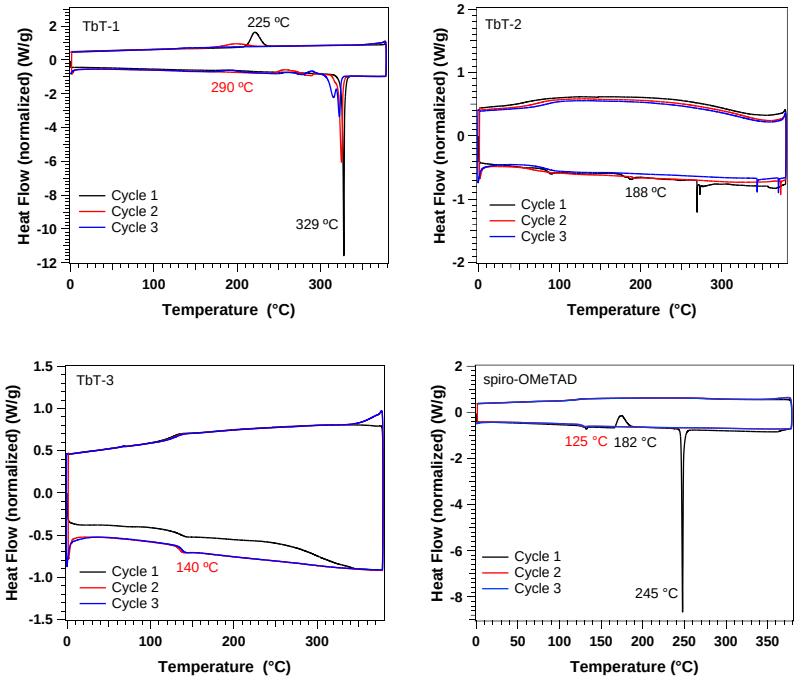

Figure 57. DSC experiment of **TbT-1**, **TbT-2**, **TbT-3** and spiro-OMeTAD at scan rate of 20 ºC/min.

TbT-1 exhibits different behaviour with respect to **TbT-2** and **TbT-3** in DSC. During the first heating scan its melting point was detected as a sharp endothermic peak at 329 ºC and a crystallization peak at (T_c) 225 ºC. After consecutive heating/cooling cycles rather small changes in the T_m were observed and no more crystallization peaks were detected. Remarkably, two melting processes were observed during the third cycle for **TbT-1**. In addition, a slight peak at 290 ºC was tentatively assigned to its T_g.

TbT-2 and **TbT-3** show a similar DSC behaviour. After consecutive heating and cooling cycles, a glass transition (T_g) at 188 ºC and 140 ºC appears, respectively, which indicate their amorphous nature. In comparison, the well-studied spiro-OMeTAD displays both glass transition at 125 ºC and melting of the crystal at 245 ºC. Additionally, a crystallization process is detected at 174 ºC.

Table 20. Thermal properties of TbT-derivatives in comparison to spiro-OMeTAD.

HTM	T_{dec} (ºC)[a]	T_m (ºC)[b]	T_c (ºC)[c]	T_g (ºC)[d]
TbT-1	440	329	225	290
TbT-2	210	-	-	188
TbT-3	440	-	-	140
spiro-OMeTAD[e]	449	245	182	125

[a] Decomposition temperature determined from TGA (5 % weight loss). [b] Melting temperature and [c] crystal temperature determined from the first cycle. [d] Glass transition temperature determined from the second cycle. All experiments under N_2 atmosphere. [e] Values reported.[149]

b) Optical characterization

UV-vis absorption and emission experiments were carried out with the aim of studying the photophysical properties of the new TbT-derivatives. Figure 58 illustrates the normalized absorption and emission curves of **TbT-1**, **TbT-2** and **TbT-3**. In addition, the relevant optical features are collected in table 21.

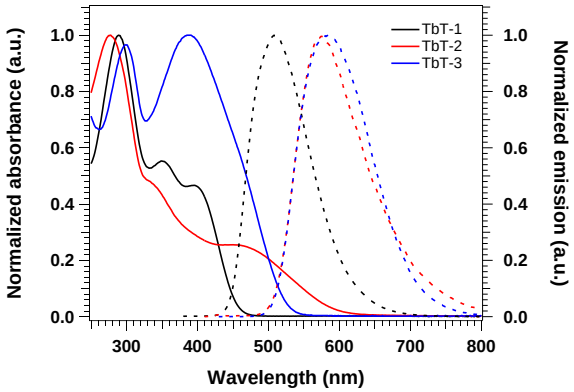

Figure 58. Normalized absorbance (solid line) and emission (dashed line) curves of **TbT-1**, **TbT-2** and **TbT-3** in DCM at r.t.

The UV-vis absorption spectra in solution of **TbT-1**, **TbT-2** and **TbT-3** have been normalized with the relative maximum ($\lambda_{max,\ abs}$) centered at 291 nm, 280 nm and 390 nm, for **TbT-1**, **TbT-2** and **TbT-3**, respectively. Relevantly, increasing the π-conjugation of the spacer resulted in the case of **TbT-3**, in a wider absorbance in the visible range. In addition, **TbT-1** exhibits two additional absorption peaks at 350 nm and 400 nm, **TbT-2** two small shoulders at 330 nm

and 460 nm and, finally, **TbT-3** presents an additional strong absorption peak at 310 nm. The wider absorption of **TbT-3** is attributed to the more extended conjugation of the backbone with an absorbance onset ≈ 600 nm. On the other hand, the emission spectra exhibit a maximum centered at 510 nm, 580 nm and 590 nm for **TbT-1**, **TbT-2** and **TbT-3**, respectively.

The optical band gap corresponding to $E^{0\text{-}0}$ value was estimated at the intersection of normalized absorption and emission spectra for each molecule.

Table 21. Optical parameters of TbT-derivatives in comparison to spiro-OMeTAD.

HTM	$\lambda_{max,\ abs}$ (nm)[a]	$\lambda_{max,\ em}$ (nm)[a]	$E^{0\text{-}0}$ (eV) [b]
TbT-1	291	510	2.76
TbT-2	280	580	2.43
TbT-3	390	590	2.43
spiro-OMeTAD	386	419	3.05

[a] λ_{max} of absorption and emission measured in DCM. [b] $E^{0\text{-}0}$ was determined at the intersection of normalized absorption and emission spectra and by using eq. 2.

c) Cyclic voltammetry (CV) experiments and energy levels

An important point to estimate the future behaviour of the HTM candidates in the PV device is to know the HOMO and LUMO levels of the novel molecules. For this purpose, cyclic voltammetry experiments were performed. The measured redox potentials are summarized in table 22 together with the HOMO energies estimated from the first half-wave oxidation potential ($E^{ox}_{1/2}$) and the LUMO energies. The measurements were conducted in 0.1 M solution of (*n*-Bu)$_4$NPF$_6$ (TBAPF$_6$) in dry DCM under N_2 atmosphere using glassy carbon as working electrode and platinum wire as reference and counter electrode. Fc/Fc$^+$ was used as internal standard.

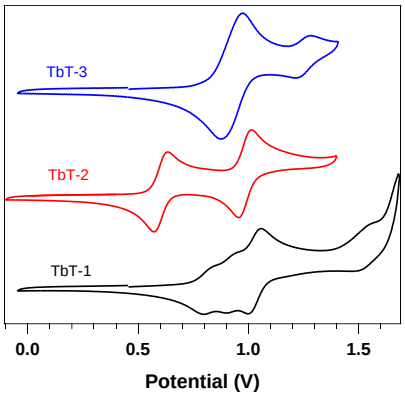

Figure 59. Cyclic voltammograms of **TbT-1**, **TbT-2** and **TbT-3** measured at r.t.

As shown in figure 59, the new family of molecules are only active in the anodic region, positive potential, although their electrochemical behaviour is notably different. The cyclic voltamogram of **TbT-1** exhibits four oxidation waves with $E^{ox}_{1/2}$ value of 0.81 V, 0.93 V, 1.03 V and 1.53 V vs. NHE. The first three oxidation waves are tentatively assigned to a consecutive extraction, mainly, from the four triphenylamine units corresponding to one-, one- and two-electron process. **TbT-2** exhibits two reversible oxidation waves, whose $E^{ox}_{1/2}$ values are 0.60 V and 0.98 V, attributed to the oxidation process of the diphenylamines corresponding to two electrons each wave. For **TbT-3**, the cyclic voltamogram reveals two reversible oxidation waves with $E^{ox}_{1/2}$ values of 0.92 V and 1.2 V and significantly different intensities. The HOMO energies experimentally estimated from $E^{ox}_{1/2}$ are found to be -5.32 eV, -5.00 eV and -5.21 eV for **TbT-1**, **TbT-2** and **TbT-3**, respectively.

Table 22. Oxidation potentials and HOMO-LUMO energy levels calculated for TbT-derivatives in comparison to spiro-OMeTAD.

HTM	$E^{ox}_{1/2}$ (V)[a]	HOMO (eV)[b]	LUMO (eV)[c]
TbT-1	0.81	-5.32	-2.56
TbT-2	0.60	-5.00	-2.57
TbT-3	0.92	-5.21	-2.78
spiro-OMeTAD[d]	0.72	-5.16	-2.11

[a] First half-wave oxidation potential from CV measurements vs. NHE. [b] E_{HOMO} was estimated by using eq. 3. [c] E_{LUMO} was estimated by using eq. 4. [d] For comparison purposes, the CV of the spiro-OMeTAD was measured under the same conditions.

Both **TbT-1** and **TbT-3** exhibit energetically lower HOMO level than spiro-OMeTAD, whereas **TbT-2** presents the higher HOMO value of the three TbT-derivatives which confirms its donor-capacity. Remarkably, it is observed that increasing the π-conjugation of the spacer resulted in a decreasing of the band gap. This fact could be explained due to the increase in conjugation in **TbT-2** and **TbT-3** structures related to **TbT-1**. Although the HOMO values obtained for TbT-derivatives deviate from the reference value, their energetic levels continue being successfully aligned to the valence band edge of the perovskite.

• Devices fabrication and characterization

Chapter 1. Hole-transporting materials for perovskite solar cells

3. DEVICES FABRICATION AND CHARACTERIZATION

3.1. Perovskite solar cells employing TAE-1 as a HTM

The star-shaped **TAE-1** based on TAE central core endowed with *p*-methoxydiphenylamine (**68**) was used as hole-transporting layer in perovskite-based solar cells. This study has been carried out in collaboration with Prof. Emilio Palomares's group (ICIQ, Tarragona, Spain) and it was reported in 2015 (*Chem. Commun.*, **2015**, 51, 13980-13982). **TAE-1** was incorporated as a HTM, without any additives, using the standard methylammonium lead iodide ($MAPbI_3$) perovskite and metal electrode in a final device whose structure is shown in the figure 60. A competitive PCE of 11.0 % was achieved under AM1G solar simulation, in comparison to the widely used spiro-OMeTAD (13.5 %).

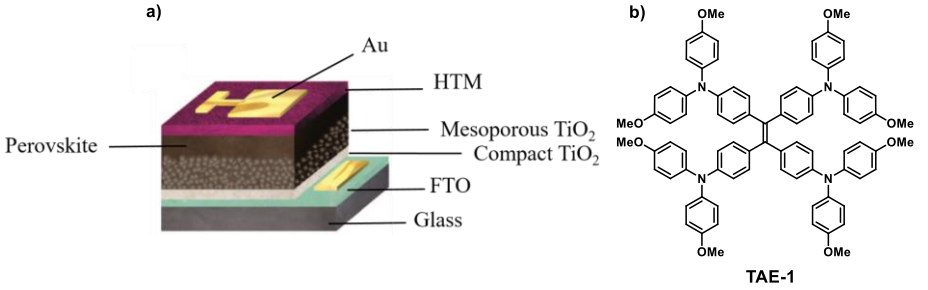

Figure 60. a) Simplified model of PV device; **b**) **TAE-1** structure.

3.1.1. Perovskite-based device fabrication

A dense blocking layer of TiO_2 (0.65 mL of Ti (IV) isopropoxide, 0.38 mL of acetylacetone in 5 mL of ethanol) was spin coated at 3000 rpm for 60 s onto the fluorine-doped tin oxide (FTO). The substrates were calcined at 500 ºC for 30 min and immersed in a $TiCl_4$ (40 mM) solution at 70 ºC for 30 min. A solution of TiO_2 paste (18 NR-T) in ethanol (2:7 w/w) was spin coated at 5000 rpm for 30 s. After that, substrates were heated at 325 ºC for 30 min, 375 ºC for 5 min, 450 ºC for 15 min and 500 ºC for 30 min. CH_3NH_3I was synthesized following a protocol previously reported.[179] The synthesized CH_3NH_3I and $PbCl_2$ were mixed in DMF in 3:1 molar ratio. Perovskite precursor was deposited onto the substrate by spin coating at 2000 rpm for 45 s at controlled humidity of 20 %.

179. J. H. Im, C. R. Lee, J.-W. Lee, S. W. Park, N. G. Park, "6.5% Efficient perovskite quantum-dot-sensitized solar cell", *Nanoscale*, **2011**, *3*, 4088-4093.

Substrates were heated at 100 ºC for 1 hour. A 56 mM solution of **TAE-1** or spiro-OMeTAD, for comparison purpose, in chlorobenzene was deposited by spin coating at 2000 rpm for 60 s. Finally, an 80 nm layer of Au was deposited by thermal evaporation.

3.1.2. Device performance

Firstly, in order to achieve an effective operation, it is important to know the relationship between the energy levels of the different components. Figure 61 shows the energy levels of the different layers that form the device in this particular case. As it can be observed, the HOMO energy value of the studied **TAE-1** is above the $MAPbI_3$ perovskite valence band energy (-5.44 eV), which ensures efficient hole transfer from the $MAPbI_3$ perovskite to the molecule. Besides, this value is very close to that of well-known spiro-OMeTAD.

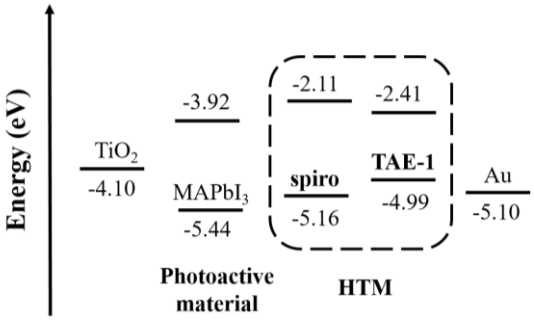

Figure 61. Energy levels diagram of the different components in the PV device.

Figure 62 presents the J-V curves under dark and illumination for a perovskite device employing as a HTM **TAE-1** and spiro-OMeTAD, for comparison purpose. The performance parameters measured under standard conditions are summarized in table 23.

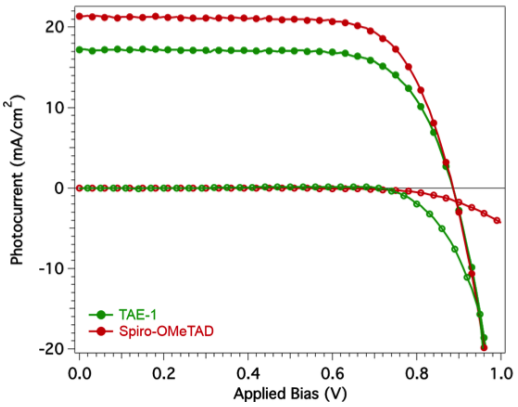

Figure 62. J-V Curves measured under AM1G solar simulation conditions and in the dark.

Table 23. Measured performance parameters of the devices.

HTM	V_{oc} (V)	J_{sc} (mA·cm^{-2})	FF (%)	PCE (%)
TAE-1	0.89 (0.81)	17.2 (17.2)	72.2 (62.9)	11.0 (8.9)
spiro-OMeTAD	0.89 (0.86)	21.4 (21.0)	71.4 (64.3)	13.5 (11.7)

The average values (5 devices for each HTM) are provided in parentheses

As can be seen, the device fabricated with **TAE-1** has an identical V_{oc} and very close value of fill factor (FF) to those using spiro-OMeTAD. Despite many efforts to optimize the **TAE-1** film thickness, it was not possible to match the J_{sc} value to that for spiro-OMeTAD. Nonetheless, it is worthy to notice that it was avoided the use of chemical oxidants in both cases. Although higher light-to-electrical conversion efficiency have frequently been reported[147] using additives in the HTM solutions, the use of dopants may lead to greater solar cell instability due to the partial oxidation of the HTM layer. Therefore, it is important to know the behaviour of the devices without doping in order to give more stability to the system.

In addition, hole mobility properties of **TAE-1** were measured in comparison to the reference spiro-OMeTAD. For this purpose, devices with the following structure: ITO/PEDOT:PSS/HTM/Au were fabricated, where the HTM was either **TAE-1** or spiro-OMeTAD. The values obtained were $5.92 \cdot 10^{-5}$ cm^2·V^{-1}·s^{-1} for **TAE-1** and $2.55 \cdot 10^{-4}$ cm^2·V^{-1}·s^{-1}·cm^{-1}, one order of magnitude higher for

spiro-OMeTAD determined by the SCLC (space charge limited current) method (figure 63).

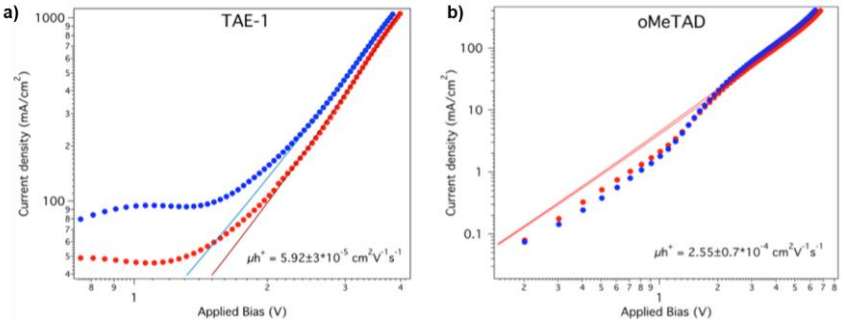

Figure 63. a) Mobility measurements for **TAE-1, b**) spiro-OMeTAD at space charge limited conditions. The red symbols correspond to the measurement under illumination and the blue symbols correspond to the measurement under dark condition.

In conclusion, it has been synthesized and characterized a novel HTM that has been used to fabricate efficient $MAPbI_3$-based PSCs reaching a PCE of 11.0 %. As **TAE-1** requires only two straightforward synthetic steps with good yield (72 %), this molecule and its possible derivatives would be good candidates for top efficient $MAPbI_3$-based solar cells.

3.2. Perovskite solar cells employing BTT-derivatives as HTMs

The planarized BTT-based molecules **BTT-1** to **BTT-5** (figure 64) synthesized in this thesis, were tested in solution-processed lead trihalide perovskite-based solar cells as HTMs. PCE in the range of 16.0 % to 19.0 % were obtained under AM 1.5 G for the five derivatives. These values are comparable to those obtained with today's most commonly used HTM spiro-OMeTAD, which point them out as promising candidates to be used as easily attainable and cost-effective alternatives for PSCs. This study was carried out in collaboration with Prof. M. K. Nazeeruddin's group at EPFL (Sion, Switzerland) and it was published in 2016 (*Angew. Chem. Int. Ed.*, **2016**, 55, 6270 - 6274) and in 2017 (*J. Mater. Chem. A*, **2017**, 5, 8317-8324). In addition, an application of these HTMs have been protected through a *European patent* (A. Molina-Ontoria, I. Zimmermann, I. Garcia-Benito, P. Gratia, C. Roldán-Carmona, M. Graetzel, M. K. Nazeeruddin, N. Martín, Application number PCT/IB2016/057475).

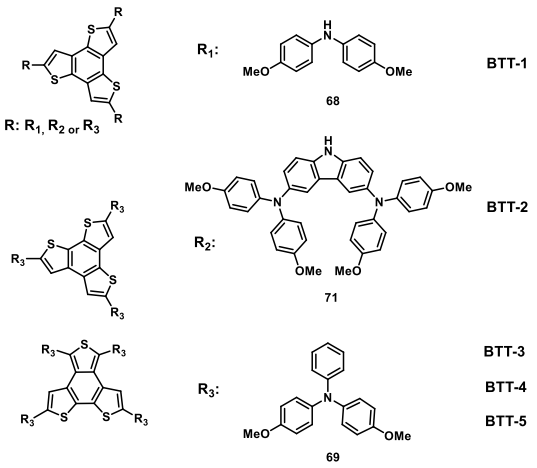

Figure 64. Molecular structure of the BTT-based HTMs.

3.2.1. Perovskite-based device fabrication

Solar cell devices were fabricated onto conductive FTO coated glass substrates. The substrates were cut and cleaned by sequential treatment with a 2 % aqueous Helmanex solution and isopropanol in an ultrasonic bath for 30 and 5 minutes respectively, followed by a 15 minutes UV-ozone exposure. The titania blocking layer was applied by spray pyrolysis from a precursor solution of titanium diisopropoxide bis(acetylacetonate) and acetylacetonate in ethanol at 450 ºC in ambient atmosphere. Around 150 nm thick mesoporous TiO_2 layer was deposited by spin coating a 30 nm titanium dioxide particle (30 NR-D) paste from Dyesol diluted (150 mg/mL) in ethanol. The substrates were then sintered at 450 ºC for 30 min under a dry air flow in the case of the devices with **BTT-1** to **BTT-3** as a HTM. When **BTT-4** and **BTT-5** were employed as HTMs, a 200-300 nm thick mesoporous TiO_2 layer was obtained by spin-coating at 2000 rpm for 10 s followed by a sintering step at 500 ºC for 20 min. After cooling down the substrates, a Li-treatment was applied by spin-coating 60 µL of a solution of Li-TFSI in acetonitrile (10 mg/mL) onto the mesoporous layer, followed by a sintering step at 500 ºC for 10 min to decompose the Li-salt as previously described.[180] Slightly differences were introduced in the device fabrication based

180. A. A. F. Giordano, J. P. Correa, M. Saliba, T. Matsui, S. H. Im, S. M. Zakeeruddin, M. K. Nazeeruddin, A. Hagfeldt, M. Graetzel, "Enhanced electronic properties in mesoporous TiO_2 via lithium doping for high-efficiency perovskite solar cells", *Nat. Comm.*, **2016**, *7*, 10379-10385.

on **BTT-1** to **BTT-3** and **BTT-4** and **BTT-5** which are commented bellow. In the case of the devices employing **BTT-1** to **BTT-3** as HTMs, the perovskite layer was applied by spin coating a precursor solution consisting of 1.25 M methylammonium iodide and 1.4 M lead iodide in dimethyl sulfoxide for $MAPbI_3$ and a solution of 1.4 M lead iodide, 0.17 M lead bromide, 0.15 M methylammonium bromide and 1.08 M formamidinium iodide in a 4:1 mixture of dimethylformamide and dimethyl sulfoxide for the compositional modification $(FAPbI_3)_{0.85}(MAPbI_3)_{0.15}$ respectively. The spin coating sequence includes two steps, the first one is at 1500 rpm for 10 s with a ramp of 200 rpm s^{-1}, and the second one is at 4000 rpm for 30 s with a ramp of 2000 rpm s^{-1}. 10 s Prior to the end of the second step 120 µl of chlorobenzene are poured onto the spinning substrate. At the end of the spin program the substrate is immediately transferred onto a hotplate. The perovskite layer was kept at 100 ºC for 1.5 hours under nitrogen atmosphere.

On the other hand, for the devices based on **BTT-4** and **BTT-5** as HTMs only compositionally engineered perovskite was used. **BTT-3** was measured under the same conditions for investigating the isomerism effect on the PV performance. The perovskite layers were fabricated by a single step spin-coating procedure reported by Seok and co-workers.[181] For the perovskite precursor solution, 508 mg of PbI_2, 68 mg PbI_2, 180.5 mg of formamidinium iodide (FAI) and 20.7 mg of methylammonium bromide (MABr) were dissolved in a 1:4 mixture of DMSO:DMF. The perovskite solution was spun at 5000 rpm for 30 s using a ramp of 3000 rpm s^{-1}. 15 s Prior to the end of the spin-coating sequence, 100 µL of chlorobenzene were poured onto the spinning substrate. Afterwards, the substrates were transferred onto a heating plate and annealed at 100 ºC for 45 min. The composition of the perovskite material is $(FAPbI_3)_{0.85}(MAPbBr_3)_{0.15}$ with 5 % of PbI_2 excess.

The HTMs were applied from solutions in chlorobenzene. Optimized concentrations were found to be 60 mM for spiro-OMeTAD, 10 mM for **BTT-1**, 30 mM for **BTT-2** and **BTT-3** and 20 mM for **BTT-4** and **BTT-5**. By changing the concentration of the precursor solutions, the thickness of the layer was optimized to obtain the best device performance for each molecule. *t*-BP,

181. N. J. Jeon, J. H. Noh, Y. C. Kim, W. S. Yang, S. Ryu, S. I. Seok, "Solvent engineering for high-performance inorganic–organic hybrid perovskite solar cells", *Nat. Mater.*, **2014**, *13*, 897-903.

Li-TFSI and cobalt complex (FK209) were added as additives. Equimolar amounts of additives were added for all HTMs: 330 mol% *t*-BP, 50 mol% Li-TFSI from a 1.8 M stock solution in acetonitrile and 3 mol% FK209 from a 0.25 M stock solution in acetonitrile. The final HTM solutions were spin-coated dynamically onto the perovskite layers at 4000 rpm for 20 s. Finally, the gold electrodes were deposited by thermal evaporation of around 70-100 nm layer of gold using a shadow mask under high-vacuum conditions.

3.2.2. Device performance employing BTT-1, BTT-2 and BTT-3

High resolution scanning electron microscopy (SEM) cross-section images displayed in figure 65 show the cell architecture of the best device using **BTT-1**, **BTT-2** or **BTT-3** as HTMs. As photoactive layer, both different perovskites were tested, the standard $MAPbI_3$ perovskite and the modified composition $(FAPbI_3)_{0.85}(MAPbBr_3)_{0.15}$ perovskite recently introduced by Seok.[182]

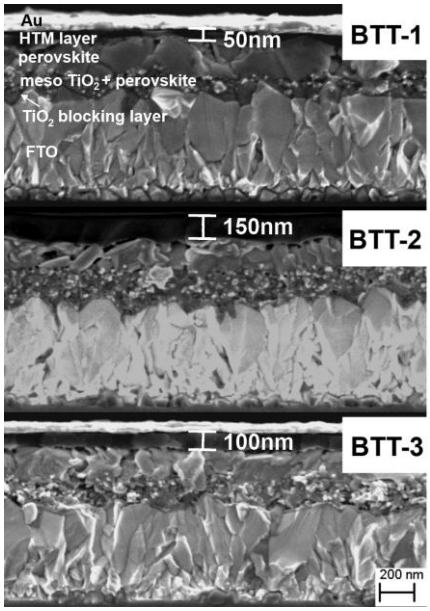

Figure 65. Cross sectional images of devices fabricated with **BTT-1**, **BTT-2** and **BTT-3** on $MAPbI_3$ perovskite. The thickness of the hole-transporting layer is indicated.

182. N. J. Jeon, J. H. Noh, W. S. Yang, Y. C. Kim, S. Ryu, J. Seo, S. I. Seok, "Compositional engineering of perovskite materials for high-performance solar cells", *Nature*, **2015**, *517*, 476-480.

From SEM images, it is possible to identify the different layers that constitute the device. The thicknesses of the layer are, approximately, 30 nm of compact TiO_2 blocking layer, 150-250 nm of mesoporous TiO_2, 400 nm of perovskite, 50 nm (**BTT-1**), 150 nm (**BTT-2**), 100 nm (**BTT-3 to 5**) of the HTM layer and 70-100 nm of gold electrode. Compared to the standard perovskite devices, the composite material has a thicker capping layer of around 400 nm, three times larger than the value observed when using the standard. An ideal positive charge extraction layer should have good hole mobility and a HOMO energy level compatible with the valence band of the perovskite. Therefore, it is important to know the relation between the energy levels of the different components in the device (figure 66).

The HOMO level of **BTT-1** and **BTT-2** is very similar to the one for spiro-OMeTAD, whereas the **BTT-3** exhibits slightly lower HOMO level. Therefore, the novel HTMs feature a suited band alignment with the valence band edge of both perovskites, which ensures an effective hole extraction from the perovskite to the HTM.

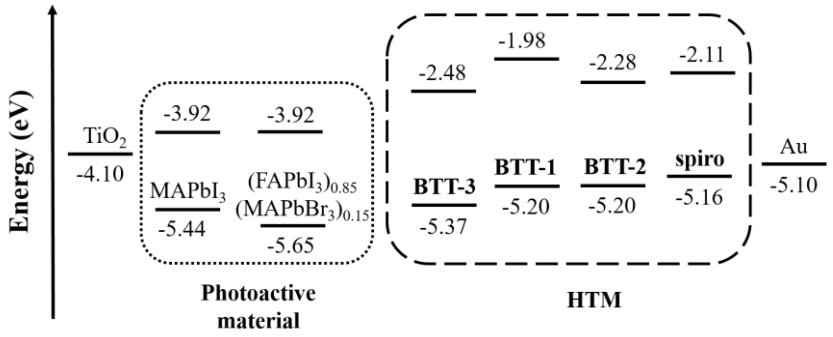

Figure 66. Energy diagram of the different components in the PV device.

The PV performance of the devices was measured under AM 1.5 G conditions and J-V curves were recorded by applying a forward bias with a scan rate of 10 $mV \cdot s^{-1}$ in order to minimize the hysteresis effects stemming from the perovskite material.[54]

Figure 67 shows the J-V curves of the PSCs prepared by using **BTT-1**, **BTT-2** and **BTT-3** as HTMs and standard $MAPbI_3$ perovskite (figure 67a) and compositional modified perovskite $(FAPbI_3)_{0.85}(MAPbBr_3)_{0.15}$ (figure 67b). The device parameters are summarized in the table 24.

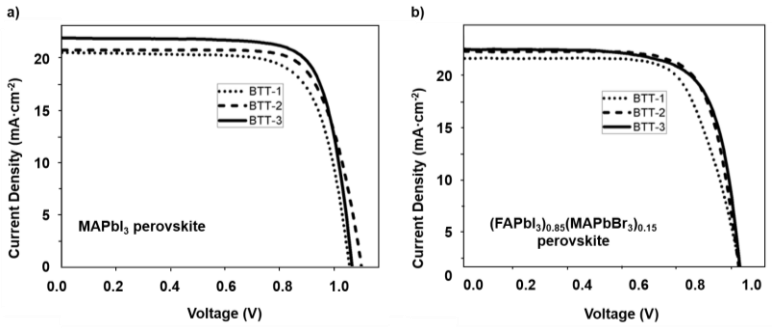

Figure 67. I-V curves showing the performance of perovskite devices prepared by using **BTT-1**, **BTT-2** and **BTT-3**.

Table 24. Measured performance parameters of the devices.

	$MAPbI_3$				**$(FAPbI_3)_{0.85}(MAPbBr_3)_{0.15}$**			
HTM	**V_{oc} (V)**	**J_{sc} ($mA \cdot cm^{-2}$)**	**FF (%)**	**PCE (%)**	**V_{oc} (V)**	**J_{sc} ($mA \cdot cm^{-2}$)**	**FF (%)**	**PCE (%)**
BTT-1	1.04	20.4	72.3	16.0	1.04	21.6	70.6	16.0
BTT-2	1.09	20.6	76.7	17.0	1.03	22.3	74.7	17.5
BTT-3	1.07	21.9	76.7	18.2	1.04	22.7	72.4	17.3
spiro-OMeTAD	1.09	21.6	76.8	18.1	1.07	22.6	71.4	17.5

Performance parameters measured under AM 1.5. Averaged values obtained by at least 10 cells.

The results show excellent performances for the three-benzotrithiophene derivatives, being **BTT-3** slightly better than its analogous **BTT-1** and **BTT-2**. PCEs above 18.2 % were observed on standard $MAPbI_3$-based solar cells, with almost no hysteresis when tested under the described conditions. The average PCEs of 17.7 ± 0.4 % indicates a very good reproducibility for this molecule. Comparing the results obtained for the three derivatives, the main difference when using **BTT-3** is the high J_{sc} (21.9 $mA \cdot cm^{-2}$). In fact, these values are very close to those obtained with the spiro-OMeTAD reference. On the other hand, devices with **BTT-2** show markedly high V_{oc} of almost 1.09 V, resulting in PCEs up to 17 % (average: 15.6 ± 1.1 %). **BTT-1** shows the lower performance, which might be also related to its low solubility in chlorobenzene compared to **BTT-2** and **BTT-3**, making it more difficult to obtain uniform films and reproducible

results, which can be seen from the relatively high standard deviation on the average PCE value of 13.9 ± 1.5 %. Nevertheless, PCE values of up to 16 % are still possible to be obtained by using this molecule. Comparing the devices prepared with the composite perovskite $(FAPbI_3)_{0.85}(MAPbBr_3)_{0.15}$ and BTT-based HTMs, the resulting performances are very similar. As previously observed, **BTT-1** is the least effective HTM, leading to lower fill factor and J_{sc}. On the contrary, compounds **BTT-2** and **BTT-3** behave similarly and excellent PCE values of up to 17.5 % are obtained. As a general trend, the presented chemical structures seem to favour the formation of homogeneous thin films with a good morphology and conductivity, which lead to excellent FF values (> 70 %) comparable to those obtained for spiro-OMeTAD. These experimental findings suggest high carrier mobility in these new materials.

As can be observed in the insets of figure 68, the trend in conductivity clearly supports the observation of the device performance obtained for the BTT-derivatives. **BTT-1** exhibits the lowest conductivity ($6.0 \cdot 10^{-6}$ S·cm^{-1}), followed by **BTT-2** ($1.3 \cdot 10^{-5}$ S·cm^{-1}) and **BTT-3** ($2.79 \cdot 10^{-5}$ S·cm^{-1}). Although this value is still about one order of magnitude lower than the reported value for spiro-OMeTAD ($8.7 \cdot 10^{-4}$ S·cm^{-1}),[107] it seems to be sufficient for obtaining a high performance when a thin HTM layer is used.

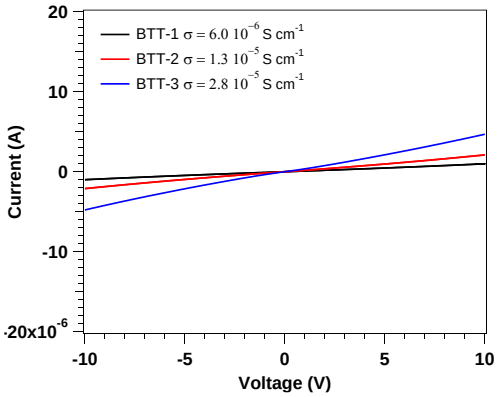

Figure 68. Conductivity of doped **BTT-1**, **BTT-2** and **BTT-3**.
(Conductivity values calculated using Ohm's law).

According to the results, the lower conductivity of **BTT-1** requires a very thin layer in order to have a good performance. Values for the shunt resistance of the three derivatives, estimated from the slope close to short circuit current, are very

similar for the champion devices (> 2000 Ohm). Nevertheless, using a thinner HTM layer, it is more likely to generate shunting paths due to for example, roughness of the perovskite layer, which is reflected in the bad reproducibility of devices when employing thin (< 100 nm) HTM layers. Thicker HTM layers (> 100 nm) allowed a good reproducibility in **BTT-3**-based devices.

3.2.3. Device performance employing BTT-3, BTT-4 and BTT-5

The three and four-armed molecules based on isomeric forms of BTT, **BTT-4** and **BTT-5** were also studied as HTMs in PSCs. The isomerism impact on the optical, electrochemical and photophysical properties of these molecules have been addressed previously. In this section, their PV performance is systematically investigated in comparison to their analogous **BTT-3**. PSCs using **BTT-4** and **BTT-5** as HTMs showed remarkable PCE values of 19.0 % and 18.2 %, respectively, under standard measurement conditions. These results confirm that BTT-derivatives as readily available heteroaromatic compounds and highly efficient HTMs for the preparation of PSCs.

The SEM image of a device using **BTT-4** as the HTM is shown in figure 69 as well as the energy alignments of the components in the devices (figure 70).

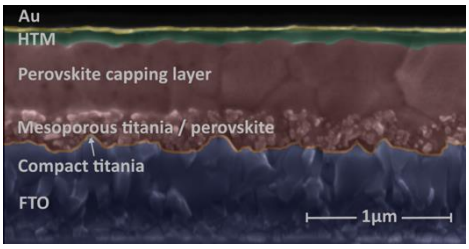

Figure 69. Cross-sectional SEM image of a PSC device with **BTT-4** as the HTM showing the different layers: FTO, 30 nm compact TiO_2 blocking layer, 250 nm mesoporous TiO_2, 600 nm perovskite capping layer, 100 nm HTM and 70 nm gold electrode.

BTT-4 and **BTT-5** exhibit a suited band alignment with the valence band edge of the perovskite, which led not only to an effective hole extraction from the perovskite to the HTM but also an effective electron-blocking. **BTT-4** presents similar HOMO level than **BTT-3**, both lower than that for spiro-OMeTAD. However, **BTT-5** exhibits a higher energetic value of HOMO, similar to that observed for spiro-OMeTAD.

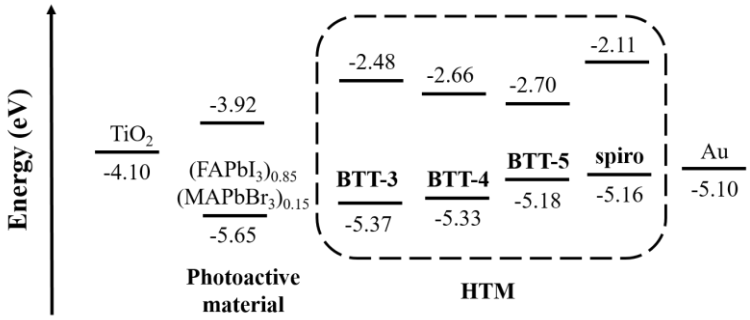

Figure 70. Energy diagram of the different components in the PV device.

PV testing of the PSC devices was performed under 1 sun AM 1.5 G (100 $mW \cdot cm^{-2}$) simulated sunlight. Figure 71 illustrates the complete study of the device performance with $(FAPbI_3)_{0.85}(MAPbBr_3)_{0.15}$ perovskite as an active layer.

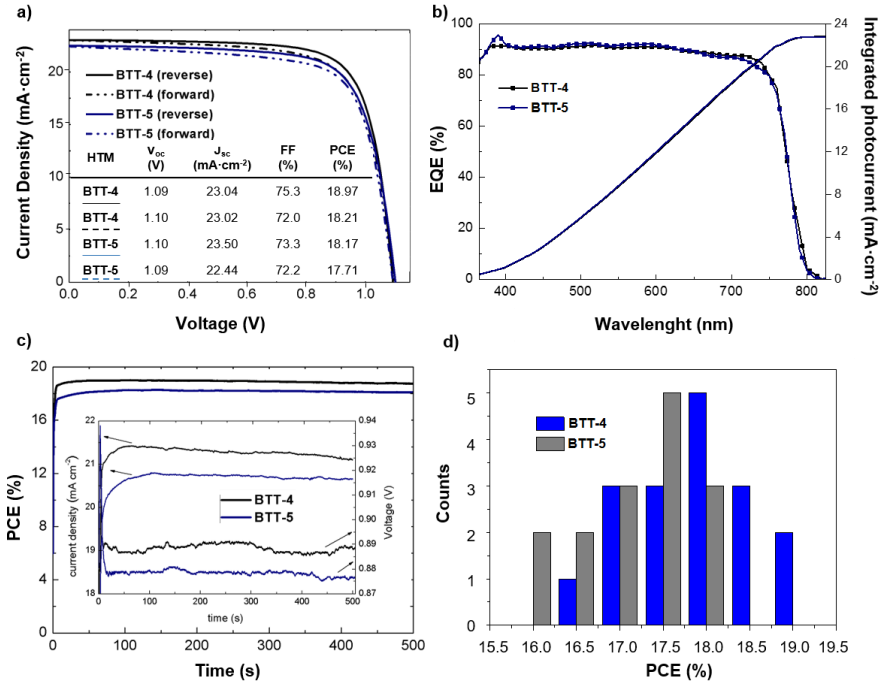

Figure 71. a) Reverse and forward J-V curves of **BTT-4** and **BTT-5** measured at 20 $mV \cdot s^{-1}$. **b**) External quantum efficiency (EQE) plots with corresponding integrated current. **c**) Stabilized PCE at maximum power point. Variations in V and J are shown in the inset. **d**) Efficiency distribution of 15 devices fabricated with each HTM.

The current J-V curves for **BTT-4** and **BTT-5** recorded under reverse bias (solid line) and forward bias (dashed lines) scans direction are shown in the figure 71a and the corresponding PV parameters are summarized as an insert. Both molecules show excellent PCEs of 18.2 % for **BTT-5** and 19.0 % for **BTT-4** with only little hysteresis. The V_{oc} is around 1.10 V for both compounds. Compared to **BTT-5**, **BTT-4** shows a slightly higher J_{sc} of 23.0 mA·cm^{-2} and a better FF of 75.3 % (22.5 mA·cm^{-2} and 73.3 % for **BTT-5**). The J_{sc} found by J-V measurements match well the ones calculated from the integrated external quantum efficiency (EQE) measurements shown in figure 71b. For both compounds, integrated currents were found to be around 22.5 mA·cm^{-2}. To further confirm the efficiencies obtained from the J-V measurements, peak power tracking experiments were performed to monitor the performance of the PSCs at their maximum power point for several minutes. (figure 71c). The measurements show stabilized efficiencies of 18 % for **BTT-5** and 19 % for **BTT-4**. The slight decrease in efficiency with time is associated with heating up of the device and is fully recovered after storing the device in dry air overnight. Efficiency stadistic distribution of 15 devices fabricated with **BTT-4** and **BTT-5** is shown in figure 71d. Good reproducibility is achieved for both compounds with average PCE values of 17.9 ± 0.7 % for **BTT-4** and 17.2 ± 0.6 % for **BTT-5**. The results were further confirmed by comparing the conductivity of the BTT-based HTMs.

As it was previously discussed in the general background, the hysteresis behavior in the PSCs has been found to depend on many factors. Device performance can depend markedly on voltage sweep rate or direction, or both. The nature (crystal size and shape), composition of the perovskite and the charge selective contacts, are hysteresis determining factors. To investigate the hysteresis behavior of the devices, J-V characteristics were measured at scan rate of 0.1 V·s^{-1} in the forward (-0.2 to 1.2 V) and reverse (1.2 to -0.2 V) bias. To obtain more quantitative information about J-V hysteresis, the hysteresis index (HI) was estimated using the equation (6):

$$HI = \frac{J_{rev}\cdot(0.8\cdot V_{oc}) - J_{fwd}(0.8\cdot V_{oc})}{J_{rev}(0.8\cdot V_{oc})} \quad (6)$$

where $J_{rev}(0.8\cdot V_{oc})$ and $J_{fwd}(0.8\cdot V_{oc})$ represent photocurrent density at 80 % of V_{oc} for the reverse and forward, respectively. The hysteresis index was calculated according to equation 6 and it was minimum in the case of **BTT-4**

(0.044) and **BTT-5** (0.031) and comparable to those obtained with spiro-OMeTAD (0.041).[183] These low values suggested that the fabrication method of the pervoskite layer is good enough to prevent such anomalous behaviors in these devices.

In addition, the conductivity values were measured using a linear fit and Ohm's law, nicely follow the trend found in the device efficiency (figure 72).

For the measurement, the molecules were spin-coated onto substrates having interdigitated gold electrodes (channel length 2.5 μm) using the same procedure as for the device preparation, adding 3 mol% of FK209 as a dopant in all of them. The thickness of the individual HTM layers was adjusted to obtain the best efficiencies.

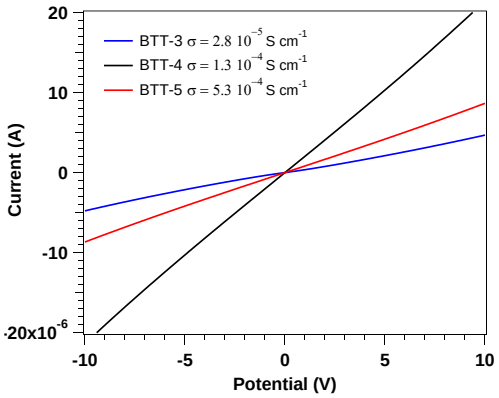

Figure 72. Conductivity of doped **BTT-3**, **BTT-4** and **BTT-5**.
(Conductivity values calculated using Ohm's law).

The highest conductivity was observed for **BTT-4** molecule with $\sigma = 5.3 \cdot 10^{-4}$ $S \cdot cm^{-1}$ closely followed by **BTT-5**. This value is around twenty times higher than **BTT-3** ($\sigma = 2.8 \cdot 10^{-5}$ $S \cdot cm^{-1}$) and indeed significantly higher to what is reported for spiro-OMeTAD ($\sigma = 4.7 \cdot 10^{-4}$ $S \cdot cm^{-1}$).[107] Compared to **BTT-3**, the new HTMs, **BTT-4** and **BTT-5**, having asymmetric central cores show enhanced device efficiencies. This is especially true for **BTT-4**, which can be directly

183. M. Salado, J. Idigoras, L. Calio, S. Kazim, M. K. Nazeeruddin, J. A. Anta, S. Ahmad, "Interface play between perovskite and hole selective layer on the performance and stability of perovskite solar cells", *ACS Appl. Mater. Interfaces*, **2016**, *8*, 34414-34421.

compared with **BTT-3**, as both molecules have three side arms, and shows a remarkable improvement from around 18 % to 19 %. The explanations could be that the sulfur atoms facing each other in the BTT core of **BTT-4** and **BTT-5** may further benefit the interaction with the perovskite material, thus allowing even better hole extraction compared to **BTT-3**. On the other hand, the asymmetric core might also have influence on the packing of the HTM molecules, which could be the reason for an increased hole mobility or conductivity.

In summary, BTT-derivatives have been efficiently synthesized by crosslinking a benzotrithiophene (BTT) core with different triphenylamine based ligands following a facile straightforward synthetic route. The impact that the isomerism of the BTT core has not only on the optical, electrochemical and photophysical properties but also on the PV performance has been studied. The novel multi-armed molecules were employed in PSCs and showed excellent performances, comparable to the state-of-the-art perovskite-based devices. PCEs of up to 16 % and 17 % were obtained for **BTT-1** and **BTT-2**, respectively, and a PCE value above 18 % for **BTT-3**, which is comparable to the reference spiro-OMeTAD. Impressive light-to-energy conversion efficiencies of 19 % for **BTT-4** and 18.2 % for **BTT-5** are measured, which even surpass the efficiency exhibited by **BTT-3** and the widely used spiro-OMeTAD. The difference in the performance obtained for the five BTT-derivatives could be accounted for by the different conductivity values obtained for the solid thin films. According to the results, the conductivity in **BTT-1** and **BTT-2** is considerably lower than that found for **BTT-3**, thus limiting the amount of current extracted from the device. **BTT-4** shows the highest conductivity, which nicely follows the trend found in the device efficiency. This could be due to the interaction with the perovskite material, which may be possible for the *cis* arrangement of the sulfur atoms facing each other in the **BTT-4** core, allowing even better hole extraction. Additionally, the asymmetric core might also have influence on the packing of the HTMs, which could also be the reason for an increased hole mobility or conductivity. Therefore, the results presented here further confirm the potential of the BTT family as a high efficient alternative to replacement the costly and widely establish spiro-OMeTAD as HTMs.

3.3. Perovskite solar cells employing BTF and BTP as HTMs

With an eye toward carrying out a complete and systematic study of the HTM impact on the PV performance, two new derivatives (figure 73) based on three pyrrole and three furan rings fused to a benzene central ring as central core, **BTP** and **BTF**, respectively, were studied in PSCs, in comparison to their analogous **BTT-3**.

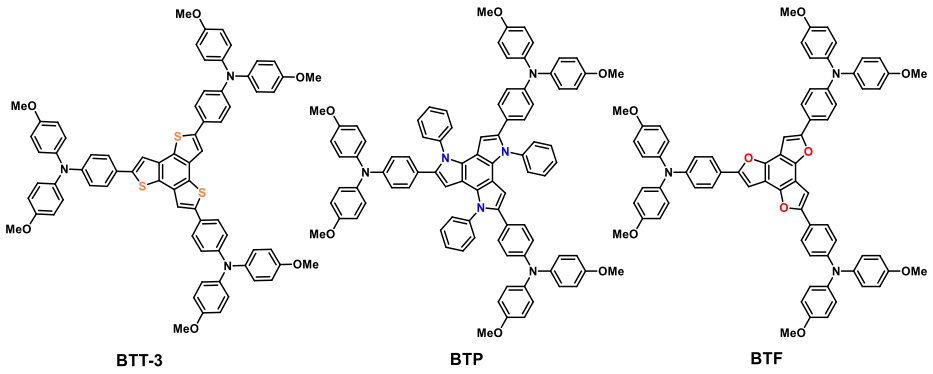

Figure 73. Molecular structure of the new HTMs tested in PSCs.

In addition to the detailed optical, electrochemical and thermal properties of the new HTMs studied in previous sections, mesoporous PSCs were prepared with **BTP** and **BTF** as HTMs showing remarkable efficiencies in combination with compositionally engineered perovskite $(FAPbI_3)_{0.85}(MAPbBr_3)_{0.15}$, comparable to those obtained by the isostructural **BTT-3** and spiro-OMeTAD.

3.3.1. Perovskite-based device fabrication

Following a similar procedure as before, mesoporous PSCs were fabricated from a stack of thin-layers onto FTO coated glass, with the following device configuration FTO/c-TiO_2 (30 nm)/m-TiO_2 (200 nm)/ $(FAPbI_3)_{0.85}(MAPBr_3)_{0.15}$ perovskite (400 nm)/HTM/Au (80 nm). For preparing the perovskite layer, stoichiometric amounts of PbI_2, $PbBr_2$, FAI, MABr in a mixture of DMF:DMSO (4:1) were spin-coated in two-step deposition procedure. Small amount of chlorobenzene (100 µl) was added during the spin-coating process as a mean to obtain shiny and smooth perovskite layer after the annealing process. Then, HTMs were deposited dynamically onto the thus-obtained perovskite layer by spin-coating a 20 mM and 30 mM chlorobenzene solution containing Li-TFSI,

t-BP and FK209 as additives, for **BTP** and **BTF**, respectively. Finally, gold electrodes were deposited by thermal evaporation using a shadow mask.

3.3.2. Device performance employing BTP and BTF as HTMs

Figure 74 shows the SEM image of a device using **BTP** as the HTM and figure 75 the energy diagram of the different components, using **BTF** or **BTP** as the HTM in comparison to spiro-OMeTAD and **BTT-3.**

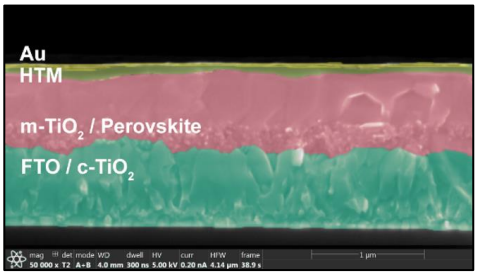

Figure 74. Cross sectional SEM image of a device fabricated with **BTP** as a HTM on $(FAPbI_3)_{0.85}(MAPbBr_3)_{0.15}$ perovskite.

The energetics of the **BTF** and **BTP** systems along with those of spiro-OMeTAD and **BTT-3** are represented in figure 75. The HOMO energy of all new compounds are higher in energy than the valence band of the $(FAPbI_3)_{0.85}(MAPbBr_3)_{0.15}$, which indicates that all of them are energetically favorable for hole scavenging from the perovskite. In addition, compared with spiro-OMeTAD, **BTF** and **BTT-3** exhibit lower-lying HOMO level, indicating that higher V_{oc} are expected. The LUMO energy of **BTF** and **BTP** are located above the conduction band of the perovskite, therefore, the new HTMs will also act as electron-blocking layer in PSCs.

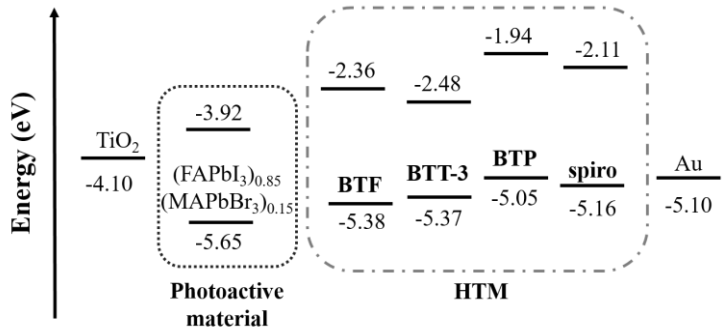

Figure 75. Energy diagram of the different components in the PV device.

The recorded J-V curves, EQE (figure 76a and 76b) and the PV parameters (table 25) corresponding to the aforementioned HTMs were measured in the same standard conditions as previous HTMs.

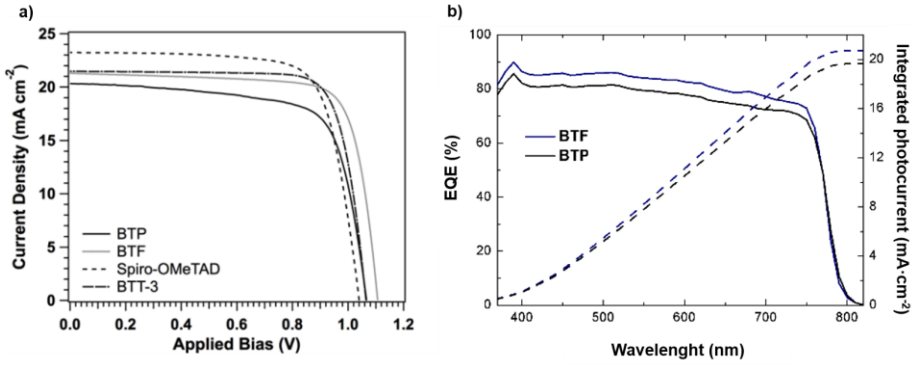

Figure 76. a) J-V curves showing the performance of PSCs prepared by using **BTP** and **BTF** in comparison to **BTT-3** and spiro-OMeTAD; **b**) EQE plots with corresponding integrated current.

PV devices incorporating **BTF** as a HTM yield an excellent PCE of 18.2 % with almost no hysteresis (figure 77), similar to that of the reference, spiro-OMeTAD. Moreover, remarkable high V_{oc} of 1.10 V were obtained along with J_{sc} of 21.3 mA·cm^{-2} and FF of 77.2 %. Nevertheless, **BTP** exhibits a dramatically lower PCE of 15.5 % with a J_{sc} of 20.3 mA·cm^{-2}, a FF of 71.3 % and an V_{oc} 1.06 V with pronounced hysteresis. This behaviour is envisaged to the non-planar structure of **BTP**, which may hinder the charge extraction/transport towards the Au electrode and increasing the carrier recombination, which eventually lead to lower FF. Relevantly, the higher V_{oc} for **BTF** is indeed expected, owing to the deeper HOMO energy of the **BTF**, which is supported by the estimated value from the electrochemical measurements. On the other hand, the isostructural **BTT-3** shows similar performance (18 %) than **BTF**. This slightly difference could be ascribed to the more planar structure of the **BTF**, which results not only in enhanced intermolecular interaction but also improved charge extraction. This result represents the higher PCE reported so far for a furan-based HTM.

Table 25. Device performances of **BTP** and **BTF** in comparison to **BTT-3** and spiro-OMeTAD.

HTM	V_{oc} (V)	J_{sc} (mA·cm^{-2})	FF (%)	PCE (%)
BTF	1.11	21.3	77.2	18.2
BTP	1.07	20.3	71.3	15.5
BTT-3	1.08	22.0	75.4	18.0
spiro-OMeTAD	1.04	23.2	74.3	18.0

Device parameters measured under AM 1.5. Averaged values obtained by at least 10 cells.

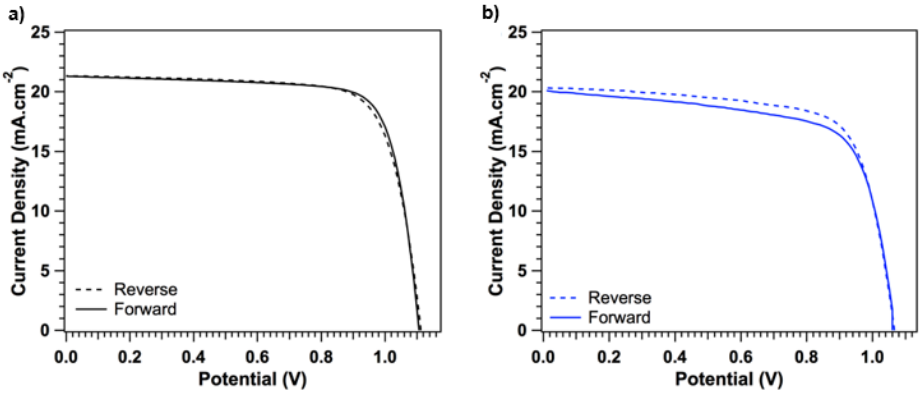

Figure 77. Hysteresis curve of a device with **a**) **BTF** and **b**) **BTP** on $(FAPbI_3)_{0.85}(MAPbBr_3)_{0.15}$ perovskite measured at 10 mV·s^{-1}.

BTF based devices showed almost negligible degree of hysteresis, in sharp contrast to the **BTF** based devices. J-V characteristics were measured at scan rate of 0.1 V s^{-1} in the reverse ($V_{oc} \rightarrow J_{sc}$) and forward ($J_{sc} \rightarrow V_{oc}$) bias as shown in figure 77. The hysteresis index was calculated following the equation (6). The hysteresis index for **BTF** and **BTP** are 0.005 and 0.050, respectively. Assuming that the preparation of the perovskite layer followed the same procedure, the main difference in the hysteresis index is likely related with the specific ionic accumulation in the interface perovskite/HTM.

In order to get more insight into the charge transport conductivity of the new HTMs, lateral thin-film conductivity of **BTF** and **BTP** was measured on OFET substrates. The evaluated conductivity of **BTF**, **BTP** and **BTT-3** (figure 78) are $1.4 \cdot 10^{-5}$ S·cm^{-1}, $1.7 \cdot 10^{-5}$ S·cm^{-1} and $2.8 \cdot 10^{-5}$ S·cm^{-1}, respectively. Surprisingly,

BTF shows the lowest conductivity despite possessing a more planar structure, as revealed by the XRD. In this regard, an improved interaction with the perovskite along with better hole extraction by **BTF** is surmised to be the main reason for the higher efficiencies achieved by **BTF**. On the other hand, **BTP** exhibits lower conductivity than **BTT-3**, which is attributed to its non-planar structure, which clearly affect the charge extraction and transport.

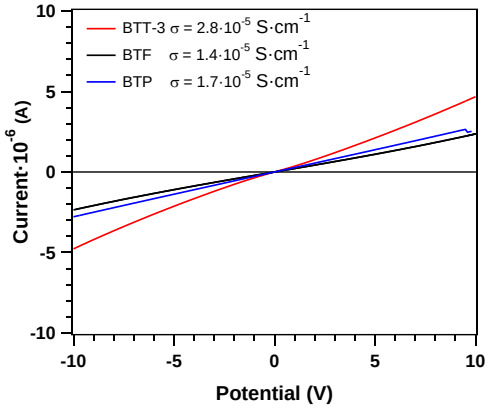

Figure 78. Conductivity of the **BTT-3**, **BTF** and **BTP** (values calculated using Ohm's law).

According to the above results, it can be concluded that the presence of heteroatoms in the structure plays an important role in the structural disposition of the hole-transporting layer, which has effect in the device performance. This candidate **BTF** exhibits a great behaviour in PSCs reaching an efficiency up to 18 %. On the other hand, **BTP** displays a non-planar structure due to the orthogonal *N*-phenyl substitution, which may affect the charge extraction and transport. It could be confirmed that this molecule does not present an ideal PV behaviour, reaching PCE values not higher than 16 %.

3.4. Perovskite solar cells employing TbT-based HTMs

The three star-shaped TbT-based molecules **TbT-1** to **TbT-3** synthesized in this thesis (figure 79), were also tested on solution-processed lead trihalide perovskite-based solar cells as HTMs. Maxima PCEs of 11.1 % for **TbT-1**, 14.3 % for **TbT-2** and 18.4 % for **TbT-3** were obtained under AM 1.5 sun. The promising value obtained with **TbT-3** as the HTM is comparable to that obtained with today's most commonly used HTM spiro-OMeTAD. The devices based on

the novel HTMs were prepared during the stay in Prof. M. K. Nazeeruddin's group at EPFL (Sion, Switzerland).

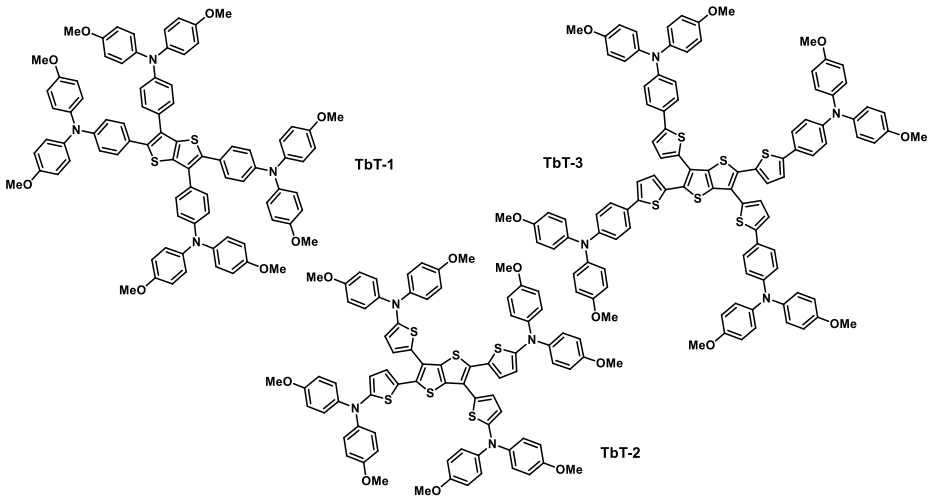

Figure 79. Molecular structure of the TbT-based HTMs tested in PSCs.

3.4.1. Device performance employing TbT-derivatives

The PV performance employing **TbT-1**, **TbT-2** and **TbT-3** as HTMs was studied in mesoporus $(FAPbI_3)_{0.85}(MAPbBr_3)_{0.15}$ perovskite-based devices. These were fabricated following the same protocol than the previously described for **BTP** and **BTF**.

Cross-section SEM image in figure 80 demonstrates the typical device structure based on different TiO_2 layers, perovskite and a HTM. As can be seen, the perovskite penetrates into the m-TiO_2 layer and forms an overlayer. The HTM then fill in the remaining pores in the TiO_2/perovskite layer and forms a thin capping layer on the top. Finally, the devices were completed by evaporation of gold electrode.

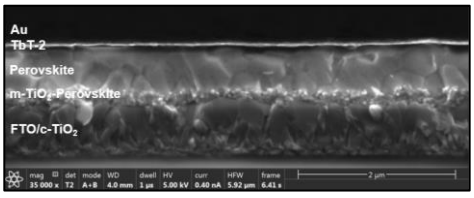

Figure 80. Cross sectional SEM image of a device fabricated with **TbT-2** on $(FAPbI_3)_{0.85}(MAPbBr_3)_{0.15}$ perovskite.

Figure 81 presents the energy levels of the components in the corresponding device.

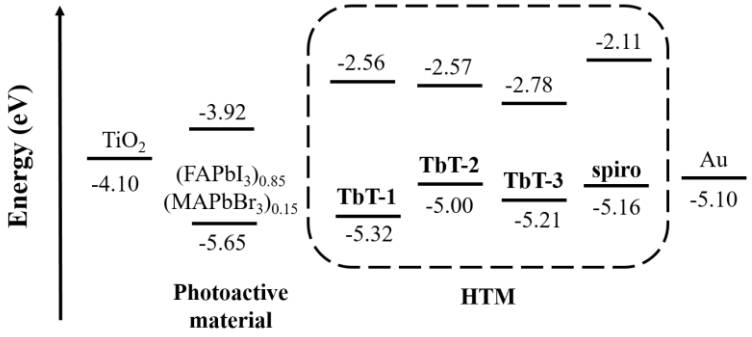

Figure 81. Energy diagram of the different components in the PV device.

Both **TbT-1** and **TbT-3** present a lower HOMO energy than that for spiro-OMeTAD, whereas **TbT-2** exhibits a slightly energetically higher value than that for the reference. Nevertheless, the three TbT-derivatives show a correct alignment with the valence band of the perovskite, which makes possible not only the extraction of the holes but also the electron-blocking.

Figure 82 shows the J-V curves of PSCs based on **TbT-1**, **TbT-2**, **TbT-3** and spiro-OMeTAD as HTMs, and the corresponding PV parameters are given in table 26. The **TbT-1**-based PSCs provided a J_{sc} of 14.7 mA·cm^{-2}, V_{oc} of 1.00 V and a FF of 75.0 %, affording an overall PCE of 11.1 %. Under the same conditions, the **TbT-2**-based cell showed a J_{sc} of 22.5 mA·cm^{-2}, a V_{oc} of 0.91 V and an FF of 69.0 %, corresponding to a PCE value of 13.8 %. Finally, **TbT-3**-based cells showed a J_{sc} of 21.9 mA·cm^{-2}, a V_{oc} of 1.08 V and a FF of 78.0 %, displaying an overall PCE of 18.4 %. The latter PV parameters are comparable to that of the cell based on spiro-OMeTAD (J_{sc} of 23.2 mA·cm^{-2}, V_{oc} of 1.04 V, FF of 74.0 %, and a PCE of 18 %). Clearly, the PV performance is quite sensitive to the structural molecular modification. The PCE value of **TbT-3**-based cell is significantly higher than that of **TbT-1** and **TbT-2** owing to an improved V_{oc} and FF. The higher FF recorded for **TbT-3** could be ascribed to an enhanced conductivity in comparison to **TbT-1** and **TbT-2.** It is clear that the design of new HTMs with a more extended 3D molecular structure and higher molecular weight can improve the PV performance of PSCs. The fundamental reason to explain this noticeable difference in the corresponding devices is the processing of the HTMs. **TbT-1** is considerably insoluble in the solvents used for the spin-

coating deposition, which is a very important parameter for the preparation of smooth thin-films. **TbT-2** presents better solubility but still lower than **TbT-3**, which is completely soluble allowing the formation of very smooth and uniform thin-films.

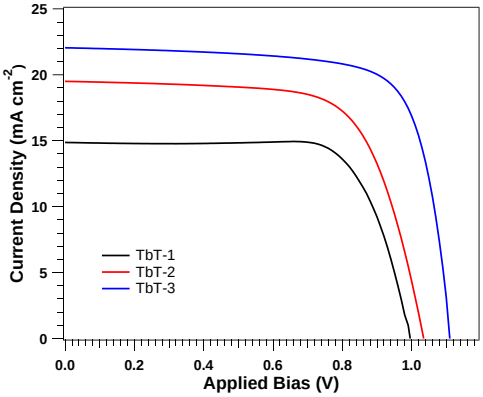

Figure 82. J-V curves showing the performance of perovskite solar cells prepared by using **TbT-1**, **TbT-2** and **TbT-3**.

Table 26. Performance parameters of the best devices employing TbT-derivatives as HTMs.

HTM	V_{oc} (V)	J_{sc} (mA·cm^{-2})	FF (%)	PCE (%)
TbT-1	1.00	14.7	75.5	11.1
TbT-2	1.03	19.5	68.4	13.8
TbT-3	1.08	21.9	77.8	18.4
spiro-OMeTAD	1.04	23.2	74.3	18.0

Device parameters measured under AM 1.5. Averaged values obtained by at least 10 cells.

In addition, **TbT-3** presents almost no hysteresis in its J-V curve (figure 83). The hysteresis index was calculated according to equation 6 and it was minimum in the case of **TbT-3** (0.041) similar to that obtained with spiro-OMeTAD (0.041) and higher for **TbT-2** (0.219) and **TbT-1** (0.418).

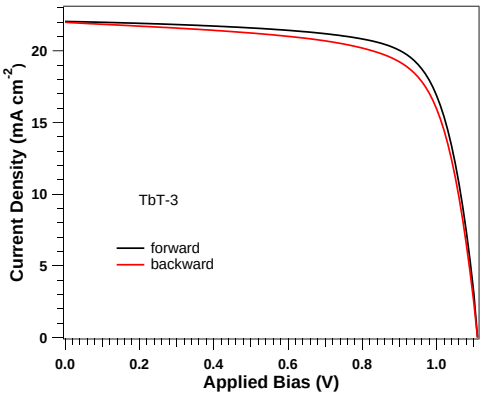

Figure 83. Hysteresis curve of a device with BTF on $(FAPbI_3)_{0.85}(MAPbBr_3)_{0.15}$ perovskite measured at 10 $mV \cdot s^{-1}$.

• Experimental Procedure

Chapter 1. Hole-transporting materials
for perovskite solar cells

4. EXPERIMENTAL SECTION

General Methods. Chemicals and reagents were purchased from commercial suppliers and used as received. All solvents were dried according to standard procedures. Air-sensitive reactions were carried out under nitrogen atmosphere. The device preparation was done in a glovebox under nitrogen atmosphere. Flash chromatography was performed using silica gel (Merck, Kieselgel 60, 230-240 mesh or Scharlau 60, 230-240 mesh). Analytical thin layer chromatography (TLC) was performed using aluminum coated Merck Kieselgel 60 F254 plates. NMR spectra were recorded on a Bruker Advance 400 (^{1}H: 400 MHz; ^{13}C: 100 MHz) spectrometer at 298 K using partially deuterated solvents as internal standards. Coupling constants (*J*) are denoted in Hz and chemical shifts (δ) in ppm. Multiplicities are denoted as follows: s: singlet, d: doublet, t: triplet, m: multiplet. FT-IR spectra were recorded on a Bruker Tensor 27 (ATR device) spectrometer. UV-vis spectra were recorded in a Varian Cary 50 spectrophotometer. Emission spectra were recorded in the Fluorolog TCSPC (Horiba Jobin Yvon) fluorescence equipment. MALDI-TOF experiments were recorded on a MAT 95 thermo spectrometer and a Bruker REFLEX spectrometer respectively. Dithranol or DCTB was used as a matrix in general experiments and a polymeric fraction (PEG, PEGMe, PPG, PMMA) was also added in the case of high resolution/HRMS. Cyclic voltammetry (CV) experiments were recorded on a BAS CV50W electrochemical analyser. They were conducted in 0.1 M solution of (n-Bu)$_4$NPF$_6$ (TBAPF$_6$) and in particularly indicated solvent, using glassy carbon and platinum wire as a working and counter electrode respectively. As reference electrode platinum wire or Ag^+/AgCl were used and ferrocene was added as an internal standard. Its oxidation potential in DCM was positioned at 0.7 V vs. NHE and new molecules' oxidation potential were calculated relative to NHE.; Before each measurement, solution was degassed with N_2 and the experiments were recorded using a scan rate of 50 mV/s. Thermogravimetric analysis (TGA) was performed using a TA Instruments TGAQ500 with a ramp of 10 ºC/min under N_2 from 100 to 1000 ºC. DSC was performed on a Discovery DSC from TA instruments. Three cycles were recorded under nitrogen, heating (until 400 ºC) and cooling (50 ºC) at 20 ºC/min of scanning rate.

Solar cell characterization (EPFL)

High resolution cross-section images of the devices were recorded with a ZEISS Merlin HR-SEM scanning electron microscope. The PV device performance was analyzed using a VeraSol LED solar simulator (Newport) producing 1 sun AM 1.5 G (100 W cm^{-2}) sunlight. Current density-voltage (J-V) curves were measured in air with a potentiostat (Keithley). The light intensity was calibrated with an NREL certified KG5 filtered Si reference diode. The solar cells were masked with a metal aperture of 0.16 cm^2 to define the active area. The J-V curves were recorded scanning at 10 or 20 $mV \cdot s^{-1}$.

1. Synthesis of tetraarylethene derivatives: TAEs

***p*-Methoxydiphenylamine[131] (68)**

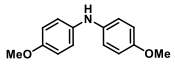

This compound was synthesized according to a previously reported procedure and showed identical spectroscopic properties to those reported therein. ^{1}H NMR (400 MHz, $CDCl_3$, 298 K) δ: 7.10-6.75 (m, 4H), 6.80 (d, *J* = 7.9 Hz, 4H), 3.77 (s, 6H).

***p*-Methoxytriphenylamine[184] (69)**

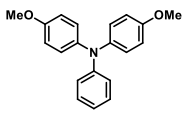

This compound was synthesized according to a previously reported procedure and showed identical spectroscopic properties to those reported therein.^{1}H NMR (400 MHz, $CDCl_3$, 298 K) δ: 7.21-7.16 (m, 2H), 7.06 (m, 4H), 6.95 (d, *J* = 7.6 Hz, 2H), 6.87 (t, *J* = 7.3 Hz, 1H), 6.83 (m, 4H), 3.80 (s, 6H); ^{13}C NMR (100 MHz, $CDCl_3$, 298 K) δ: 155.7, 148.8, 141.2, 128.9, 126.4, 120.9, 120.6, 114.6, 55.5.

3,6-Dimethoxy-9*H*-carbazole[185] (70)

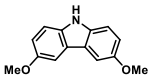

This compound was synthesized according to a previously reported procedure and showed identical spectroscopic properties to those reported therein. ^{1}H NMR (400 MHz, $CDCl_3$, 298 K) δ:

184. M. A. Topchiy, P. B. Dzhevakov, M. S. Rubina, O. S. Morozov, A. F. Asachenko, M. S. Nechaev, "Solvent-free Buchwald-Hartwig (hetero)arylation of anilines, diarylamines, and dialkylamines mediated by expanded-ring *N*-heterocyclic carbene palladium complexes", *Eur. J. Org. Chem.*, **2016**, *2016*, 1908-1914.
185. A. Bucinskas, G. Bagdziunas, A. Tomkeviciene, D. Volynyuk, N. Kostiv, D. Gudeika, V. Jankauskas, M. Rutkis, J. V. Grazulevicius, "Structure-property relationship of isomeric diphenylethenyl-disubstituted dimethoxycarbazoles", *RSC Adv.*, **2015**, *5*, 49577-49589.

7.76 (s, 1 H), 7.50 (d, *J* = 2.4 Hz, 2H), 7.31 (d, *J* = 8.7 Hz, 2H), 7.05 (dd, *J* = 8.7, *J* = 2.4 Hz, 2H), 3.93 (s, 6H).

3,6-Bis[*N*,*N*-bis(4-methoxyphenyl)amino]carbazole (71)

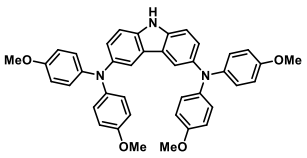

To a solution of compound **76** (430 mg, 0.50 mmol) in toluene (50 mL), TBAF (261 mg, 1 mmol) was added and the reaction mixture was stirred at r.t. for 10 minutes. The removal of the organic solvent under vacuum led to the crude product, which was purified by column chromatography (silica gel, DCM) to afford the desired compound **71** as a green solid (298 mg, 0.48 mmol, 96 %). ^{1}H NMR (400 MHz, DMSO-d_6, 298 K) δ: 11.17 (s, 1H), 7.64 (s, 2H), 7.41 (d, *J* = 8.4 Hz, 2H), 7.07 (dd, *J* = 8.8 Hz, 2H), 6.87-6.79 (m, 16H), 3.70 (s, 12H).

4-Iodo-*N*,*N*-bis(4-methoxyphenyl)aniline[186] (72)

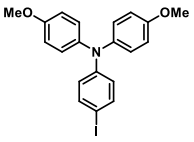

This compound was synthesized according to a previously reported procedure and showed identical spectroscopic properties to those reported therein. ^{1}H NMR (400 MHz, acetone-d_6, 298 K) δ: 7.47-7.45 (m, 2 H), 7.07-7.05 (m, 4 H), 6.93-6.90 (m, 4 H), 6.64-6.62 (m, 2 H), 3.79 (s, 6 H). MALDI-TOF calcd. for $C_{20}H_{18}INO_2$, m/z: 431.3; found 431.3.

4-(4,4,5,5-Tetramethyl-1,3,2-dioxaborolan-2-yl)-*N*,*N*-bis(4-methoxyphenyl) aniline[187] (73)

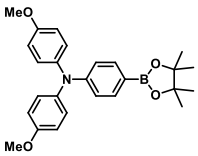

This compound was synthesized according to a previously reported procedure and showed identical spectroscopic properties to those reported therein. ^{1}H NMR (400 MHz, $CDCl_3$, 298 K) δ: 7.61-7.58 (m, 2 H), 7.08-7.04 (m, 4 H), 6.88-6.81 (m, 6 H), 3.80 (s, 6 H), 1.31 (s, 12 H); ^{13}C NMR

186. H. C. Schmidt, M. Spulber, M. Neuburger, C. G. Palivan, M. Meuwly, O. S. Wenger, "Charge transfer pathways in three isomers of naphthalene-bridged organic mixed valence compounds", *J. Org. Chem.*, **2016**, *81*, 595-602.
187. L. Yu, J. Xi, H. T. Chan, T. Su, L. J. Antrobus, B. Tong, Y. Dong, W. K. Chan, D. L. Phillips, "Novel organic D-π-2A sensitizer for dye sensitized solar cells and its electron transfer kinetics on TiO_2 surface", *J. Phys. Chem. C*, **2013**, *117*, 2041-2052.

(100 MHz, $CDCl_3$, 298 K) δ: 156.2, 140.4, 135.7, 127.1, 118.7, 114.7, 83.4, 55.5, 24.8.

3,6-Dibromo-9*H*-carbazole[188] (74)

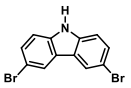

This compound was synthesized according to a previously reported procedure and showed identical spectroscopic properties to those reported therein. ^{1}H NMR (400 MHz, $CDCl_3$, 298 K) δ: 10.37 (s, 1H), 8.13 (d, *J* = 1.9 Hz, 2H), 7.52 (d, *J* = 8.6 Hz, 2H), 7.31 (dd, *J* = 8.6 Hz, *J* = 1.9 Hz, 2H).

3,6-Dibromo-9-(*tert*-butyldiphenylsilyl)-9*H*-carbazole (75)

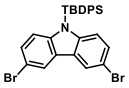

To a solution of 3,6-dibromo-9*H*-carbazole (**74**) (1.06 g, 1.88 mmol) in DMF (30 mL), NaH (123 mg, 5.10 mmol) and ClTBDPS (1 mL, $3.9 \cdot 10^{-3}$ mmol) were added and the reaction was stirred for 3 hours at r. t. The reaction mixture was extracted with toluene (3x50 mL) and washed with an aqueous solution of $NaHCO_3$. The combined organic extracts were dried over Na_2SO_4 and concentrated *in vacuo*. The crude product was purified by flash column chromatography (silica gel, 1:2, 2:1 and 1:0 toluene/hexane) to afford **75** (1.58 g, $2.80 \cdot 10^{-3}$ mmol, 86 %), which was washed several times with acetone.^{1}H NMR (400 MHz, $CDCl_3$, 298 K) δ: 7.96 (d, *J* = 1.9, 2H), 7.64 (m, 4H), 7.52 (d, *J* = 8.6, 2H), 7.25 (m, 2H), 7.12 (m, 2H), 7.04 (m, 2H), 7.0 (dd, *J* = 8.6, *J* = 1.92, 2H), 1.24 (s, 9H).

9-(*Tert*-butyldiphenylsilyl)-3,6-bis[*N*,*N*-bis(4-methoxyphenyl)amino] carbazole (76)

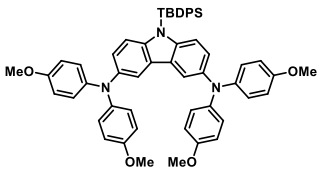

To a dry round bottom flask equipped with a stirrer bar, compound **75** (336 mg, 0.60 mmol), compound **68** (314 mg, 1.37 mmol), XPhos (28 mg, 0.06 mmol) and $Pd_2(dba)_3$ (27 mg, 0.03 mmol) were dissolved in dry toluene (20 mL). The resulting mixture was degassed for 30 minutes. Finally, Na^{t}BuO (172 mg, 1.79 mmol) was added to the solution, which was heated to 111 ºC for 2 hours. The reaction mixture was extracted with toluene (3x30 mL), the combined organic

188. M. Ludwiczak, M. Majchrzak, M. Bayda, B. Marciniak, M. Kubicki, B. Marciniec, "Stereoselective synthesis and luminescence properties of novel trans-regular *N*-alkylcarbazolylene–silylene–vinylene polymers", *J. Organomet. Chem.*, **2014**, *750*, 150-161.

layers were dried over Na_2SO_4 and the solvent was removed under reduced pressure. The crude product was purified by column chromatography (silica gel, DCM and then 120:1 DCM/AcOEt). Compound **9** was afforded as a white solid (434 mg, 0.50 mmol, 84 %). ^{1}H NMR (400 MHz, $CDCl_3$, 298 K) δ: 7.64 (d, *J* = 1.9, 2H), 7.41 (d, *J* = 8.4 Hz, 2H), 7.19 (m, 4H) 7.14 (m, 4H), 7.07 (dd, *J* = 8.8 Hz, 2H), 7.04 (m, 2H), 6.87-6.79 (m, 16H), 3.70 (s, 12H), 1.24 (s, 9H).

4,4′-Bis[*N*,*N*-bis(4-methoxyphenyl)amino]benzophenone[189] (77)

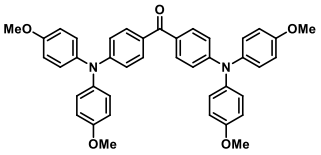

This compound was synthesized according to a previously reported procedure and showed identical spectroscopic properties to those reported therein. ^{1}H NMR (400 MHz, acetone-d_6, 298 K) δ: 7.60 (d, *J* = 8.9 Hz, 4H), 7.18 (d, *J* = 9.0 Hz, 8H), 6.97 (d, *J* = 9.0 Hz, 8H), 6.78 (d, *J* = 8.9 Hz, 4H), 3.81 (s, 12H).

4,4',4'',4'''-Tetrakis [*N*,*N*-bis(4-methoxyphenyl) amino]-1,1,2,2-tetraphenylethene, TAE-1

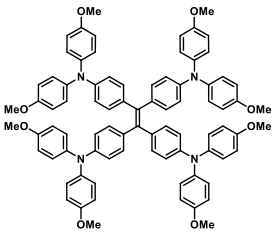

Compound **77** (830 mg, 1.30 mmol) in dry THF (10 mL) was added to a slurry of Zn dust (426 mg, 6.51 mmol) and $TiCl_3$ (1M in 1:2 THF/DCM, 3.25 mL, 3.25 mmol) and heated at reflux for 4 hours under inert atmosphere. The reaction mixture was filtered and concentrated under reduced pressure. The crude product was purified by flash column chromatography (silica gel, DCM) to afford **TAE-1** as a yellow solid, which was washed several times with acetone (1.16 g, 0.94 mmol, 72 %). ^{1}H NMR (400 MHz, $CDCl_3$, 298 K) δ: 7.01 (m, 16H), 6.87 (m, 8H), 6.79 (m, 16H), 6.69 (m, 8H), 3.77 (s, 24H); ^{13}C NMR (100 MHz, $CDCl_3$, 298 K) δ: 155.6, 146.6, 141.2, 137.1, 132.3, 126.3, 120.0, 114.7, 55.6; FTIR (neat) ν: 3036, 2932, 2833, 1500, 1238, 1034, 826 cm^{-1}; HRMS [MALDI-TOF] calcd. for $C_{82}H_{72}N_4O_8$ [M^+], 1240.5345; found 1240.5334; elemental analysis calcd. for $C_{82}H_{72}N_4O_8$, C: 79.33, H: 5.85, N: 4.51; found C: 78.71, H: 5.77, N: 4.45; m.p.: 278-280 ºC.

189. V. Mimaite, J. V. Grazulevicius, R. Laurinaviciute, D. Volyniuk, V. Jankauskas, G. Sini, "Can hydrogen bonds improve the hole-mobility in amorphous organic semiconductors? Experimental and theoretical insights", *J. Mater. Chem. C*, **2015**, *3*, 11660-11674.

1,1,2,2-Tetrakis(4-bromophenyl)ethene[190] (80)

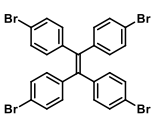

This compound was synthesized according to a previously reported procedure and showed identical spectroscopic properties to those reported therein. ^{1}H NMR (400 MHz, $CDCl_3$, 298 K) δ: 7.29 (m, 8H), 6.88 (m, 8H); ^{13}C NMR (100 MHz, $CDCl_3$, 298 K) δ: 141.5, 139.6, 132.7, 131.3, 121.3.

4,4',4'',4'''-Tetrakis(3,6-dimethoxycarbazol-9-yl)-1,1,2,2-tetraphenylethene, TAE-2

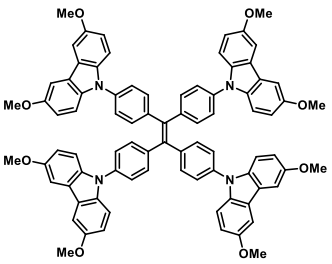

To a dry round bottom flask equipped with a stirrer bar, compounds **80** (50 mg, 0.08 mmol) and **70** (88 mg, 0.39 mmol), XPhos (20 mg, 0.04 mmol) and $Pd_2(dba)_3$ (7 mg, 0.01 mmol) were dissolved in dry toluene (15 mL). The resulting mixture was degassed for 30 minutes. Finally, Na^{t}BuO (414 mg, 4.31 mmol) was added to the solution, which was heated to 100 ºC for 1.5 hours. The mixture was extracted with toluene (3x30 mL) and washed with water. The combined organic layers were dried over Na_2SO_4 and the solvent was removed under reduced pressure. The crude product was purified by column chromatography (silica gel, DCM and then 100:1 DCM/AcOEt) to afford **TAE-2** as a light yellow solid, which was washed several times with methanol (60 mg, 0.05 mmol, 61 %). ^{1}H NMR (400 MHz, $CDCl_3$, 298 K) δ: 7.56 (d, J = 2.5 Hz, 8H), 7.47 (s, 16H), 7.36 (m, 8H), 6.98 (m, 8H), 3.94 (s, 24H); ^{13}C NMR (100 MHz, $CDCl_3$, 298 K) δ: 154.6, 142.0, 136.5, 133.3, 126.4, 124.2, 115.6, 111.1, 103.6, 56.6; FTIR (neat) ν: 3042, 2994, 2941, 2830, 1605, 1580, 1512, 1465, 1434, 1365, 1329, 1289, 1204, 1155, 1108, 1033, 948, 905, 836, 798, 734, 664, 588 cm^{-1}; HRMS [MALDI-TOF] calcd. for $C_{82}H_{64}N_4O_8$ [M^+], 1232.4719; found 1232.4703; elemental analysis calcd. for $C_{82}H_{64}N_4O_8$, C: 79.85, H: 5.23, N: 4.54; found C: 78.76, H: 5.22, N: 4.37; m.p.: 319-320 ºC.

190. K. Yuan, P. Guo-Wang, T. Hu, L. Shi, R. Zeng, M. Forster, T. Pichler, Y. Chen, U. Scherf, "Nanofibrous and graphene-templated conjugated microporous polymer materials for flexible chemosensors and supercapacitors", *Chem. Mater.*, **2015**, *27*, 7403-7411.

4,4',4'',4'''-Tetrakis[3,6-bis(*N*,*N*-bis(4-methoxyphenyl)amino)carbazol-9-yl]-1,1,2,2-tetraphenylethene, TAE-3

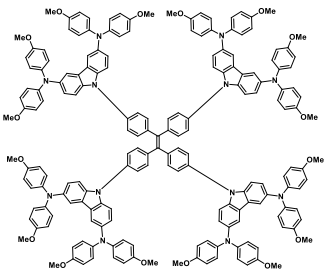

To a dry round bottom flask equipped with a stirrer bar, compounds **80** (112 mg, 0.17 mmol), compound **71** (536 mg, 0.86 mmol) XPhos (45 mg, 0.09 mmol) and $Pd_2(dba)_3$ (16 mg, 0.02 mmol) were dissolved in dry toluene (30 mL). The resulting mixture was degassed for 30 minutes. Finally, Na^{t}BuO (91 mg, 0.95 mmol) was added to the solution, which was heated to 100 ºC for 2 hours. The reaction mixture was extracted with toluene (3x50 mL) and washed with brine. The combined organic layers were dried over Na_2SO_4 and the solvent was removed under reduced pressure. The crude product was purified by column chromatography (silica gel, 100:1 and then 20:1 DCM/AcOEt). **TAE-3** was obtained as a yellow solid (428 mg, 0.15 mmol, 88 %), which was washed several times with methanol, hexane and acetone. ^{1}H NMR (400 MHz, THF-d_8, 298 K) δ: 7.62 (d, *J* = 1.5 Hz, 8H), 7.51-7.40 (m, 16H), 7.30 (d, *J* = 8.8 Hz, 8H), 7.08 (dd, *J* = 8.8, 2.1 Hz, 8H), 6.97 (m, 32H), 6.76 (m, 32H), 3.77 (s, 48H); ^{13}C NMR (100 MHz, $CDCl_3$, 298 K) δ: 154.7, 142.5, 141.8, 141.6, 140.6, 137.2, 136.7, 132.8, 125.9, 124.4, 124.3, 124.1, 116.5, 114.6, 110.5, 55.5; FTIR (neat) ν: 3040, 2996, 2833, 1604, 1503, 1458, 1364, 1318, 1270, 1235, 1175, 1107, 1035, 914, 821, 731, 643, 605, 570 cm^{-1}; HRMS [MALDI-TOF] calcd. for $C_{186}H_{152}N_{12}O_{16}$ [M$^+$], 2809.1444; found 2809.1430; elemental analysis calcd. for $C_{186}H_{152}N_{12}O_{16}$, C: 79.47, H: 5.45, N: 5.98; found C: 78.44, H: 5.43, N: 5.74; m.p.:210-213 ºC.

2. Synthesis of bifluorenylidene derivatives: BFs

3,6-Dibromophenanthrene-9,10-dione[191] (81)

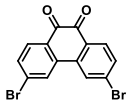

This compound was synthesized according to a previously reported procedure and showed identical spectroscopic properties to those reported therein. ^{1}H NMR (400 MHz, $CDCl_3$, 298 K) δ: 8.17

191. K. Brunner, A. Van Dijken, H. Börner, J. J. a. M. Bastiaansen, N. M. M. Kiggen, B. M. W. Langeveld, "Carbazole compounds as host materials for triplet emitters in organic light-emitting diodes: Tuning the homo level without influencing the triplet energy in small molecules", *J. Am. Chem. Soc.*, **2004**, *126*, 6035-6042.

(d, *J* = 1.5 Hz, 2H), 8.13 (d, *J* = 8 Hz, 2H), 7.72 (dd, *J* = 1.5 Hz, *J* = 8 Hz, 2H). ^{13}C NMR (100 MHz, $CDCl_3$, 298 K) δ: 178.2, 136.3, 134.6, 133.1, 132.5, 130.2, 127.3.

3,6-Dibromo-9*H*-fluoren-9-one[191] (82)

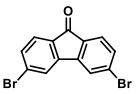

This compound was synthesized according to a previously reported procedure and showed identical spectroscopic properties to those reported therein. ^{1}H NMR (400 MHz, $CDCl_3$, 298 K) δ: 7.71 (d, *J* = 1.5 Hz, 2H), 7.58 (d, *J* = 8 Hz, 2H), 7.52 (dd, *J* = 1.5 Hz, *J* = 8 Hz, 2H); ^{13}C NMR (100 MHz, $CDCl_3$, 298 K) δ: 145.2, 133.3, 130.5, 126.2, 124.7.

3,3',6,6'-Tetrabromo-9,9'-bifluorenylidene (83)

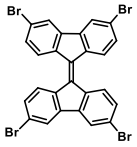

Compound **82** (1.50 g, 4.44 mmol) and Lawesson's reagent (898 mg, 2.22 mmol) were dissolved in 90 mL of toluene under nitrogen atmosphere. The mixture was stirred at 111 ºC for 18 hours. After evaporation of the solvent, the mixture was purified by flash column chromatography (silica gel, heated toluene) affording a solid which was washed with methanol and hexane. Compound **15** was obtained as an orange solid (902 mg, 1.40 mmol, 63 %).^{1}H NMR (400 MHz, $CDCl_3$, 298 K) δ: 8.03 (d, *J* = 8.4 Hz, 4H), 7.73 (d, *J* = 1.9 Hz, 4H), 7.29 (dd, *J* = 8.4, *J* = 1.19 Hz, 4H). MALDI-TOF calcd. for $C_{26}H_{12}Br_4$ [M^+], 643.8; found 643.9.

3,3',6,6'-Tetrakis[*N*,*N*-bis(4-methoxyphenyl)amino]-9,9'-bifluorenylidene, BF-1

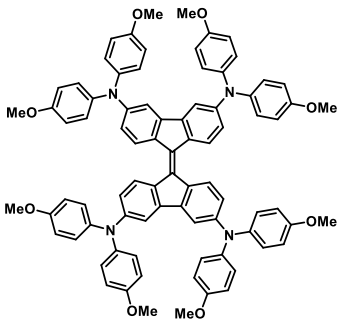

To a dry round bottom flask equipped with a stirrer bar, compounds **83** (100 mg, 0.16 mmol), **68** (178 mg, 0.78 mmol) XPhos (40 mg, 0.02 mmol) and $Pd_2(dba)_3$ (15 mg, 0.02 mmol) were dissolved in dry toluene (35 mL). The resulting mixture was degassed for 30 minutes. Finally, Na^{t}BuO (82 mg, 0.85 mmol) was added to the solution which was heated to 100 ºC for 3 hours. The reaction mixture was extracted with toluene (3x50 mL) and washed with water. The combined organic layers were dried over Na_2SO_4 and the solvent was removed under reduced pressure. The crude product was purified by column chromatography (silica gel, DCM and then 100:2 DCM/AcOEt). **BF-1** was afforded as a blue solid which was washed several times with methanol, hexane

and ether (124 mg, 0.10 mmol, 63 %).^{1}H NMR (400 MHz, THF-d_8, 298 K) δ: 7.92 (d, *J* = 8.7 Hz, 4H), 7.03 (d, *J* = 2.2 Hz, 4H), 6.96-6.82 (m, 16H), 6.77-6.64 (m, 16H), 6.54 (dd, *J* = 8.7, *J* = 2.2 Hz, 4H), 3.63 (s, 24H); ^{13}C NMR (700 MHz, $CDCl_3$, 298K) δ 155.7, 148.4, 141.2, 141.0, 132.4, 127.0, 126.3, 119.9, 114.7, 112.3, 55.5; FTIR (neat) ν: 3042, 2996, 2937, 2834, 1598, 1557, 1504, 1448, 1320, 1270, 1237, 1176, 1116, 1034, 825, 721, 575 cm^{-1}; HRMS [MALDI-TOF] calcd. for $C_{82}H_{68}N_4O_8$ [M^+], 1236.5032; found 1236.5029; elemental analysis calcd. for $C_{82}H_{68}N_4O_8$, C: 79.59, H: 5.54, N: 4.53; found C: 79.13, H: 5.70, N: 4.08. m.p. > 330 ºC.

3,3',6,6'-Tetrakis(3,6-dimethoxycarbazol-9-yl)-9,9'-bifluorenylidene, BF-2

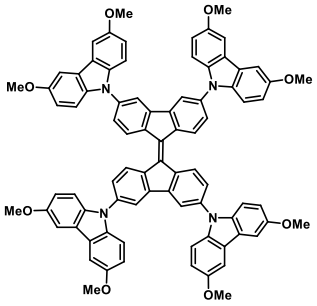

To a dry round bottom flask equipped with a stirrer bar, compounds **83** (100 mg, 0.16 mmol), **70** (177 mg, 0.78 mmol), XPhos (37 mg, 0.08 mmol) and $Pd_2(dba)_3$ (14 mg, 0.02 mmol) were dissolved in dry toluene (30 mL). The resulting mixture was degassed for 30 minutes. Finally, Na^{t}BuO (82 mg, 0.85 mmol) was added to the solution which was heated to 100 °C for 4 hours. The reaction mixture was extracted with toluene (3x50 mL) and washed with water. The combined organic layers were dried over Na_2SO_4 and the solvent was removed under reduced pressure. The crude product was purified by column chromatography (silica gel, $CHCl_3$ and then 25:1 $CHCl_3$/AcOEt) to afford **BF-2** as a purple solid (122 mg, 0.10 mmol, 62 %), which was washed several times with methanol and hexane.^{1}H NMR (400 MHz, $CDCl_3$, 298 K) δ: 8.73 (d, *J* = 8.4 Hz, 4H), 7.95 (d, *J* = 1.9 Hz, 4H), 7.58-7.56 (m, 12H), 7.51 (d, *J* = 8.9 Hz, 8H), 7.07 (dd, *J* = 8.9, *J* = 2.5 Hz, 8H), 3.96 (s, 24H); ^{13}C NMR (100 MHz, $CDCl_3$, 298 K) δ: 154.5, 142.4, 139.4, 136.8, 136.0, 128.0, 125.2, 124.3, 118.0, 115.4, 111.0, 103.2, 56.4; FTIR (neat) ν: 2989, 2937, 2828, 1608, 1465, 1432, 1328, 1289, 1202, 1159, 1106, 1038, 913, 827, 788, 669, 585 cm^{-1}; HRMS [MALDI-TOF] calcd. for $C_{82}H_{60}N_4O_8$ [M^+], 1228.4406; found 1228.4446; elemental analysis calcd. for $C_{82}H_{60}N_4O_8$, C: 80.11, H: 4.92, N: 4.56; found C: 78.94, H: 5.14, N: 4.31; m.p. > 330 ºC.

3. Synthesis of benzotrithiophene derivatives: BTTs

Benzo[1,2-*b*:3,4-*b'*:5,6-*b''*]trithiophene[156] (84)

This compound was synthesized according to a previously reported procedure and showed identical spectroscopic properties to those reported therein. ^{1}H NMR (400 MHz, $CDCl_3$, 298 K) δ: 7.61 (d, *J* = 5.4 Hz, 3H) 7.51 (d, *J* = 5.4 Hz, 3H); MALDI-TOF calcd. for $C_{12}H_6S_3$ [M^+], 246.4; found 246.4.

Benzo[1,2-*b*:3,4-*b'*:6,5-*b''*]trithiophene[161] (85)

This compound was synthesized according to a previously reported procedure and showed identical spectroscopic properties to those reported therein. ^{1}H NMR (400 MHz, acetone-d_6, 298 K) δ: 7.98 (d, *J* = 5.3 Hz, 1H), 7.97 (d, *J* = 5.3 Hz, 1H), 7.80 (d, *J* = 5.4 Hz, 1H), 7.77 (d, *J* = 5.3 Hz, 1H), 7.76 (d, *J* = 5.4 Hz, 1H), 7.74 (d, *J* = 5.3 Hz, 1H); MALDI-TOF calcd. for $C_{12}H_6S_3$ [M^+], 246.4; found 246.4.

Benzo[1,2-*b*:6,5-*b'*:3,4-*c''*]trithiophene[160](86)

This compound was synthesized according to a previously reported procedure and showed identical spectroscopic properties to those reported therein. ^{1}H NMR (400 MHz, $CDCl_3$, 298 K) δ: 7.70 (s, 2H), 7.24 (d, *J* = 5.3 Hz, 2H), 7.08 (d, *J* = 5.3 Hz, 2H); ^{13}C NMR (100 MHz, $CDCl_3$, 298 K) δ: 133.8, 131.2, 131.1, 124.2, 123.9, 116.0. MALDI-TOF calcd. for $C_{12}H_6S_3$ [M^+], 246.0; found 246.0.

1,3,5-Trichloro-2,4,6-triiodobenzene[192] (87)

This compound was synthesized according to a previously reported procedure and showed identical spectroscopic properties to those reported therein. ^{13}C NMR (100 MHz, dioxane/$CDCl_3$, 350 K) δ: 144.95, 97.13; MALDI-TOF calcd. for $C_6Cl_3I_3$ [M^+], 559.1; found 559.1.

192. J. J. Wolff, F. Gredel, T. Oeser, H. Irngartinger, H. Pritzkow, "Crystal engineering with symmetrical threefold acceptor-substituted triaminobenzenes", *Chem. Eur. J.*, **1999**, *5*, 29-38.

((2,4,6-Trichlorobenzene-1,3,5-triyl)tris(ethyne-2,1 diyl))tris(trimethylsilane)[157] (88)

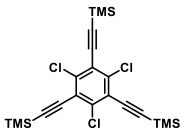

This compound was synthesized according to a previously reported procedure and showed identical spectroscopic properties to those reported therein. ^{1}H NMR (400 MHz, $CDCl_3$, 298 K) δ: 0.29 (s, 27H); MALDI-TOF calcd. for $C_{21}H_{27}Cl_3Si_3$ [M^+], 470.1; found 470.1.

2,5,8-Tribromobenzo[1,2-*b*:3,4-*b'*:5,6-*b''*]trithiophene[156] (89)

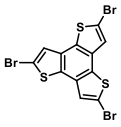

This compound was synthesized according to a previously reported procedure and showed identical spectroscopic properties to those reported therein. ^{1}H NMR (400 MHz, DMSO-d_6, 298 K) δ: 8.05 (s, 3H); MALDI-TOF calcd. for $C_{12}H_3S_3Br_3$, m/z: 483.7; found 483.7.

2,5,8-Tris[*N*,*N*-bis(4-methoxyphenyl)amino]benzo[1,2-*b*:3,4-*b'*:5,6-*b''*] trithiophene, BTT-1

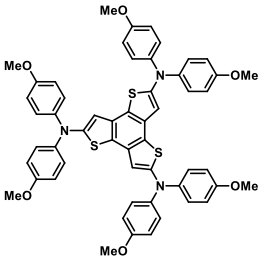

Tribromo-BTT (**89**) (150 mg, 0.31 mmol), **68** (250 mg, 1.08 mmol), $Pd_2(dba)_3$ (20 mg, 0.02 mmol) and XPhos (15 mg, 0.03 mmol) were dissolved in 21 mL of toluene. The mixture was degassed for 30 minutes at room temperature. After that, sodium Na^{t}BuO (180 mg, 1.86 mmol) was added and the reaction was heated at 100 ºC for 3.5 hours under nitrogen atmosphere. After cooling to room temperature, the mixture was quenched by adding water and extracted with toluene. The combined organic extracts were dried over Na_2SO_4. After removal the solvent under reduced pressure the crude product was purified by flash column chromatography (silica gel, DCM) to afford **BTT-1** as a yellow solid (174 mg, 0.19 mmol, 60 %).^{1}H NMR (400 MHz, $CDCl_3$, 298 K) δ: 7.18-7.16 (m, 12H), 6.86-6.83 (m, 12H), 6.53 (s, 3H), 3.79 (s, 18H); ^{13}C NMR (100 MHz, $CDCl_3$, 298 K) δ: 156.4, 153.0, 140.9, 130.6, 125.5, 121.6, 114.6, 107.6, 55.5; FTIR (neat) ν: 3039, 2905, 2833, 1502, 1239, 1033, 866 cm^{-1}; HRMS [MALDI-TOF] calcd. for $C_{54}H_{45}N_3O_6S_3$ [M^+], 927.2465; found 927.2446; elemental analysis calcd. for $C_{54}H_{45}N_3O_6S_3$, C: 69.88, H: 4.89, N: 4.53, S: 10.36; found C: 69.54, H: 4.97, N: 4.52; S: 10.38; m.p.: 292-293 ºC.

2,5,8-Tris[3,6-*bis*(*N*,*N*-bis(4-methoxyphenyl)amino)carbazol-9-yl]benzo [1,2-*b*:3,4-*b'*:5,6-*b''*]trithiophene, BTT-2

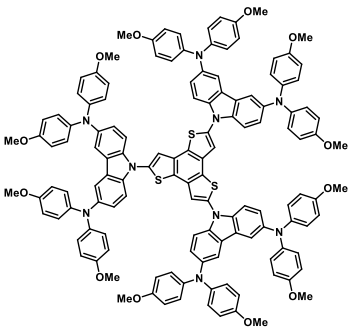

Tribromo-BTT (**89)** (300 mg, 0.62 mmol), **71** (1.27 g, 2.04 mmol), $Pd_2(dba)_3$ (39 mg, 0.04 mmol) and XPhos (29 mg, 0.06 mmol) were dissolved in toluene (41 mL). The mixture was purged with nitrogen for 30 minutes at room temperature. After that, sodium Na^tBuO (358 mg, 3.72 mmol) was added. The reaction was heated at 100 ºC for 4 hours under nitrogen atmosphere. The mixture was quenched by adding water and extracted with toluene. The combined organic extracts were dried over Na_2SO_4. After removal the solvent under reduced pressure the crude product was purified by flash column chromatography (silica gel, DCM and then 120:1 DCM/AcOEt) to afford **BTT-2** as a yellow solid (842 mg, 0.40 mmol, 64 %).^{1}H NMR (400 MHz, THF-d_8, 298 K) δ: 7.99 (s, 3H), 7.69 (d, *J* = 2.1 Hz, 6H), 7.55 (d, *J* = 8.8 Hz, 6H), 7.15 (dd, *J* = 8.8, *J* = 2.1 Hz, 6H), 6.95 (m, 24H), 6.76 (m, 24H), 3.71 (s, 36H); ^{13}C NMR (100 MHz, $CDCl_3$, 298 K) δ: 154.9, 142.3, 139.2, 138.1, 129.8, 129.4, 124.7, 124.6, 124.3, 118.6, 116.0, 114.6, 111.0, 55.5; FTIR (neat) ν: 3040, 2939, 2831, 1501, 1452, 1234, 1033, 819 cm^{-1}; HRMS [MALDI-TOF] calcd. for $C_{132}H_{105}N_9O_{12}S_3$ [M^+], 2103.7039; found 2103.7085; elemental analysis calcd. for $C_{132}H_{105}N_9O_{12}S_3$: C: 75.30, H: 5.03, N: 5.99, S: 4.57; found C: 74.90, H: 5.12, N: 5.98, S: 4.55; m.p.: 236-238 ºC.

2,5,8-Tris[*N*,*N*-(4-methoxyphenyl)amino-4-phenyl]benzo[1,2-*b*:3,4-*b'*:5,6-*b''*]trithiophene, BTT-3

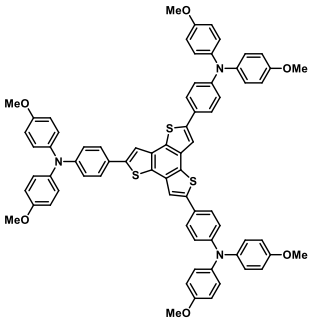

A solution of tribromo-BTT (**89**) (300 mg, 0.62 mmol), compound **73** (1.07 g, 2.48 mmol), K_3PO_4 (3.16 g, 14.90 mmol) and $Pd(PPh_3)_4$ (179 mg, 0.15 mmol) in DMF (22 mL) was degassed for 1 hour under nitrogen. The reaction was heated at 80 ºC for 18 hours. The mixture was cooled to r. t. and washed with NH_4Cl. The combined organic extracts (DCM) were dried over Na_2SO_4. After removal the solvent under reduced pressure the crude product was purified by flash column chromatography (silica gel, DCM and then (120:1

DCM/AcOEt) to afford **BTT-3** as a yellow solid (382 mg, 0.33 mmol, 54 %).^{1}H NMR (400 MHz, THF-d_8, 298 K) δ: 7.82 (s, 3H), 7.68 (d, *J* = 8.7 Hz, 6H), 7.12 (m, 12H), 6.98 (d, *J* = 8.7 Hz, 6H), 6.91 (m, 12H), 3.81 (s, 18H); ^{13}C NMR (100 MHz, $CDCl_3$, 298 K) δ: 156.1, 148.8, 143.6, 140.5, 132.5, 129.7, 126.9, 126.8, 126.0, 120.2, 116.0, 114.8, 55.5; FTIR (neat) ν: 3035, 2945, 2832, 1499, 1239, 1034, 821 cm^{-1}; HRMS [MALDI-TOF] calcd. for $C_{72}H_{57}N_3O_6S_3$ [M^+], 1155.3404; found 1155.3374; elemental analysis calcd. for $C_{72}H_{57}N_3O_6S_3$: C: 74.78, H: 4.97, N: 3.63, S: 8.32; found C: 74.10, H: 5.08, N: 3.58; S: 8.20; m.p.: 303-305 ºC.

2,2':3',2''-*Tert*-thiophene[193] (90)

This compound was synthesized according to a previously reported procedure and showed identical spectroscopic properties to those reported therein. ^{1}H NMR (400 MHz, $CDCl_3$, 298 K) δ: 7.32 (dd, *J*= 5.2, *J* = 1.2, 1H), 7.28 (d, *J* = 5.3, 1H), 7.25 (dd, *J* = 5.2, *J* = 1.2, 1H), 7.18, (d, *J* = 5.3, 1H), 7.13 (dd, *J* = 3.6, *J* = 1.2, 1H), 7.04 (dd, *J* = 3.6, *J* = 1.2, 1H), 7.02 (dd, *J* = 5.2, *J* = 1.2, 1H), 7.01 (dd, *J* = 5.2, *J* = 1.2, 1H); MALDI-TOF calcd. for $C_{12}H_8S_3$ [M^+], 248.4; found 248.5.

2,5,8-Tribromobenzo[1,2-*b*:3,4-*b'*:6,5-*b''*]trithiophene (91)

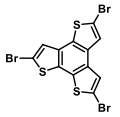

NBS (1.51 g, 8.53 mmol) was added portionwise to a solution of compound **85** (500 mg, 2.03 mmol) in a mixture 2:1 $CHCl_3$/CH_3COOH (15 mL) under light exclusion conditions. The reaction was then heated to reflux under nitrogen atmosphere. The resulting precipitate was filtered and washed with water, methanol and $CHCl_3$ to afford the tribromo derivative **91** as a brown solid (638 mg, 1.32 mmol, 65 %). ^{1}H NMR (400 MHz, DMSO-d_6, 298 K) δ: 8.29 (s, 1H), 8.26 (s, 1H), 8.10 (s, 1H). Given the low solubility of this compound ^{13}C NMR was not possible; MALDI-TOF calcd. for $C_{12}H_3Br_3S_3$ [M^+], 483.1; found 483.1.

193. N. K. Jayasuriya, J., "The synthesis of bithienyls and terthienyls by nickel-catalyzed coupling of grignard reagents", *Heterocycles*, **1986**, *24*, 2261-2264.

2,5,8-Tris[*N*,*N*-(4-methoxyphenyl)amino-4-phenyl]benzo[1,2-*b*:3,4-*b'*:6,5-*b''*]trithiophene, BTT-4

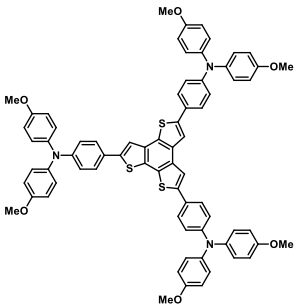

A solution of **91** (145 mg, 0.30 mmol), compound **73** (453 mg, 1.05 mmol), K_3PO_4 (1.52 g, 7.2 mmol) and $Pd(PPh_3)_4$ (70 mg, 0.06 mmol) in DMF (6 mL) was degassed for 30 minutes under nitrogen. The reaction was heated at 105 ºC for 3 hours. The mixture was cooled to room temperature and water was added. The resulting precipitate was filtered and washed with water and dissolved in hot chloroform. The organic phase was dried over Na_2SO_4. The solvent was removed under reduced pressure and the crude product was purified by flash column chromatography (silica gel, DCM and then 100:2 DCM/AcOEt) to afford **BTT-4** as a yellow solid (233 mg, 0.25 mmol), yield 67 %. ^{1}H NMR (400 MHz, THF-d_8, 298 K) δ 8.04 (s, 1H), 8.03 (s, 1H), 7.78 (s, 1H), 7.64-7.60 (m, 6H), 7.10-7.06 (m, 12H), 6.95-6.93 (m, 6H), 6.89-6.85 (m, 12H), 3.77 (s, 18H); ^{13}C NMR (100 MHz, $CDCl_3$, 298 K) δ: 160.3, 160.2(2), 152.8, 152.6(2), 147.1, 146.5, 146.2, 144.1, 144.01, 143.9(2), 137.6, 137.3, 135.9, 133.9, 132.8, 131.8, 130.4(2), 130.3, 130.2, 130.1, 129.7, 129.5, 129.2, 123.6, 123.5, 123.4, 120.4(2), 119.4, 118.2, 58.2; FTIR (neat) ν: 3035, 2996, 2832, 1600, 1503, 1318, 1282, 1239, 1034, 824 cm^{-1}; HRMS [MALDI-TOF] calcd. for $C_{72}H_{57}N_3O_6S_3$ [M^+], 1155.3404; found 1155.3362; elemental analysis calcd. for $C_{72}H_{57}N_3O_6S_3$, C: 74.78, H: 4.97, N: 3.63, S: 8.32; found C: 74.23, H: 5.10, N: 3.64; S: 8.22; m.p.: 143-150 ºC.

3,3'-Bis((trimethylsilyl)ethynyl)-2,2'-bithiophene[160] (92)

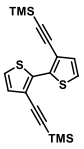

This compound was synthesized according to a previously reported procedure and showed identical spectroscopic properties to those reported therein. ^{1}H NMR (400 MHz, $CDCl_2$, 298 K) δ: 7.24 (d, *J* = 5.3 Hz, 2H), 7.08 (d, *J* = 5.3 Hz, 2H), 0.27 (s, 18H). ^{13}C NMR (100 MHz, $CDCl_2$, 298 K) δ: 139.2, 130.9, 124.5, 119.7, 102.0, 100.8, -0.37.

2,4,6,8-Tetrabromobenzo[1,2-*b*:6,5-*b'*:3,4-*c''*]trithiophene (93)

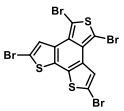

NBS (394 mg, 2.2 mmol) was added portionwise to a solution of compound **86** (173 mg, 0.44 mmol) in a mixture of 2:1 $CHCl_3$/AcOEt (15 mL) under light exclusion conditions. Then, the reaction was heated to reflux under nitrogen atmosphere. The

resulting precipitate was filtered and washed with water, methanol and $CHCl_3$ to afford the tetrabromo derivative **93**, in 57 % yield as a brownish solid. Given the low solubility of this compound. ^1H NMR and ^{13}C NMR were not possible. MALDI-TOF calcd. for $C_{12}H_2Br_4S_3$ [M^+], 561.6; found 561.6.

2,5,8-Tris[*N*,*N*-(4-methoxyphenyl)amino-4-phenyl]benzo[1,2-*b*:6,5-*b′*:3,4-*c′′*]trithiophene, BTT-5

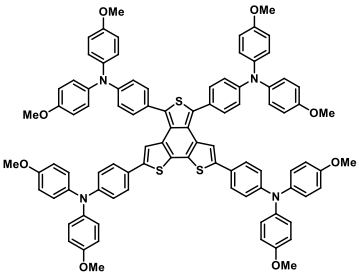

A solution of bromo-derivative **86** (115 mg, 0.20 mmol), compound **73** (397 mg, 0.92 mmol), K_3PO_4 (1.04 g, 4.9 mmol) and $Pd(PPh_3)_4$ (47 mg, 0.04 mmol) in DMF (6 mL) was degassed for 30 minutes under nitrogen. The reaction was heated at 100 ºC for 2 hours. The mixture was cooled to r. t. and water was added. The resulting precipitate was filtered and washed with water and dissolved in hot $CHCl_3$. The organic phase was dried over Na_2SO_4. The solvent was removed under reduced pressure and the crude product was purified by flash column chromatography (silica gel, DCM and then 100:2 DCM/AcOEt) to afford **BTT-5** as an orange solid (165 mg, 0.25 mmol, 56 %). ^1H NMR (400 MHz, THF-d_8, 298 K) δ: 7.44-7.41 (m, 4H), 7.38 (s, 2H), 7.37-7.34 (m, 4H), 7.14-7.06 (m, 16H), 7.05-7.02 (m, 4H), 6.97-6.93 (m, 4H), 6.91-6.86 (m, 8H), 6.84-6.80 (m, 8H), 3.77 (s, 12H), 3.72 (s, 12H); ^{13}C NMR (100 MHz, $CDCl_3$, 298 K) δ: 156.0, 148.9, 148.3, 140.7, 140.5, 133.3, 131.4, 130.3, 129.7, 126.7, 126.6, 126.4, 120.4, 120.0, 119.0, 114.8, 55.4(2); FTIR (neat) ν: 3037, 2948, 2833, 1603, 1500, 1320, 1280, 1239, 1034, 824 cm^{-1}; HRMS [MALDI-TOF] calcd. for $C_{92}H_{74}N_4O_8S_3$ [M^+], 1458.4663; found 1458.4706; elemental analysis calcd. for $C_{92}H_{74}N_4O_8S_3$, C: 75.69, H: 5.11, N: 3.84, S: 6.59; found C: 75.09, H: 5.59, N: 3.54; S: 6.23; m.p.: 158-160 ºC.

1,3,5-Trifluoro-2,4,6-triyodobenceno[194] (96)

This compound was synthesized according to a previously reported procedure and showed identical spectroscopic properties to those reported therein. ^{13}C NMR (100 MHz, $CDCl_3$, 298 K) δ: 162.3, 63.7; MALDI-TOF calcd. for $C_6F_3I_3$ [M^+], 509.8; found 509.8.

194. G. Hennrich, A. M. Echavarren, "New persubstituted 1,3,5-trisethynyl benzenes via sonogashira coupling", *Tetrahedron Lett.*, **2004**, *45*, 1147-1149.

2,4,6-Trifluoro-1,3,5-tris(2-(4-bromophenyl)etin-1-yl)benzene[173] (97)

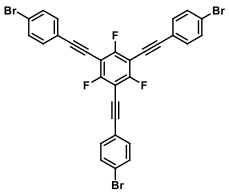

This compound was synthesized according to a previously reported procedure and showed identical spectroscopic properties to those reported therein. ^{1}H NMR (500 MHz, $CDCl_3$, 298 K) δ: 7.53 (d, *J* = 8.3 Hz, 6H), 7.44 (d, *J* = 8.3 Hz, 6H); ^{13}C NMR (100 MHz, $CDCl_3$, 298 K) δ: 161.9, 133.2, 131.8, 123.8, 120.9, 99.7, 98.8, 75.1.

2,5,8-Tris(4-bromophenyl)-1,4,7-triphenyl-4,7-dihydro-1*H*-dipyrrolo[2,3-*e*:2',3'-*g*]indol[173] (98)

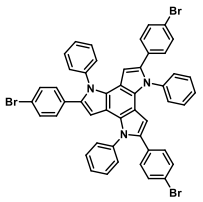

This compound was synthesized according to a previously reported procedure and showed identical spectroscopic properties to those reported therein. ^{1}H NMR (400 MHz, $CDCl_3$, 298 K) δ: 7.53-7.50 (m, 9H), 7.46-7.42 (m, 6H), 7.25 (d, *J* = 8.0 Hz, 6H), 6.93 (d, *J* = 8.0 Hz, 6H), 5.83 (s, 3H); ^{13}C NMR (100 MHz, $CDCl_3$, 298 K) δ: 139.7, 134.8, 131.9, 131.1, 130.4, 129.8, 129.6, 129.3, 128.6, 120.4, 109.2, 101.5.

2,5,8-Tris(*N*,*N*-di(4-methoxyphenyl)amino-4-phenyl)-1,4,7-triphenyl benzo[1,2-*b*:3,4-*b'*:5,6-*b''*]tripyrrol, BTP

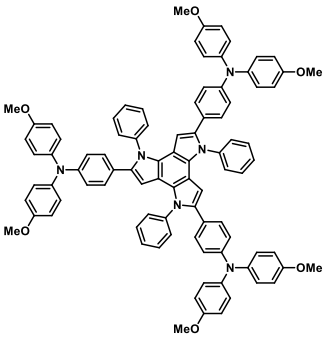

To a dry round bottom flask equipped with a stirrer bar, compound **98** (74 mg, 0.083 mmol), derivative **73** (66 mg, 0.29 mmol) XPhos (6 mg, 0.01 mmol) and $Pd_2(dba)_3$ (6 mg, 0.01 mmol) were dissolved in dry toluene (35 mL). The resulting mixture was degassed for 30 minutes. Finally, Na^{t}BuO (48 mg, 0.5 mmol) was added to the solution which was heated to 100 ºC for 6 hours. After cooling to room temperature, the mixture was filtered through celite and washed with water. The organic layer was dried over Na_2SO_4 and the solvent was removed under vacumm. The crude product was purified by column chromatography (silica gel, DCM) to afford the desired compound **BTP** as a light yellow solid (73 mg, 0.06 mmol, 66%). ^{1}H NMR (400 MHz, THF-d_8, 298 K) δ: 7.53-7.40 (m, 15H), 6.97-6.90 (m, 12H), 6.86-6.81 (m, 6H), 6.80-6.76 (m, 12H), 6.60-6.56 (m, 6H), 5.74 (s, 3H), 3.73 (s, 18H); ^{13}C NMR (100 MHz, $CDCl_3$, 298 K) δ: 155.7, 146.8, 140.7, 140.5, 129.8, 128.9,

128.7, 128.1, 126.6, 125.2, 119.5, 114.6, 100.1, 55.4; FTIR (neat) ν: 3039, 2998, 2930, 2833, 1503, 1239, 1035, 791, 698, 614, 575 cm^{-1}; HRMS [MALDI-TOF] calcd. for $C_{90}H_{72}N_6O_6$ [M^+], 1332.5508; found 1332.5471; elemental analysis calcd. for $C_{90}H_{72}N_6$, C: 81.06, H: 5.44, N: 6.30; found C: 80.37, H: 5.72, N: 5.93, m.p.: 295-297 ºC.

2,5,8-Tris(4-bromophenyl)benzo[1,2-*b*:3,4-*b'*:5,6-*b''*]trifurane[173](99)

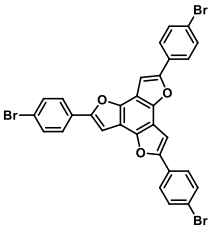

This compound was synthesized according to a previously reported procedure and showed identical spectroscopic properties to those reported therein. ^{1}H NMR (400 MHz, $CDCl_3$, 298 K) δ: 7.78 (d, *J* = 8.6 Hz, 6H), 7.39 (s, 3H), 7.61 (d, *J* = 8.6 Hz, 6H); ^{13}C NMR (100 MHz, $CDCl_3$, 298 K) δ: 154.0, 146.1, 132.0, 129.3, 125.9, 122.2, 110.9, 98.9.

2,5,8-Tris[*N*,*N*-(4-methoxyphenyl)amino-4-phenyl]-benzo[1,2-*b*:3,4-*b'*:5,6-*b''*]trifurane, BTF

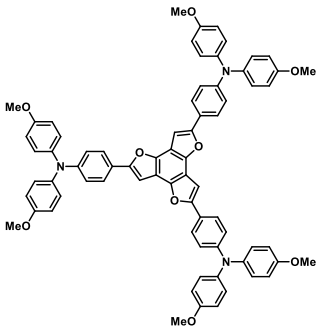

To a dry round bottom flask equipped with a stirrer bar, tribromo derivative **99** (150 mg, 0.23 mmol), compound **73** (182 mg, 0.79 mmol), XPhos (16 mg, 0.034 mmol) and $Pd_2(dba)_3$ (16 mg, 0.017 mmol) were dissolved in dry toluene (8 mL). The resulting mixture was degassed for 30 minutes. Finally, Na^{t}BuO (130 mg, 1.36 mmol) was added to the solution which was heated to 100 ºC for 6 hours. After cooling to room temperature, the mixture was filtered through celite and washed with water. The organic layer was dried over Na_2SO_4 and the solvent was removed under vacuum. The crude was purified by column chromatography (silica gel, DCM) to afford the desired compound **BTF** as a yellowish solid (81 mg, 0.073 mmol, 32 %). ^{1}H RMN (400 MHz, THF-d_8, 298 K) δ: 7.78-7.71 (m, 6H), 7.37 (s, 3H), 7.15-7.05 (m, 12H), 6.99-6.94 (m, 6H), 6.91-6.85 (m, 12H), 3.77 (s, 18H); ^{13}C NMR (100 MHz, $CDCl_3$, 298 K) δ: 156.3, 155.5, 148.9, 145.4, 140.7, 126.9, 125.5, 122.9, 120.4, 114.8, 111.3, 96.8, 55.7; FTIR (neat) ν: 3039, 2995, 2929, 2834, 1499, 1240, 1035, 827cm^{-1}; HRMS [MALDI-TOF] calcd. for $C_{72}H_{57}N_3O_6S_3$ [M^+], 1107.4089; found 1107.4071; elemental analysis calcd. for $C_{72}H_{57}N_3O_9$, C: 78.03, H: 5.18, N: 3.79; found C: 77.3, H: 5.58, N: 3.48.

4. Synthesis of thieno[3,2-*b*]thiophene-based derivatives, TbTs

Perbromic thieno[3,2-*b*]thiophene[195] (104)

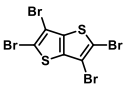

This compound was synthesized according to a previously reported procedure and showed identical spectroscopic properties to those reported therein. MS-EI (m/z) calcd. for $C_6Br_4S_2$ [M], 455.0; found 455.1.

2,3,5,6-Tetrakis[*N*,*N*-bis(4-methoxyphenyl)amino-4-phenyl]thieno[3,2-*b*]thiophene, TbT-1

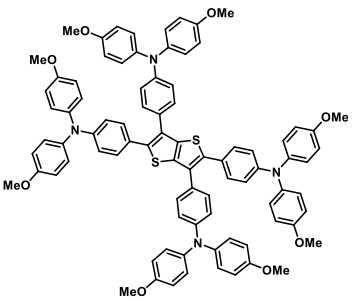

Tetrabromo derivative **104** (100 mg, 0.22 mmol), compound **73** (425 mg, 0.99 mmol), K_3PO_4 (1.12 g, 5.28 mmol) and $Pd(PPh_3)_4$ (50.9 mg, 0.044 mmol) were dissolved in dry DMF (10 mL). The mixture was degassed for 20 minutes and stirred at 100 ºC for 2 hours. After cooling to r.t., the mixture was filtered and washed with water and methanol. The solid was then dissolved in hot $CHCl_3$ and dried over Na_2SO_4. The solvent was removed under reduced pressure and the crude product was purified by chromatography column (silica gel, DCM) to afford **TbT-1** as a yellow solid (76.9 mg, 0.06 mmol, 26 %). ^{1}H NMR (400 MHz, THF-d_8, 298 K) δ: 7.26 (d, *J* = 8.8 Hz, 4H), 7.16 (d, *J* = 8.8 Hz, 4H), 7.07 (m, 8H), 7.03 (m, 8H), 6.84 (m, 20H), 6.76 (d, *J* = 8.8 Hz, 4H), 3.75 (s, 12H), 3.75 (s, 12H); ^{13}C NMR (100 MHz, $CDCl_3$, 308 K) δ:156.3, 156.2, 148.1, 148.0, 141.0, 140.8, 138.3, 137.9, 129.8, 129.8, 129.7, 127.3, 127.1, 127.0, 120.0, 119.8, 114.9, 55.7; FTIR (neat) ν: 2923, 2831, 1502, 1465, 1283, 1239, 1033, 827, 576 cm^{-1}; HRMS [MALDI-TOF] calcd. for $C_{86}H_{72}N_4O_8S_2$ [M^+], 1352.4786; found 1352.4766; elemental analysis calcd. for $C_{86}H_{72}N_4O_8S_2$, C: 76.31, H: 5.36, N: 4.14, S: 4.74; found C: 74.94, H: 5.66, N: 3.87, S: 4.42. m.p.: 160-162 ºC.

195. B. A. Coombs, S. R. Rutter, A. E. Goeta, H. A. Sparkes, A. S. Batsanov, A. Beeby, "2,5-bis(arylethynyl)thienyl systems: Preparation and photophysical properties. Part II", *RSC Advances*, **2012**, *2*, 1870-1876.

2,3,5,6-Tetra(thiophen-2-yl)thieno[3,2-*b*]thiophene[196] (105)

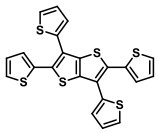

This compound was synthesized according to a previously reported procedure and showed identical spectroscopic properties to those reported therein. ^{1}H NMR (400 MHz, acetone-d_6, 298 K) δ: 7.64 (dd, *J* = 6.8 Hz, 2H), 7.60 (dd, *J* = 6.8 Hz,2H), 7.32 (dd, *J* = 4.8 Hz, 2H), 7.29 (dd, *J* = 4.8 Hz, 2H), 7.20 (dd, *J* = 6.8 Hz, 2H), 7.14 (dd, *J* = 6.8 Hz, 2H).

2,3,5,6-Tetrakis(5-bromothiophen-2-yl)thieno[3,2-*b*]thiophene (106)

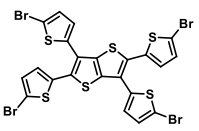

NBS (341.7 mg, 1.92 mmol) was added portionwise to a solution of compound **105** (150 mg, 0.32 mmol) in dry THF (10 mL) under light exclusion conditions. The mixture was stirred overnight at r.t. After adding water, the resulting precipitate was filtered and washed with water and acetone, to afford the tetrabromo derivative **106** (213 mg, 0.27 mmol, 85 %) as a yellow solid. ^{1}H NMR (400 MHz, $CDCl_3$, 298 K) δ: 7.08 (d, *J* = 3.8 Hz, 2H), 7.01 (d, *J* = 3.8 Hz, 4H), 6.95 (dd, *J* = 3.8 Hz, 2H). Given the low solubility of this compound ^{13}C NMR was not possible. MALDI-TOF calcd. for $C_{22}H_8Br_4S_6$ [M^+] 783.6; found 783.6.

2,3,5,6-Tetrakis[*N*,*N*-bis(4-methoxyphenyl)amino-5-thien-2-yl]thieno[3,2-*b*]thiophene, TbT-2

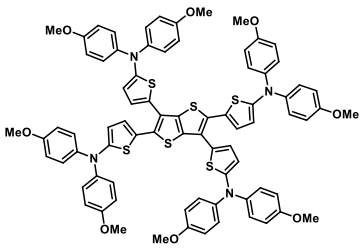

Tetrabrominated derivative **105** (150 mg, 0.19 mmol), compound **68** (225 mg, 0.96 mmol), $Pd_2(dba)_3$ (10 mg, $9.6\cdot10^{-3}$ mmol) and XPhos (9 mg, 0.019 mmol) were dissolved in dry toluene (10 mL) and degassed for 20 min. Then, Na^{t}BuO (115 mg, 1.15 mmol) was added and the mixture was heated at 105 ºC for 3 hours. The reaction was quenched with H_2O (10 mL) and extracted with toluene (3x25 mL). After removing the solvent *in vacuo*, the residue was purified by column chromatography (silica gel, DCM to afford **TbT-2** as an orange solid (186 mg, 0.14 mmol, 71 %).^{1}H NMR (400 MHz, THF-d_8, 298K) δ: 7.08 (m, 16H), 6.97 (d, *J* = 3.9 Hz, 2H), 6.88 (d, *J* = 3.9 Hz, 2H), 6.83 (m, 16H), 6.32 (d, *J* = 3.9 Hz,

196. Y. Liu, Q. Liu, X. Zhang, L. Ai, Y. Wang, R. Peng, Z. Ge, "Synthesis, crystal structure, and polymerization of butterfly-shaped thieno[3,2-*b*]thiophene oligomers", *New J. Chem.*, **2013**, *37*, 1189-1194.

2H), 6.24 (s, *J* = 3.9 Hz, 2H), 3.74 (s, 12H), 3.74 (s, 12H); ^{13}C NMR (100 MHz, $CDCl_3$, 298 K) δ: 157.6, 157.5, 157.0, 155.9, 142.3, 142.1, 137.9, 133.2, 128.2, 127.3, 126.4, 126.1, 125.9, 125.6, 125.3, 116.0, 115.5, 115.4(2), 55.7.; FTIR (neat) ν: 2926, 2856, 1736, 1646, 1606, 1502, 1464, 1374, 1242, 1175, 1106, 1034, 826, 788, 724, 590 cm^{-1}; HRMS [MALDI-TOF] calcd. for $C_{78}H_{64}N_4O_8S_6$ [M^+]1376.3020; found 1376.3043; elemental analysis calcd. for $C_{78}H_{64}N_4O_8S_6$, C: 68.16, H: 5.15, N: 3.97; S: 13.64; found C: 67.41, H: 5.61, N: 3.37, S: 11.39; m.p.: 136-137 ºC.

2,3,5,6-Tetrakis[*N*,*N*-bis(4-methoxyphenyl)amino-4-phenyl-5-thien-2-yl] thieno[3,2-*b*]thiophene, TbT-3

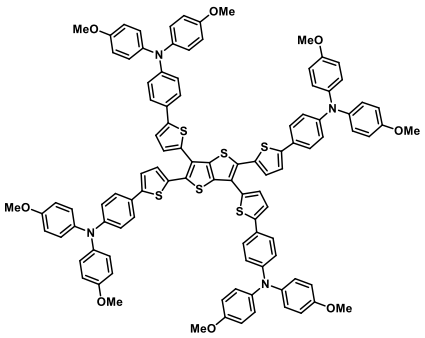

Tetrabrominated derivative **105** (160 mg, 0.20 mmol), compound **73** (380 mg, 0.88 mmol), $Pd(PPh_3)_4$ (24 mg, $2.10 \cdot 10^{-2}$ mmol) were dissolved in dry DMF (10 mL) and degassed for 20 min. Then, K_3PO_4 (1.04 g, 4.92 mmol) was added and the mixture was heated at 105 ºC for 3 hours. The reaction was quenched with H_2O (10 mL) and the precipitate was filtered and washed with water to remove DMF completely. The solid was dissolved in hot $CHCl_3$, dried over Na_2SO_4.The mixture was evaporated to dryness and after purification of the residue by column chromatography (silica gel, DCM) **TbT-3** was obtained as a red solid (272 mg, 0.16 mmol, 81 %). ^{1}H NMR (400 MHz, $CDCl_3$, 298K) δ: 7.48-7.39 (m, 8H), 7.29-7.27 (m, 4H), 7.23-7.20 (d, *J* = 3.9, 2H), 7.21 (d, *J* = 3.9, 2H), 7.09-7.04 (m, 16H), 6.92-6.85 (m, 24H), 3.70 (s, 24H); ^{13}C NMR (100 MHz, $CDCl_3$, 298 K) δ: 156.1, 156.0, 148.5, 148.4, 146.2, 145.4, 140.7, 140.6, 138.1, 133.3, 133.1, 133.0, 128.9, 128.6, 126.7, 126.6, 126.5, 126.2, 126.0, 124.41, 121.9, 120.6, 120.4, 114.8; FTIR (neat) ν: 3036, 2998, 2935, 2833, 1603, 1503, 1239, 1034, 826, 729, 576 cm^{-1}; HRMS [MALDI-TOF] calcd. for $C_{102}H_{80}N_4O_8S_6$ [M^+], 1680.4295; found 1680.4310; elemental analysis calcd. for $C_{102}H_{80}N_4O_8S_6$, C: 72.89, H: 5.36, N: 3.24, S: 11.12; found C: 72.46, H: 5.02, N: 3.33, S: 11.11; m.p.: 153-155 ºC.

• Conclusions

Chapter 1. Hole-transporting materials
for perovskite solar cells

5. CONCLUSIONS

Since spiro-OMeTAD is known to be a good hole-transporting material, a wide number of related molecules have been investigated in the field of perovskite solar cells. With the aim of reaching great performance devices, different families of hole-transporting materials have been designed in chapter 1 of this thesis. Essential points have been considered such as easily attainable, low cost of preparation and appropriate optical, electrochemical and thermal properties.

Part 1. *Hole-transporting materials based on tetraarylethene (TAE) and bifluorenylidene (BF).*

It has been described the synthesis and features of two new series of low-cost and straightforward preparation TAE- and BF-derivatives. Particularly, **TAE-1** was studied as a novel promising hole-transporting material in free-dopant perovskite solar cells. The synthesis of **TAE-1** requires only two synthetic steps from commercially available precursors for an overall yield of 72 %. The optical and electrochemical properties and promising undoped-performance, make this molecule and its possible derivatives, excellent candidates for top efficiency $MAPbI_3$-based solar cells.

Part 2. *Hole-transporting materials based on benzotrithiophene (BTT).*

Three new star-shaped small molecule hole-conducting materials **BTT-1**, **BTT-2** and **BTT-3** have been efficiently obtained by linking a BTT core with different triphenylamine based ligands following a facile and straightforward synthetic route. The new compounds were employed in PSCs and showed excellent performances, comparable to the state-of-the-art. Energy conversion efficiencies of up to 16 % and 17 % were obtained for **BTT-1** and **BTT-2**, respectively, and a PCE value above 18 % for **BTT-3**, which is comparable to the reference spiro-OMeTAD, when employed them as hole-conducting materials in two different perovskite-based devices ($MAPbI_3$ and $(FAPbI_3)_{0.85}(MAPbBr_3)_{0.15}$). To the best of our knowledge, this is among the highest PCE values observed for PSCs using a small molecule as an alternative to spiro-OMeTAD. The difference in the performance obtained for the three BTT-derivatives could be accounted for the different conductivity values obtained for the solid thin films. According to the results, the conductivity in **BTT-1** and **BTT-2** is considerably lower than that found for **BTT-3**, thus limiting the amount of current extracted from the device. Furthermore,

compound **BTT-3** shows an excellent alignment with the valance band of $MAPbI_3$ perovskite and, thus, it can be used as an efficient candidate for a cost-effective replacement of the widely established spiro-OMeTAD. In addition, the laboratory synthesis costs of these HTMs are estimated in the range of 50-80 US$ g^{-1}, which is very competitive in comparison to other commercially available HTMs. These price values validate the potential of these readily available materials for competing favorably with spiro-OMeTAD in the perovskites-based PV market. In addition, it is expected a significant price drops once the economy of scale applies. An application of these HTMs have been protected through a *European patent* (A. Molina-Ontoria, I. Zimmermann, I. Garcia-Benito, P. Gratia, C. Roldán-Carmona, M. Graetzel, M. K. Nazeeruddin, N. Martín, Application number PCT/IB2016/057475).

Part 3. *Hole-transporting materials based on benzotrithiophene (BTT)-isomers.*

In this section, it is presented the syntheses and a systematic study of the impact that the isomerism of the BTT core has on the optical, electrochemical and photophysical properties and the PV performance of novel multi-armed hole-transporting materials. The new HTMs (**BTT-4** and **BTT-5**) were obtained by crosslinking the BTT-cores with *p*-methoxytriphenylamines in four simple synthetic steps. The BTT-based molecules are good electron donors, and their HOMO levels are properly aligned with the valence band of the perovskite, which suggests an efficient hole-injection from the HTM. In addition, **BTT-4** and **BTT-5** exhibit a remarkably good thermal stability of up to 430 ºC. Impressive light-to-energy conversion efficiencies of 19.0 % for **BTT-4** and 18.2 % for **BTT-5** were measured, which even surpass the efficiency exhibited by **BTT-3** and the widely-used spiro-OMeTAD. **BTT-4** shows higher conductivity than the other BTT derivatives, which follows the trend found in the device efficiency. It is surmised that the *cis* arrangement of the sulfur atoms facing each other in the **BTT-4** core may further benefit the interaction with the perovskite material, thus allowing even better hole extraction. The results presented here further confirm the potential of the BTT family as a high efficient alternative to the costly spiro-OMeTAD as realistic HTMs.

Part 4. *Hole-transporting materials based on sulfur-free core.*

Remarkably, it was possible to compare the impact on the PV performance of the incorporation of heteroatoms in the isostructural central core of new three-

armed sulfur-free HTMs. The new derivatives present three pyrrole or three furan rings fused to a benzene central ring as a central core endowed with *p*-methoxytriphenylamines as electron donor unit. An in-depth study of their electrochemical and optical properties has been carried out. Furthermore, the structure of **BTF** was unambiguously confirmed by X-ray diffraction of a single crystal formed from a solution of toluene. An impressive maximum efficiency of 18.2 % was achieved with the furan-based derivative as the HTM in $(FAPbI_3)_{0.85}(MAPbBr_3)_{0.15}$-based devices, which is until now the highest efficiency for a furan-based HTMs with only little hysteresis. It is important to highlight that the conductivity is not the only parameter that defines a good HTM but also the possible interactions with the own perovskite.

Part 5. *Hole-transporting materials based on thieno[3,2-b]thiophene (TbT).*

Finally, thienothiophenes have been incorporated as central core in three additional four-armed HTMs. As electron donor fragment *p*-methoxydiphenylamine was employed incorporating different spacer groups. The influence of the spacer group has been determined, not only by means of the optoelectronic and thermal properties, but also on their PV performance. The three TbT-derivatives prepared through a facile synthetic route presented a notable different behaviour in PSCs, reaching efficiencies from 11.1 % with **TbT-1** to a promising 18.4 % with negligible hysteresis employing **TbT-3**. According to these results, it can be concluded that solubility (*i.e*. processability) is a key issue in order to obtain highly efficient HTMs. Furthermore, when suitably incorporated in TbT-derivatives make these new HTMs materials of choice for efficient PSCs.

Chapter 2

Electron-transporting materials
for perovskite solar cells

•• Background

Chapter 2. Electron-transporting materials
for perovskite solar cells

1. BACKGROUND

The exceptional semiconducting properties and ambipolar behaviour of perovskites allow different configurations of the devices. The structure of the solar cells could be considered n-i-p or p-i-n, where light enters through the n-type or the p-type layer and the perovskite is an intrinsic semiconductor.[28] The current section emphasizes on the foremost ETMs that have been employed for p-i-n perovskite solar cells. As it is illustrated in figure 84, the inverted configuration (p-i-n) is formed by the substrate - hole transporting layer (p) - perovskite (i) - electron transporting layer (n) and a metal cathode.[53]

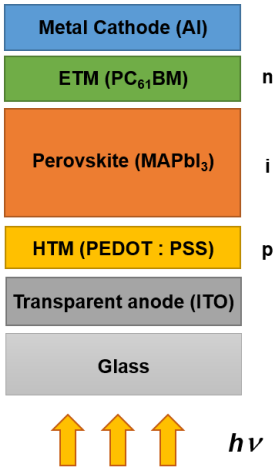

Figure 84. Schematic diagram of inverted planar structure (p-i-n) of PSCs.

In the inverted configuration, the perovskite crystals are formed on top of a transparent substrate covered with a hole transport layer. Poly(3,4-ethylenedioxythiophene) doped with poly(styrenesulfonate) (PEDOT:PSS) or NiO_x are the commonly employed HTMs in this type of structures nowadays. In this configuration, the electron selective contact layer is deposited directly on top of the photoactive perovskite layer and its properties have been proven to have a significant impact on the device performance and stability.[197]

197. C. Y. Chang, W. K. Huang, Y. C. Chang, "Highly-efficient and long-term stable perovskite solar cells enabled by a cross-linkable n-doped hybrid cathode interfacial layer", *Chem. Mater.*, **2016**, *28*, 6305-6312.

1.1. Role of electron-transporting materials

In the last few years, HTMs have undergone to an impressive development showing great performance and stability in regular structure PSCs (chapter 1). However, the pace of developing suitable electron-transporting materials (ETMs) is lagging behind.[198] Despite the rapid progress of planar p-i-n PV solar cells, the corresponding choice of a ETM has been rather limited.[199] There are some basic requirements to be considered for an ideal ETM, such as high electron mobility and efficient hole-blocking properties. In addition, the deposition process of electron-transporting layer should not damage the perovskite active layers and should cover the perovskite film completely to avoid potential reactions between ETMs and perovskites as well as prevent the potential reaction with the metal cathode (e.g., Al or Ag). In addition, this direct contact will avoid current leakage.[50] A variety of transition metal oxides such as Al_2O_3, TiO_2 and ZrO_2 have been investigated as ETMs for PSCs. However, the employment of metal oxides involves sophisticated and high-temperature procedures, which limit their use in large scale and makes them incompatible with perovskite layers that cannot tolerate temperatures above 100 ºC.[200] Therefore, the fabrication of inverted cells with metal oxide as ETMs where metal oxide layers are deposited on top of perovskite, has remained a challenge. To overcome this issue organic n-type materials are being employed to replace metal oxides and making possible low-temperature solution processing of PSCs.[201]

The first inverted planar structure of PSCs adopted a similar device structure to the organic solar cell. Fullerene derivatives and the traditional organic transport layer, PEDOT:PSS, were directly implemented as the ETM and HTM,

198. D. Zhao, Z. Zhu, M. Y. Kuo, C. C. Chueh, A. K. Y. Jen, "Hexaazatrinaphthylene derivatives: Efficient electron-transporting materials with tunable energy levels for inverted perovskite solar cells", *Angew. Chem. Int. Ed.*, **2016**, *55*, 8999-9003.
199. X. Meng, Y. Bai, S. Xiao, T. Zhang, C. Hu, Y. Yang, X. Zheng, S. Yang, "Designing new fullerene derivatives as electron transporting materials for efficient perovskite solar cells with improved moisture resistance", *Nano Energy*, **2016**, *30*, 341-346.
200. M. Ye, X. Hong, F. Zhang, X. Liu, "Recent advancements in perovskite solar cells: Flexibility, stability and large scale", *J. Mater. Chem. A*, **2016**, *4*, 6755-6771.
201. S. Chang, G. D. Han, J. G. Weis, H. Park, O. Hentz, Z. Zhao, T. M. Swager, S. Gradečak, "Transition metal-oxide free perovskite solar cells enabled by a new organic charge transport layer", *ACS Appl. Mater. Interfaces*, **2016**, *8*, 8511-8519.

respectively, in a perovskite device.[51] In the pioneering work, Guo and co-workers firstly demonstrated in 2013 the feasibility of the conventional thin-planar heterojunction configuration.[202] C_{60} and some C_{60}-derivatives were used to construct the perovskite/fullerene junctions. Employing $PC_{61}BM$ (phenylC_{61}-butyric acid methyl ester), the most used fullerene derivative in PV, as a ETM, PCE of 3.9 % was delivered. It is worth mentioning that shortly after, Lam *et al.* further improved the device performance to 7.4 % using $PC_{61}BM$ as a ETM in all-solution processable planar heterojunction device.[203] In this case, the perovskite precursor solution concentration was optimized as well as the blending ratio of PbI_2 and MAI showing a pure bilayer $MAPbI_3/PC_{61}BM$ solar cell. Additionally, high-efficiency PSCs were reported employing mesoscopic metal oxide, such as Al_2O_3,[25] TiO_2 or ZrO_2[67] reaching efficiencies of 10.9 %, 9.5 % and 10.8 %.

Remarkably, Nazeeruddin, Henk and co-workers reported the first device in which the methylammonium lead iodide perovskite layer is sandwiched between two thin organic charge-transporting layers ($PC_{61}BM$ and polyarylamine (polyTPD)), reaching a PCE of 12 % (figure 85).[204] To ensure a high purity, the perovskite layers were prepared by slow evaporation in a high-vacuum chamber.

202. J. Y. Jeng, Y. F. Chiang, M. H. Lee, S. R. Peng, T. F. Guo, P. Chen, T. C. Wen, "$CH_3NH_3PbI_3$ perovskite/fullerene planar-heterojunction hybrid solar cells", *Adv. Mater.*, **2013**, *25*, 3727-3732.
203. S. Sun, T. Salim, N. Mathews, M. Duchamp, C. Boothroyd, G. Xing, T. C. Sum, Y. M. Lam, "The origin of high efficiency in low-temperature solution-processable bilayer organometal halide hybrid solar cells", *Energy Environ. Sci.*, **2014**, *7*, 399-407.
204. O. Malinkiewicz, A. Yella, Y. H. Lee, G. M. Espallargas, M. Graetzel, M. K. Nazeeruddin, H. J. Bolink, "Perovskite solar cells employing organic charge-transport layers", *Nat. Photonics*, **2014**, *8*, 128-132.

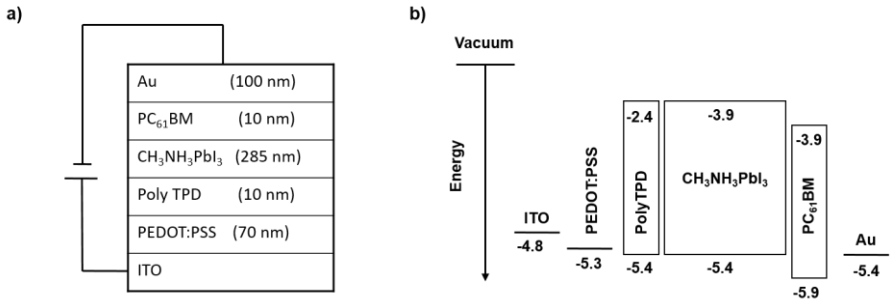

Figure 85. a) Stacked layer structure of the device. **b**) Relative energy levels of each layer.

The efficiency of the planar p-i-n device has improved significantly due to the use of advanced materials and preparation methods such as a multicycle solution coating process and the design of new configurations. Dong *et al.* reported the efficient device shown in figure 86, reaching an efficiency of 18.9 %.[205]

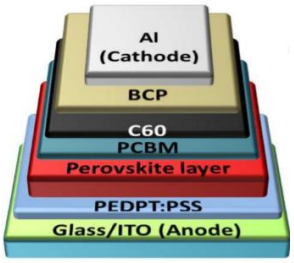

Figure 86. Structure of the perovskite-based device reported by Dong *et al.*

Recently, a maximum efficiency of simple invert solar cells was reported by Gong and co-workers,[206] who delivered a champion PCE of 18.3 % with a stabilized output efficiency of 17.6 % at the maximum power point. The optimized devices also exhibited negligible J-V hysteresis under the scanning conditions. In this section, a brief tour of some materials that have been used as ETMs throughout the development of inverted PSCs is presented. These ETMs

205. Q. Dong, Y. Yuan, Y. Shao, Y. Fang, Q. Wang, J. Huang, "Abnormal crystal growth in $CH_3NH_3PbI_{3-x}Cl_x$ using a multi-cycle solution coating process", *Energy Environ. Sci.*, **2015**, *8*, 2464-2470.
206. L. Zhao, D. Luo, J. Wu, Q. Hu, W. Zhang, K. Chen, T. Liu, Y. Liu, Y. Zhang, F. Liu, T. P. Russell, H. J. Snaith, R. Zhu, Q. Gong, "High-performance inverted planar heterojunction perovskite solar cells based on lead acetate precursor with efficiency exceeding 18 %", *Adv. Funct. Mater.*, **2016**, *26*, 3508-3514.

have been mainly categorized into three groups: fullerene-based, non-fullerene-based and inorganic ETMs.

1.2. Fullerene-based electron-transporting materials

Fullerene and its derivatives are by far the most frequently used ETMs in inverted configuration. It is worth noting that some advantages in the use of fullerene derivatives such as room temperature, orthogonal solvent processability and decent electron mobility make them successful candidates to prevent the degradation of the underlying perovskite layer for high-performance PV solar cells.[207]

[60]Fullerene (C_{60}) has been considered to be the ideal acceptor for organic solar cells for its promising properties. It presents a truncated icosahedral structure in the nanometre scale and spherical symmetry (figure 87). The triply degenerated LUMO of C_{60}[208] endows the molecule with a very high electron affinity relative to the numerous potential organic donors, being able to reversibly accept 6 electrons, thus illustrating its ability to stabilize negative charges. In addition, this molecule possesses small reorganization energy, ability to transport charge, stability and multi-gram scale availability.[5,209] These fundamental properties, coupled with the ability of soluble fullerene derivatives to pack effectively in crystalline structures conductive to charge transport,[210] have made [60]fullerene a promising acceptor material for PV applications, from BHJ solar cells to PSCs. The importance of this discovery led to the recognition of Kroto, Smalley and Curl with the Nobel Prize in 1996 for the discovery of fullerenes.

207. P. W. Liang, C. C. Chueh, S. T. Williams, A. K. Y. Jen, "Roles of fullerene-based interlayers in enhancing the performance of organometal perovskite thin-film solar cells", *Adv. Energy Mater.*, **2015**, *5*, 1402321-1402328.
208. P. M. Allemand, A. Koch, F. Wudl, Y. Rubin, F. Diederich, M. M. Alvarez, S. J. Anz, R. L. Whetten, "Two different fullerenes have the same cyclic voltammetry", *J. Am. Chem. Soc.*, **1991**, *113*, 1050-1051.
209. J. L. Delgado, P.-A. Bouit, S. Filippone, M. A. Herranz, N. Martin, "Organic photovoltaics: A chemical approach", *Chem. Commun.*, **2010**, *46*, 4853-4865.
210. M. T. Rispens, A. Meetsma, R. Rittberger, C. J. Brabec, N. S. Sariciftci, J. C. Hummelen, "Influence of the solvent on the crystal structure of PCBM and the efficiency of MDMO-PPV:PCBM 'plastic' solar cells", *Chem. Commun.*, **2003**, 2116-2118.

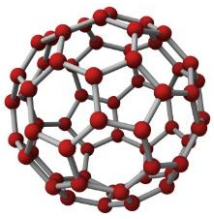

Figure 87. [60]Fullerene.

Specifically, the well-known $PC_{61}BM$ is the fullerene derivative most commonly featured for PV applications (figure 88). It was firstly prepared by Hummelen and Wudl in 1995[211] and its first application in solar cells was reported in the same year.[212] In addition, it has been widely employed in a variety of PV devices.

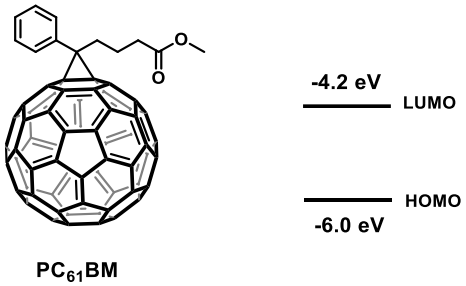

Figure 88. Molecular structure of $PC_{61}BM$ and its HOMO and LUMO energy levels.

Its processability in solution, appropriate energy levels for efficient excitons dissociation and good electron transport properties make this molecule a potential candidate ETM to be used in PSCs. In particular, $PC_{61}BM$ has been widely employed as n-type charge transport material in p-i-n architectures.[213] However, recent studies show that C_{60} should be more effective than $PC_{61}BM$ as a ETM due to the higher mobility and conductivity of C_{60}. Jen and co-workers showed that the PCE of fullerene-derived PSCs improves with increasing electron mobility in the fullerene layer, indicating the critical role of bulk transport through fullerene in promoting charge dissociation/transport.[207] Many

211. J. C. Hummelen, B. W. Knight, F. Lepeq, F. Wudl, J. Yao, C. L. Wilkins, "Preparation and characterization of fulleroid and methanofullerene derivatives", *J. Org. Chem.*, **1995**, *60*, 532-538.
212. G. Yu, J. Gao, J. C. Hummelen, F. Wudl, A. J. Heeger, "Polymer photovoltaic cells: Enhanced efficiencies via a network of internal donor-acceptor heterojunctions", *Science*, **1995**, *270*, 1789-1791.
213. P. Gao, M. Graetzel, M. K. Nazeeruddin, "Organohalide lead perovskites for photovoltaic applications", *Energy Environ. Sci.*, **2014**, *7*, 2448-2463.

examples of $PC_{61}BM$ for PV applications can be found in the literature.[197,214,215] Particularly, it is shown an example of the use of $PC_{61}BM$ as a ETM in inverted PSCs. Petrozza and co-workers presented a comparative study employing TiO_2 and $TiO_x/PC_{61}BM$ as the ETM in planar PSCs with a standard structure. The stabilized PCE was 17.6 % with an V_{oc} of 1.11 V and negligible hysteresis. Such excellent figures of merit were achieved by engineering a solution-processed electron buffer layer that does not require high temperature steps. A compact thin film of perovskite absorber was grown onto the electron extraction layer by implementing a novel two-step procedure. Therefore, a novel, hybrid deposition method for hybrid perovskites was presented, which produces good quality polycrystalline thin film independently of the nature of beneath layers, thus opening the solar cell design to a large library of ETMs.[216]

Although $PC_{61}BM$ has been widely used as hole blocking/electron transporting material in p-i-n PSCs, this monoadduct presents some chemical limitations as well as morphological instability under thermal annealing[217] and in films (i.e., aggregation)[201] which may limit the performance of solar cells. Besides, its room temperature solubility in aromatic solvents is limited to approximately 20 mg/mL, limiting the maximum achievable layer thickness.

To overcome that issue, a large number of candidates and new methodologies have been proposed in the literature in order to improve the properties of electron transporting layer in PSCs.

214. W. Ma, C. Yang, X. Gong, K. Lee, A. J. Heeger, "Thermally stable, efficient polymer solar cells with nanoscale control of the interpenetrating network morphology", *Adv. Funct. Mater.*, **2005**, *15*, 1617-1622.
215. X. Yang, J. Loos, S. C. Veenstra, W. J. H. Verhees, M. M. Wienk, J. M. Kroon, M. A. J. Michels, R. A. J. Janssen, "Nanoscale morphology of high-performance polymer solar cells", *Nano Lett.*, **2005**, *5*, 579-583.
216. C. Tao, S. Neutzner, L. Colella, S. Marras, A. R. Srimath Kandada, M. Gandini, M. D. Bastiani, G. Pace, L. Manna, M. Caironi, C. Bertarelli, A. Petrozza, "17.6 % stabilized efficiency in low-temperature processed planar perovskite solar cells", *Energy Environ. Sci.*, **2015**, *8*, 2365-2370.
217. Y. C. Huang, S. Y. Chuang, M. C. Wu, H. L. Chen, C. W. Chen, W. F. Su, "Quantitative nanoscale monitoring the effect of annealing process on the morphology and optical properties of poly(3-hexylthiophene)/[6,6]-phenyl C_{61}-butyric acid methyl ester thin film used in photovoltaic devices", *J. Appl. Phys.* , **2009**, *106*, 034506.

$PC_{71}BM$ (figure 89), as fullerene analogue of $PC_{61}BM$, have also been explored as ETMs in PSCs. Significantly higher absorption coefficient in the visible region of the $PC_{71}BM$, made it attractive for photodiodes, photodetectors and PV applications.[218] $PC_{71}BM$ was used as a ETM in high quality perovskite-based devices. PEDOT:PSS was employed as hole-transport layer and the perovskite active layer was deposited by an optimized two-step spin-coating process. A champion cell reached a PCE of 16.3 % with a remarkably high V_{oc} of 1.05 V and FF of 78 %. The results presented by Wu and co-workers demonstrated that fabricating highly efficient inverted perovskite devices in a more controllable manner is possible via a new perovskite film preparation method and careful interface engineering.[219]

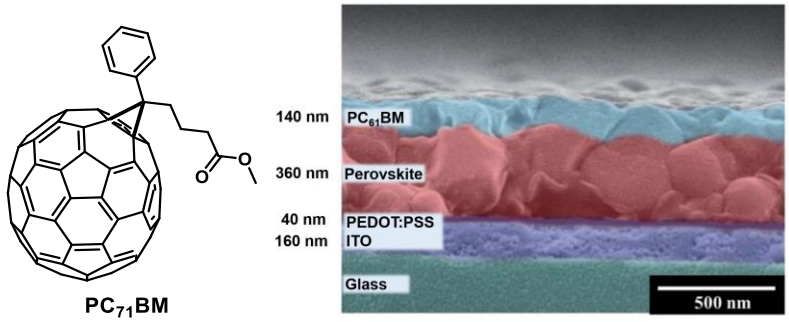

Figure 89. $PC_{71}BM$ molecular structure and SEM image of the cross-section of the champion cell (without the Al electrode).

The synthesis of a new monoadduct isobenzofulvene-C_{60}-epoxide (ETM-**107**, figure 90) as alternative to $PC_{61}BM$ and metal oxides for PSCs processed in air was reported by Chang and co-workers in 2015. This novel ETM was employed with ($MAPbI_{3-x}Cl_x$)-based perovskite in solar cells, both in the regular and inverted device configurations. ETM-**107** presented superior morphological stability and provides higher PV device performance compared to the conventional acceptor $PC_{61}BM$ under the same conditions (6.9 % *vs.* 2.5 % in the regular and 9.0 % *vs.* 5.3 % in the inverted device configuration).[201]

218. M. M. Wienk, J. M. Kroon, W. J. H. Verhees, J. Knol, J. C. Hummelen, P. A. Van Hal, R. a. J. Janssen, "Efficient methano[70]fullerene/MDMO-PPV bulk heterojunction photovoltaic cells", *Angew. Chem. Int. Ed.*, **2003**, *42*, 3371-3375.
219. C. H. Chiang, Z. L. Tseng, C. G. Wu, "Planar heterojunction perovskite/ $PC_{71}BM$ solar cells with enhanced open-circuit voltage via a (2/1)-step spin-coating process", *J. Mater. Chem. A*, **2014**, *2*, 15897-15903.

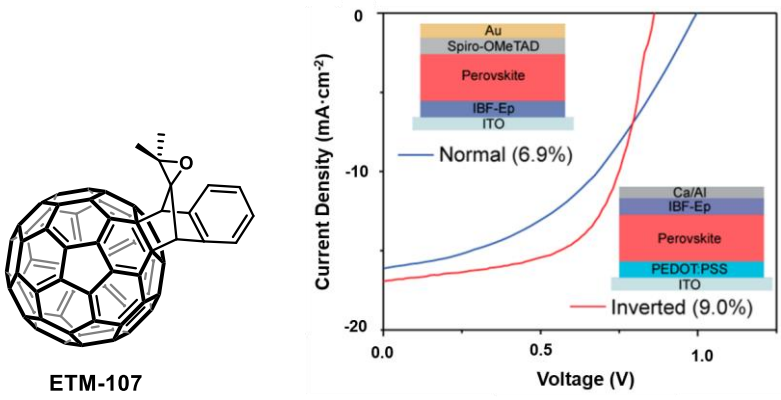

Figure 90. ETM-**107** as a ETM in regular and inverted device configuration.

On the other hand, a new fullerene derivative named ETM-**108**, was employed by Yang and co-workers in planar p-i-n PSCs. Compared with $PC_{61}BM$, this fullerene derivative features a higher hydrophobicity (figure 91), higher LUMO energy level and higher ability of self-assembly. With the device structure of FTO/NiO_x/$MAPbI_3$/ETM-**108**/Ag, ETM-**108** showed PCEs of up to 17.6 % with negligible hysteresis, which is higher than $PC_{61}BM$ (16.1 %) in the same conditions.[199]

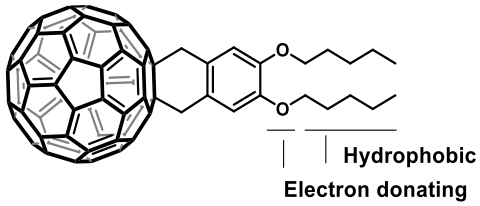

Figure 91. ETM-**108** as a ETM for PSCs.

Echegoyen and co-workers reported two fulleropyrrolidine derivatives comparing their PV behaviour to $PC_{61}BM$ and $PC_{71}BM$. 2,5-(Dimethyl ester)C_{60}-fulleropyrrolidine (ETM-**109**) and the analogous C_{70}-derivative (ETM-**110**) (figure 92) were synthesized in high yield via a 1,3-dipolar cycloaddition reaction at room temperature and incorporated into $MAPbI_3$-based PSCs as ETMs. Possibly because the attached pyrrolidine ester groups are able to coordinate with the perovskite layer, the devices based on ETM-**109** and

ETM-**110** achieved not only good PCEs (15.2 % and 16.4 %, respectively) but also good stability, higher than those based on $PC_{61}BM$ and $PC_{71}BM$.[220]

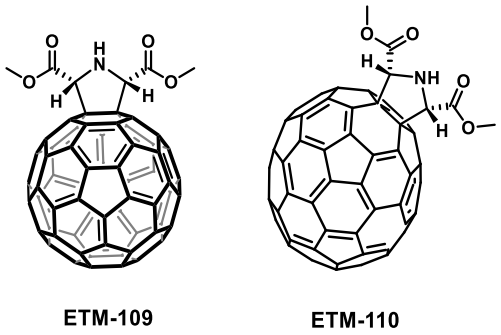

Figure 92. ETM-**109** and ETM-**110** structures as ETMs for PSCs.

It is known that the addition of organic addends to double bonds of the fullerene increase the LUMO energy level.[221] In addition, the LUMO energy of the acceptor directly affects the V_{oc} in the devices, following the model proposed by Scharber *et al.*[222] and Koster *et al.*[223] Therefore, looking for improving the device performance, multiadducts of fullerene have also been explored. A clear correlation between the charge-transporting properties (electron mobility) of fullerene-based ETMs and PV performance was reported by Jen and co-workers, employing C_{60}, $PC_{61}BM$ and $IC_{60}BA$ (figure 93). The PCEs of the fullerene-derived PSCs (8.1 % for $IC_{60}BA$, 13.4 % for $PC_{61}BM$ and 15.4 % for C_{60}) clearly followed the trend of increased electron mobility in the fullerene layer ($6.9 \cdot 10^{-3}$ $cm^2 \cdot V \cdot s^{-1}$ for $IC_{60}BA$, $6.1 \cdot 10^{-2}$ $cm^2 \cdot V \cdot s^{-1}$ for $PC_{61}BM$, and 1.6 $cm^2 \cdot V \cdot s^{-1}$ for C_{60}), which confirmed that high-mobility fullerenes can effectively promote charge dissociation/transport in PSCs.[207]

220. C. Tian, E. Castro, T. Wang, G. Betancourt-Solis, G. Rodriguez, L. Echegoyen, "Improved performance and stability of inverted planar perovskite solar cells using fulleropyrrolidine layers", *ACS Appl. Mater. Interfaces*, **2016**, *8*, 31426-31432.
221. Y. Matsuo, J. Kawai, H. Inada, T. Nakagawa, H. Ota, S. Otsubo, E. Nakamura, "Addition of dihydromethano group to fullerenes to improve the performance of bulk heterojunction organic solar cells", *Adv. Mater.*, **2013**, *25*, 6266-6269.
222. M. C. Scharber, D. Mühlbacher, M. Koppe, P. Denk, C. Waldauf, A. J. Heeger, C. J. Brabec, "Design rules for donors in bulk-heterojunction solar cells-towards 10 % energy-conversion efficiency", *Adv. Mater.*, **2006**, *18*, 789-794.
223. L. J. A. Koster, V. D. Mihailetchi, P. W. M. Blom, "Ultimate efficiency of polymer/fullerene bulk heterojunction solar cells", *Appl. Phys. Lett.*, **2006**, *88*, 093511.

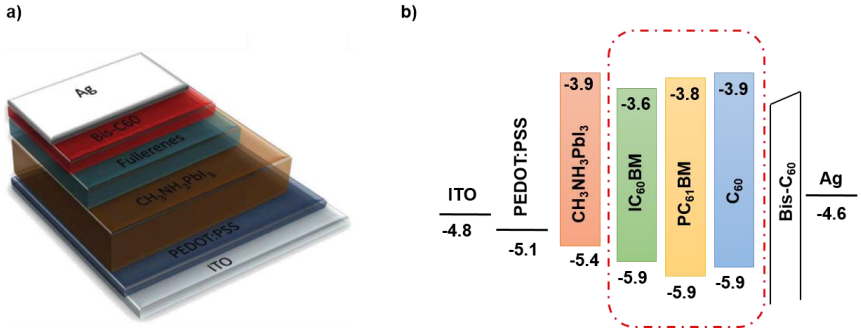

Figure 93. a) Device configuration. **b**) Energy diagram of each layer in devices.

Yang and co-workers developed a simple three-layered efficient perovskite device by replacing the commonly employed $PC_{61}BM$ with an ultrathin fulleropyrrolidinium iodide (ETM-**111**, figure 94) as a ETM in an inverted p-i-n architecture. An average PCE of 13.5 % and a maximum efficiency of 15.2 % were achieved. Steady-state photoluminescence and time-resolved photoluminescence measurements show that the high performance is attributed to the efficient blocking of holes and high extraction efficiency of electrons by ETM-**111**, due to a favourable energy level alignment between the $MAPbI_3$-perovskite and the Ag electrodes.[224]

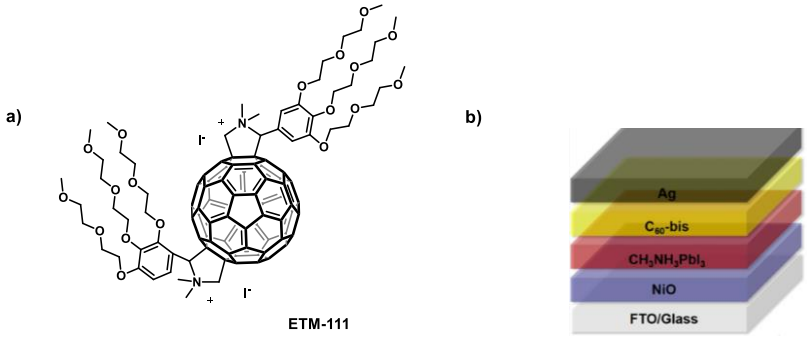

Figure 94. a) ETM-**111** structure. **b**) Simplified perovskite-based device.

224. J. Huang, X. Yu, J. Xie, C. Z. Li, Y. Zhang, D. Xu, Z. Tang, C. Cui, D. Yang, "Fulleropyrrolidinium iodide as an efficient electron transport layer for air-stable planar perovskite solar cells", *ACS Appl. Mater. Interfaces*, **2016**, *8*, 34612-34619.

1.3. Non-fullerene-based electron-transporting materials

Despite the attractive properties offered by fullerenes, they present some disadvantages such as high cost, poor ambient stability and monotonous tunability in terms of frontier energy levels.[225] In addition, for the inverted structure, electron transport layer is exposed to the ambient air except for metal electrode. It was found that the fullerene could absorb oxygen or water onto the surface, leading to a dipole moments and a large resistance as a result of degradation. Furthermore, $PC_{61}BM$ has a stability issue for PV solar cells due to hydrophilicity of the ester group.[226]

Therefore, there is an urgent need to develop efficient non-fullerene organic ETMs with tuneable energy levels and comparable properties to fullerenes for application in PV solar cells. Some examples of non-fullerenic ETMs for perovskite-based devices are highlighted below.

Jen and co-workers reported one of the first non-fullerene small-molecule ETMs for inverted PV solar cells. A series of hydrophobic hexaazatrinaphthylene derivatives peripherally functionalized with alkylsulfanyl chains of different lengths and with different sulfur oxidation states (sulfide, ETM-**112**, sulfoxide, ETM-**113** and sulfone, ETM-**114**) were prepared. Hexaazatrinaphthylene derivatives had attracted attention as promising ETMs as a result of their low cost, high charge mobility and large band gap. The PCE reported using ETM-**113**, up to 17.6 % with negligible hysteresis, was among the highest value reported for inverted solar cells using non-fullerene ETMs. Moreover, their potential ability to passivate the surface traps of perovskites endow the resulting PV solar cells with significantly improved device stability.[198]

225. A. Anctil, C. W. Babbitt, R. P. Raffaelle, B. J. Landi, "Material and energy intensity of fullerene production", *Environ. Sci. Technol.*, **2011**, *45*, 2353-2359.
226. Q. Bao, X. Liu, S. Braun, M. Fahlman, "Oxygen- and water-based degradation in [6,6]-phenyl-C_{61}-butyric acid methyl ester (PCBM) films", *Adv. Energy Mater.*, **2014**, *4*, 1301272-1301279.

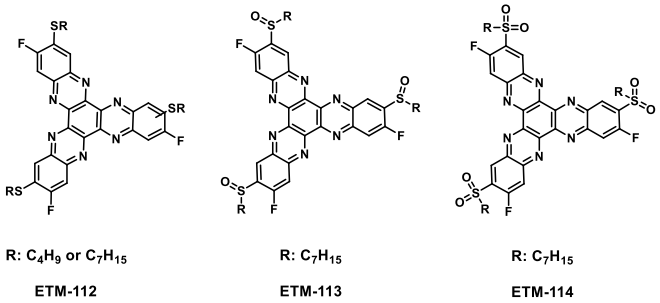

Figure 95. Hexaazatrinaphthylene (ETM-**112**, ETM-**113** and ETM-**114**) derivatives as effective ETMs for PSCs.

Additionally, organic compounds have been employed for regular planar heterojunction PSC structures. For the first time, Wang and co-workers introduced amino-substituted perylenediimide derivative, such as ETM-**115**, as an alternative to replace the commonly used TiO_2 in planar heterojunction PSCs. A maximum PCE of 17.7 % was obtained with this structure: glass/FTO/ ETM-**106**/$MAPbI_{3-x}Cl_x$ /spiro-MeOTAD/Au (figure 96).[227]

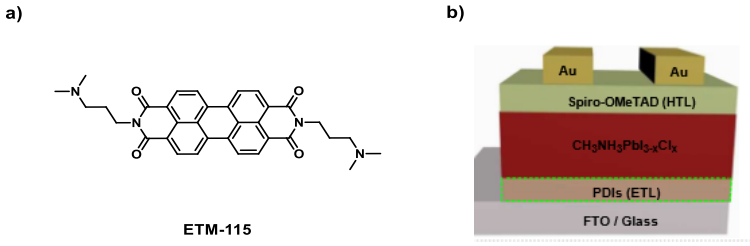

Figure 96. a) Molecular structure of the ETM-**115**, **b**) device architecture of the regular PSC used.

The published results revealed that the terminal amino group in ETM-**115** resulted in the enhanced wetting capability of surfaces to perovskite and the lower the surface work function of FTO substrate as well as passivate the surface trap states of perovskite films. The results confirm that small molecule semiconductor ETM-**115** can serve as an effective ETM for achieving high-

227. H. Zhang, L. Xue, J. Han, Y. Q. Fu, Y. Shen, Z. Zhang, Y. Li, M. Wang, "New generation perovskite solar cells with solution-processed amino-substituted perylene diimide derivative as electron-transport layer", *J. Mater. Chem. A*, **2016**, *4*, 8724-8733.

performance PSCs and draw molecular design guidelines for electron selective contacts with perovskite.

In addition, it has been studied the influence of n-doped electron-transporting molecules. Jo and co-workers introduced a perylenediimide dimer (ETM-**116**) as a solution processible non-fullerene ETM for inverted PSCs. ETM-**116** shows electron accepting ability comparable to $PC_{61}BM$, which is evidenced by PL quenching and exhibits a moderate PCE of 7.1 % with a J_{sc} of 17.2 $mA \cdot cm^{-2}$ in inverted PSCs. Furthermore, when ETM-**116** is doped by 1 wt % DMBI, the efficiency of the device with the DMBI-doped ETM-**116** is remarkably increased to 10.0 % with a J_{sc} of 21.6 $mA \cdot cm^{-2}$. This enhancement was mainly attributed to increased electrical conductivity of ETM-**116** by n-doping.[228]

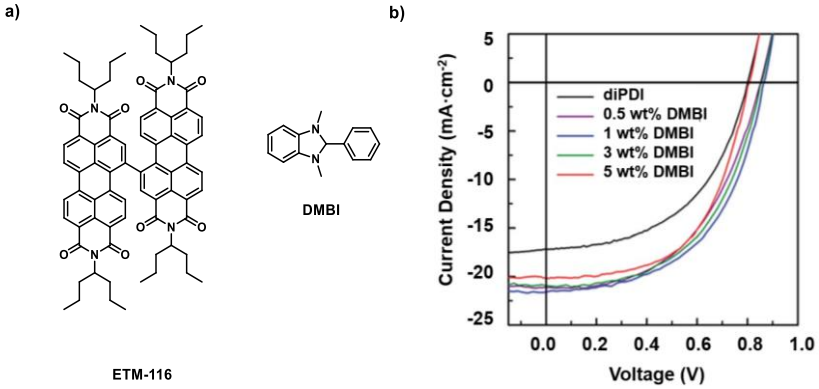

Figure 97. a) Chemical structures of ETM-**116** and DMBI, **b**) J-V curves.

On the other hand, polymers have been widely studied as electron-transporting layer in inverted PSCs. It is worth noting the study of three n-type polymers of the naphthalenediimidebithiophene family as electron extraction layers in hybrid PSCs, reported by Loi and co-workers (figures 98 and 99). It was studied how the structural, photophysical and charge transport properties of the perovskite/n-type polymer electron extraction layer interface affect hybrid PSC device performance. PCEs of 10.8 % were achieved using the high mobility n-type polymers P(NDI2OD-T2) (ETM-**117**) and P(NDI2DT-T2) (ETM-**118**) whereas the device using the low mobility n-type polymer P(NDI2OD-TET) (ETM-**119**)

228. S. S. Kim, S. Bae, W. H. Jo, "A perylene diimide-based non-fullerene acceptor as an electron transporting material for inverted perovskite solar cells", *RSC Adv.*, **2016**, *6*, 19923-19927.

as the ETM showed a very low PCE. Even though the offsets between the conduction band of the perovskite and the polymer LUMOs were quite small difference, optical measurements confirmed the efficient extraction of electrons. Trap assisted recombination was evidenced in devices using all the three n-type polymers as ETMs.[229]

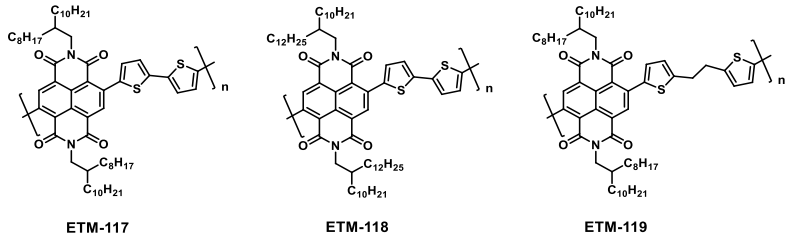

Figure 98. Chemical structure of ETM-**117**, ETM-**118** and ETM-**119**.

Finally, it could be concluded that the ETM bulk electron mobility, rather than the energy offset between the perovskite and the electron extraction layer LUMO energy, plays the dominant role in the charge collection in hybrid PSCs.

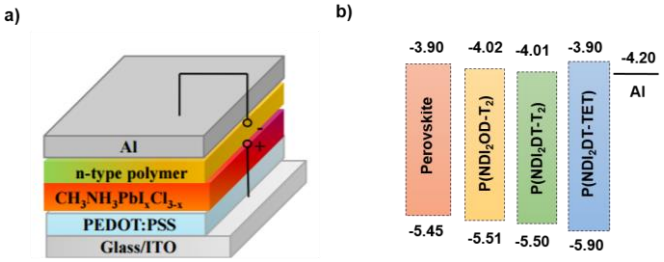

Figure 99. a) Device structure described in this study. **b**) Energy levels of the perovskite and of the three n-type polymers.

1.4. Inorganic ETMs

On the other hand, a variety of transition metal oxides have been also investigated as electron-transporting layers for PSCs. These solar cells are generally fabricated on nanostructured metal oxide substrates to maximize the interfacial area for efficient charge collection. Although n-type inorganics, such

229. S. Shao, Z. Chen, H. H. Fang, G. H. Ten Brink, D. Bartesaghi, S. Adjokatse, L. J. A. Koster, B. J. Kooi, A. Facchetti, M. A. Loi, "n-Type polymers as electron extraction layers in hybrid perovskite solar cells with improved ambient stability", *J. Mater. Chem. A*, **2016**, *4*, 2419-2426.

as TiO_2, ZnO[230] and ZrO_2[67] have been utilized in the regular PSCs, the use of n-type inorganic single layer as electron selective contact were seldom reported in the inverted PSCs.[50] However, the processing of the metal oxides involves a high-temperature sintering step, which makes them incompatible with perovskite layers that cannot tolerate temperatures above 100 ºC. Therefore, the fabrication of inverted cells with an metal oxide as the ETM, where metal oxide layers are deposited on top of perovskite, has remained a challenge.[27]

230. J. You, L. Meng, T. B. Song, T. F. Guo, Y. Yang, W. H. Chang, Z. Hong, H. Chen, H. Zhou, Q. Chen, Y. Liu, N. De Marco, Y. Yang, "Improved air stability of perovskite solar cells via solution-processed metal oxide transport layers", *Nat. Nanotechnol.*, **2016**, *11*, 75-81.

•• Results and discussion

Chapter 2. Electron-transporting materials
for perovskite solar cells

2. RESULTS AND DISCUSSION

Successive improvements in perovskite composition, deposition methods, cell configurations and electron and hole transporting materials have produced high certified performance devices in a short period of time. Nevertheless, many aspects remain unclear and are still under debate. One of them is the role of the charge selective contacts, not only in terms of the overall efficiency but also in terms of the anomalous phenomena widely observed in PSCs; for instance, the hysteresis present in J-V curves. Many different contacts have been studied for PSCs, which confirm their important role on the solar cell efficiency, stability and hysteresis.[9,10] In addition, the PV performance does not only depend on the light absorbing material. The efficient charge extraction at the selective contacts is also important.[15] Particularly, organic electron selective contacts are receiving increasing attention, being TiO_2 probably the most extensively used electron selective contact in PSCs.[16]

Remarkable, fullerenes have received a lot of interest for PV applications, from BHJ solar cells[231,232] to perovskite-based devices.[206] C_{60} and its derivatives exhibit high electron affinity and good electron acceptor properties. Their π-conjugated structure enables the charge delocalization, thus enhancing the electron extraction. Owing to these promising properties C_{60}-based materials have been extensively explored in PV applications. In the present thesis, several C_{60}-derivatives are reported as potential candidates for being used in perovskite-based solar cells.

2.1. Design and synthesis of C_{60}-derivatives bearing benzoid acid

In this section, a series of C_{60}-based carboxylic acid has been prepared. It is well-stablished that the carboxylic acid is an effective anchoring group to link with TiO_2 by a coordination bond between the carboxylic group and the Ti

231. H. J. Bolink, E. Coronado, A. Forment-Aliaga, M. Lenes, A. La Rosa, S. Filippone, N. Martin, "Polymer solar cells based on diphenylmethanofullerenes with reduced sidechain length", *J. Mater. Chem.*, **2011**, *21*, 1382-1386.
232. G. Garcia-Belmonte, P. P. Boix, J. Bisquert, M. Lenes, H. J. Bolink, A. La Rosa, S. Filippone, N. Martín, "Influence of the intermediate density-of-states occupancy on open-circuit voltage of bulk heterojunction solar cells with different fullerene acceptors", *J. Phys. Chem. Lett.*, **2010**, *1*, 2566-2571.

atoms.[233,234] This approach has been widely employed for the development of DSSCs.

2.1.1. C_{60}-monoadducts bearing benzoid acid

The synthesis of four monoadducts functionalized with a carboxyl group is presented in this section. The corresponding syntheses of the precursors and intermediates (**120, 121**, **123** and **124**) are presented first (scheme 18, 19, 20 and 21 respectively). The intermediate 4-((carboxymethyl) amino)benzoic acid (**120**) was obtained following a procedure previously described in the literature.[235] Starting from commercially available 4-aminobenzoic acid and ethyl chloroformiate in refluxing water, compound **120** was obtained in excellent yields after crystallization from ethanol.

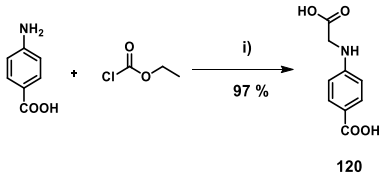

Scheme 18. *Reagents and conditions*: **i**) H_2O, 100 ºC.

The synthesis of the desired intermediate **121** was carried out in one-step synthesis as it is shown in scheme 19. Starting from commercially available 3,4-dimethylbenzoic acid, in the presence of benzoyl peroxide and NBS in CCl_4, it was possible to obtain the compound **121**.

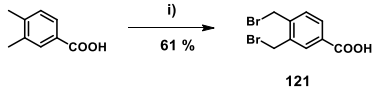

Scheme 19. *Reagents and conditions:* **i**) benzoyl peroxide, NBS, CCl_4, 76 ºC.

233. A. Abrusci, S. D. Stranks, P. Docampo, H. L. Yip, A. K. Y. Jen, H. J. Snaith, "High-performance perovskite-polymer hybrid solar cells via electronic coupling with fullerene monolayers", *Nano Lett.*, **2013**, *13*, 3124-3128.
234. S. K. Hau, H. L. Yip, O. Acton, N. S. Baek, H. Ma, A. K. Y. Jen, "Interfacial modification to improve inverted polymer solar cells", *J. Mater. Chem.*, **2008**, *18*, 5113-5119.
235. S. Specklin, E. Decuypere, L. Plougastel, S. Aliani, F. Taran, "One-pot synthesis of 1,4-disubstituted pyrazoles from arylglycines via copper-catalyzed sydnone–alkyne cycloaddition reaction", *J. Org. Chem.*, **2014**, *79*, 7772-7777.

The intermediate **123** was synthesized by a two-step synthetic reaction. The commercially available 5-oxo-5-phenylpentanoic acid, in the presence of oxalyl dichloride and methanol, gives to the formation of the compound **122**. Subsequently, compound **122** with NH_2NHTos in ethanol affords the target intermediate **123** (scheme 20).

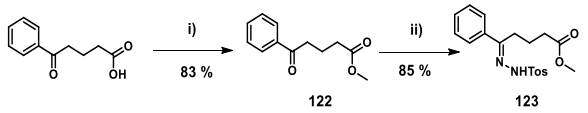

Scheme 20. *Reagents and conditions*: **i**) oxalyl dichloride, methanol, 65 ºC; **ii**) NH_2NHTos, ethanol, 78 ºC.

Finally, the synthetic route for preparing the intermediate **124** was conducted in one-step as it is illustrated in scheme 21. Starting from C_{60} in the presence of diethyl malonate and I_2 in toluene and DBU, monoadduct **124** was obtained.

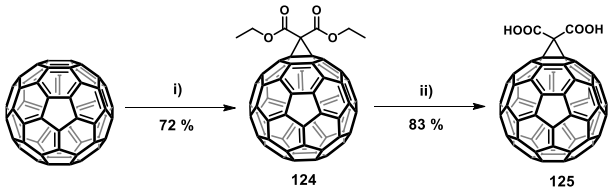

Scheme 21. *Reagents and conditions*: **i**) diethyl malonate, I_2, toluene, DBU, 111 ºC; **ii**) *a*. NaH, toluene, 60 ºC, *b*. methanol, 2 M H_2SO_4:water.

The saponification of the malonate derivative **124** under basic conditions was inappropriate since either the conversions to the acid derivative is incomplete or it is accompanied by nucleophilic additions of hydroxide to the fullerene core. However, the corresponding C_{60}-based carboxylic acid (**125**) was successfully accomplished by stirring derivative **124** in toluene under nitrogen in the presence of NaH at 60 ºC. The quantitative precipitation of the sodium salt of the fullerene malonic acid took place after the addition of methanol. After centrifugation and removal the liquid phase, the precipitated was washed with toluene and 2 M H_2SO_4:water.

Finally, the others C_{60}-based carboxylic acid monoadducts (compounds **126** to **128**) were synthesized as it is depicted in scheme 22.

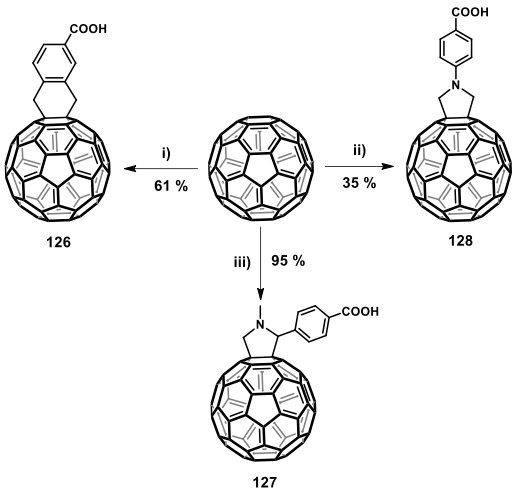

Scheme 22. *Reagents and conditions:* **i**) **121**, KI, 18-Crown-6, toluene, 111 ºC; **ii**) **120**, *p*-formaldehyde, C_{60}, chlorobenzene, 130 ºC; **iii**) C_{60}, 4-formylbenzoic acid, sarcosine, toluene, 111 ºC.

A one-step procedure was followed to prepare the target monoadduct **126**.[236] Starting from C_{60} completely dissolved in toluene, in the presence of 3,4-bis (bromomethyl)benzoic acid, KI and 18-Crown-6, the desired compound **126** was obtained by a Diels-Alder reaction. C_{60}-subsituted benzoic acid **127** was synthesized by a straightforward route.[237] Starting from commercially available C_{60}, 4-formylbenzoic acid and sarcosine, it was possible to obtain the desired compound by 1,3-dipolar cycloaddition reaction in good yield. Finally, monoadduct **128** was prepared by one-step 1,3-dipolar cycloaddition reaction in presence of the intermediate **120**, synthesized according to scheme 18, C_{60} and *p*-formaldehyde.

Complete structural characterization of the final compounds and the corresponding intermediates was accomplished using standard spectroscopic techniques such as ^{1}H NMR and ^{13}C NMR in order to confirm that they present

236. P. Belik, A. Guegel, A. Kraus, M. Walter, K. Muellen, "Diels-Alder adduct of C_{60} and 4-carboxy-*o*-quinodimethane: Synthesis and chemical transformations", *J. Org. Chem.*, **1995**, *60*, 3307-3310.
237. S. K. Hau, Y. J. Cheng, H. L. Yip, Y. Zhang, H. Ma, A. K. Y. Jen, "Effect of chemical modification of fullerene-based self-assembled monolayers on the performance of inverted polymer solar cells", *ACS Appl. Mater. Interfaces*, **2010**, *2*, 1892-1902.

identical spectroscopic properties to those reported. In the case of the novel derivative **128**, MS-MALDI experiments were carried out which confirm the molecular peak of the target compound.

2.1.2. C_{60}-bisadducts bearing benzoic acid

With an eye toward carrying out a systematic comparative study of C_{60}-derivatives with different LUMO energy, two new bisadducts were synthesized. Benzoic acid group was incorporated to C_{60}-derivatives already reported, dicyanofullerene[238] and $PC_{61}BM$.[211] The desired bisadducts (compounds **130** and **131**) were obtained by a 1,3-dipolar cycloaddition reaction in the presence of the corresponding monoadduct, 4-formylbenzoic acid and sarcosine through a straightforward route (scheme 23).

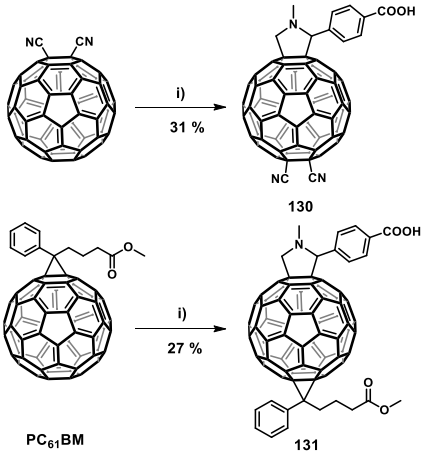

Scheme 23. *Reagents and conditions*: **i)** 4-formylbenzoic acid, sarcosine, chlorobenzene, 130 ºC.

Structural characterization of the final compounds was accomplished using standard spectroscopic techniques in order to confirm that they present identical spectroscopic properties to those reported. The novel C_{60}-derivative **130** presents a complex ^1H NMR spectrum characterized by broad signals. However, the presence of the desired compound was also confirmed by ESI-MS m/z 950.1 $[M+H]^+$.

238. M. Keshavarz-K, B. Knight, G. Srdanov, F. Wudl, "Cyanodihydrofullerenes and dicyanodihydrofullerene: The first polar solid based on C_{60}", *J. Am. Chem. Soc.*, **1995**, *117*, 11371-11372.

2.2. Characterization of C_{60}-derivatives bearing carboxylic acid and devices

It has been reported in the literature that the use of C_{60} in either perovskite-based solar cells or BHJ devices, not only significantly improves the V_{oc} and the FF, but also reduces the losses from recombination processes.[17,18] This fact indicates a better electron extraction when the fullerene derivatives substitute the TiO_2 or they are on the top of the TiO_2 layer. Therefore, modifying the ETM-perovskite interface can significantly enhance the electron injection and electron transfer, as well as reducing the charge recombination.[216,239]

On the other hand, it is commonly established in the literature that the use of interlayers based on fullerene, such as SAMs (self-assembly monolayers) in PSCs with inverted configuration,[240] apart from significantly reducing the photoluminescence life-time, it may improve the efficiency and produce devices without J-V hysteresis. However, recent articles demonstrate that this statement cannot be generalized. For example, significant hysteresis has been detected at low temperature even with the presence of fullerene derivatives.[11,12]

In collaboration with Prof. Iván Mora's group (Jaime I University, Castellón, Spain), it was published the influence of SAM of C_{60}-derivatives in solar cell performance and hysteresis. Through the use of fullerene derivatives specifically functionalized, it was possible to study the effect of inserting additional functional groups on the fullerene unit in the SAM used as interface in the device. The three C_{60}-derivatives studied (**126**, **127** and **130**) are shown in figure 100.

239. K. Wojciechowski, S. D. Stranks, A. Abate, G. Sadoughi, A. Sadhanala, N. Kopidakis, G. Rumbles, C.-Z. Li, R. H. Friend, A. K. Y. Jen, H. J. Snaith, "Heterojunction modification for highly efficient organic–inorganic perovskite solar cells", *ACS Nano*, **2014**, *8*, 12701-12709.
240. N. K. Noel, A. Abate, S. D. Stranks, E. S. Parrott, V. M. Burlakov, A. Goriely, H. J. Snaith, "Enhanced photoluminescence and solar cell performance via lewis base passivation of organic–inorganic lead halide perovskites", *ACS Nano,* **2014**, *8*, 9815-9821.

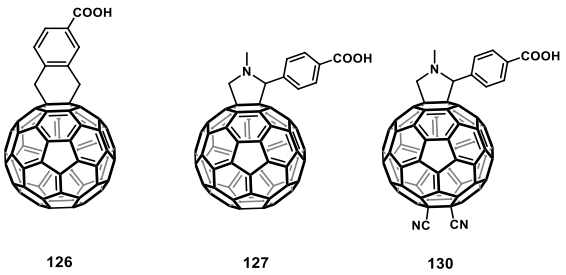

126 127 130

Figure 100. C_{60}-derivatives studied as interface SAM in PSCs.

The monoadduct **126** contains a carboxylic acid based anchoring group linked to C_{60} through a fused tetrahydronaphthalene unit. C_{60}-derivatives **127** and **130**, share the same benzoic acid moiety, however, the C_{60}-bisadduct **130** possesses also two cyano groups saturating a second double bond. This fact significantly modifies the reduction potential values of the molecule and provides further anchoring group through the lone pair nitrogen atoms. Fullerene derivative **127**, previously studied in the literature,[239] was used as a reference in the study. In this case, a benzoic acid is linked to the fullerene through a *N*-methylpyrrolidine ring. The modifications in the C_{60}-derivatives employed, allow the study not only on the influence of the bridging functional group that connects the fullerene with the oxide substrate, but also on the influence of the functional groups that contact directly with the perovskite layer, i.e., the cyanide groups from **130** and acid from **127**.

2.2.1. Optical and electrochemical properties

To determine the fundamental properties of the molecules studied such as optical characteristics and HOMO-LUMO energy levels, UV-vis absorption and electrochemical experiments were carried out. The detailed features are collected in table 27. Figure 101 illustrates the normalized absorption curves of the C_{60}-monoaducts (**126** and **127**) and the C_{60}-bisaduct (**130**).

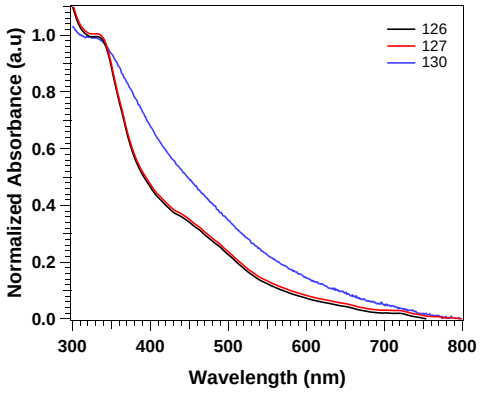

Figure 101. Normalized absorption curves of C_{60}-derivatives **126**, **127** and **130** in thin films at r.t.

The absorption spectrum of the three compounds in thin film, presents a maximum around 350 nm. The monoadducts **126** and **127** present the same UV-vis curve being slightly more intense the absorbance corresponding to bisadduct, **130**.

Figure 102 shows the cyclic voltammograms for each compound. The measurements were carried out using 0.1 M solution of $(n\text{-Bu})_4NPF_6$ ($TBAPF_6$) in *o*-DCB. Glassy carbon was used as working electrode and platinum wires as counter and reference electrodes. Ferrocene was used as internal standard reference.

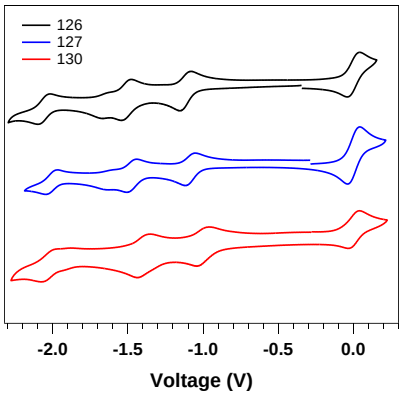

Figure 102. Cyclic voltammograms of C_{60}-derivatives **126**, **127** and **130** measured at r.t.

The cyclic voltammograms of the C_{60}-derivatives are active in the cathodic region. Compounds **126**, **127** and **130** show four and three reduction waves with $E_{1/2}$ values of: -1.08 V, -1.47 V, -1.62 V and -1.99 V for **126**; -1.11 V, -1.51 V, -1.67 V and -2.05 V for **127** and -0.99 V, -1.39 V, -2.01 V for **130**.Three of them correspond to one-electron reversible reduction processes of the C_{60}.

Taking into account the value of the first reduction wave, the LUMO energy levels were calculated using the equation 7. The energy inferred for the LUMO of compound **126**, **127** and **130**, is -5.75 eV, -5.71 eV and -6.00 eV, respectively. The HOMO energies were calculated from the LUMO values and the optical band gap, determined from the absorption spectra (1.70 eV, 1.70 eV and 1.65 eV, for compound **126**, **127** and **130**, respectively) using equation 7.

$$E_{LUMO}\ (eV) = -\ (E^{red}_{1/2} + 5.1) \qquad (7)$$

Table 27. Wavelength of the maximum absorption, optical gap, reduction potentials, HOMO and LUMO energy of C_{60}-derivatives **126**, **127** and **130**.

C_{60}-deriv.	**λ_{max}[a] (nm)**	**$E_{gap,opt}$[a] (eV)**	**E^1_{red}[b] (V)**	**E^2_{red}[b] (V)**	**E^3_{red}[b] (V)**	**E^4_{red}[b] (V)**	**HOMO[c] (eV)**	**LUMO[d] (eV)**
126	332	1.70	-1.08	-1.47	-1.62	-1.99	-5.75	-4.00
127	332	1.70	-1.11	-1.51	-1.67	-2.05	-5.71	-4.06
130	336	1.65	-0.99	-1.39	-	-2.01	-6.00	-4.20

[a] Determined from the normalized absorption spectra. [b] Half-wave reduction potential from CV measurements *vs.* NHE. [c] E_{HOMO} was estimated by using eq. 3. [d] E_{LUMO} was estimated by using eq. 7.

In this sense, it is especially interesting to analyze how a single fullerene monolayer can affect the electron selective contact-perovskite interface properties. It is worth pointing out that such interesting approach constitutes a valuable tool for a better understanding of the hysteresis origin and its subsequent minimization, while it is based on easy and material-saving procedures compared to the approach based on the exploitation of a thin layer of a fullerene derivative. Additionally, it was studied how the SAM of the fullerene derivatives behave when no compact TiO_2 layer is employed. The presence of compact TiO_2 and/or fullerene derivative SAM has a huge impact on the J-V hysteresis, and an appropriate choice of the fullerene derivative can avoid the photocurrent reduction observed when no compact TiO_2 is used.

In order to analyze the effect of the fullerene-SAM, the probably most extended configuration for PSCs (figure 103a) was chosen. In this configuration, a compact layer (CL) of TiO_2 was deposited on top of a glass/FTO substrate. A mesoporous layer of TiO_2 was subsequently deposited. The deposited perovskite $MAPbI_3$, not only infiltrates into the mesoporous layer of TiO_2 but also produces a perovskite capping layer on top. Finally, spiro-OMeTAD as a hole selective contact and a gold layer were deposited in order to efficiently extract the photo-generated holes. A similar configuration but with no TiO_2 compact layer (NCL) has also been studied (figure 103b).

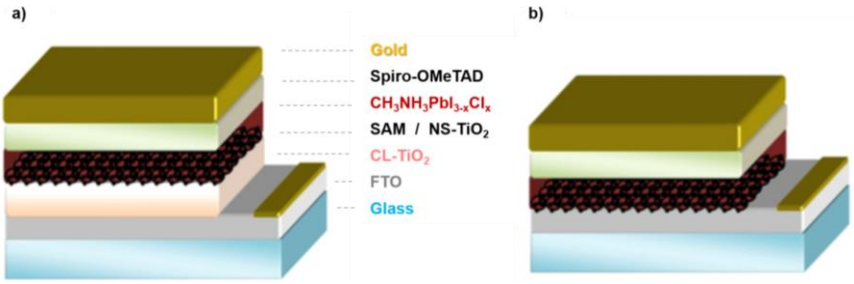

Figure 103. a) with (CL) and **b**) without (NCL) TiO_2 compact layer on top of FTO. Nanostructured TiO_2 layer (NS-TiO_2) was used for all the samples.

Very recently, capacitive and noncapacitive components, whose origins are believed to arise from different physical and/or chemical mechanisms, have been identified in the hysteresis of PSCs.[241] Capacitive hysteresis is directly proportional to the J-V curve scan rate. The change of the scan rate direction consequently produces a change in the sign of the current provoking the hysteresis. Additionally, it has also been observed another hysteresis feature at applied voltages of around 0.5 V at very low scan rates and, consequently, this is believed to arise from a noncapacitive process. Noncapacitive hysteresis is not proportional to scan rate and has a different physical origin. It has been suggested that the origin of noncapacitive hysteresis could be related to the reactivity of the perovskite at the interface with the contact. In this study, it could be observed that the PSCs prepared with a SAM of fullerene derivatives present a mixed hysteresis behavior: first, they exhibit the typical capacitive component of a

241. O. Almora, C. Aranda, I. Zarazua, A. Guerrero, G. Garcia-Belmonte, "Noncapacitive hysteresis in perovskite solar cells at room temperature", *ACS Energy Lett.*, **2016**, *1*, 209-215.

standard PSCs prepared with TiO_2 as an electron selective contact, although the hysteresis is significantly less pronounced when the fullerene SAM is introduced; second, a noncapacitive hysteresis previously observed also in inverted PSCs with fullerene was also detected in PSCs with a SAM. The averaged values of the solar cell parameters obtained in this study are summarized in table 28, where the hysteresis index (HI) was calculated using equation 8 for the corresponding J-V curves obtained.

Table 28. Characteristic parameters of the solar cells analyzed.

Device	Scan direction	J_{sc} (mA·cm^{-2})	V_{oc} (mV)	FF (%)	PCE[a] (%)	HI
CL	reverse	19.8±0.6	909±15	75.4±2	13.5±0.6	0.067±0.004
	forward	19.3±0.6	827±18	63.4±2	10.1±0.7	
CL/127	reverse	19.2±0.5	822±13	71.4±2	11.2±0.3	0.019±0.005
	forward	18.7±0.8	797±15	70.3±2	10.47±0.22	
CL/126	reverse	19.2±0.6	839±12	67±4	10.9±0.8	0.036±0.003
	forward	18.7±0.5	818±8	66±5	10.0±0.8	
CL	reverse	17.1±1.3	792±18	68±5	9.1±0.9	0.20±0.07
	forward	14.5±2.2	728±54	49±9	5.4±1.7	
NCL	reverse	11.9±.1.7	817±16	64±5	6.2±1.0	0.32±0.03
	forward	11.2±1.8	768±35	41±3	3.6±0.7	
CL/130	reverse	18.1±1.3	780±11	63±13	8.9±1.9	0.092±0.016
	forward	16.6±0.9	779±6	71.4±2	9.2±0.5	
NCL/130	reverse	17.4±1.9	753±17	64±6	8.4±1.6	0.198±0.014
	forward	14±3	708±61	43±6	4.4±1.3	

Configuration of the PSCs analyzed in this work: devices with (CL) and without (NCL) TiO_2 compact layer on top of FTO. [a] Averaged values and the corresponding standard errors have been calculated using the results obtained by at least 10 cells. The HI was calculated using eq. 8.

$$HI = \frac{J_{rev}\cdot\left(V_{oc}/_2\right) - J_{for}\cdot\left(V_{oc}/_2\right)}{J_{rev}\cdot\left(V_{oc}/_2\right)} \quad (8)$$

where $J_{rev}\cdot(V_{oc}/2)$ and $J_{for}\cdot(V_{oc}/2)$ are the currents when half of the V_{oc} is applied for reverse (from V_{oc} to zero) and for forward (from zero to V_{oc}) voltage scans, respectively. A device without hysteresis presents a HI of zero, while higher values of HI indicate a more pronounced hysteresis. When **126** and **127** SAMs are used, the HI is significantly reduced, 2- and 4-fold, respectively.

The most conspicuous effect of the presence of the SAM was a clear reduction of the hysteresis. The properties of the TiO_2-perovskite interfaces were modified after SAM deposition, as could be clearly observed from the strong quenching of the PL (figure 104c), conventionally attributed to an improved charge extraction. However, in contrast to previous reports, it did not detect any increase of the photocurrent, which was not altered or was even slightly reduced when the fullerene SAM was introduced (figure 104), respectively. In addition, the slight decrease of V_{oc} detected for samples with SAM and the larger dark current detected when SAM was used, in some cases, made that it was not possible to discard an increase of the recombination when SAM was used.

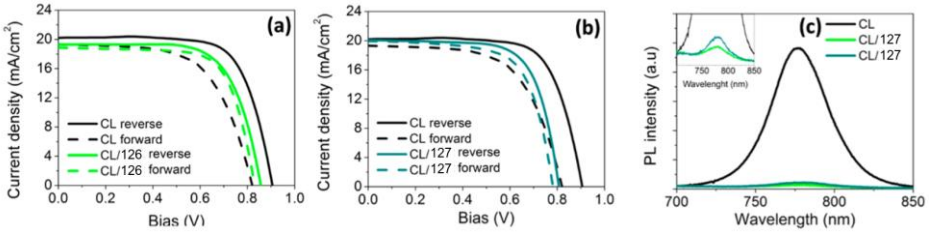

Figure 104. J-V curves for forward and revers scans for PSCs with a SAM of **a**) compound **126** and **b**) compound **127**. **c**) Photoluminescence (PL) intensity of reference sample (compound **121**) and with SAM of compound **126** and **127**.

The different [60]fullerene derivative SAMs analyzed at the electron-selective contacts-perovskite interface, induces in all the cases an important reduction of the J-V curve hysteresis.

It has been determined that the hysteresis reduction is due to the decrease of the capacitive hysteresis typically observed for oxide-based anodes in PSCs. SAM samples also present noncapacitive hysteresis in the dark J-V curve, observed at low scan rates, typically observed in inverted PSCs with organic contacts and,

to a lesser extent, in standard PSCs with compact TiO_2 electron selective contact. To this extent, PSCs with SAMs of fullerene derivatives are midway devices between standard and inverted PSCs. In addition, it was demonstrated by the inclusion of cyanide groups that enhance the direct coupling with the perovskite layer, thus improving the solar cell parameters, as photocurrent, compared to the reference device with no SAM.

However, other aspects as the increase of recombination need to be controlled to optimize the system. The beneficial effect of the SAM can even be extended to the complete removal of the ESC. Only a slight reduction of the hysteresis was observed when one SAM was used with no compact TiO_2 layer; the one SAM passivates the FTO surface, thus maintaining the device photocurrent.

Therefore, this work explains the origin of the hysteresis reduction when a fullerene derivative SAM is employed and paves the way for a future enhancement of PSCs by means of a tailored design of the fullerene molecules that could actuate as an electron selective contact by themselves, without further need of a TiO_2 compact layer.

2.3. Synthesis of ThCBM

Many modifications have been introduced in the $PC_{61}BM$ structure in the recent years in order to tune the miscibility, thermal properties and energy levels of the final materials. Different substituents on the phenyl ring,[242] have been explored as well as exchanging methyl groups with long alkyl chains, among others.[243] The resulting C_{60}-derivatives have been successfully used to control the film morphology and improve the device performance, raising the V_{oc} and the device stability.[244]

242. Y. Zhang, H. L. Yip, O. Acton, S. K. Hau, F. Huang, A. K. Y. Jen, "A simple and effective way of achieving highly efficient and thermally stable bulk-heterojunction polymer solar cells using amorphous fullerene derivatives as electron acceptor", *Chem. Mater.*, **2009**, *21*, 2598-2600.
243. L. Zheng, Q. Zhou, X. Deng, M. Yuan, G. Yu, Y. Cao, "Methanofullerenes used as electron acceptors in polymer photovoltaic devices", *J. Phys. Chem. B*, **2004**, *108*, 11921-11926.
244. H. Zhao, X. Guo, H. Tian, C. Li, Z. Xie, Y. Geng, F. Wang, "Alkyl substituted [6,6]-thienyl-C_{61}-butyric acid methyl esters: Easily accessible acceptor materials for bulk-heterojunction polymer solar cells", *J. Mater. Chem.*, **2010**, *20*, 3092-3097.

Taking into account that thiophene is an aromatic ring characterized by easy modification, recently, a $PC_{61}BM$ analogue, 2-thienylC_{61}-butyric acid methyl ester (ThCBM), was reported to exhibit device performance close to $PC_{61}BM$ in bulk heterojunction solar cells.[244,245] To extend the study toward PSCs, two monoadducts, **135** and **136** were synthesized. Their structures are similar to $PC_{61}BM$ but changing the benzene for a thiophene ring.

The under coordination of the lead atom during the annealing of the perovskite can act as electronic trap states within the perovskite layer. This vacancy positions can be coordinated with sufficiently weak Lewis bases. The lone pair of the sulfur atom of the thiophene ring can interact through electronic attraction with the positive charge of the metal. This effect is known as passivation, which is likely to improve the PV performance along with reducing hysteresis.[240]

Well-stablished protocols reported in the literature were followed to synthesize the two C_{60}-derivatives (scheme 24).[244]

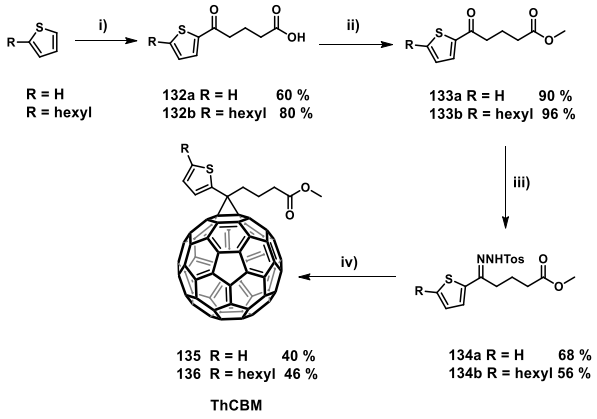

Scheme 24. *Reagents and conditions*: **i**) Glutaric anhydride, $AlCl_3$, DCM, 0 ºC; **ii**) methanol, HCl, 65 ºC; **iii**) $TsNHNH_2$, methanol, ethanol, 75 ºC; **iv**) C_{60}, CH_3ONa, *o*-DCB, pyridine, 75 ºC.

245. P. A. Troshin, H. Hoppe, J. Renz, M. Egginger, J. Y. Mayorova, A. E. Goryachev, A. S. Peregudov, R. N. Lyubovskaya, G. Gobsch, N. S. Sariciftci, V. F. Razumov, "Material solubility-photovoltaic performance relationship in the design of novel fullerene derivatives for bulk heterojunction solar cells", *Adv. Funct. Mater.*, **2009**, *19*, 779-788.

The two C_{60}-monoaducts were prepared by a four-step synthetic procedure. Firstly, compounds **132a,b** were obtained from the commercially available compounds thiophene and 2-hexylthiophene by a Friedel-Crafts acylation. The subsequent esterification reaction was necessary to get **133a**,**b** and these compounds, in the presence of *p*-toluenesulfonyl hydrazide in methanol, afford compounds **134a,b**, respectively. Finally, the reaction with C_{60}, MeONa and pyridine afforded the desired **135** and **136** compounds in yields of 40 and 49 %, respectively. The solubility of **126** in chlorobenzene is 50 ± 5 mg/mL, lower than 80 ± 5 mg/mL of **$PC_{61}BM$**. However, the solubility of **136** is as high as 180 ± 10 mg/mL. This high solubility of **136** is promising for the device fabrication.

Structural characterization of the final C_{60}-monoaducts and the corresponding intermediates was accomplished using standard spectroscopic techniques in order to confirm that they present identical spectroscopic properties to those reported.[244]

2.4. Synthesis of DPM-6-$PC_{61}BM$ bisadduct

Both DPM-6 and $PC_{61}BM$ are really well-known as appealing fullerene materials for PV. Not only their synthesis and properties[211, 231] but also their behaviour in a large number of applications. For that reason, the bisadduct **139** was thought to be an interesting molecule to be synthesized, in order to compare its properties and PV behaviour with respect to DPM-6 and $PC_{61}BM$.

The synthesis of DPM-6 has been carried out in three synthetic steps. From commercially available 4,4'-dihydroxybenzophenone, the intermediate **137** was obtained. Compound **137** reacted with NH_2NHTos in toluene in the presence of PTSA to afford the intermediate **138**. This compound with [60]fullerene under basic conditions (Bamford–Stevens reaction) in refluxing *o*-DCB, affords DPM-6 in moderate yield, according to the procedure described in the literature (scheme 25).[231] Subsequently, the target DPM-6-$PC_{61}BM$ bisadduct (**139**) was synthesized as it is illustrated in the last step of scheme 25. A solution of DPM-6 in *o*-DCB in the presence of the corresponding compound **123** and MeONa, afford the target bisadduct **139**.

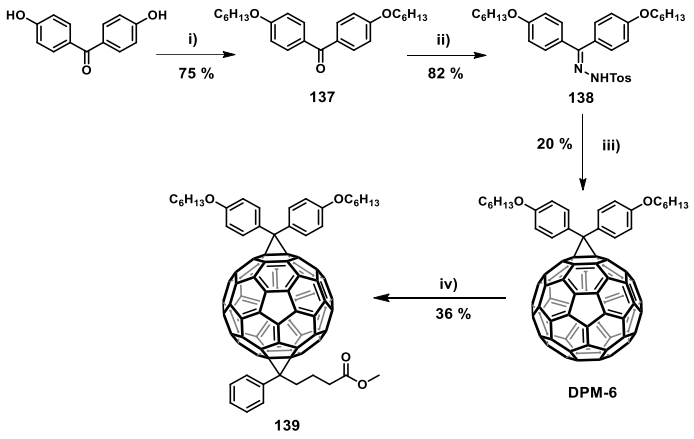

Scheme 25. *Reagent and conditions*: **i**) $C_6H_{13}Br$, K_2CO_3, DMF, 65 ºC; **ii**) NH_2NHTos, PTSA, toluene, 111 ºC; **iii**) C_{60}, MeONa, pyridine, *o*-DCB, 180 ºC; **iv**) **123**, DPM-6, MeONa, pyridine, *o*-DCB, 180 ºC

Structural characterization of the final C_{60}-bisaduct **139** and the corresponding intermediates was accomplished using standard spectroscopic techniques. Due to the number of possible site- and regio-isomers, broad signals were observed in the ^{1}H NMR spectrum (figure 105) corresponding to the moieties of DPM-6 and $PC_{61}BM$. In addition, HRMS [MALDI-TOF] confirmed the presence of the target bisadduct with a molecular peak at 1276.3539 m/z (1276.3547 m/z).

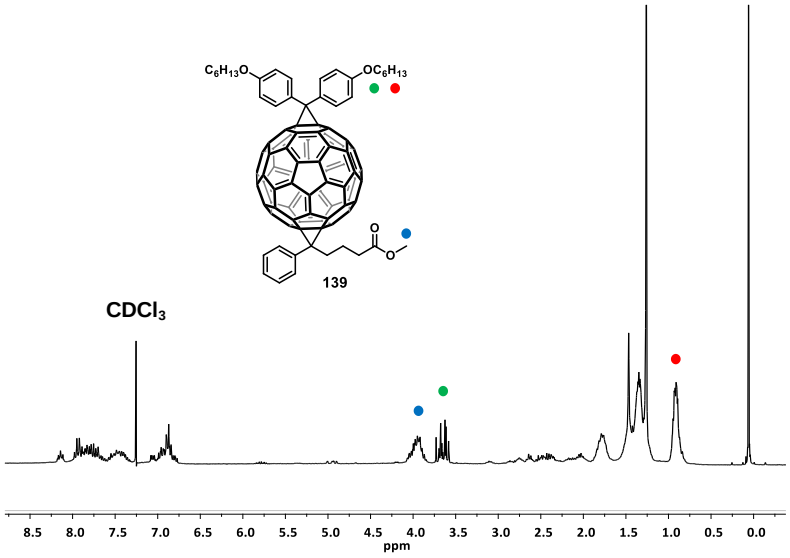

Figure 105. ^{1}H NMR spectrum (400 MHz, $CDCl_3$, 298 K) of bisadduct **139**.

With the aim of knowing the optical characteristics and the HOMO energy level, cyclic voltammetry and absorption experiments were carried out for the bisadduct **139**, as it is illustrated in figure 106.

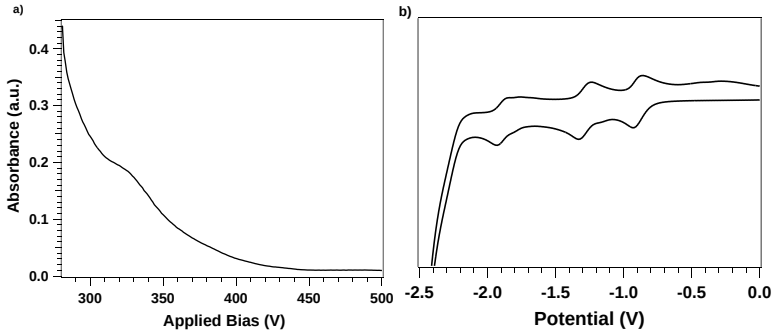

Figure 106. Absorption spectrum and cyclic voltammogram of bisadduct **139**.

The cyclic voltammetry measurements were conducted in 0.1 M solution of $(n\text{-Bu})_4NPF_6$ ($TBAPF_6$) in *o*-DCB/Acetonitrile (4:1) using glassy carbon as working electrode, Ag/Ag^+ as reference electrode and platinum as counter electrode with Fc/Fc^+ as internal standard. According to the voltammogram, it can be observed, three reversible reduction waves in the cathodic region at -0.89 V, -1.28 V and -1.90 V. The value of the first reduction potential is energetically lower than that for C_{60} (-0.73 V) and DPM-6 (-0.81 V). Therefore, the estimated energy of the LUMO of the bisadduct is higher than those obtained for C_{60} and DPM-6.

•• Devices fabrication and characterization

Chapter 2. Electron-transporting materials for perovskite solar cells

3. DEVICES FABRICATION AND CHARACTERIZATION

3.1. Device performance employing ThCBM derivatives as ETMs

To further improve the PV device performance, a wide variety of C_{60}- derivatives have been explored and particularly, many modifications of $PC_{61}BM$ skeleton have been successfully employed. Recently, 2-ThienylC_{61}-butyric acid methyl ester (ThCBM) and its derivatives have been reported to exhibit a device performance close to $PC_{61}BM$ with bulk-heterojunction polymer solar cells.[244] To extend the PV application of these easily made and high performance C_{60}-based acceptors, two $PC_{61}BM$ analogues were synthesized, **135** (ThCBM) and **136**, ThCBM endowed with an hexyl chain (figure 107). The incorporation of the thiophene ring in the $PC_{61}BM$-like structure could lead to some interactions with the perovskite active layer in PSCs, thus improving the device performance.

Figure 107 illustrates the C_{60}-based derivatives studied as ETMs in inverted PSCs. The devices were based on $MAPbI_2$ perovskite and presented the following structure: ITO/PEDOT:PSS/ perovskite/ETM/Al.

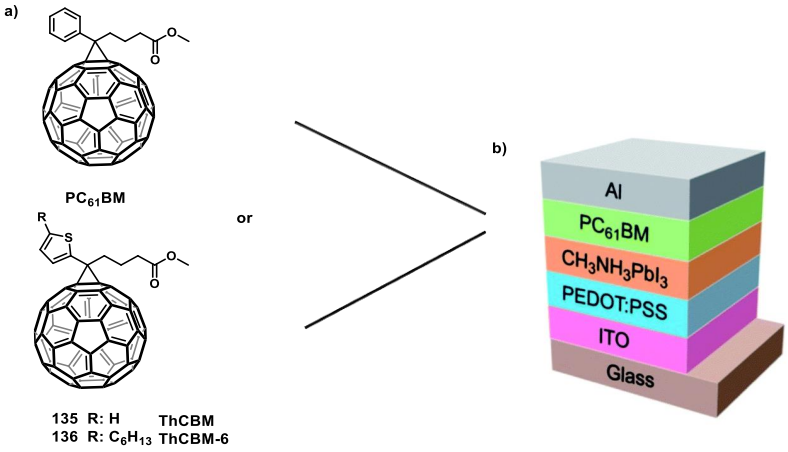

Figure 107. Structure of the C_{60}-derivatives ($PC_{61}BM$ and ThCBM) employed as ETMs (left) and schematic structure of the device (right).

Devices were prepared on cleaned ITO substrates by spin coating a thin layer of PEDOT:PSS from the commercial aqueous dispersion (1200 r.p.m. for 30 s which resulted in a thickness of 70 nm). On top of this layer, a thin film of polyTPD was deposited from a chlorobenzene solution (10 mg/mL). Then the

substrates were transferred to an inert glovebox. The perovskite layer was deposited by two different methods, evaporation and solution process. The C_{60}-based layer was deposited from a chlorobenzene solution (10 mg/mL) in ambient conditions. The device was completed by the thermal evaporation of the top metal electrode with a thickness of 100 nm.

The preliminary results including the performance parameters of the different devices (V_{oc}, J_{sc}, FF and PCE) are listed in table 29.

Table 29. Performance parameters of the devices employing C_{60}-derivatives as ETMs.

ETM	J_{sc} (mA·cm^{-2})	V_{oc} (V)	FF (%)	PCE (%)
135[a]	15.63	1.05	68.1	11.7
136[a]	14.94	1.04	66.2	10.3
$PC_{61}BM$[a]	16.35	1.05	73.9	12.7
135[b]	14.01	0.87	66.3	9.4
$PC_{61}BM$[b]	13.33	0.88	69.8	9.9

Deposition of the perovskite [a] by evaporation [b] from solution.

The results clearly confirm that the evaporation method led to higher performances in all cases. In the devices deposited by evaporation, the V_{oc} is similar in all cases. In contrast, the lowest value obtained for J_{sc} in the case of **136** is due to a less favorable morphology owing to the long alkyl chains. In this context, the PCE values are lower in both cases in comparison to the $PC_{61}BM$. Therefore, improvements in the devices and optimization of the conditions are still necessary.

Moreover, figure 108 illustrates the IPCE (incident photon-to-current efficiency) and J-V curves of the devices, in which the perovskite was deposited by evaporation.

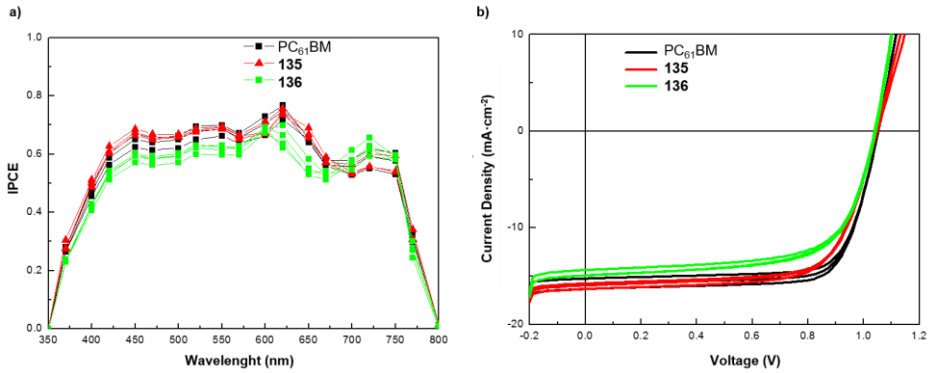

Figure 108. a) Stabilized IPCE at maximum power point; **b**) J-V curve of each ETM. $PC_{61}BM$ was used as reference (left).

The IPCE curve (figure 108a) represents a measure of how efficiently the device converts the incident light into electrical energy, in this case at 350-800 nm wavelength range. It can be observed that this value is about 70 % from 450 nm to 650 nm, comparable to the reference ($PC_{61}BM$). On the other hand, the prelimilary J-V curves (figure 108b) show similar behavior between the derivative **135** (ThCBM) and $PC_{61}BM$.

3.2. Device fabrication and performance employing bisadduct 139 as ETMs

Bisadduct **139** which combines the characteristic moieties of the well-known $PC_{61}BM$ and DPM-6 (figure 109), was tested as electron transporting layer in inverted PSCs. For comparison purposes, $PC_{61}BM$ and DPM-6 were also used under the same conditions. This study was carried out in collaboration with Prof. Henk Bolink's group (ICMol, Valencia, Spain).

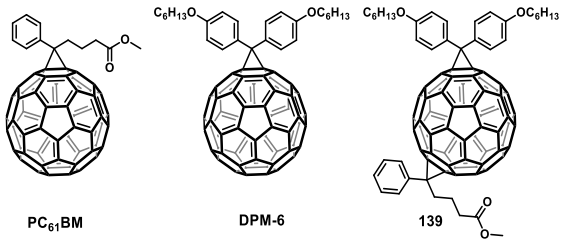

Figure 109. Structure of the C_{60}-derivatives employed as ETMs in PSCs.

Bisadduct **139** was incorporated as the ETM in inverted PSCs employing the standard $MAPbI_2$ perovskite (PbI_2/MAI ratio 5.5). The device presented this structure: ITO/PEDOT (80 nm)/polyTPD (20 nm)/perovskite (260 nm)/ETM (20

nm)/Au. By now, only preliminary results of the performance parameters are available. The performance parameters of the C_{60}-derivative **139** are listed in table 30, together with the values for $PC_{61}BM$ and DPM-6.

Table 30. Performance parameters of the devices employing C_{60}-derivatives as ETMs.

ETM	V_{oc} (V)	J_{sc} (mA·cm^{-2})	FF (%)	PCE (%)
139	1.09	17.0	16.4	4.2
$PC_{61}BM$	1.09	18.5	61.6	11.5
DPM-6	1.09	16.9	54.1	9.8

The performance parameters such as V_{oc} and J_{sc} for bisadduct **139** are comparable to those for the references, $PC_{61}BM$ and DPM-6. However, the FF is notably lower. A possible explanation for that is the inhomogeneous layer that bisadduct could form not only for its asymmetry but also to the different possible isomers. This is reflected in the low PCEs of the devices. In addition, the preliminary results presented J-V curves most lead to an S-shape which indicates some extraction barrier, probably due to a too high LUMO of the bisadduct **139** in comparison to $PC_{61}BM$ or DPM-6 (≈ -4.2 eV). These results are still under study.

• • Experimental procedure

Chapter 2. Electron-transporting materials
for perovskite solar cells

4. EXPERIMENTAL PROCEDURE

4-[(Carboxymethyl)amino]benzoic acid[235] (120)

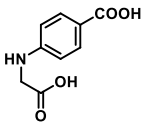

This compound was synthesized according to a previously reported procedure and showed identical spectroscopic properties to those reported therein. ^{1}H NMR (400 MHz, DMSO-d_6, 298K) δ: 7.67 (d, *J* = 8.7 Hz, 2H), 6.66 (s, 1H), 6.57 (d, *J* = 8.7 Hz, 2H), 3.87 (s, 2H); ^{13}C NMR (100 MHz, DMSO-d_6, 298K) δ: 172.1, 167.5, 152.1, 131.0, 117.6, 111.2, 44.1.

3,4-Bis(bromomethyl)benzoic acid[236] (121)

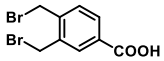

This compound was synthesized according to a previously reported procedure and showed identical spectroscopic properties to those reported therein. ^{1}H NMR (400 MHz, $CDCl_3$, 298 K) δ: 13.08 (s, 1H), 8.10 (d, *J* = 2 Hz, 1H), 8.02 (dd, *J* = 8 Hz, *J* = 2 Hz, 1H), 7.47 (d, *J* = 8 Hz, 1H), 4.67 (s, 2H), 4.66 (s, 2H).

Methyl 5-oxo-5-phenylpentanoate[211] (122)

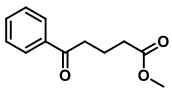

This compound was synthesized according to a previously reported procedure and showed identical spectroscopic properties to those reported therein. ^{1}H NMR (400 MHz, $CDCl_3$, 298 K) δ: 7.88 (d, *J* = 7.1 Hz, 2H,), 7.52-7.35 (m, 3H), 3.61 (s, 3H), 2.98 (t, *J* = 7.2 Hz, 2H,), 2.38 (t, *J* = 7.2 Hz, 2H,), 2.25-2.00 (m, *J* = 7.3, 2H); ^{13}C NMR (100 MHz, $CDCl_3$, 298 K) δ: 200.0, 174.1, 137.2, 133.5, 129.0, 128.4, 52.0, 37.8, 33.5, 19.7.

Methyl (*E*)-5-phenyl-5-(2-tosylhydrazone)pentanoate[211] (123)

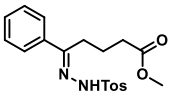

This compound was synthesized according to a previously reported procedure and showed identical spectroscopic properties to those reported therein. ^{1}H NMR (400 MHz, $CDCl_3$, 298 K) δ: 9.30 (s, 1H), 7.93 (d, *J* = 8.5 Hz, 2H), 7.66-7.65 (m, 2H), 7.34-7.32 (m, 3H), 7.28 (d, *J* = 8.5 Hz, 2H), 3.79 (s, 3H), 2.64-2.62 (m, 2H) 2.40 (s, 3H), 2.33-2.30 (m, 2H), 1.69-1.66 (m, 2H). ^{13}C NMR (100 MHz, $CDC1_3$, 298 K) δ: 174.5, 153.9, 143.6, 136.0, 135.8, 129.5, 129.4, 128.3, 127.7, 126.1, 52.0, 32.0, 25.7, 21.4, 20.8.

1'1'-Diethoxycarbonyl-1,2-methano[60]fullerene [246] (124)

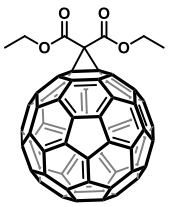

This compound was synthesized according to a previously reported procedure and showed identical spectroscopic properties to those reported therein. ^{1}H NMR (400 MHz, $CDCl_3$, 298 K) δ: 4.57 (m, 4H), 1.49 (t, *J* = 7.13 Hz, 6H); ^{13}C NMR (100 MHz, $CDC1_3$, 298 K) δ: 163.6, 145.4, 145.3, 145.2, 144.9, 144.7, 144.7, 144.6, 143.9, 143.1, 143.0, 142.2, 142.9, 140.9, 139.0, 71.6, 63.4, 52.3, 14.2.

1'1-Dicarboxyl-1,2-methano[60]fullerene [247] (125)

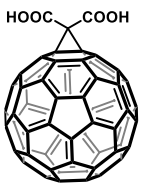

This compound was synthesized according to a previously reported procedure and showed identical spectroscopic properties to those reported therein. ^{13}C NMR (100 MHz, THF-d_8, 298 K) δ: 163.3, 147.0, 145.7, 145.4, 145.3, 144.9, 144.9, 144.6, 144.1, 143.2, 142.4, 142.2, 141.0, 139.4, 73.5; ESI-MS m/z calcd: 886.0; found: 886.1 $[M+H]^+$.

6'-Carboxyl-1,2,3,4-tetrahydronaphatleno-[2',3':1,2][60]fullerene[236, 237] (126)

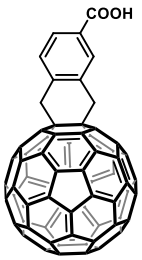

This compound was synthesized according to a previously reported procedure and showed identical spectroscopic properties to those reported therein. ^{1}H NMR (400 MHz, DMSO-d_6, 298 K) δ: 13.1 (s, 1H), 8.35 (d, *J* = 1.6 Hz, 1H), 8.14 (dd, *J* = 7.8 Hz, *J* = 1.6 Hz, 1H), 7.90 (d, *J* = 7.8 Hz, 1H), 5.06 (m, 2H), 4.66 (m, 2H); ESI-MS (m/z): calcd. for $C_{69}H_8O_2$: 868.1; found, 868.2.

246. C. Bingel, "Cyclopropanierung von fullerenen", *Chem. Ber.*, **1993**, *126*, 1957-1959.
247. I. Lamparth, A. Hirsch, "Water-soluble malonic acid derivatives of C_{60} with a defined three-dimensional structure", *J. Chem. Soc. Chem. Commun.*, **1994**, 1727-1728.

2'-(4-Carboxyphenyl)*N*-methylpyrrolidino[3,4:1,2][60]fullerene[237] (127)

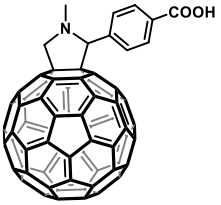

This compound was synthesized according to a previously reported procedure and showed identical spectroscopic properties to those reported therein. ^{1}H NMR (400 MHz, DMSO-d_6, 298 K) δ: 13.05 (s, 1H), 8.04 (d, *J* = 7.6 Hz, 2H), 7.94 (d, *J* = 7.8 Hz, 2H), 5.22 (s, 1H), 5.11 (d, *J* = 9.4, 1H), 4.35 (d, *J* = 9.4 Hz, 1H), 3.17 (s, 3H); ESI-MS (m/z) calcd. for $C_{70}H_{11}NO_2$: 897.1; found, 897.0.

***N*-(4-Carboxyphwnyl)pyrrolidino[3,4:1,2][60]fullerene (128)**

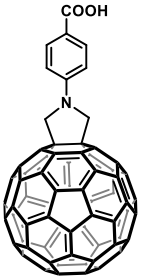

A mixture of compound **120** (33.7 mg, 0.17 mmol), C_{60} (100 mg, 0.14 mmol) and *p*-formaldehyde (4 mg, 0.13 mmol) were dissolved in chlorobenzene (20 mL) and the mixture was heated at 130 ºC for 6 hours. The reaction mixture was allowed to reach r. t. and the solvent was removed under vacuum. The crude product was purified by column chromatography (silica gel, 2:1 toluene/THF). The black solid obtained was further purified by repeated (3x) precipitation and centrifugation in methanol to yield the corresponding adducts as a black solid. ^{1}H NMR (400 MHz, DMSO-d_6, 298 K) δ: 12.54 (br, s, 1H), 8.01 (d, *J* = 7.8, 2H), 7.50 (d, *J* = 7.8, 2H), 5.40 (s, 4H).

1,2-Dicyano[60]fullerene[238] (129)

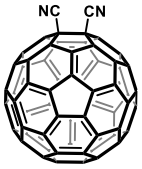

This compound was synthesized according to a previously reported procedure and showed identical spectroscopic properties to those reported therein. ^{13}C NMR (100 MHz, TCE-d_2, 298 K) δ: 147.7, 146.7, 146.4, 146.1, 145.4, 145.1, 144.2, 143.4, 143.1, 142.0, 141.6, 141.0, 140.6, 134.8, 116.7, 57.1; MALDI-TOF: calcd. for $C_{62}N_2$: 772.0; found 772.0.

2'-(4-Carboxyphenyl)-*N*-methyl pyrrolidino[3,4:1,2][60]fullerene (130)

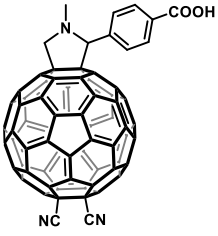

A mixture of 4-formylbenzoic acid (14.2 mg, 0.09 mmol), C_{60}-(CN_2) (80 mg, 0.10 mmol) and sarcosine (41.4 mg, 0.47 mmol) were dissolved in chlorobenzene (20 mL) and the mixture was refluxed for 20 hours. The reaction mixture was allowed to reach r. t. and the solvent was removed under vacuum. The crude was purified by flash column

chromatography on SiO_2, using CS_2/toluene and then 2:1 toluene/THF. The black solid obtained was further purified by repeated (3x) precipitation and centrifugation in methanol to yield the corresponding hybrids as black solid.^{1}H NMR (400 MHz, DMSO-d_6, 298 K) δ: 13.05 (s, 1H), 8.25-7.59 (m, 4H), 5.02-4.56 (m, 3H), 2.90-2.60 (m, 3H); ESI-MS m/z calcd: 950.1, found: 950.1 $[M+H]^+$.

PhenylC_{61}-butyric acid methyl ester, $PC_{61}BM$

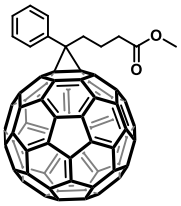

This compound was synthesized according to reported procedures[211] and showed identical spectroscopic properties to those reported therein. ^{1}H NMR (400 MHz, CS_2, 298 K) δ: 7.87 (d, *J* = 7.5 Hz, 2H), 7.50 (m, 2H), 7.37 (m, 1H), 3.50 (s, 3H), 2.01 (m, 2H), 1.58 (m, 2H), 1.37 (m, 2H).

$PC_{61}BM$-127 bisadduct[237] (131)

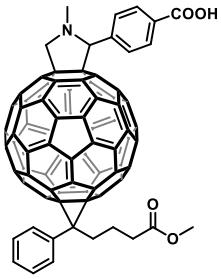

This compound was synthesized according to a previously reported procedure and showed identical spectroscopic properties to those reported therein. ^{1}H NMR (400 MHz, $CDCl_3$, 298 K): 10.15 (s, 1H), 8.30 (d, *J* = 8.2 Hz, 2H), 8.20-7.90 (m, 2H), 8.03 (d, *J* = 8.4 Hz, 2H), 7.90-7.30 (m, 3H), 7.00 (s, 2H), 6.58 (s, 1H), 3.78-3.56 (m, 3H), 2.86-2.72 (m, 3H), 2.61-2.37 (m, 2H), 1.90-1.86 (m, 4H); ESI-MS (m/z) calcd. for $C_{82}H_{25}NO_4$, 1087.2; found, 1082.2.

5-Oxo-5-(thien-2-yl)pentanoic acid[244] (132a)

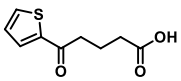

This compound was synthesized according to a previously reported procedure and showed identical spectroscopic properties to those reported therein. ^{1}H NMR (400 MHz, $CDCl_3$, 298 K) δ: 7.71 (dd, *J* = 0.9 Hz, *J* = 0.9 Hz, 1H), 7.64 (dd, *J* = 0.9 Hz, *J* = 0.9 Hz, 1H), 7.14 (dd, *J* = 3.9 Hz, *J* = 3.9 Hz, 1H), 3.02 (t, *J* = 7.2 Hz, 2H), 2.51 (t, *J* = 7.2 Hz, 2H), 2.04-2.14 (m, 2H); MALDI-TOF calcd. for $C_9H_{10}O_3S$ $[M^+]$ 198.24; found 198.24.

5-(5'-Hexylthien-2-yl)-5-oxopentanoic acid[244] (132b)

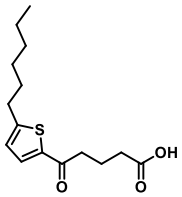

This compound was synthesized according to a previously reported procedure and showed identical spectroscopic properties to those reported therein. ^{1}H NMR (400 MHz, $CDCl_3$, 298 K) δ: 7.56 (d, *J* = 3.9 Hz, 1H), 6.79 (d, *J* = 3.9 Hz, 1H), 3.01 (t, *J* = 7.5 Hz, 2H), 2.77 (t, *J* = 7.2 Hz, 2H), 2.50 (t, *J* = 7.5 Hz, 2H), 2.06-2.08 (m, 2H), 1.30-1.38 (m, 8H), 0.87-0.92 (m, 3H); MALDI-TOF calcd. for $C_{15}H_{22}O_3S$ [M^+] 282.40; found 282.40.

Methyl 5-oxo-5-(thien-2-yl)pentanoate[244] (133a)

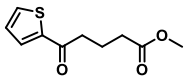

This compound was synthesized according to a previously reported procedure and showed identical spectroscopic properties to those reported therein. ^{1}H NMR (400 MHz, $CDCl_3$, 298 K) δ: 7.71 (dd, *J* = 0.9 Hz, *J* = 0.9 Hz, 1H), 7.64 (dd, *J* = 0.9 Hz, *J* = 0.9 Hz, 1H), 7.14 (dd, *J* = 3.9 Hz, *J* = 3.9 Hz, 1H), 3.69 (s, 3H), 2.99 (t, *J* = 7.2 Hz, 2H), 2.45 (t, *J* = 7.2 Hz, 2H), 2.13-2.03 (m, 2H); MALDI-TOF calcd. for $C_{10}H_{12}O_3S$ [M^+] 212.26; found 212.26.

Methyl 5-(5'-hexylthien-2-yl)-5-oxopentanoate[244] (133b)

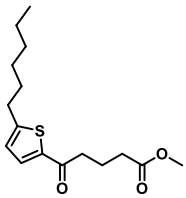

This compound was synthesized according to a previously reported procedure and showed identical spectroscopic properties to those reported therein. ^{1}H NMR (400 MHz, $CDCl_3$, 298 K) δ: 7.56 (d, *J* = 3.9 Hz, 1H), 6.79 (d, *J* = 3.9 Hz, 1H), 3.69 (s, 3H), 2.98 (t, *J* = 7.5 Hz, 2H), 2.71 (t, *J* = 7.2 Hz, 2H), 2.50 (t, *J* = 7.5 Hz, 2H), 2.07-2.05 (m, 2H), 1.39-1.31 (m, 8H), 0.92-0.87 (m, 3H); MALDI-TOF calcd. for $C_{16}H_{24}O_3S$ [M^+] 296.43; found 296.43.

***N*-Tosylhydrazone of 3-(methoxycarbonyl)propyl-2-thienylketone[244] (134a)**

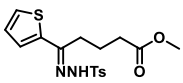

This compound was synthesized according to a previously reported procedure and showed identical spectroscopic properties to those reported therein. ^{1}H NMR (400 MHz, $CDCl_3$, 298 K) δ: 8.98 (s, 1H), 7.91, (d, *J* = 8.4 Hz, 2H), 7.30 (d, *J* = 1.2 Hz, 1H), 7.29 (d, *J* = 8.4 Hz, 2H), 7.18 (dd, *J* = 1.2 Hz, *J* = 1.2 Hz, 1H), 6.97 (dd, *J* = 3.9 Hz, *J* = 3.6 Hz, 1H), 3.80 (s, 3H), 2.61 (t, *J* = 7.8 Hz, 2H), 2.40 (s, 3H), 2.31 (t,

J = 6.0 Hz, 2H), 1.68-1.78 (m, 2H); MALDI-TOF calcd. for $C_{17}H_{20}N_2O_4S_2$ [M^+] 380.48; found 380.48.

_N_-Tosylhydrazone of 3-(methoxycarbonyl)propyl-2-(5-hexyl)thienyl ketone[244] (134b)

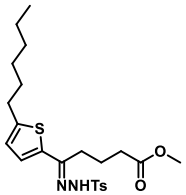

This compound was synthesized according to a previously reported procedure and showed identical spectroscopic properties to those reported therein. ^{1}H NMR (400 MHz, $CDCl_3$, 298 K) δ: 8.82 (s, 1H), 7.91 (d, *J* = 8.4 Hz, 2H), 7.29 (d, *J* = 8.4 Hz, 2H), 6.99 (d, *J* = 3.6 Hz, 1H), 6.63 (d, *J* = 3.6 Hz, 1H), 3.78 (s, 3H), 2.75 (t, *J* = 7.5 Hz, 2H), 2.56 (t, *J* = 7.5 Hz, 2H), 2.40 (s, 3H), 2.30 (t, *J* = 6.0 Hz, 2H), 1.63-1.74 (m, 2H), 1.31-1.39 (m, 8H), 0.87-0.92 (m, 3H); MALDI-TOF calcd. for $C_{23}H_{32}N_2O_4S_2$ [M^+] 464.6; found 464.6.

2-ThienylC_{61}-butyric acid methyl ester (ThCBM)[244] (135)

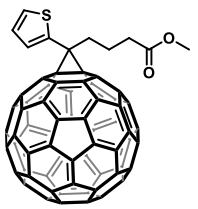

This compound was synthesized according to a previously reported procedure and showed identical spectroscopic properties to those reported therein. ^{1}H NMR (400 MHz, $CDCl_3$, 298 K) δ: 7.50-7.47 (m, 2H), 7.15-7.13 (m, 1H), 3.69 (s, 3H), 2.96 (t, *J* = 4.8 Hz, 2H), 2.58 (t, *J* = 7.2 Hz, 2H), 2.26-2.22 (m, 2H); ^{13}C NMR (100 MHz, $CDCl_3$, 298 K) δ: 173.5, 148.3, 147.5, 145.7, 145.3, 145.2, 145.5, 145.2, 145.1, 144.8, 144.7, 144.7, 144.6, 144.5, 144.2, 143.8, 143.8, 143.1, 143.1, 143.0, 143.0, 142.2, 142.2, 142.1, 141.0, 140.8, 139.5, 138.2, 132.0, 126.2, 79.9, 51.7, 45.8, 34.0, 33.7, 22.5; MALDI-TOF calcd. for $C_{70}H_{12}O_2S$ [M^+] 916.1; found 916.0.

5'-Hexyl-2-thienylC_{61}-butyric acid methyl ester (ThPCBM-6)[244] (136)

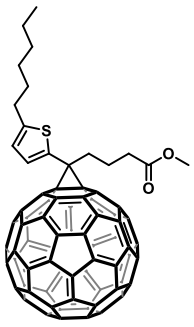

This compound was synthesized according to a previously reported procedure and showed identical spectroscopic properties to those reported therein. ^{1}H NMR (400 MHz, $CDCl_3$, 298 K) δ: 7.26 (d, *J* = 4.5 Hz, 1H), 6.76 (d, *J* = 4.5 Hz, 1H), 3.69 (s, 3H), 2.95-2.87 (m, 4H), 2.58 (t, *J* = 7.2 Hz, 2H), 2.29-2.21 (m, 2H), 1.79-1.72 (m, 2H), 1.43-1.35 (m, 6H), 0.92-0.87 (m, 3H); ^{13}C NMR (100 MHz, $CDCl_3$, 298 K) δ: 173.5, 148.5, 147.7, 147.0, 145.8, 145.2, 145.2, 145.1, 144.8, 144.7, 144.6, 144.6, 144.5, 144.1, 143.8, 143.8, 143.1, 143.1,

143.0, 142.9, 142.9, 142.3, 142.2, 142.1, 140.9, 140.7, 138.3, 138.1, 136.0, 131.8, 122.8, 80.1, 51.7, 46.2, 33.8, 33.7, 31.5, 31.4, 30.4, 28.9, 22.6, 22.5, 14.1.

4,4'-Bis(hexyloxy)benzophenone[231] (137)

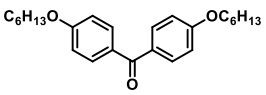

This compound was synthesized according to a previously reported procedure and showed identical spectroscopic properties to those reported therein. ^{1}H NMR (400 MHz, $CDCl_3$, 298 K) δ: 7.78 (d, *J* = 8.4 Hz, 4H), 6.96 (t, *J* = 8.4 Hz, 4H), 4.04 (t, *J* = 6.5 Hz, 4H), 1.82 (m, 4H), 1.51 (m, 4H), 1.36 (m, 8H), 0.92 (t, *J* = 6.9 Hz, 6H); ^{13}C NMR (100 MHz, $CDCl_3$, 298 K) δ: 162.5, 132.2, 130.6, 113.9, 68.3, 31.6, 29.1, 25.7, 22.6, 14.0.

***N*-Tosylhydrazone of 4,4'-dihexyloxybenzophenone[231] (138)**

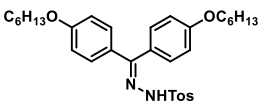

This compound was synthesized according to a previously reported procedure and showed identical spectroscopic properties to those reported therein. ^{1}H NMR (400 MHz, $CDCl_3$, 298 K) δ: 7.85 (d, *J* = 8.3 Hz, 2H), 7.78 (d, *J* = 8.8 Hz, 2H), 7.37 (d, *J* = 8.8 Hz, 2H), 7.32 (d, *J* = 8.3 Hz, 2H), 6.95 (d, *J* = 8.8 Hz, 4H), 6.79 (d, *J* = 8.8 Hz, 2H), 3.99 (dt, 4H), 1.87 (m, 4H), 1.49 (m, 4H), 1.36 (m, 8H), 0.92 (t, *J* = 6.8 Hz, 6H). ^{13}C NMR (100 MHz, $CDCl_3$, 298 K) δ: 194.5, 162.5, 154.6, 143.9, 135.7, 132.2, 129.9, 129.6, 129.3, 127.9, 115.5, 114.1, 113.9, 68.3, 31.6, 29.2, 25.7, 25.7, 22.6, 22.6, 21.6, 14.0.

1',1'-Bis(4-hexyloxyphenyl)-1,2-methano[60]fullerene,[231] DPM-6

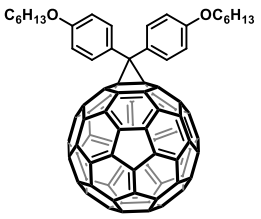

This compound was synthesized according to a previously reported procedure and showed identical spectroscopic properties to those reported therein. ^{1}H NMR (400 MHz, $CDCl_3$, 298 K) δ: 7.98 (d, *J* = 8.8 Hz, 4H), 6.99 (d, *J* = 8.8 Hz, 4H), 3.99 (t, *J* = 6.4 Hz, 4H), 1.80 (m, 4H), 1.48 (m, 4H), 1.36 (m, 8H), 0.92 (t, *J* = 6.8 Hz, 6H). ^{13}C NMR (100 MHz, $CDCl_3$, 298 K) δ: 159.1, 149.0, 145.8, 145.6, 145.5, 145.1, 144.6, 144.6, 144.2, 143.3, 142.7, 142.5, 141.2, 138.6, 132.2, 131.7, 115.0, 68.5, 57.8, 32.0, 29.7, 26.2, 23.0, 14.4; MALDI-TOF calcd. for $C_{85}H_{34}O_2$ [M^-], 1086.26; found 1086.20.

DPM-6-$PC_{61}BM$-bisadduct (139)

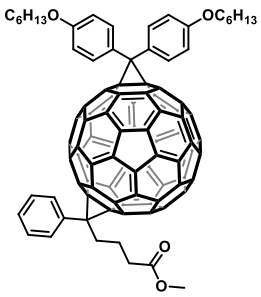

Compound **47** (67.39 mg, 0.23 mmol) was dissolved in 8 ml of pyridine under nitrogen atmosphere. sodium methoxide (7.28 mg, 0.13 mmol) was added into solution stepwise. After, 15 minutes, a sonicated solution of **DPM-6** (500 mg, 0.46 mmol) in 73 ml of *o*-DCB, was added stepwise. The reaction mixture was heated at reflux temperature for 16 h. The mixture was cooled to r.t. and washed and the solvent was removed under reduced pressure. The crude product was purified by column choromatography (silica gel, CS_2) and washed with methanol to afford the bisadduct **139** (234.85, 0.18 mmol) as a brown solid. ^{1}H NMR (400 MHz, $CDCl_3$, 298 K) δ: 8.27-7.30 (m, 13H), 4.21-3.80 (m, 4H), 3.74-3.46 (m, 5H), 1.79-1.76 (m, 6H), 1.47-1.34 (m, 14H), 0.94-0.89 (m, 6H); HRMS [MALDI-TOF] calcd. for $C_{97}H_{48}O_4$ [M^-], 1276.3547; found 1276.3539.

•• Conclusions

Chapter 2. Electron-transporting materials for perovskite solar cells

5. CONCLUSIONS

To further improve the PV device performance, a wide variety of C_{60}-derivatives has been reported in the literature as promising ETMs for PSCs. The design of differently functionalized fullerenes plays an important role in the overall solar cell performance. The collection of fullerene derivatives presented in this thesis, with different chemical functionalization and LUMO energy levels has permitted a deep study in different PSCs architectures.

On one hand, the appropriate functionalization of monoadducts and bisadducts of fullerene with a benzoic acid as anchoring group was presented highlighting their organization in SAMs. Particularly, the incorporation of three different [60]fullerene derivatives, two monoadducts and one bisadduct, as electron-selective contact interface SAMs in PSCs, which induced, in all the cases, an important reduction of the J-V curve hysteresis. It has been possible to determine that the hysteresis reduction was due to the decrease of the capacitive hysteresis. In addition, it was demonstrated that the inclusion of cyanide groups in the molecular structure enhances the direct coupling with the perovskite layer, thus improving the solar cell parameters, such as the photocurrent, compared to the reference device with no SAM. Therefore, it was confirmed that the design of new fullerene derivatives plays a very important role in the overall solar cell performance. Furthermore, with the results, it could be explained the origin of the hysteresis reduction when a fullerene derivative SAM is employed and paves the way for a future enhancement of PSCs by means of a tailored design of the fullerene molecules that could act as ETMs by themselves, without further need of a TiO_2 compact layer.

Taking into account that thiophene is an aromatic ring characterized by easy modification and the possible interaction between the sulfur atom of the ring and the positive charge of the metal from the perovskite, $PC_{61}BM$-analogues were presented. Easy to prepare 2-thienylC_{61}-butyric acid methyl ester (ThCBM) and with a hexyl chain were explored in inverted $MAPbI_3$-based solar cells. The results are very promising and comparable to the reference $PC_{61}BM$, although they are not still optimized. On the other hand, it was presented the synthesis and characterization of a C_{60}-bisadduct, which combines the moieties from the well-known $PC_{61}BM$ and DPM-6. Although the results of its employment as the ETM in inverted $MAPbI_3$-based PSCs are still preliminary, the optimization of the conditions could lead to interesting results.

REFERENCES

1. *http://www.iea.org*.
2. N. Armaroli, V. Balzani, "The future of energy supply: Challenges and opportunities", *Angew. Chem. Int. Ed.*, **2007**, *46*, 52-66.
3. *http://www.ren21.net/*.
4. E. Espíldora, J. L. Delgado, N. Martín, "Donor-acceptor hybrids for organic electronics", *Isr. J. Chem.*, **2014**, *54*, 429-439.
5. J. L. Delgado, P. A. Bouit, S. Filippone, M. A. Herranz, N. Martin, "Organic photovoltaics: A chemical approach", *Chem. Commun.*, **2010**, *46*, 4853-4865.
6. R. F. Service, "Is it time to shoot for the sun?", *Science*, **2005**, *309*, 548-551.
7. *www.desertec.org*.
8. *http://www.meteonorm.com*.
9. D. M. Chapin, C. S. Fuller, G. L. Pearson, "A new silicon p-n junction photocell for converting solar radiation into electrical power", *J. Appl. Physics.*, **1954**, *25*, 676-677.
10. M. A. Green, K. Emery, Y. Hishikawa, W. Warta, E. D. Dunlop, D. H. Levi, A. W. Y. Ho-Baillie, "Solar cell efficiency tables (version 49)", *Prog. Photovolt.: Res. Appl.*, **2017**, *25*, 3-13.
11. J. Ahmad, K. Bazaka, L. J. Anderson, R. D. White, M. V. Jacob, "Materials and methods for encapsulation of OPV: A review", *Renew. Sustainable Energy Rev.*, **2013**, *27*, 104-117.
12. *https://www.solaronix.com; http://www.dyesol.com*.
13. *www.heliatek.com*.
14. N. Martín, "Carbon nanoforms for photovoltaics: Myth or reality?", *Adv. Energy Mater.*, **2016**, 1601102-1601110.
15. K. A. Mazzio, C. K. Luscombe, "The future of organic photovoltaics", *Chem. Soc. Rev.*, **2015**, *44*, 78-90.
16. C. W. Tang, "Two-layer organic photovoltaic cell", *Appl. Phys. Lett.*, **1986**, *48*, 183-185.
17. B. O'Regan, M. Graetzel, "A low-cost, high-efficiency solar cell based on dye-sensitized colloidal TiO_2 films", *Nature*, **1991**, *353*, 737-740.
18. A. Hagfeldt, G. Boschloo, L. Sun, L. Kloo, H. Pettersson, "Dye-sensitized solar cells", *Chem. Rev.*, **2010**, *110*, 6595-6663.
19. J. Jean, P. R. Brown, R. L. Jaffe, T. Buonassisi, V. Bulovic, "Pathways for solar photovoltaics", *Energy Environ. Sci.*, **2015**, *8*, 1200-1219.
20. M. Graetzel, "Dye-sensitized solar cells", *J. Photochem. Photobiol. C: Photochem. Rev.*, **2003**, *4*, 145-153.
21. S. Mathew, A. Yella, P. Gao, R. Humphry-Baker, B. F. E. Curchod, N. Ashari-Astani, I. Tavernelli, U. Rothlisberger, M. K. Nazeeruddin, M. Graetzel, "Dye-sensitized solar cells with 13 % efficiency achieved

through the molecular engineering of porphyrin sensitizers", *Nat. Chem.*, **2014**, *6*, 242-247.
22. Z. Yu, N. Vlachopoulos, M. Gorlov, L. Kloo, "Liquid electrolytes for dye-sensitized solar cells", *Dalton Trans.*, **2011**, *40*, 10289-10303.
23. U. Bach, D. Lupo, P. Comte, J. E. Moser, F. Weissortel, J. Salbeck, H. Spreitzer, M. Graetzel, "Solid-state dye-sensitized mesoporous TiO_2 solar cells with high photon-to-electron conversion efficiencies", *Nature*, **1998**, *395*, 583-585.
24. Y. Z. D. Deng, J. Zhang, Z. Wang, L. Zhu, J. Fang, B. Xia, Z. Wang, K. Lu, W. Ma, Z. Wei, "Fluorination-enabled optimal morphology leads to over 11 % efficiency for inverted small-molecule organic solar cells", *Nat. Comm.*, **2016**, *7*, 13740-13749.
25. M. M. Lee, J. Teuscher, T. Miyasaka, T. N. Murakami, H. J. Snaith, "Efficient hybrid solar cells based on meso-superstructured organometal halide perovskites", *Science*, **2012**, *338*, 643-647.
26. *N.R.E.L. (National Renewable Energy Laboratory)*, **2016**; *http://www.nrel.gov.*
27. A. Polman, M. Knight, E. C. Garnett, B. Ehrler, W. C. Sinke, "Photovoltaic materials: Present efficiencies and future challenges", *Science*, **2016**, *352*, 307-317.
28. S. Ameen, M. A. Rub, S. A. Kosa, K. A. Alamry, M. S. Akhtar, H. S. Shin, H. K. Seo, A. M. Asiri, M. K. Nazeeruddin, "Perovskite solar cells: Influence of hole transporting materials on power conversion efficiency", *ChemSusChem*, **2016**, *9*, 10-27.
29. M. A. Green, A. Ho-Baillie, H. J. Snaith, "The emergence of perovskite solar cells", *Nat. Photonics*, **2014**, *8*, 506-514.
30. L. J. Schmidt, "Tracking down the truth of Perovski", *38th Rochester Mineralogical Symp. Program Notes* **2011**, 31-32.
31. D. B. Mitzi, "Organic-inorganic perovskites containing trivalent metal halide layers: The templating influence of the organic cation layer", *Inorg. Chem.*, **2000**, *39*, 6107-6113.
32. S. Kazim, M. K. Nazeeruddin, M. Graetzel, S. Ahmad, "Perovskite as light harvester: A game changer in photovoltaics", *Angew. Chem. Int. Ed.*, **2014**, *53*, 2812-2824.
33. C. C. Stoumpos, M. G. Kanatzidis, "The Renaissance of Halide Perovskites and Their Evolution as Emerging Semiconductors", *Acc. Chem. Res.*, **2015**, 48, 2791-2802.
34. J. H. Noh, S. H. Im, J. H. Heo, T. N. Mandal, S. I. Seok, "Chemical management for colorful, efficient, and stable inorganic–organic hybrid nanostructured solar cells", *Nano Lett.*, **2013**, *13*, 1764-1769.
35. G. E. Eperon, S. D. Stranks, C. Menelaou, M. B. Johnston, L. M. Herz, H. J. Snaith, "Formamidinium lead trihalide: A broadly tunable perovskite for

efficient planar heterojunction solar cells", *Energy Environ. Sci.*, **2014**, *7*, 982-988.
36. G. Xing, N. Mathews, S. Sun, S. S. Lim, Y. M. Lam, M. Graetzel, S. Mhaisalkar, T. C. Sum, "Long-range balanced electron- and hole-transport lengths in organic-inorganic $CH_3NH_3PbI_3$", *Science*, **2013**, *342*, 344-347.
37. S. D. Stranks, G. E. Eperon, G. Grancini, C. Menelaou, M. J. P. Alcocer, T. Leijtens, L. M. Herz, A. Petrozza, H. J. Snaith, "Electron-hole diffusion lengths exceeding 1 micrometer in an organometal trihalide perovskite absorber", *Science*, **2013**, *342*, 341-344.
38. A. Kojima, K. Teshima, Y. Shirai, T. Miyasaka, "Organometal halide perovskites as visible-light sensitizers for photovoltaic cells", *J. Am. Chem. Soc.*, **2009**, *131*, 6050-6051.
39. J. H. Im, C. R. Lee, J. W. Lee, S. W. Park, N. G. Park, "6.5 % efficient perovskite quantum-dot-sensitized solar cell", *Nanoscale*, **2011**, *3*, 4088-4093.
40. H. S. Kim, C. R. Lee, J. H. Im, K. B. Lee, T. Moehl, A. Marchioro, S. J. Moon, R. Humphry-Baker, J. H. Yum, J. E. Moser, M. Graetzel, N. G. Park, "Lead iodide perovskite sensitized all-solid-state submicron thin film mesoscopic solar cell with efficiency exceeding 9 %", *Sci. Rep.*, **2012**, *2*, 591.
41. J. Y. Jeng, K. C. Chen, T. Y. Chiang, P. Y. Lin, T. D. Tsai, Y. C. Chang, T. F. Guo, P. Chen, T. C. Wen, Y. J. Hsu, "Nickel oxide electrode interlayer in $CH_3NH_3PbI_3$ perovskite/PCBM planar-heterojunction hybrid solar cells", *Adv. Mater.*, **2014**, *26*, 4107-4113.
42. F. Zhang, X. Yang, H. Wang, M. Cheng, J. Zhao, L. Sun, "Structure engineering of hole-conductor free perovskite-based solar cells with low-temperature-processed commercial carbon paste as cathode", *ACS Appl. Mater. Interfaces*, **2014**, *6*, 16140-16146.
43. A. Yella, L. P. Heiniger, P. Gao, M. K. Nazeeruddin, M. Graetzel, "Nanocrystalline rutile electron extraction layer enables low-temperature solution processed perovskite photovoltaics with 13.7 % efficiency", *Nano Lett.*, **2014**, *14*, 2591-2596.
44. D. Y. Son, J. H. Im, H. S. Kim, N. G. Park, "11 % efficient perovskite solar cell based on ZnO nanorods: An effective charge collection system", *J. Phys. Chem. C*, **2014**, *118*, 16567-16573.
45. F. Hao, C. C. Stoumpos, R. P. H. Chang, M. G. Kanatzidis, "Anomalous band gap behavior in mixed sn and pb perovskites enables broadening of absorption spectrum in solar cells", *J. Am. Chem. Soc.*, **2014**, *136*, 8094-8099.
46. M. Liu, M. B. Johnston, H. J. Snaith, "Efficient planar heterojunction perovskite solar cells by vapour deposition", *Nature*, **2013**, *501*, 395-398.

47. N. J. Jeon, J. H. Noh, Y. C. Kim, W. S. Yang, S. Ryu, S. I. Seok, "Solvent engineering for high-performance inorganic–organic hybrid perovskite solar cells", *Nat. Mater.*, **2014**, *13*, 897-903.
48. T. Swetha, S. P. Singh, "Perovskite solar cells based on small molecule hole transporting materials", *J. Mater. Chem. A*, **2015**, *3*, 18329-18344.
49. T. Salim, S. Sun, Y. Abe, A. Krishna, A. C. Grimsdale, Y. M. Lam, "Perovskite-based solar cells: Impact of morphology and device architecture on device performance", *J. Mater. Chem. A*, **2015**, *3*, 8943-8969.
50. T. Liu, K. Chen, Q. Hu, R. Zhu, Q. Gong, "Inverted perovskite solar cells: Progresses and perspectives", *Adv. Energy Mater.*, **2016**, *6*, 1600457-1600474.
51. L. Meng, J. You, T. F. Guo, Y. Yang, "Recent advances in the inverted planar structure of perovskite solar cells", *Acc. Chem. Res.*, **2016**, *49*, 155-165.
52. A. Marchioro, J. Teuscher, D. Friedrich, M. Kunst, R. Van De Krol, T. Moehl, M. Graetzel, J. E. Moser, "Unravelling the mechanism of photoinduced charge transfer processes in lead iodide perovskite solar cells", *Nat. Photon*, **2014**, *8*, 250-255.
53. Z. Song, S. C. Watthage, A. B. Phillips, M. J. Heben, "Pathways toward high-performance perovskite solar cells: Review of recent advances in organo-metal halide perovskites for photovoltaic applications", *J. Photon. Energy.*, **2016**, *6*, 022001-022001.
54. W. Tress, N. Marinova, T. Moehl, S. M. Zakeeruddin, M. K. Nazeeruddin, M. Graetzel, "Understanding the rate-dependent J-V hysteresis, slow time component, and aging in $CH_3NH_3PbI_3$ perovskite solar cells: The role of a compensated electric field", *Energy Environ. Sci.*, **2015**, *8*, 995-1004.
55. E. L. Unger, E. T. Hoke, C. D. Bailie, W. H. Nguyen, A. R. Bowring, T. Heumuller, M. G. Christoforo, M. D. Mcgehee, "Hysteresis and transient behavior in current-voltage measurements of hybrid-perovskite absorber solar cells", *Energy Environ. Sci.*, **2014**, *7*, 3690-3698.
56. C. Eames, J. M. Frost, P. R. F. Barnes, B. C. O'Regan, A. Walsh, M. S. Islam, "Ionic transport in hybrid lead iodide perovskite solar cells", *Nat. Commun.*, **2015**, *6*, 7497-7505.
57. V. W. Bergmann, S. a. L. Weber, F. Javier Ramos, M. K. Nazeeruddin, M. Graetzel, D. Li, A. L. Domanski, I. Lieberwirth, S. Ahmad, R. Berger, "Real-space observation of unbalanced charge distribution inside a perovskite-sensitized solar cell", *Nat. Commun.*, **2014**, *5*, 5001-5010.
58. J. M. Frost, K. T. Butler, A. Walsh, "Molecular ferroelectric contributions to anomalous hysteresis in hybrid perovskite solar cells", *APL Mater.*, **2014**, *2*, 81506-81516.

59. T. Leijtens, G. E. Eperon, N. K. Noel, S. N. Habisreutinger, A. Petrozza, H. J. Snaith, "Stability of metal halide perovskite solar cells", *Adv. Energy Mater.*, **2015**, *5*, 1500963-1500986.
60. S. Van Reenen, M. Kemerink, H. J. Snaith, "Modeling anomalous hysteresis in perovskite solar cells", *J. Phys. Chem. Lett.*, **2015**, *6*, 3808-3814.
61. A. Mei, X. Li, L. Liu, Z. Ku, T. Liu, Y. Rong, M. Xu, M. Hu, J. Chen, Y. Yang, M. Graetzel, H. Han, "A hole-conductor–free, fully printable mesoscopic perovskite solar cell with high stability", *Science*, **2014**, *345*, 295-298.
62. S. D. Stranks, H. J. Snaith, "Metal-halide perovskites for photovoltaic and light-emitting devices", *Nat. Nanotechnol.*, **2015**, *10*, 391-402.
63. J. Gong, S. B. Darling, F. You, "Perovskite photovoltaics: Life-cycle assessment of energy and environmental impacts", *Energy Environ. Sci.*, **2015**, *8*, 1953-1968.
64. B. Hailegnaw, S. Kirmayer, E. Edri, G. Hodes, D. Cahen, "Rain on methylammonium lead iodide based perovskites: Possible environmental effects of perovskite solar cells", *J. Phys. Chem. Lett.*, **2015**, *6*, 1543-1547.
65. J. W. Lee, D. J. Seol, A. N. Cho, N. G. Park, "High-efficiency perovskite solar cells based on the black polymorph of $HC(NH_2)_2PbI_3$", *Adv. Mater.*, **2014**, *26*, 4991-4998.
66. J. H. Im, I. H. Jang, N. Pellet, M. Graetzel, N. G. Park, "Growth of $CH_3NH_3PbI_3$ cuboids with controlled size for high-efficiency perovskite solar cells", *Nat. Nanotechnol.*, **2014**, *9*, 927-932.
67. D. Bi, S. J. Moon, L. Haggman, G. Boschloo, L. Yang, E. M. J. Johansson, M. K. Nazeeruddin, M. Graetzel, A. Hagfeldt, "Using a two-step deposition technique to prepare perovskite ($CH_3NH_3PbI_3$) for thin film solar cells based on ZrO_2 and TiO_2 mesostructures", *RSC Adv.*, **2013**, *3*, 18762-18766.
68. G. E. Eperon, V. M. Burlakov, P. Docampo, A. Goriely, H. J. Snaith, "Morphological control for high performance, solution-processed planar heterojunction perovskite solar cells", *Adv. Funct. Mater.*, **2014**, *24*, 151-157.
69. L. Calió, S. Kazim, M. Graetzel, S. Ahmad, "Hole-transport materials for perovskite solar cells", *Angew. Chem. Int. Ed.*, **2016**, *55*, 14522-14545.
70. Z. Yu, L. Sun, "Recent progress on hole-transporting materials for emerging organometal halide perovskite solar cells", *Adv. Energy Mater.*, **2015**, *5*, 1500213-1500230.
71. T. P. I. Saragi, T. Spehr, A. Siebert, T. Fuhrmann-Lieker, J. Salbeck, "Spiro compounds for organic optoelectronics", *Chem. Rev.*, **2007**, *107*, 1011-1065.
72. T. Malinauskas, M. Saliba, T. Matsui, M. Daskeviciene, S. Urnikaite, P. Gratia, R. Send, H. Wonneberger, I. Bruder, M. Graetzel, V. Getautis, M.

K. Nazeeruddin, "Branched methoxydiphenylamine-substituted fluorene derivatives as hole transporting materials for high-performance perovskite solar cells", *Energy Environ. Sci.*, **2016**, *9*, 1681-1686.

73. J. Krüger, R. Plass, L. Cevey, M. Piccirelli, M. Graetzel, U. Bach, "High efficiency solid-state photovoltaic device due to inhibition of interface charge recombination", *Appl. Phys. Lett.*, **2001**, *79*, 2085-2087.
74. J. Burschka, A. Dualeh, F. Kessler, E. Baranoff, N. L. Cevey-Ha, C. Yi, M. K. Nazeeruddin, M. Graetzel, "Tris(2-(1*H*-pyrazol-1-yl)pyridine)cobalt(III) as p-type dopant for organic semiconductors and its application in highly efficient solid-state dye-sensitized solar cells", *J. Am. Chem. Soc.*, **2011**, *133*, 18042-18045.
75. J. Burschka, N. Pellet, S. J. Moon, R. Humphry-Baker, P. Gao, M. K. Nazeeruddin, M. Graetzel, "Sequential deposition as a route to high-performance perovskite-sensitized solar cells", *Nature*, **2013**, *499*, 316-319.
76. F. Huang, Y. Dkhissi, W. Huang, M. Xiao, I. Benesperi, S. Rubanov, Y. Zhu, X. Lin, L. Jiang, Y. Zhou, A. Gray-Weale, J. Etheridge, C. R. Mcneill, R. A. Caruso, U. Bach, L. Spiccia, Y. B. Cheng, "Gas-assisted preparation of lead iodide perovskite films consisting of a monolayer of single crystalline grains for high efficiency planar solar cells", *Nano Energy*, **2014**, *10*, 10-18.
77. D. Bi, W. Tress, M. I. Dar, P. Gao, J. Luo, C. Renevier, K. Schenk, A. Abate, F. Giordano, J. P. Correa Baena, J. D. Decoppet, S. M. Zakeeruddin, M. K. Nazeeruddin, M. Graetzel, A. Hagfeldt, "Efficient luminescent solar cells based on tailored mixed-cation perovskites", *Sci. Adv.*, **2016**, *2*.
78. M. Saliba, T. Matsui, J. Y. Seo, K. Domanski, J. P. Correa-Baena, M. K. Nazeeruddin, S. M. Zakeeruddin, W. Tress, A. Abate, A. Hagfeldt, M. Graetzel, "Cesium-containing triple cation perovskite solar cells: Improved stability, reproducibility and high efficiency", *Energy Environ. Sci.*, **2016**, *9*, 1989-1997.
79. A. Gheno, S. Vedraine, B. Ratier, J. Bouclé, "Π-conjugated materials as the hole-transporting layer in perovskite solar cells", *Metals*, **2016**, *6*, 21.
80. K. Zhang, L. Wang, Y. Liang, S. Yang, J. Liang, F. Cheng, J. Chen, "A thermally and electrochemically stable organic hole-transporting material with an adamantane central core and triarylamine moieties", *Synth. Met.*, **2012**, *162*, 490-496.
81. L. P. Hammett, "The effect of structure upon the reactions of organic compounds. Benzene derivatives", *J. Am. Chem. Soc.*, **1937**, *59*, 96-103.
82. N. J. Jeon, H. G. Lee, Y. C. Kim, J. Seo, J. H. Noh, J. Lee, S. I. Seok, "*O*-methoxy substituents in spiro-ometad for efficient inorganic–organic hybrid perovskite solar cells", *J. Am. Chem. Soc.*, **2014**, *136*, 7837-7840.

83. M. Franckevicius, A. Mishra, F. Kreuzer, J. Luo, S. M. Zakeeruddin, M. Graetzel, "A dopant-free spirobi[cyclopenta[2,1-*b*:3,4-*b'*]dithiophene] based hole-transport material for efficient perovskite solar cells", *Mater. Horiz.*, **2015**, *2*, 613-618.
84. D. Bi, B. Xu, P. Gao, L. Sun, M. Graetzel, A. Hagfeldt, "Facile synthesized organic hole transporting material for perovskite solar cell with efficiency of 19.8 %", *Nano Energy*, **2016**, *23*, 138-144.
85. P. Ganesan, K. Fu, P. Gao, I. Raabe, K. Schenk, R. Scopelliti, J. Luo, L. H. Wong, M. Graetzel, M. K. Nazeeruddin, "A simple spiro-type hole transporting material for efficient perovskite solar cells", *Energy Environ. Sci.*, **2015**, *8*, 1986-1991.
86. M. Saliba, S. Orlandi, T. Matsui, S. Aghazada, M. Cavazzini, J. P. Correa-Baena, P. Gao, R. Scopelliti, E. Mosconi, K. H. Dahmen, F. De angelis, A. Abate, A. Hagfeldt, G. Pozzi, M. Graetzel, M. K. Nazeeruddin, "A molecularly engineered hole-transporting material for efficient perovskite solar cells", *Nat. Energy*, **2016**, *1*, 15017.
87. N. J. Jeon, J. Lee, J. H. Noh, M. K. Nazeeruddin, M. Graetzel, S. I. Seok, "Efficient inorganic–organic hybrid perovskite solar cells based on pyrene arylamine derivatives as hole-transporting materials", *J. Am. Chem. Soc.*, **2013**, *135*, 19087-19090.
88. B. Xu, E. Sheibani, P. Liu, J. Zhang, H. Tian, N. Vlachopoulos, G. Boschloo, L. Kloo, A. Hagfeldt, L. Sun, "Carbazole-based hole-transport materials for efficient solid-state dye-sensitized solar cells and perovskite solar cells", *Adv. Mater.*, **2014**, *26*, 6629-6634.
89. Y. D. Lin, B. Y. Ke, K. M. Lee, S. H. Chang, K. H. Wang, S. H. Huang, C. G. Wu, P. T. Chou, S. Jhulki, J. N. Moorthy, Y. J. Chang, K. L. Liau, H. C. Chung, C. Y. Liu, S. S. Sun, T. J. Chow, "Hole-transporting materials based on twisted bimesitylenes for stable perovskite solar cells with high efficiency", *ChemSusChem*, **2016**, *9*, 274-279.
90. H. Nishimura, N. Ishida, A. Shimazaki, A. Wakamiya, A. Saeki, L. T. Scott, Y. Murata, "Hole-transporting materials with a two-dimensionally expanded π-system around an azulene core for efficient perovskite solar cells", *J. Am. Chem. Soc.*, **2015**, *137*, 15656-15659.
91. C. C. Mattheus, G. A. De Wijs, R. A. De Groot, T. T. M. Palstra, "Modeling the polymorphism of pentacene", *J. Am. Chem. Soc.*, **2003**, *125*, 6323-6330.
92. S. Kazim, F. J. Ramos, P. Gao, M. K. Nazeeruddin, M. Graetzel, S. Ahmad, "A dopant free linear acene derivative as a hole transport material for perovskite pigmented solar cells", *Energy Environ. Sci.*, **2015**, *8*, 1816-1823.
93. J. Zhang, Y. Hua, B. Xu, L. Yang, P. Liu, M. B. Johansson, N. Vlachopoulos, L. Kloo, G. Boschloo, E. M. J. Johansson, L. Sun, A. Hagfeldt, "The role of 3D molecular structural control in new hole

transport materials outperforming spiro-OMeTAD in perovskite solar cells", *Adv. Energy Mater.*, **2016**, *6*, 1601062-1601071.
94. T. Krishnamoorthy, F. Kunwu, P. P. Boix, H. Li, T. M. Koh, W. L. Leong, S. Powar, A. Grimsdale, M. Graetzel, N. Mathews, S. G. Mhaisalkar, "A swivel-cruciform thiophene based hole-transporting material for efficient perovskite solar cells", *J. Mater. Chem. A*, **2014**, *2*, 6305-6309.
95. H. Li, K. Fu, A. Hagfeldt, M. Graetzel, S. G. Mhaisalkar, A. C. Grimsdale, "A simple 3,4-ethylenedioxythiophene based hole-transporting material for perovskite solar cells", *Angew. Chem. Int. Ed.*, **2014**, *53*, 4085-4088.
96. M. L. Petrus, T. Bein, T. J. Dingemans, P. Docampo, "A low cost azomethine-based hole transporting material for perovskite photovoltaics", *J. Mater. Chem. A*, **2015**, *3*, 12159-12162.
97. H. Li, K. Fu, P. P. Boix, L. H. Wong, A. Hagfeldt, M. Graetzel, S. G. Mhaisalkar, A. C. Grimsdale, "Hole-transporting small molecules based on thiophene cores for high efficiency perovskite solar cells", *ChemSusChem*, **2014**, *7*, 3420-3425.
98. A. Krishna, D. Sabba, J. Yin, A. Bruno, P. P. Boix, Y. Gao, H. A. Dewi, G. G. Gurzadyan, C. Soci, S. G. Mhaisalkar, A. C. Grimsdale, "Facile synthesis of a furan–arylamine hole-transporting material for high-efficiency, mesoscopic perovskite solar cells", *Chem. Eur. J.*, **2015**, *21*, 15113-15117.
99. Y. Shi, K. Hou, Y. Wang, K. Wang, H. Ren, M. Pang, F. Chen, S. Zhang, "Two methoxyaniline-substituted dibenzofuran derivatives as hole-transport materials for perovskite solar cells", *J. Mater. Chem. A*, **2016**, *4*, 5415-5422.
100. H. Choi, H. Jo, S. Paek, K. Koh, H. M. Ko, J. K. Lee, J. Ko, "Efficient hole-transporting materials with triazole core for high-efficiency perovskite solar cells", *Chem. Asian. J.*, **2016**, *11*, 548-554.
101. K. Do, H. Choi, K. Lim, H. Jo, J. W. Cho, M. K. Nazeeruddin, J. Ko, "Star-shaped hole transporting materials with a triazine unit for efficient perovskite solar cells", *Chem. Commun.*, **2014**, *50*, 10971-10974.
102. K. Lim, M. S. Kang, Y. Myung, J. H. Seo, P. Banerjee, T. J. Marks, J. Ko, "Star-shaped hole transport materials with indeno[1,2-*b*] thiophene or fluorene on a triazine core for efficient perovskite solar cells", *J. Mater. Chem. A*, **2016**, *4*, 1186-1190.
103. H. Choi, S. Paek, N. Lim, Y. H. Lee, M. K. Nazeeruddin, J. Ko, "Efficient perovskite solar cells with 13.63 % efficiency based on planar triphenylamine hole conductors", *Chem. Eur. J.*, **2014**, *20*, 10894-10899.
104. H. Choi, S. Park, S. Paek, P. Ekanayake, M. K. Nazeeruddin, J. Ko, "Efficient star-shaped hole transporting materials with diphenylethenyl side arms for an efficient perovskite solar cell", *J. Mater. Chem. A*, **2014**, *2*, 19136-19140.

105. K. Rakstys, A. Abate, M. I. Dar, P. Gao, V. Jankauskas, G. Jacopin, E. Kamarauskas, S. Kazim, S. Ahmad, M. Graetzel, M. K. Nazeeruddin, "Triazatruxene-based hole transporting materials for highly efficient perovskite solar cells", *J. Am. Chem. Soc.*, **2015**, *137*, 16172-16178.
106. I. Cho, N. J. Jeon, O. K. Kwon, D. W. Kim, E. H. Jung, J. H. Noh, J. Seo, S. I. Seok, S. Y. Park, "Indolo[3,2-*b*]indole-based crystalline hole-transporting material for highly efficient perovskite solar cells", *Chem. Sci.*, **2017**, *8*, 734-741.
107. P. Gratia, A. Magomedov, T. Malinauskas, M. Daskeviciene, A. Abate, S. Ahmad, M. Graetzel, V. Getautis, M. K. Nazeeruddin, "A methoxydiphenylamine-substituted carbazole twin derivative: An efficient hole-transporting material for perovskite solar cells", *Angew. Chem. Int. Ed.*, **2015**, *54*, 11409-11413.
108. X. Liu, F. Kong, T. Cheng, W. Chen, Z. A. Tan, T. Yu, F. Guo, J. Chen, J. Yao, S. Dai, "Tetraphenylmethane-arylamine hole-transporting materials for perovskite solar cells", *ChemSusChem*, **2017**, 968-975.
109. P. Qin, H. Kast, M. K. Nazeeruddin, S. M. Zakeeruddin, A. Mishra, P. Bauerle, M. Graetzel, "Low band gap s,n-heteroacene-based oligothiophenes as hole-transporting and light absorbing materials for efficient perovskite-based solar cells", *Energy Environ. Sci.*, **2014**, *7*, 2981-2985.
110. C. Chen, M. Cheng, P. Liu, J. Gao, L. Kloo, L. Sun, "Application of benzodithiophene based A-D-A structured materials in efficient perovskite solar cells and organic solar cells", *Nano Energy*, **2016**, *23*, 40-49.
111. M. Cheng, B. Xu, C. Chen, X. Yang, F. Zhang, Q. Tan, Y. Hua, L. Kloo, L. Sun, "Phenoxazine-based small molecule material for efficient perovskite solar cells and bulk heterojunction organic solar cells", *Adv. Energy Mater.*, **2015**, *5*, 1401720-1401729.
112. J. H. Heo, S. H. Im, J. H. Noh, T. N. Mandal, C. S. Lim, J. A. Chang, Y. H. Lee, H.-J. Kim, A. Sarkar, M. K. Nazeeruddin, M. Graetzel, S. I. Seok, "Efficient inorganic-organic hybrid heterojunction solar cells containing perovskite compound and polymeric hole conductors", *Nat. Photonics*, **2013**, *7*, 486-491.
113. W. S. Yang, J. H. Noh, N. J. Jeon, Y. C. Kim, S. Ryu, J. Seo, S. I. Seok, "High-performance photovoltaic perovskite layers fabricated through intramolecular exchange", *Science*, **2015**, *348*, 1234-1237.
114. Y. Guo, C. Liu, K. Inoue, K. Harano, H. Tanaka, E. Nakamura, "Enhancement in the efficiency of an organic-inorganic hybrid solar cell with a doped P3HT hole-transporting layer on a void-free perovskite active layer", *J. Mater. Chem. A*, **2014**, *2*, 13827-13830.
115. J. Kim, G. Kim, T. K. Kim, S. Kwon, H. Back, J. Lee, S. H. Lee, H. Kang, K. Lee, "Efficient planar-heterojunction perovskite solar cells achieved via

interfacial modification of a sol-gel zno electron collection layer", *J. Mater. Chem. A*, **2014**, *2*, 17291-17296.
116. F. J. Ramos, M. Ince, M. Urbani, A. Abate, M. Graetzel, S. Ahmad, T. Torres, M. K. Nazeeruddin, "Non-aggregated Zn(II)octa(2,6-diphenylphenoxy) phthalocyanine as a hole transporting material for efficient perovskite solar cells", *Dalton Trans.*, **2015**, *44*, 10847-10851.
117. M. Sun, S. Wang, Y. Xiao, Z. Song, X. Li, "Titanylphthalocyanine as hole transporting material for perovskite solar cells", *J. Energy Chem.*, **2015**, *24*, 756-761.
118. G. Sfyri, C. V. Kumar, Y. L. Wang, Z. X. Xu, C. A. Krontiras, P. Lianos, "Tetra methyl substituted Cu(II) phthalocyanine as alternative hole transporting material for organometal halide perovskite solar cells", *Appl. Surf. Sci.*, **2016**, *360, Part B*, 767-771.
119. K. T. Cho, O. Trukhina, C. Roldán-Carmona, M. Ince, P. Gratia, G. Grancini, P. Gao, T. Marszalek, W. Pisula, P. Y. Reddy, T. Torres, M. K. Nazeeruddin, "Molecularly engineered phthalocyanines as hole-transporting materials in perovskite solar cells reaching power conversion efficiency of 17.5 %", *Adv. Energy Mater.*, **2016**, 1601733-1601740.
120. J. A. Christians, R. C. M. Fung, P. V. Kamat, "An inorganic hole conductor for organo-lead halide perovskite solar cells. Improved hole conductivity with copper iodide", *J. Am. Chem. Soc.*, **2014**, *136*, 758-764.
121. S. Chavhan, O. Miguel, H. J. Grande, V. Gonzalez-Pedro, R. S. Sanchez, E. M. Barea, I. Mora-Sero, R. Tena-Zaera, "Organo-metal halide perovskite-based solar cells with CuSCN as the inorganic hole selective contact", *J. Mater. Chem. A*, **2014**, *2*, 12754-12760.
122. S. Ye, W. Sun, Y. Li, W. Yan, H. Peng, Z. Bian, Z. Liu, C. Huang, "CuSCN-based inverted planar perovskite solar cell with an average PCE of 15.6 %", *Nano Lett.*, **2015**, *15*, 3723-3728.
123. L. Li, E. A. Gibson, P. Qin, G. Boschloo, M. Gorlov, A. Hagfeldt, L. Sun, "Double-layered NiO photocathodes for p-type DSSCs with record IPCE", *Adv. Mater.*, **2010**, *22*, 1759-1762.
124. J. R. Manders, S. W. Tsang, M. J. Hartel, T.-H. Lai, S. Chen, C. M. Amb, J. R. Reynolds, F. So, "Solution-processed nickel oxide hole transport layers in high efficiency polymer photovoltaic cells", *Adv. Funct. Mater.*, **2013**, *23*, 2993-3001.
125. K. C. Wang, P. S. Shen, M. H. Li, S. Chen, M. W. Lin, P. Chen, T. F. Guo, "Low-temperature sputtered nickel oxide compact thin film as effective electron blocking layer for mesoscopic $NiO/CH_3NH_3PbI_3$ perovskite heterojunction solar cells", *ACS Appl. Mater. Interfaces*, **2014**, *6*, 11851-11858.
126. W. Chen, Y. Wu, Y. Yue, J. Liu, W. Zhang, X. Yang, H. Chen, E. Bi, I. Ashraful, M. Graetzel, L. Han, "Efficient and stable large-area perovskite

solar cells with inorganic charge extraction layers", *Science,* **2015**, *350*, 944-948.
127. I. S. Yang, M. R. Sohn, S. D. Sung, Y. J. Kim, Y. J. Yoo, J. Kim, W. I. Lee, "Formation of pristine CuSCN layer by spray deposition method for efficient perovskite solar cell with extended stability", *Nano Energy,* **2017**, *32*, 414-421.
128. J. Ge, C. R. Grice, Y. Yan, "Cu-based quaternary chalcogenide Cu_2BaSnS_4 thin films acting as hole transport layers in inverted perovskite $CH_3NH_3PbI_3$ solar cells", *J. Mater. Chem. A,* **2017**, *5*, 2920-2928.
129. S. F. Völker, S. Collavini, J. L. Delgado, "Organic charge carriers for perovskite solar cells", *ChemSusChem,* **2015**, *8*, 3012-3028.
130. J. Wang, K. Liu, L. Ma, X. Zhan, "Triarylamine: Versatile platform for organic, dye-sensitized, and perovskite solar cells", *Chem. Rev.,* **2016**, *116*, 14675-14725.
131. X. Zhu, Q. Zhang, W. Su, "Solvent-free *N*-arylation of amines with arylboronic acids under ball milling conditions", *RSC Adv.,* **2014**, *4*, 22775-22778.
132. V. Merz, W. Weith, "Vermischte mittheilungen", *Berichte der deutschen chemischen Gesellschaft,* **1873**, *6*, 1511-1520.
133. C. Y. Chen, J. G. Chen, S. J. Wu, J. Y. Li, C. G. Wu, K. C. Ho, "Multifunctionalized ruthenium-based supersensitizers for highly efficient dye-sensitized solar cells", *Angew. Chem. Int. Ed.,* **2008**, *47*, 7342-7345.
134. C. W. Chu, J. Ouyang, J. H. Tseng, Y. Yang, "Organic donor–acceptor system exhibiting electrical bistability for use in memory devices", *Adv. Mater.,* **2005**, *17*, 1440-1443.
135. Y. Dong, J. W. Y. Lam, A. Qin, J. Liu, Z. Li, B. Z. Tang, J. Sun, H. S. Kwok, "Aggregation-induced emissions of tetraphenylethene derivatives and their utilities as chemical vapor sensors and in organic light-emitting diodes", *Appl. Phys. Lett.,* **2007**, *91*, 011111.
136. J. Luo, Z. Xie, J. W. Y. Lam, L. Cheng, H. Chen, C. Qiu, H. S. Kwok, X. Zhan, Y. Liu, D. Zhu, B. Z. Tang, "Aggregation-induced emission of 1-methyl-1,2,3,4,5-pentaphenylsilole", *Chem. Commun.*, **2001**, 1740-1741.
137. K. K. T. Förster, *Int. J. Res. Phys. Chem. Chem. Phys.*, **1954**, *1*, 275.
138. K. Y. Pu, B. Liu, "Conjugated polyelectrolytes as light-up macromolecular probes for heparin sensing", *Adv. Funct. Mater.,* **2009**, *19*, 277-284.
139. Z. Zhao, J. W. Y. Lam, B. Z. Tang, "Tetraphenylethene: A versatile AIE building block for the construction of efficient luminescent materials for organic light-emitting diodes", *J. Mater. Chem. A*, **2012**, *22*, 23726-23740.
140. Y. Sagara, T. Kato, "Mechanically induced luminescence changes in molecular assemblies", *Nat. Chem.,* **2009**, *1*, 605-610.
141. Z. Chi, X. Zhang, B. Xu, X. Zhou, C. Ma, Y. Zhang, S. Liu, J. Xu, "Recent advances in organic mechanofluorochromic materials", *Chem. Soc. Rev.,* **2012**, *41*, 3878-3896.

142. F. G. Brunetti, X. Gong, M. Tong, A. J. Heeger, F. Wudl, "Strain and Hückel aromaticity: Driving forces for a promising new generation of electron acceptors in organic electronics", *Angew. Chem. Int. Ed.*, **2010**, *49*, 532-536.
143. M. Rabinovitz, I. Agranat, A. Weitzen-Dagan, "Pathways for thermal z,e isomerization in tetrabenzopentafulvalenes: Transition-state stabilization combined with ground-state destabilization", *Tetrahedron Lett.*, **1974**, *15*, 1241-1244.
144. Y. Cohen, J. Klein, M. Rabinovitz, "Stable polycyclic anions: Dianions from overcrowded ethylenes", *J. Chem. Soc., Chem. Commun.*, **1986**, 1071-1073.
145. B. L. Feringa, A. M. Schoevaars, W. F., Jager, B. De Lange, N. P. M. Huck, "Switching of chirality by light", *Enantiomer*, **1996**, *273*, 325-335.
146. P. U. Biedermann, J. J. Stezowski, I. Agranat, "Conformational space and dynamic stereochemistry of overcrowded homomerous bistricyclic aromatic enes -a theoretical study", *Eur. J. Org. Chem.*, **2001**, *2001*, 15-34.
147. H. Choi, K. Do, S. Park, J. S. Yu, J. Ko, "Efficient hole transporting materials with two or four *N*,*N*-di(4-methoxyphenyl)aminophenyl arms on an ethene unit for perovskite solar cells", *Chem. Eur. J.*, **2015**, *21*, 15919-15923.
148. A. Levy, M. Goldschmidt, I. Agranat, "A simple facile synthesis of bifluorenylidenes", *Lett. Org. Chem.*, **2006**, *3*, 579-584.
149. T. Malinauskas, D. Tomkute-Luksiene, R. Sens, M. Daskeviciene, R. Send, H. Wonneberger, V. Jankauskas, I. Bruder, V. Getautis, "Enhancing thermal stability and lifetime of solid-state dye-sensitized solar cells via molecular engineering of the hole-transporting material spiro-OMeTAD", *ACS Appl. Mater. Interfaces*, **2015**, *7*, 11107-11116.
150. M. C. Alonso García, J. L. Balenzategui, "Estimation of photovoltaic module yearly temperature and performance based on nominal operation cell temperature calculations", *Renew. Energ.*, **2004**, *29*, 1997-2010.
151. A. Mishra, P. Bäuerle, "Small molecule organic semiconductors on the move: Promises for future solar energy technology", *Angew. Chem. In. Ed.*, **2012**, *51*, 2020-2067.
152. H. Bronstein, Z. Chen, R. S. Ashraf, W. Zhang, J. Du, J. R. Durrant, P. Shakya Tuladhar, K. Song, S. E. Watkins, Y. Geerts, M. M. Wienk, R. a. J. Janssen, T. Anthopoulos, H. Sirringhaus, M. Heeney, I. Mcculloch, "Thieno[3,2-*b*]thiophene-diketopyrrolopyrrole-containing polymers for high-performance organic field-effect transistors and organic photovoltaic devices", *J. Am. Chem. Soc.*, **2011**, *133*, 3272-3275.
153. P. Liu, Y. Wu, H. Pan, Y. Li, S. Gardner, B. S. Ong, S. Zhu, "Novel high-performance liquid-crystalline organic semiconductors for thin-film transistors", *Chem. Mater.*, **2009**, *21*, 2727-2732.

154. J. H. Seo, E. B. Namdas, A. Gutacker, A. J. Heeger, G. C. Bazan, "Solution-processed organic light-emitting transistors incorporating conjugated polyelectrolytes", *Adv. Funct. Mater.*, **2011**, *21*, 3667-3672.
155. Y. Nicolas, P. Blanchard, E. Levillain, M. Allain, N. Mercier, J. Roncali, "Planarized star-shaped oligothiophenes with enhanced π-electron delocalization", *Org. Lett.*, **2004**, *6*, 273-276.
156. T. Taerum, O. Lukoyanova, R. G. Wylie, D. F. Perepichka, "Synthesis, polymerization, and unusual properties of new star-shaped thiophene oligomers", *Org. Lett.*, **2009**, *11*, 3230-3233.
157. T. Kashiki, S. Shinamura, M. Kohara, E. Miyazaki, K. Takimiya, M. Ikeda, H. Kuwabara, "One-pot synthesis of benzo[*b*]thiophenes and benzo[*b*]selenophenes from *o*-halo-substituted ethynylbenzenes: Convenient approach to mono-, bis-, and tris-chalcogenophene-annulated benzenes", *Org. Lett.*, **2009**, *11*, 2473-2475.
158. R. De Bettignies, Y. Nicolas, P. Blanchard, E. Levillain, J. M. Nunzi, J. Roncali, "Planarized star-shaped oligothiophenes as a new class of organic semiconductors for heterojunction solar cells", *Adv. Mater.*, **2003**, *15*, 1939-1943.
159. R. Proetzsch, D. Bieniek, F. Korte, " Hochdruckreaktionen IV: Verhalten von thiolactonen unter hohen drucken ", *Tetrahedron Lett.*, **1972**, *13*, 543-544.
160. X. Guo, S. Wang, V. Enkelmann, M. Baumgarten, K. Müllen, "Making benzotrithiophene a stronger electron donor", *Org. Lett.*, **2011**, *13*, 6062-6065.
161. N. Jayasuriya, J. Kagan, J. E. Owens, E. P. Kornak, D. M. Perrine, "Photocyclization of terthiophenes", *J. Org. Chem.*, **1989**, *54*, 4203-4205.
162. T. Kashiki, M. Kohara, I. Osaka, E. Miyazaki, K. Takimiya, "Synthesis and characterization of benzo[1,2-*b*:3,4-*b′*:5,6-*b″*]trithiophene (BTT) oligomers", *J. Org. Chem.*, **2011**, *76*, 4061-4070.
163. L. Meng, F. Wu, H. Liu, B. Zhao, J. Zhang, J. Zhong, Y. Pei, H. Chen, S. Tan, " Novel solution-processible small molecules based on benzo[1,2-*b*:3,4-*b′*:5,6-*b″*]trithiophene for effective organic photovoltaics with high open-circuit voltage ", *RSC Adv.*, **2015**, *5*, 14540-14546.
164. M. Nakano, K. Takimiya, "Sodium sulfide-promoted thiophene-annulations: Powerful tools for elaborating organic semiconducting materials", *Chem. Mater.*, **2017**, *29*, 256-264.
165. C. B. Nielsen, E. H. Sohn, D. J. Cho, B. C. Schroeder, J. Smith, M. Lee, T. D. Anthopoulos, K. Song, I. Mcculloch, "Improved field-effect transistor performance of a benzotrithiophene polymer through ketal cleavage in the solid state", *ACS Appl. Mater. Interfaces*, **2013**, *5*, 1806-1810.
166. G. Zhang, M. Zhu, J. Guo, J. Ma, X. Wang, H. Lu, L. Qiu, "Benzodithiophene and benzotrithiophene-based conjugated polymers for

organic thin-film transistors application: Impact of conjugated- and acyl-side chain", *Org. Electron.*, **2014**, *15*, 2608-2615.
167. C. B. Nielsen, J. M. Fraser, B. C. Schroeder, J. Du, A. J. P. White, W. Zhang, I. Mcculloch, "Benzotrithiophene - a planar, electron-rich building block for organic semiconductors", *Org. Lett.*, **2011**, *13*, 2414-2417.
168. M. L. Keshtov, Y. Geng, S. A. Kuklin, A. R. Khokhlov, E. N. Koukaras, G. D. Sharma, "Synthesis, optical and electrochemical properties new donor–acceptor (D-A) copolymers based on benzo[1,2-*b*:3,4-*b′*:6,5-*b″*] trithiophene donor and different acceptor units: Application as donor for photovoltaic devices", *Org. Electron.*, **2015**, *17*, 167-177.
169. C. B. Nielsen, R. S. Ashraf, S. Rossbauer, T. Anthopoulos, I. Mcculloch, "Post-polymerization ketalization for improved organic photovoltaic materials", *Macromolecules*, **2013**, *46*, 7727-7732.
170. X. Guo, S. R. Puniredd, M. Baumgarten, W. Pisula, K. Müllen, "Benzotrithiophene-based donor–acceptor copolymers with distinct supramolecular organizations", *J. Am. Chem. Soc.*, **2012**, *134*, 8404-8407.
171. A. Prlj, B. F. E. Curchod, C. Corminboeuf, "Excited state dynamics of thiophene and bithiophene: New insights into theoretically challenging systems", *Phys. Chem. Chem. Phys.*, **2015**, *17*, 14719-14730.
172. J. Arago, P. M. Viruela, J. Gierschner, E. Orti, B. Milian-Medina, "Oligothienoacenes versus oligothiophenes: Impact of ring fusion on the optical properties", *Phys. Chem. Chem. Phys.*, **2011**, *13*, 1457-1465.
173. H. Tsuji, G. Cantagrel, Y. Ueda, T. Chen, L. J. Wan, E. Nakamura, "Synthesis of benzotrifuran and benzotripyrrole derivatives and molecular orientations on the surface and in the solid state", *Chem. Asian J.*, **2013**, *8*, 2377-2382.
174. H. Tsuji, C. Mitsui, Y. Sato, E. Nakamura, "Bis(carbazolyl)benzodifuran: A high-mobility ambipolar material for homojunction organic light-emitting diode devices", *Adv. Mater.*, **2009**, *21*, 3776-3779.
175. H. Tsuji, Y. Yokoi, C. Mitsui, L. Ilies, Y. Sato, E. Nakamura, "Tetraaryl-substituted benzo[1,2-*b*:4,5-*b′*]dipyrroles: Synthesis, properties, and applications to hole-injection materials in OLED devices", *Chem. Asian. J.* , **2009**, *4*, 655-657.
176. C. Mitsui, J. Soeda, K. Miwa, H. Tsuji, J. Takeya, E. Nakamura, "Naphtho[2,1-*b*:6,5-*b′*]difuran: A versatile motif available for solution-processed single-crystal organic field-effect transistors with high hole mobility", *J. Am. Chem. Soc.*, **2012**, *134*, 5448-5451.
177. H. Tsuji, C. Mitsui, L. Ilies, Y. Sato, E. Nakamura, "Synthesis and properties of 2,3,6,7-tetraarylbenzo[1,2-*b*:4,5-*b′*]difurans as hole-transporting material", *J. Am. Chem. Soc.*, **2007**, *129*, 11902-11903.
178. Y. Liu, C. A. Di, C. Du, Y. Liu, K. Lu, W. Qiu, G. Yu, "Synthesis, structures, and properties of fused thiophenes for organic field-effect transistors", *Chem. Eur. J.*, **2010**, *16*, 2231-2239.

179. J. H. Im, C. R. Lee, J. W. Lee, S. W. Park, N. G. Park, "6.5 % efficient perovskite quantum-dot-sensitized solar cell", *Nanoscale,* **2011**, *3*, 4088-4093.
180. A. A. F. Giordano, J. P. Correa, M. Saliba, T. Matsui, S. H. Im, S. M. Zakeeruddin, M. K. Nazeeruddin, A. Hagfeldt, M. Graetzel, "Enhanced electronic properties in mesoporous TiO_2 via lithium doping for high-efficiency perovskite solar cells", *Nat. Comm.,* **2016**, *7*, 10379-10385.
181. N. J. Jeon, J. H. Noh, Y. C. Kim, W. S. Yang, S. Ryu, S. I. Seok, "Solvent engineering for high-performance inorganic–organic hybrid perovskite solar cells", *Nat. Mater.,* **2014**, *13*, 897-903.
182. N. J. Jeon, J. H. Noh, W. S. Yang, Y. C. Kim, S. Ryu, J. Seo, S. I. Seok, "Compositional engineering of perovskite materials for high-performance solar cells", *Nature,* **2015**, *517*, 476-480.
183. M. Salado, J. Idigoras, L. Calio, S. Kazim, M. K. Nazeeruddin, J. A. Anta, S. Ahmad, "Interface play between perovskite and hole selective layer on the performance and stability of perovskite solar cells", *ACS Appl. Mater. Interfaces,* **2016**, *8*, 34414-34421.
184. M. A. Topchiy, P. B. Dzhevakov, M. S. Rubina, O. S. Morozov, A. F. Asachenko, M. S. Nechaev, "Solvent-free Buchwald-Hartwig (hetero)arylation of anilines, diarylamines, and dialkylamines mediated by expanded-ring *N*-heterocyclic carbene palladium complexes", *Eur. J. Org. Chem.*, **2016**, *2016*, 1908-1914.
185. A. Bucinskas, G. Bagdziunas, A. Tomkeviciene, D. Volynyuk, N. Kostiv, D. Gudeika, V. Jankauskas, M. Rutkis, J. V. Grazulevicius, "Structure-property relationship of isomeric diphenylethenyl-disubstituted dimethoxycarbazoles", *RSC Adv.*, **2015**, *5*, 49577-49589.
186. H. C. Schmidt, M. Spulber, M. Neuburger, C. G. Palivan, M. Meuwly, O. S. Wenger, "Charge transfer pathways in three isomers of naphthalene-bridged organic mixed valence compounds", *J. Org. Chem.,* **2016**, *81*, 595-602.
187. L. Yu, J. Xi, H. T. Chan, T. Su, L. J. Antrobus, B. Tong, Y. Dong, W. K. Chan, D. L. Phillips, "Novel organic D-π-2A sensitizer for dye sensitized solar cells and its electron transfer kinetics on TiO_2 surface", *J. Phys. Chem. C,* **2013**, *117*, 2041-2052.
188. M. Ludwiczak, M. Majchrzak, M. Bayda, B. Marciniak, M. Kubicki, B. Marciniec, "Stereoselective synthesis and luminescence properties of novel trans-regular n-alkylcarbazolylene–silylene–vinylene polymers", *J. Organomet. Chem.,* **2014**, *750*, 150-161.
189. V. Mimaite, J. V. Grazulevicius, R. Laurinaviciute, D. Volyniuk, V. Jankauskas, G. Sini, "Can hydrogen bonds improve the hole-mobility in amorphous organic semiconductors? Experimental and theoretical insights", *J. Mater. Chem. C,* **2015**, *3*, 11660-11674.

190. K. Yuan, P. Guo-Wang, T. Hu, L. Shi, R. Zeng, M. Forster, T. Pichler, Y. Chen, U. Scherf, "Nanofibrous and graphene-templated conjugated microporous polymer materials for flexible chemosensors and supercapacitors", *Chem. Mater.*, **2015**, *27*, 7403-7411.
191. K. Brunner, A. Van Dijken, H. Börner, J. J. a. M. Bastiaansen, N. M. M. Kiggen, B. M. W. Langeveld, "Carbazole compounds as host materials for triplet emitters in organic light-emitting diodes: Tuning the homo level without influencing the triplet energy in small molecules", *J. Am. Chem. Soc.*, **2004**, *126*, 6035-6042.
192. J. J. Wolff, F. Gredel, T. Oeser, H. Irngartinger, H. Pritzkow, "Crystal engineering with symmetrical threefold acceptor-substituted triaminobenzenes", *Chem. Eur. J.*, **1999**, *5*, 29-38.
193. N. Jayasuriya, J. Kagan, "The synthesis of bithienyls and terthienyls by nickel-catalyzed coupling of grignard reagents", *Heterocycles*, **1986**, *24*, 2261-2264.
194. G. Hennrich, A. M. Echavarren, "New persubstituted 1,3,5-trisethynyl benzenes via sonogashira coupling", *Tetrahedron Lett.*, **2004**, *45*, 1147-1149.
195. B. A. Coombs, S. R. Rutter, A. E. Goeta, H. A. Sparkes, A. S. Batsanov, A. Beeby, "2,5-bis(arylethynyl)thienyl systems: Preparation and photophysical properties. Part II", *RSC Adv.*, **2012**, *2*, 1870-1876.
196. Y. Liu, Q. Liu, X. Zhang, L. Ai, Y. Wang, R. Peng, Z. Ge, "Synthesis, crystal structure, and polymerization of butterfly-shaped thieno[3,2-*b*]thiophene oligomers", *New J. Chem.*, **2013**, *37*, 1189-1194.
197. C. Y. Chang, W. K. Huang, Y. C. Chang, "Highly-efficient and long-term stable perovskite solar cells enabled by a cross-linkable n-doped hybrid cathode interfacial layer", *Chem. Mater.*, **2016**, *28*, 6305-6312.
198. D. Zhao, Z. Zhu, M. Y. Kuo, C.-C. Chueh, A. K. Y. Jen, "Hexaazatrinaphthylene derivatives: Efficient electron-transporting materials with tunable energy levels for inverted perovskite solar cells", *Angew. Chem. Int. Ed.*, **2016**, *55*, 8999-9003.
199. X. Meng, Y. Bai, S. Xiao, T. Zhang, C. Hu, Y. Yang, X. Zheng, S. Yang, "Designing new fullerene derivatives as electron transporting materials for efficient perovskite solar cells with improved moisture resistance", *Nano Energy*, **2016**, *30*, 341-346.
200. M. Ye, X. Hong, F. Zhang, X. Liu, "Recent advancements in perovskite solar cells: Flexibility, stability and large scale", *J. Mater. Chem. A*, **2016**, *4*, 6755-6771.
201. S. Chang, G. D. Han, J. G. Weis, H. Park, O. Hentz, Z. Zhao, T. M. Swager, S. Gradečak, "Transition metal-oxide free perovskite solar cells enabled by a new organic charge transport layer", *ACS Appl. Mater. Interfaces*, **2016**, *8*, 8511-8519.

202. J. Y. Jeng, Y. F. Chiang, M. H. Lee, S. R. Peng, T. F. Guo, P. Chen, T. C. Wen, "$CH_3NH_3PbI_3$ perovskite/fullerene planar-heterojunction hybrid solar cells", *Adv. Mater.*, **2013**, *25*, 3727-3732.
203. S. Sun, T. Salim, N. Mathews, M. Duchamp, C. Boothroyd, G. Xing, T. C. Sum, Y. M. Lam, "The origin of high efficiency in low-temperature solution-processable bilayer organometal halide hybrid solar cells", *Energy Environ. Sci.*, **2014**, *7*, 399-407.
204. O. Malinkiewicz, A. Yella, Y. H. Lee, G. M. Espallargas, M. Graetzel, M. K. Nazeeruddin, H. J. Bolink, "Perovskite solar cells employing organic charge-transport layers", *Nat. Photonics*, **2014**, *8*, 128-132.
205. Q. Dong, Y. Yuan, Y. Shao, Y. Fang, Q. Wang, J. Huang, "Abnormal crystal growth in $CH_3NH_3PbI_{3-x}Cl_x$ using a multi-cycle solution coating process", *Energy Environ. Sci.*, **2015**, *8*, 2464-2470.
206. L. Zhao, D. Luo, J. Wu, Q. Hu, W. Zhang, K. Chen, T. Liu, Y. Liu, Y. Zhang, F. Liu, T. P. Russell, H. J. Snaith, R. Zhu, Q. Gong, "High-performance inverted planar heterojunction perovskite solar cells based on lead acetate precursor with efficiency exceeding 18 %", *Adv. Funct. Mater.*, **2016**, *26*, 3508-3514.
207. P. W. Liang, C. C. Chueh, S. T. Williams, A. K. Y. Jen, "Roles of fullerene-based interlayers in enhancing the performance of organometal perovskite thin-film solar cells", *Adv. Energy Mater.*, **2015**, *5*, 1402321-1402328.
208. P. M. Allemand, A. Koch, F. Wudl, Y. Rubin, F. Diederich, M. M. Alvarez, S. J. Anz, R. L. Whetten, "Two different fullerenes have the same cyclic voltammetry", *J. Am. Chem. Soc.*, **1991**, *113*, 1050-1051.
209. B. C. Thompson, J. M. J. Fréchet, "Polymer–fullerene composite solar cells", *Angew. Chem. Int. Ed.*, **2008**, *47*, 58-77.
210. M. T. Rispens, A. Meetsma, R. Rittberger, C. J. Brabec, N. S. Sariciftci, J. C. Hummelen, "Influence of the solvent on the crystal structure of PCBM and the efficiency of MDMO-PPV:PCBM 'plastic' solar cells", *Chem. Commun.*, **2003**, 2116-2118.
211. J. C. Hummelen, B. W. Knight, F. Lepeq, F. Wudl, J. Yao, C. L. Wilkins, "Preparation and characterization of fulleroid and methanofullerene derivatives", *J. Org. Chem.*, **1995**, *60*, 532-538.
212. G. Yu, J. Gao, J. C. Hummelen, F. Wudl, A. J. Heeger, "Polymer photovoltaic cells: Enhanced efficiencies via a network of internal donor-acceptor heterojunctions", *Science*, **1995**, *270*, 1789-1791.
213. P. Gao, M. Graetzel, M. K. Nazeeruddin, "Organohalide lead perovskites for photovoltaic applications", *Energy Environ. Sci.*, **2014**, *7*, 2448-2463.
214. W. Ma, C. Yang, X. Gong, K. Lee, A. J. Heeger, "Thermally stable, efficient polymer solar cells with nanoscale control of the interpenetrating network morphology", *Adv. Funct. Mater.*, **2005**, *15*, 1617-1622.

215. X. Yang, J. Loos, S. C. Veenstra, W. J. H. Verhees, M. M. Wienk, J. M. Kroon, M. A. J. Michels, R. A. J. Janssen, "Nanoscale morphology of high-performance polymer solar cells", *Nano Lett.*, **2005**, *5*, 579-583.
216. C. Tao, S. Neutzner, L. Colella, S. Marras, A. R. Srimath Kandada, M. Gandini, M. D. Bastiani, G. Pace, L. Manna, M. Caironi, C. Bertarelli, A. Petrozza, "17.6 % stabilized efficiency in low-temperature processed planar perovskite solar cells", *Energy Environ. Sci.*, **2015**, *8*, 2365-2370.
217. Y. C. Huang, S. Y. Chuang, M. C. Wu, H. L. Chen, C. W. Chen, W. F. Su, "Quantitative nanoscale monitoring the effect of annealing process on the morphology and optical properties of poly(3-hexylthiophene)/[6,6]-phenyl C_{61}-butyric acid methyl ester thin film used in photovoltaic devices", *J. Appl. Phys.* , **2009**, *106*, 034506.
218. M. M. Wienk, J. M. Kroon, W. J. H. Verhees, J. Knol, J. C. Hummelen, P. A. Van Hal, R. a. J. Janssen, "Efficient methano[70]fullerene/MDMO-PPV bulk heterojunction photovoltaic cells", *Angew. Chem. Int. Ed.*, **2003**, *42*, 3371-3375.
219. C. H. Chiang, Z. L. Tseng, C. G. Wu, "Planar heterojunction perovskite/$PC_{71}BM$ solar cells with enhanced open-circuit voltage via a (2/1)-step spin-coating process", *J. Mater. Chem. A*, **2014**, *2*, 15897-15903.
220. C. Tian, E. Castro, T. Wang, G. Betancourt-Solis, G. Rodriguez, L. Echegoyen, "Improved performance and stability of inverted planar perovskite solar cells using fulleropyrrolidine layers", *ACS Appl. Mater. Interfaces*, **2016**, *8*, 31426-31432.
221. Y. Matsuo, J. Kawai, H. Inada, T. Nakagawa, H. Ota, S. Otsubo, E. Nakamura, "Addition of dihydromethano group to fullerenes to improve the performance of bulk heterojunction organic solar cells", *Adv. Mater.*, **2013**, *25*, 6266-6269.
222. M. C. Scharber, D. Mühlbacher, M. Koppe, P. Denk, C. Waldauf, A. J. Heeger, C. J. Brabec, "Design rules for donors in bulk-heterojunction solar cells-towards 10 % energy-conversion efficiency", *Adv. Mater.*, **2006**, *18*, 789-794.
223. L. J. A. Koster, V. D. Mihailetchi, P. W. M. Blom, "Ultimate efficiency of polymer/fullerene bulk heterojunction solar cells", *Appl. Phys. Lett.*, **2006**, *88*, 093511.
224. J. Huang, X. Yu, J. Xie, C. Z. Li, Y. Zhang, D. Xu, Z. Tang, C. Cui, D. Yang, "Fulleropyrrolidinium iodide as an efficient electron transport layer for air-stable planar perovskite solar cells", *ACS Appl. Mater. Interfaces*, **2016**, *8*, 34612-34619.
225. A. Anctil, C. W. Babbitt, R. P. Raffaelle, B. J. Landi, "Material and energy intensity of fullerene production", *Environ. Sci. Technol.*, **2011**, *45*, 2353-2359.

226. Q. Bao, X. Liu, S. Braun, M. Fahlman, "Oxygen- and water-based degradation in [6,6]-phenyl-C_{61}-butyric acid methyl ester (PCBM) films", *Adv. Energy Mater.*, **2014**, *4*, 1301272-1301279.
227. H. Zhang, L. Xue, J. Han, Y. Q. Fu, Y. Shen, Z. Zhang, Y. Li, M. Wang, "New generation perovskite solar cells with solution-processed amino-substituted perylene diimide derivative as electron-transport layer", *J. Mater. Chem. A*, **2016**, *4*, 8724-8733.
228. S. S. Kim, S. Bae, W. H. Jo, "A perylene diimide-based non-fullerene acceptor as an electron transporting material for inverted perovskite solar cells", *RSC Adv.*, **2016**, *6*, 19923-19927.
229. S. Shao, Z. Chen, H. H. Fang, G. H. Ten Brink, D. Bartesaghi, S. Adjokatse, L. J. A. Koster, B. J. Kooi, A. Facchetti, M. A. Loi, "n-Type polymers as electron extraction layers in hybrid perovskite solar cells with improved ambient stability", *J. Mater. Chem. A*, **2016**, *4*, 2419-2426.
230. J. You, L. Meng, T. B. Song, T. F. Guo, Y. Yang, W. H. Chang, Z. Hong, H. Chen, H. Zhou, Q. Chen, Y. Liu, N. De Marco, Y. Yang, "Improved air stability of perovskite solar cells via solution-processed metal oxide transport layers", *Nat. Nanotechnol.*, **2016**, *11*, 75-81.
231. H. J. Bolink, E. Coronado, A. Forment-Aliaga, M. Lenes, A. La Rosa, S. Filippone, N. Martin, "Polymer solar cells based on diphenylmethanofullerenes with reduced sidechain length", *J. Mater. Chem.*, **2011**, *21*, 1382-1386.
232. G. Garcia-Belmonte, P. P. Boix, J. Bisquert, M. Lenes, H. J. Bolink, A. La Rosa, S. Filippone, N. Martín, "Influence of the intermediate density-of-states occupancy on open-circuit voltage of bulk heterojunction solar cells with different fullerene acceptors", *J. Phys. Chem. Lett.*, **2010**, *1*, 2566-2571.
233. A. Abrusci, S. D. Stranks, P. Docampo, H. L. Yip, A. K. Y. Jen, H. J. Snaith, "High-performance perovskite-polymer hybrid solar cells via electronic coupling with fullerene monolayers", *Nano Lett.*, **2013**, *13*, 3124-3128.
234. S. K. Hau, H. L. Yip, O. Acton, N. S. Baek, H. Ma, A. K. Y. Jen, "Interfacial modification to improve inverted polymer solar cells", *J. Mater. Chem.*, **2008**, *18*, 5113-5119.
235. S. Specklin, E. Decuypere, L. Plougastel, S. Aliani, F. Taran, "One-pot synthesis of 1,4-disubstituted pyrazoles from arylglycines via copper-catalyzed sydnone–alkyne cycloaddition reaction", *J. Org. Chem.*, **2014**, *79*, 7772-7777.
236. P. Belik, A. Guegel, A. Kraus, M. Walter, K. Muellen, "Diels-Alder adduct of C_{60} and 4-carboxy-*o*-quinodimethane: Synthesis and chemical transformations", *J. Org. Chem.*, **1995**, *60*, 3307-3310.
237. S. K. Hau, Y. J. Cheng, H. L. Yip, Y. Zhang, H. Ma, A. K. Y. Jen, "Effect of chemical modification of fullerene-based self-assembled monolayers on

the performance of inverted polymer solar cells", *ACS Appl. Mater. Interfaces*, **2010**, *2*, 1892-1902.
238. M. Keshavarz-K, B. Knight, G. Srdanov, F. Wudl, "Cyanodihydrofullerenes and dicyanodihydrofullerene: The first polar solid based on C_{60}", *J. Am. Chem. Soc.*, **1995**, *117*, 11371-11372.
239. K. Wojciechowski, S. D. Stranks, A. Abate, G. Sadoughi, A. Sadhanala, N. Kopidakis, G. Rumbles, C.-Z. Li, R. H. Friend, A. K. Y. Jen, H. J. Snaith, "Heterojunction modification for highly efficient organic–inorganic perovskite solar cells", *ACS Nano*, **2014**, *8*, 12701-12709.
240. N. K. Noel, A. Abate, S. D. Stranks, E. S. Parrott, V. M. Burlakov, A. Goriely, H. J. Snaith, "Enhanced photoluminescence and solar cell performance via lewis base passivation of organic–inorganic lead halide perovskites", *ACS Nano*, **2014**, *8*, 9815-9821.
241. O. Almora, C. Aranda, I. Zarazua, A. Guerrero, G. Garcia-Belmonte, "Noncapacitive hysteresis in perovskite solar cells at room temperature", *ACS Energy Lett.*, **2016**, *1*, 209-215.
242. Y. Zhang, H. L. Yip, O. Acton, S. K. Hau, F. Huang, A. K. Y. Jen, "A simple and effective way of achieving highly efficient and thermally stable bulk-heterojunction polymer solar cells using amorphous fullerene derivatives as electron acceptor", *Chem. Mater.*, **2009**, *21*, 2598-2600.
243. L. Zheng, Q. Zhou, X. Deng, M. Yuan, G. Yu, Y. Cao, "Methanofullerenes used as electron acceptors in polymer photovoltaic devices", *J. Phys. Chem. B*, **2004**, *108*, 11921-11926.
244. H. Zhao, X. Guo, H. Tian, C. Li, Z. Xie, Y. Geng, F. Wang, "Alkyl substituted [6,6]-thienyl-C_{61}-butyric acid methyl esters: Easily accessible acceptor materials for bulk-heterojunction polymer solar cells", *J. Mater. Chem.*, **2010**, *20*, 3092-3097.
245. P. A. Troshin, H. Hoppe, J. Renz, M. Egginger, J. Y. Mayorova, A. E. Goryachev, A. S. Peregudov, R. N. Lyubovskaya, G. Gobsch, N. S. Sariciftci, V. F. Razumov, "Material solubility-photovoltaic performance relationship in the design of novel fullerene derivatives for bulk heterojunction solar cells", *Adv. Funct. Mater.*, **2009**, *19*, 779-788.
246. C. Bingel, "Cyclopropanierung von fullerenen", *Chem. Ber.*, **1993**, *126*, 1957-1959.
247. I. Lamparth, A. Hirsch, "Water-soluble malonic acid derivatives of C_{60} with a defined three-dimensional structure", *J. Chem. Soc. Chem. Commun.*, **1994**, 1727-1728.